

**IMPACT OF SMALL-SCALE DYNAMICS ON
UPPER TROPOSPHERE LOWER STRATOSPHERE TRANSPORT
AND MIXING:
CONTRIBUTION OF GRAVITY WAVES TO VERTICAL SHEAR**



MADHURI UMBARKAR



JOHANNES GUTENBERG
UNIVERSITÄT MAINZ

Cover Picture: Visible phenomenon influenced by gravity waves, taken in-flight and over several locations by author.

**IMPACT OF SMALL-SCALE DYNAMICS ON UPPER
TROPOSPHERE LOWER STRATOSPHERE TRANSPORT
AND MIXING: CONTRIBUTION OF GRAVITY WAVES
TO VERTICAL SHEAR**

Dissertation
zur Erlangung des Grades
“Doktor der Naturwissenschaften”
am Fachbereich Physik, Mathematik und Informatik
der Johannes Gutenberg-Universität
in Mainz

MADHURI UMBARKAR

geboren am 24.03.1998 in Sangamner, Indien

Mainz, 04 März 2026



JOHANNES GUTENBERG
UNIVERSITÄT MAINZ

This work is licensed under a Creative Commons Attribution-Non Commercial 4.0 International License (CC BY 4.0, <https://creativecommons.org/licenses/by/4.0/>)

Thesis accepted on the recommendation of

1. Supervisor:
2. Co-Supervisor:

Date of the oral examination: **May 21, 2026**

Declaration

I hereby declare that I have written this thesis entitled:

"Impact of small-scale dynamics on upper troposphere lower stratosphere transport and mixing: contribution of gravity waves to vertical shear"

independently and have not used any sources or aids (including AI-based applications or tools*) other than those specified. I have documented the AI tools used in the appendix "Use of AI tools". All passages and figures derived from published or unpublished work are clearly marked, and their sources are listed in accordance with bibliographical rules. By submitting this work, I take responsibility for the overall product submitted. I am therefore also responsible for any AI-generated content that I have included in my work. I have checked the accuracy of the (AI-generated) statements and content to the best of my knowledge and belief. Throughout this research, I complied to the rules of good scientific practice as set forth in the statutes of Johannes Gutenberg University Mainz.

Madhuri Umbarkar

Mainz, 04 March 2026

Abstract

In the extratropical upper troposphere and lower stratosphere (UTLS), the composition is shaped by quasi-horizontal transport often related to the strong upper tropospheric wind, as well as to vertical transport associated with warm conveyor belts and convective systems, and turbulent mixing. These processes are governed by planetary to small-scale dynamics. In the extratropics, mixing processes are tightly linked to dynamics of baroclinic life cycles and more particularly to tropopause folds, cut-off lows and stratospheric streamers. While the large scale dynamics in this context are rather well understood, this can not be said about the associated small scale dynamics. Especially, the role of the latter to the formation of vertical shear of horizontal wind as a potential prerequisite for the occurrence of turbulence in the extratropical tropopause region is not finally understood. One of the processes driving small-scale dynamics are atmospheric gravity waves (GWs), which often occur in relation to baroclinic waves in the extratropics and can potentially dissipate in the UTLS region.

GWs can alter the thermodynamical and dynamical structure of the UTLS by enhancing static stability, thereby increasing shear and the likelihood of dynamic instability and turbulence. These interactions further globally enhance shear in the extratropical tropopause region and result in the formation of the so-called "tropopause wind shear layer". Current understanding of GWs, vertical shear and their role in dynamic instability relies largely on the numerical model studies whose results depend on the degree of idealization and on the representation of the physical processes. In contrast, airborne in situ measurements focusing on the investigation of the relation between small-scale GWs and mixing processes across the tropopause are limited. The present work addresses this issue by investigating the contribution of GWs to transport and mixing processes in the lowermost stratosphere, with a particular focus on the tropopause shear layer.

The impact of GWs on shear is addressed first, by investigating a comprehensive set of idealized baroclinic life cycle experiments using the NWP model ICON. Dry adiabatic simulations across varying spatial resolutions reveal that shear and turbulence occur particularly in regions characterized by pronounced GW activity. Further process understanding is gained from experiments incorporating physical processes like latent heating, (vertical) turbulence, and cloud microphysics. This reveal that tropospheric moist processes significantly influence the extent and occurrence of GWs, shear and potential for turbulence occurrence, mainly driven by latent heat release and stronger baroclinic wave evolution with vigorous vertical motions.

In a subsequent step, the findings from the idealized world are evaluated under realistic atmospheric conditions. The characteristics of GWs and their impact on the distribution of trace species in the lowermost stratosphere are examined for an extratropical cyclone over the North Atlantic using airborne in-situ observations, recent reanalyses and model-forecast datasets. The observed significant correlation between GW momentum flux and enhanced shear perturbations confirms the role of GWs in driving potential turbulence and facilitating trace gas exchange in the lower stratosphere. Further analysis of turbulence diagnostics suggest that GW-induced shear can be regarded as a key mechanism for the occurrence of (clear-air) turbulence in the extratropical lowermost stratosphere.

Finally, the results are put into context of quasi-climatological analysis by means of spatial and temporal co-occurrence of GWs and shear and to the formation of tropopause shear layer in the North

Atlantic lowermost stratosphere. It is revealed that the underlying dynamic instability is forced by a layer of strong vertical shear above the tropopause and is strongly influenced by GW activity. The contribution of resolved GWs to shear is found to be notable, especially in winter, where zonal GW forcing peaks at tropopause altitudes. The analysis of these processes highlights the vital role of small-scale dynamics in shaping a quasi-permanent layer of elevated shear above the extratropical tropopause and the occurrence of turbulence in this region.

In summary, this work revisits and refines the hypothesis of Kaluza et al. (2021) by providing more insights into the role of small-scale dynamics, with a focus on GWs, in the formation of the shear layer above the extratropical tropopause. Furthermore, it has been shown that small-scale processes affect the occurrence of turbulence in this region and as such have implications for the dynamics and composition of the tropopause region.

Keywords: Atmospheric gravity waves, Tropopause shear layer, Small-scale mixing, ICOSahedral Non-hydrostatic model, Clear air turbulence

Zusammenfassung

In der extratropischen oberen Troposphäre und unteren Stratosphäre (UTLS) wird die Zusammensetzung durch quasi-horizontalen Transport geprägt, der häufig mit starken Winden in der oberen Troposphäre zusammenhängt. Ferner spielen vertikaler Transport in Verbindung mit großräumigem Aufströmen vor starken Kaltfronten (sog. warm conveyor belts) und turbulente Vermischung eine wichtige Rolle. Diese Prozesse werden durch eine Reihe von Vorgängen gesteuert, die von planetarer bis zu kleinräumiger Dynamik reichen. In den Extratropen sind Mischungsprozesse eng mit der Dynamik barokliner Lebenszyklen und insbesondere mit Tropopausenfalten, isolierten Trögen und stratosphärischen Streamern verbunden. Während die großskalige Dynamik in diesem Zusammenhang gut verstanden ist, gilt dies nicht für die damit verbundenen kleinräumige Dynamik. Insbesondere ist die Rolle der kleinskaligen Dynamik bei der Bildung von vertikaler Scherung des Horizontalwindes noch wenig verstanden, genau so wie die daraus potenziell resultierende Turbulenz. Als Teil der kleinräumigen Dynamik nehmen atmosphärische Schwerewellen (GWs) in den extratropischen Tropopausenregion eine besondere Rolle ein, vor allem solche die in Verbindung mit baroklinen Lebenszyklen stehen und solche die in der UTLS dissipieren.

GWs können die thermodynamische und dynamische Struktur der UTLS verändern, indem sie die statische Stabilität erhöhen und dadurch die Wahrscheinlichkeit dynamischer Instabilität und Turbulenzen steigern. Diese Wechselwirkungen beeinflussen das Auftreten starker Scherung und stehen in Verbindung mit der Bildung einer "Tropopausennahe Windscherungsschicht". Das derzeitige Verständnis von GWs, vertikaler Scherung und ihrer Rolle bei dynamischer Instabilität stützt sich weitgehend auf numerische Modellstudien, deren Ergebnisse vom Grad der Idealisierung und der Darstellung der physikalischen Prozesse abhängen. Im Gegensatz dazu liegen nur im begrenzten Umfang flugzeuggetragene in situ Messungen vor, die es erlauben den Zusammenhang zwischen kleinräumiger Dynamik und Vermischungsprozessen an der Tropopause zu untersuchen. Die vorliegende Arbeit befasst sich mit der Frage, welchen Beitrag Schwerewellen zur Entstehung der Scherschicht an der Tropopause ausmachen und welche Konsequenzen sich daraus auf das Auftreten von Turbulenz und Vermischung ergeben.

Zu Beginn wurde der Einfluss von GWs auf die Scherung untersucht, indem eine umfassende Reihe idealisierter Experimente barokliner Lebenszyklen mit dem numerischen Wettervorhersagemodell ICON durchgeführt wurden. In Simulationen mit konservativer Dynamik, das heißt ohne Verwendung von physikalischen Parameterisierungen, wurde der Effekt der Modellauflösung untersucht. Dabei stellte sich heraus, dass Scherung und Turbulenz insbesondere in Regionen mit ausgeprägter Schwerewellenaktivität auftreten. Experimente unter Berücksichtigung der Freisetzung von latenter Wärme zeigten, dass feuchte Prozesse in der Troposphäre das Auftreten und das Ausmaß an Schwerewellen sowie Scherung und Turbulenz in der unteren Stratosphäre stark beeinflussen. Dabei kommt vor allem der stärkeren Entwicklung der baroklinen Wellen in Verbindung mit schnell aufsteigenden Luftmassen eine bedeutende Rolle zu.

Im nächsten Schritt wurde getestet, ob die Ergebnisse aus den idealisierten Experimenten auch unter realeren Bedingungen vorzufinden sind. Dafür wurde eine extratropische Zylone über dem Nordatlantik mit Hilfe von flugzeuggetragenen in situ Messungen sowie diversen Modelldatensätzen untersucht. Die Eigenschaften von GWs und ihre Auswirkungen auf die Verteilung von Spurengasen in der untersten

Stratosphäre werden während eines außertropischen Zyklons über dem Nordatlantik anhand von luftgestützten In-situ Messungen, aktuellen Reanalysen und Modellvorhersagedatensätzen untersucht. Der dabei beobachtete Zusammenhang zwischen dem GW-Impulsfluss und verstärkter Scherung und starker Scherung in Regionen von Schwerewellen deutet auf eine wichtige Rolle dieser kleinskaligen Wellen hin, auch in Verbindung mit der Entstehung von Turbulenz und der damit einhergehenden Vermischung von Luftmassen in der unteren Stratosphäre. Insbesondere haben weiterführende Analysen gezeigt, dass durch Schwerewellen-induzierter Scherung sogenannte freie Turbulenz (clear air turbulence) in der unteren Stratosphäre auftreten kann.

Schließlich werden die Ergebnisse im Rahmen einer quasi-klimatologischen Analyse unter Berücksichtigung der räumlichen und zeitlichen Koinzidenz von GWs und Scherung sowie der Bildung der Tropopausennahe Scherungsschicht über dem Nordatlantik betrachtet. Es zeigt sich, dass die zugrunde liegende dynamische Instabilität durch eine Schicht starker vertikaler Scherung oberhalb der Tropopause hervorgerufen wird, genau dort wo auch die Aktivität von Schwerewellen am höchsten ist. Der Beitrag der aufgelösten GWs zur Scherung ist insbesondere im Winter bemerkenswert, wenn die Schwerewellenaktivität in der Tropopauseregion ihr Maximum aufweist. Die Analyse dieser Prozesse unterstreicht die entscheidende Rolle der kleinräumigen Dynamik bei der Bildung einer quasi-permanenten Schicht erhöhter Scherung über der extratropischen Tropopause und dem Auftreten von Turbulenzen in dieser Region.

Zusammenfassend lässt sich sagen, dass diese Arbeit die Hypothese von Kaluza et al. (2021) überprüft und verfeinert, indem sie weitere Einblicke in die Rolle kleinräumiger Dynamik, insbesondere von GWs, bei der Bildung der Scherschicht über der extratropischen Tropopause liefert. Darüber hinaus wurde gezeigt, dass kleinräumige Prozesse das Auftreten von Turbulenzen in dieser Region beeinflussen und somit Auswirkungen auf die Dynamik und Zusammensetzung der Tropopausenregion haben.

Keywörter: Atmosphärische Schwerewellen, Tropopausennahe Windscherungsschicht, kleinräumiger Mischung, Ikosaedrisches non-hydrostatisches Modell, Clear air turbulence

List of publications and author contribution

The following publications are included as part of dissertation in the respective chapters.

- **Umbarkar, Madhuri** and Kunkel, Daniel, 2025: *Contribution of gravity waves to shear in the extratropical lowermost stratosphere: insights from idealized baroclinic life cycle experiments*, Atmospheric chemistry and Physics, 25, 10159–10182, Copernicus, published: 09 September 2025, <https://doi.org/10.5194/acp-25-10159-2025>.

D. Kunkel conceptualized the core research questions and goals. As a first author of this work, **M. Umbarkar** conducted the experiments, wrote the post-processing code, performed data analysis, prepared all the figures, and wrote the manuscript, which was revised with input from D. Kunkel.

- **Umbarkar, Madhuri**, Kunkel Daniel, Miltenberger Annette, Lachnitt Hans-Christoph, Kaluza Thorsten, Schwenk Cornelis, and Hoor, Peter, 2025: *Evidence of gravity wave contribution to vertical shear and mixing in the lower stratosphere: a WISE case study*, in review to Atmospheric chemistry and Physics, Copernicus, <https://doi.org/10.5194/egusphere-2025-5142>.

As a first author of this work, **M. Umbarkar** performed the overall data analysis, post-processing, and prepared initial draft of the manuscript. C. Schwenk and A. Miltenberger set up and conducted the ICON simulations. T. Kaluza, H.-C. Lachnitt, and P. Hoor provided the WISE campaign data. D. Kunkel supervised the study. Finally, the manuscript was then revised by **M. Umbarkar** with input from all co-authors.

- **Umbarkar, Madhuri**, Kunkel, Daniel, and Achatz, Ulrich, 2026: *Co-occurrence of gravity waves, vertical wind shear and turbulence in the lowermost stratosphere over the North Atlantic*, in review to Weather and Climate dynamics, Copernicus, <https://doi.org/10.5194/egusphere-2026-413>.

As a first author of this work, **M. Umbarkar** conceptualized the core research questions and goals, performed overall data analysis, generated the figures and wrote the manuscript. I would like to thank D. Kunkel for his supervision on the way and for his useful comments, especially when creating the first revised version of the manuscript. I further thank U. Achatz for his valuable comments and feedback on this work.

Contents

Abstract	v
Zusammenfassung	vii
1 Introduction	1
1.1 Upper troposphere lower stratosphere (UTLS) and the tropopause definitions	1
1.2 Internal gravity waves in the atmosphere	5
1.3 The extratropical transition layer (ExTL) and cross-tropopause transport	8
1.3.1 The tropopause inversion layer (TIL)	10
1.3.2 The tropopause shear layer (TSL)	12
1.3.3 Dynamic instability and turbulence in the tropopause region	15
1.4 Current understanding of GWs in the UTLS region	17
1.5 Scientific hypotheses, research questions and outlook	20
2 Atmospheric model, data and methodology	23
2.1 Atmospheric model ICON-NWP	23
2.1.1 Model description	23
2.1.2 Physical parameterization schemes	25
2.1.3 Calculation of potential vorticity on the ICON Grid	28
2.2 The ECMWF integrated forecast system	28
2.3 Vertical derivatives and representation of GWs in models	31
2.4 Datasets	32
2.5 Analysis Methods	34
2.5.1 Gravity wave momentum flux	34
2.5.2 Extraction of GW parameters in observations	37
2.5.3 Mixing diagnostics through trace gas correlations	38
2.5.4 Calculations of turbulence diagnostics	40
3 Contribution of gravity waves to vertical shear in baroclinic life cycle experiments	43
3.1 Idealized baroclinic life cycle experiments: ICON model setup	44
3.1.1 Initial background state: DCMIP testcase	45
3.1.2 Dry and moist baroclinic life cycle experiments	46
3.2 The DCMIP baroclinic wave development and the occurrence of GWs	47
3.2.1 Baroclinic wave evolution and gravity wave appearance in the reference simulations	47
3.2.2 GW occurrence: impact of horizontal and vertical grid spacing	49
3.2.3 Evolution of BLC: the latent heat release	50
3.2.4 GW occurrence: impact of non-conservative processes	51

3.2.5	GW occurrence: connection with vertical shear	53
3.3	Shear and turbulence diagnostics in the LMS	55
3.3.1	Static stability and vertical wind shear	55
3.3.2	Dynamic instability and turbulence	57
3.4	Vertical distribution of shear and associated GW signatures	61
3.5	Testcase Intercomparison with JABW BLC experiments	64
3.6	Synthesis	65
3.6.1	Discussion and summary	65
3.6.2	Limitations and uncertainties	66
4	Evidence of GW-induced shear and mixing in the North Atlantic baroclinic environment	67
4.1	The 2017 Wave-driven ISentropic Exchange (WISE) campaign	68
4.2	Observation of GW-induced mixing in a baroclinic wave over Iceland during WISE RF05	69
4.2.1	Synoptic situation on 23 September 2017 over the North Atlantic	69
4.2.2	Identification of small-scale mixing in the LMS	70
4.2.3	Identification of flight segments affected by turbulence	70
4.2.4	Trace gas observations, tracer-tracer correlation and small-scale mixing	71
4.2.5	Observation based estimate of GW related mixing	74
4.3	Analysis of GWs and turbulence occurrence: ECMWF perspective (Part I)	76
4.3.1	GW appearance and shear in different datasets	76
4.3.2	Occurrence of potential turbulence in the LMS	79
4.3.3	GWs as a probable cause for CAT	80
4.4	Analysis of GWs and turbulence occurrence: ICON perspective (Part II)	83
4.4.1	Occurrence of GW and shear in the lower stratosphere	83
4.4.2	Diagnostics of potential turbulence and CAT in the LMS	84
4.5	Synthesis	87
4.5.1	Summary	87
4.5.2	Implications and future research	88
5	Co-occurrence of gravity waves, vertical wind shear and turbulence over the North Atlantic	91
5.1	Background	91
5.1.1	Theory and computation of resolved GW-forcing in ERA5	92
5.1.2	Synoptic situation over the Northern Hemisphere on 11 September 2017	93
5.2	Annual cycle of GWs, vertical shear and turbulence indices over the North Atlantic	94
5.2.1	Occurrence of strong vertical wind shear in a tropopause-relative framework	94
5.2.2	GW momentum flux in a tropopause-relative framework	97
5.2.3	Turbulence diagnostics in a tropopause-relative framework	98
5.3	Lower stratospheric hotspot of zonal GW forcing and momentum fluxes	101
5.4	GW perturbations and shear prone to potential turbulence in the LMS: Coincidental or correlated?	103
5.5	Summary	107

6 Conclusion, outlook and recommendations	111
6.1 Conclusion	111
6.2 Open questions	114
List of Figures	117
List of Tables	125
Acronyms	126
Bibliography	128
Appendix	144
Acknowledgement	150
Curriculum Vitae	152

1 Introduction

Objective

The introduction chapter aims to lay the foundation for understanding the research objectives and direction of this thesis. It introduces key concepts in mid-latitude atmospheric dynamics and provides an overview of the current understanding of GWs influence on the upper troposphere lower stratosphere transport and mixing. Additionally, it highlights the challenges and gaps in the existing literature and presents the research goals and questions that will be addressed throughout the thesis.

1.1 Upper troposphere lower stratosphere (UTLS) and the tropopause definitions

The Upper Troposphere Lower Stratosphere (UTLS) refers to an atmospheric region that is approximately ± 5 km around the tropopause (Gettelman et al., 2011). This boundary region is the transition zone between the two lowest layers in the Earth's atmosphere, the well-mixed troposphere and the stably stratified stratosphere. UTLS features thermodynamic changes and is shaped by various dynamical features that span from the planetary to the mesoscale.

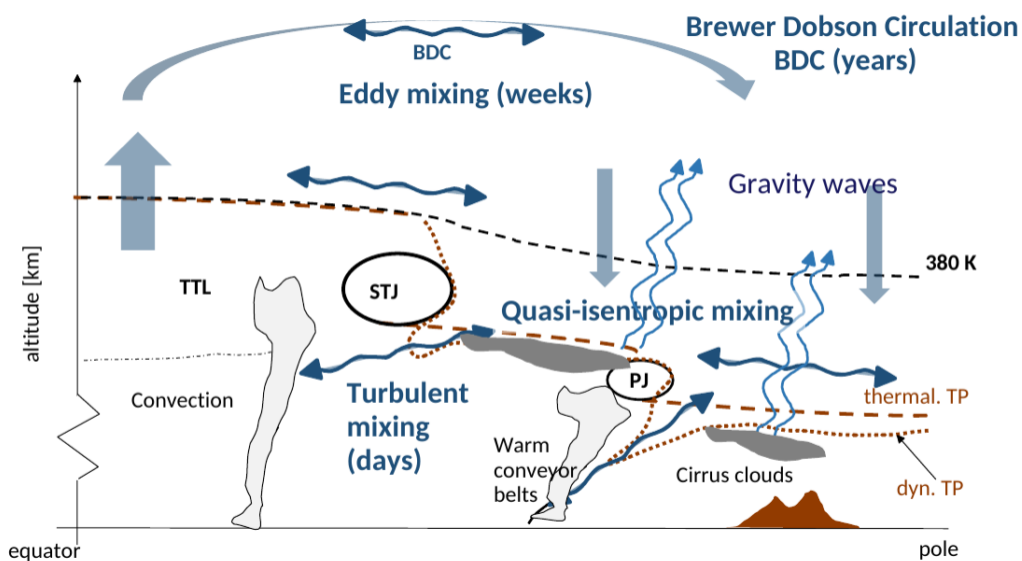


Figure 1.1: Schematic of the upper troposphere and lower stratosphere with processes and associated transport time scales, adapted from Hoor (2022).

The troposphere and stratosphere differ fundamentally in several ways. Temperature, for instance, typically decreases with height in the troposphere and increases in the overlying stratosphere. The chemical composition in both layers also varies dramatically, such as approximately 90% of atmospheric ozone resides in the stratosphere, while nearly all water vapor is confined to the troposphere. These contrasting characteristics led meteorologists in the early 20th century to introduce the concept of a boundary between two layers, the so-called *tropopause* (Teisserenc de Bort, 1902; Assmann, 1902).

This tropopause can be regarded as a partly permeable transport barrier between the troposphere and the stratosphere (Hoinka, 1997).

In the UTLS, the transport occurs through the tropopause, and is known as cross-tropopause transport or in other terms stratosphere-troposphere exchange (STE, Hoinka, 1997). The UTLS is characterized by jet streams, strong inhomogeneities in wind fields, horizontal temperature gradients, as well as abrupt changes in atmospheric stability. In recent years, there has been growing interest in understanding the contribution of small scale dynamics, to STE and mixing in the UTLS (e.g., Luderer et al., 2007; Kunkel et al., 2019; Lachnitt et al., 2023). Moreover, the UTLS is an intriguing region to study small scale processes, as it serves both as source and sink due to its distinctive dynamical and thermodynamical characteristics. In this regard, atmospheric gravity waves, identified as a small-scale dynamical feature of baroclinic life cycles, play a crucial role in middle atmospheric dynamics by transporting energy and momentum, thereby contributing to transport and coupling between atmospheric layers.

Over time, various tropopause definitions have been proposed. Basically the different definitions are driven by physics and different research approaches. Given the early reliance on balloon ascents and radiosondes as means of obtaining meteorological data, it is not surprising that the first officially established definition of tropopause was based on vertical temperature gradient obtained from atmospheric profiles. This is referred to as the (i) thermal tropopause or lapse rate tropopause (LRT). The World Meteorological Organisation (WMO) defines it as "the height of the lowest level at which the temperature lapse rate $-\frac{\partial T}{\partial z}$ decrease to values of 2 K km^{-1} or staying below this value on average between this level and any level above within next 2 km" (WMO, 1957). Later, the capability to model large-scale dynamical processes enabled the formulation of (ii) dynamical tropopause definition based on potential vorticity. Potential vorticity (PV) contains implicitly the static stability and thus the thermal tropopause and is conserved for adiabatic and frictionless flow. Early approaches considered the isentropic gradient of PV, but for simplicity, most dynamic tropopause definitions were eventually adopted as constant PV surfaces. The dynamic tropopause defined through the maximum of the isentropic gradient of the PV has again gained more attention recently through the work of Kunz et al. (2011).

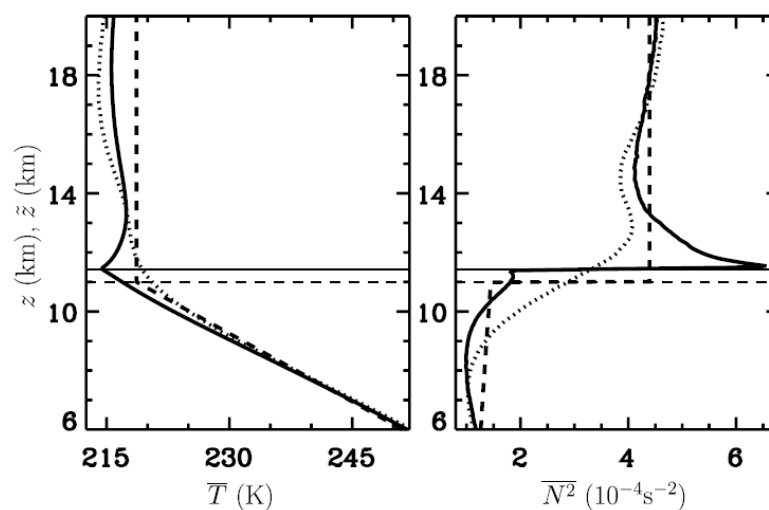


Figure 1.2: Averaged profiles of temperature (left) and buoyancy frequency squared (right) representative for northern hemispheric mid-latitudes. Dotted lines indicate sea level based average, solid lines indicate tropopause-based average, and dashed lines indicate profiles of the U.S. standard atmosphere at 45° N . Horizontal lines denote corresponding tropopause altitude. Figure adapted from Birner (2006).

Regarding the thermal tropopause, although the observed reversal of the lapse rate does not enter this definition, the vertical gradients of the potential temperature (Θ) and equivalent potential temperature (Θ_e , Bolton (1980)) indicate the dynamical implications of this thermal structure. Under dry (moist) adiabatic conditions, the temperature lapse rate is $\Gamma_{dry} = 9.8 \text{ K km}^{-1}$ ($\Gamma_{moist} \approx 5 \text{ K km}^{-1}$). Thus, a lapse rate of less than 2 K km^{-1} necessarily implies that both $\frac{\partial\Theta}{\partial z}$ and $\frac{\partial\Theta_e}{\partial z}$ are positive (i.e. stability with respect to both dry and moist adiabatic displacements). In such regime, a vertically displaced air parcel becomes warmer (cooler) than its environment when sinking (rising), and the thermal structure of its environment effectively exerts a restoring force on it. This state is known as stable stratification and its intensity can be quantified by the Brunt-Väisälä frequency N , representing the frequency of oscillation around the equilibrium position of the parcel. Its expression in terms of potential temperature reads:

$$N = \sqrt{\frac{g}{\theta} \cdot \frac{\partial\theta}{\partial z}}, \quad (1.1)$$

where g denotes the acceleration due to gravity at the Earth's surface. Moreover, the squared frequency N^2 is used to quantify the static stability. Thus, the thermal tropopause definition reflects the differences in stratification between the troposphere with low N^2 ($\sim 1 \times 10^{-4} \text{ s}^{-2}$) and the stratosphere with high N^2 ($\sim 4 \times 10^{-4} \text{ s}^{-2}$).

Birner (2006) illustrates the average vertical profiles of key variables in tropopause-based coordinates as observed by radiosondes in the mid-latitude (Figure 1.2). In the UT, temperature decreases with altitude with a typical lapse rate of approximately $6\text{--}10 \text{ K km}^{-1}$ up to the tropopause, which is characterized by a distinct temperature minimum. Above the tropopause, a temperature inversion (variable in thickness, but on average roughly $1\text{--}2 \text{ km}$ deep) is followed by a nearly isothermal temperature profile in the LS. The reversal of the vertical temperature gradient across the tropopause leads to a rapid change of the stratification from the UT to the LS, which is reflected in the profile of N^2 . From a typically low mean value in the UT, N^2 abruptly maximizes in a distinct peak occurring at the tropopause altitude. This is further discussed in detail in section 1.3.1.

Another approach is the PV based dynamical tropopause. In general, the PV value of an air parcel describes its capacity to rotate, and thus provides information on the combination of dynamics and stratification of the atmosphere. Similar to potential temperature, PV is conserved under frictionless and adiabatic flow conditions. Because of the stratification above the tropopause, PV experiences a strong increase across the tropopause, which enables the identification of the dynamical tropopause. It is defined either by the maximum of the isentropic gradient of the PV (Kunz et al., 2011), or more commonly, by threshold values corresponding to enhanced PV gradients (Hoskins et al., 1985). Following the definition of Ertel (1942), PV can be written as:

$$Q = \frac{1}{\rho} \vec{\eta} \cdot \vec{\nabla}\Theta, \quad (1.2)$$

where ρ is the density of the medium, $\vec{\eta} = \vec{\nabla} \times \vec{u} + 2\vec{\Omega}$ the vector of the absolute vorticity $\vec{\eta}$ which is composed of the rotation of the three dimensional wind field $\vec{u} = (u, v, w)$, and the vector of the angular velocity of the earth $\vec{\Omega}$. Its unit is the potential vorticity unit (PVU), where $1 \text{ PVU} = 10^{-6} \text{ m}^2 \text{ s}^{-1} \text{ K kg}^{-1}$.

The term $\vec{\nabla}\Theta$ is the gradient of the potential temperature;

$$\Theta = T \left(\frac{p_0}{p} \right)^{\frac{R_d}{c_p}}, \quad (1.3)$$

with the temperature T , pressure p and reference pressure $p_0 = 1000$ hPa, the specific gas constant for dry air $R_d = 287.06$ Jkg⁻¹ K⁻¹ and the specific heat capacity $c_p = 1004.05$ Jkg⁻¹ K⁻¹.

Moreover, the dynamical tropopause presents a more general transport barrier, which is due to the conservation properties of PV. The material derivative of the PV is given by (Hoskins et al., 1985);

$$\frac{D}{Dt}Q = \frac{1}{\rho} \left(\vec{\eta} \cdot \frac{D\Theta}{Dt} + \vec{\nabla} \times \vec{F} \cdot \vec{\nabla}\Theta \right), \quad (1.4)$$

where \vec{F} denotes non-conservative forces, i.e., frictional, diffusive and turbulent processes. Thus, the PV of an air parcel is materially conserved in the absence of non-conservative processes and diabatic heating $\frac{D\Theta}{Dt}$ under adiabatic frictionless flow conditions. The first term in Eq.1.4 describes the change in PV due to diabatic heating rate gradients. It is important to note that even in locally adiabatic or quasi-adiabatic flow ($\delta\Theta \approx 0$), PV can vary significantly if large gradients of Θ are present.

While early proposals for PV-based tropopause definitions were focused on the PV gradient (e.g., Reed, 1955; Kunz et al., 2011; Turhal et al., 2024; Weyland et al., 2025), the vast majority of studies have adopted the dynamic tropopause using constant PV surfaces to simplify evaluating the tropopause. In 1986, the WMO identified 1.5 PVU as the ideal cut-off for the troposphere. Later studies, however, suggested that higher PV values may more accurately represent the tropopause. Throughout history, several PV values have been used, with 1.5, 2.0 and 3.5 PVU standing out as the most commonly used thresholds (Hoerling et al., 1991). These threshold values are positive in the Northern Hemisphere and negative in the Southern hemisphere, as absolute vorticity changes sign. The dynamical tropopause is not defined near the equator, as (potential) vorticity experiences a singularity in that region. In the tropics, the tropical tropopause is therefore often represented by a fixed value of potential temperature, commonly set to 380 K, or alternatively combination with the thermal tropopause have been suggested (Wilcox et al., 2011; Weyland et al., 2025).

Following a commonly used PV-based tropopause definition in the literature, the extratropical dynamical tropopause is identified as the 3.5 PVU isoline throughout this study. This representation of dynamical tropopause in the form of material surface enables observing STE features in the zones of its deformation. The areas of tropopause highs are called as "domes" and those of the tropopause lows are called "folds".

Additionally, the tropopause can also be defined based on the chemical tracers species, since it acts as a barrier for transport and mixing and thus leads to the formation of species gradients. A typical vertical profile of ozone (O₃) is characterized as: (a) fairly well-mixed troposphere, (b) a sharp gradient across the tropopause and, (c) increasing mixing ratios with height in the lower stratosphere. Due to its characteristics, O₃ is well suited for defining a tropopause based on changes in its vertical gradient. However, When using ozone as a diagnostic, it must be noted that it is not chemically inert and exhibits pronounced seasonality. Given that the tropopause acts as a dynamic transport barrier, as it exhibits long lived trace gases with strong gradients, absolute mixing ratios of chemical tracers e.g., O₃, N₂O can also be used to define a so-called (iii) chemical tropopause. Another way to determine the tropopause is to

correlate different trace gases, such as O₃ and carbon monoxide (CO) (Fischer et al., 2000; Zahn et al., 2000; Hoor et al., 2002; Pan et al., 2004), or N₂O and CO (Assonov et al., 2013; Müller et al., 2015). A more detailed discussion is extended in section 1.3.

1.2 Internal gravity waves in the atmosphere

In a stably stratified fluid, a vertical displacement of a fluid parcel generates a buoyancy force that acts to restore the parcel toward its equilibrium level. Owing to inertia, the parcel may overshoot this level and, in the absence of strong viscous damping, undergo oscillatory motion about the equilibrium position. The local displacement of fluid causes this oscillation to spread within the whole domain as transverse wave, commonly known as (internal) gravity waves. In simplest form, internal gravity waves are ubiquitous buoyancy oscillations of a fluid within a fluid. This process is illustrated schematically in Figure 1.3 which shows the motion of an air parcel displaced from its equilibrium in a stably stratified atmosphere.

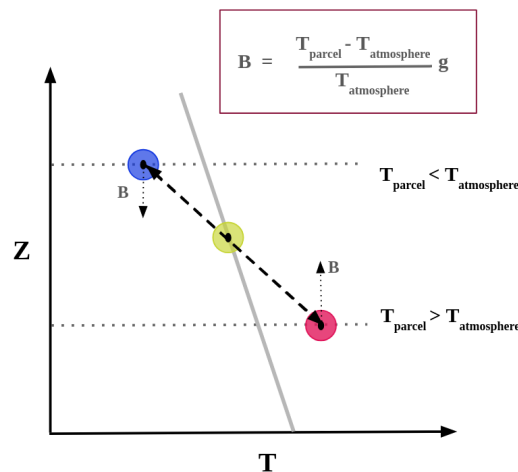


Figure 1.3: Schematic diagram of an oscillating air parcel in stably stratified atmosphere, where temperature changes with altitude shown by grey line. The temperature of the air parcel follows the dry adiabatic lapse rate T_d (Eq. 3.53 from Wallace and Hobbs, 2006) given as $\Gamma_d = \frac{g}{c_p} = -\left(\frac{dT}{dz}\right)_{dry}$. The buoyancy (B) acts as a restoring force and is calculated from the temperature (T) difference between atmosphere and air parcel temperature and acceleration due to gravity (g). Figure is adapted from Gisinger (2018).

Atmospheric gravity waves (hereafter referred to as GWs) are disturbances of wind, temperature, density, and pressure fields that can propagate through the atmosphere when generated by vertical displacements in a stably stratified fluid. In addition to buoyancy, the Coriolis force due to Earth's rotation can act as an additional restoring force that causes horizontal oscillations. The resulting mixed waves are called inertia-GWs (Lin, 2007). The necessary, though not sufficient, conditions of existence of GWs are: (i) presence of the gravity field and (ii) a stable fluid stratification. In the Earth's atmosphere, the former condition is satisfied naturally, while the latter requires density and pressure to vary with height in the medium. Changes in density may occur both continuously and discontinuously, mainly due to changes in temperature and wind.

GWs may appear virtually everywhere in the atmosphere and exist on a wide range of spatial scales, from a few kilometers to thousands of kilometers. Although the waves themselves are not directly visible, we can see the effects of these waves have on the atmosphere (e.g., the phenomena shown in

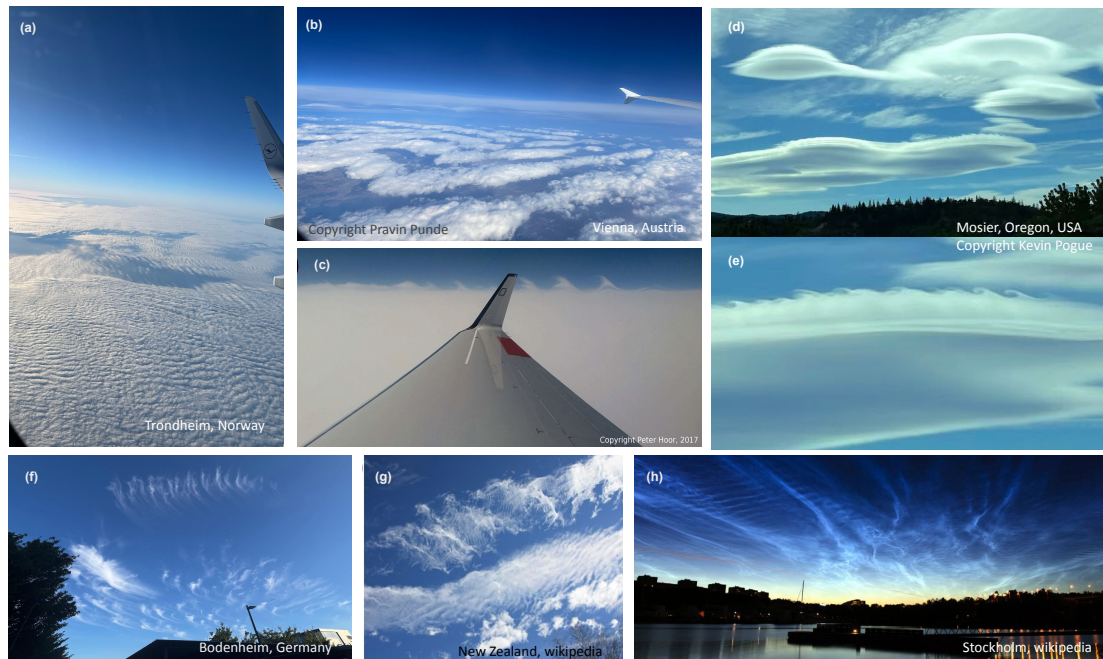


Figure 1.4: Visible phenomena influenced by gravity waves: (a) undulatus clouds over Trondheim, Norway, (b) rotor clouds over Vienna, Austria (photo by P. Punde), (c) photo taken on board German High Altitude LOnG (HALO) research aircraft at 27.09.2017, 15:03 UTC during WISE RF07 showing Kelvin–Helmholtz cloud billows on top of a cirrus cloud deck (photo by P. Hoor), (d) lenticular clouds above Mosier, Oregon, USA, (e) wind shear along the upper surface of one cloud was producing Kelvin-Helmholtz billows (photo by K. Pogue), (f) small-scale structures in cirrus clouds over Bodenheim, taken directly south of Mainz (by author), and (g) New Zealand (photo by B. Kaifler), (h) wave structures in noctilucent clouds over Stockholm (photo by K. Cho). Source: Photo in d, e, g, and h are taken from Wikipedia.

Figure 1.4). In mountainous regions, the probably most prominent visible phenomenon caused by GWs are lenticular and rotor clouds.

GWs have well-known importance for atmospheric dynamics, transport and coupling between atmospheric layers. Mainly, GWs are one of the important coupling mechanism between the lower, middle, and upper atmosphere. GWs carry momentum and energy both vertically and horizontally from their source region to the region where they dissipate, and so impact the atmospheric dynamics. These two regions can be separated by several hundred kilometers or even more. During their breaking or dissipation stages, GWs can locally lead to enhanced turbulence, promote turbulent mixing of passive tracers and disrupt large-scale flows, thereby transporting energy down the turbulent cascade from large to small-scales. For this to happen, the waves must reach instability. In fact, GWs breaking is a *sine qua non* for understanding the global atmospheric as well as oceanic circulation and represent an important phenomenon in the middle atmosphere (Remmler, 2016).

The UTLS region featuring dramatic increase in static stability at the tropopause, at which waves are refracted to shorter vertical wavelengths of about 2-10 km. These wave are primarily lower-frequency GWs, as dictated by the dispersion relation, and exhibit relatively large amplitude wind variability. It is, nowadays, well known that the GWs are not only important in the middle atmosphere but also play a critical role in shaping thermodynamical structure of the UTLS. In order to study the mechanism and coupling between these processes, we first discuss a basic analytical description of GWs and use it to rigorously identify GWs across scales.

Albeit their importance, the representation of GWs in global atmospheric simulations remains in-

complete, as the horizontal resolutions of general circulation models and global climate models are typically too coarse to resolve the important part of the GW spectrum. In almost all cases, since most GWs have wavelengths smaller than the model grid spacing, the modelers are left with two choices: (i) either increase the horizontal and vertical resolution of the models or (ii) account the effect of GWs on the global circulation by some parameterization based on combinations of linear wave theory, empirical observations of time-mean energy spectra and simplified treatments of the breaking process. Till date, the highest resolution of global climate models is ~ 20 km (i.e., a grid spacing of $\sim 3-4$ km) which is still greater than the wavelength of such important waves. Thus, modelers requires a comprehensive understanding of the complex links between small-scale GW fluxes of energy and momentum and the dynamics of the middle and upper atmosphere. Nevertheless, within the face of these complexities, the linear theory continues to provide a robust and useful framework for describing behavior of GWs and their impact on large-scales. Perturbation effects of GWs, i.e., Linear theory, is discussed briefly in the subsequent section.

Atmospheric motion is generally governed by the fundamental fluid equations expressing conservation of momentum, mass, and energy for a stratified flow. To better understand the physical nature of GWs, these equations are commonly reformulated in a simplified mathematical framework that describe their motion through the atmosphere. Perturbation theory provides theoretical backbone for a physical analysis of such waves. Under the assumption that all field variables of the atmosphere can be separated into a background atmosphere (or basic state) and local perturbations from the background, which are deviations for the field that are small and rapid compared to the variations in the background state. Having said that, it explains a method to simplify atmospheric wave motion in such a way that the complex nonlinear systems of fundamental equations can be solved, for example by applying linearization and standard methods such as wave ansatz. A detailed derivation from the linearized system to this dispersion relation is given in Fritts and Alexander (2003).

Moreover, GWs are present across a broad spectrum of horizontal scales and typically feature time scales short enough as such rotation, heat transfer, and friction can be ignored (Köhler, 2021). GWs are mainly generated in the lower atmosphere due to various sources such as topography, jet imbalances, fronts, convection, and shear instability (Fritts and Alexander, 2003; Achatz et al., 2024, and references therein). Jet imbalances refer to regions within jet streams where deviations from geostrophic balance produce strong vertical wind shear. GWs generated in the troposphere, i.e., the altitude range below ≈ 12 km, are subject to wave dispersion as they propagate into the middle atmosphere. These GWs propagate both vertically and horizontally with a major portion of their momentum flux originating from tropospheric sources. During ascent, their amplitude increase due to decrease in atmospheric density. This amplification, in turn, can lead to wave saturation and eventually breaking. In this process, GWs deposit momentum, which in turn acts as a forcing mechanism for the large-scale circulation in the stratosphere and mesosphere (Andrews et al., 1987). Locally, GW breaking can also generate turbulence and mixing in these regions (Hodges Jr., 1967).

GWs can also break in all other areas of the atmosphere, for example in the tropopause region (e.g., Schilling et al., 1999; Wang, 2003; Lane and Sharman, 2006; Smith et al., 2008; Wagner et al., 2017), or at the edge of the polar vortex (e.g., Hartmann et al., 1989; Plumb, 2002; Shepherd, 2007; Günther et al., 2008). In the polar regions, the breaking of GWs can lead, for example, to dynamic and chemical disturbances in the polar vortex (e.g., Holton et al., 1995; Günther et al., 2008).

Overall, propagating GWs are one of the main processes by which energy and momentum are transferred vertically through the atmosphere upon breaking and dissipation, and, as such, can affect the thermodynamical as well as chemical composition of the tropopause and lower stratospheric region, which can have influence on the global radiative and atmospheric energy budget. This, in turn, can also have large impacts on aviation, atmospheric chemistry and the general circulation including other atmospheric phenomena. The impact of GWs are further discussed in the following sections.

1.3 The extratropical transition layer (ExTL) and cross-tropopause transport

The tropopause fold brings the stratospheric air down towards the middle/upper troposphere and that the tropopause is actually permeable (Danielsen, 1959). Danielsen (1968) initiated intense studies of the processes leading to the cross-tropopause exchange. Nowadays, the concept of such exchange is referred to as stratosphere–troposphere exchange. The downward branch of this exchange is termed stratosphere–to–troposphere transport (STT), while the upward exchange is known as troposphere–to–stratosphere transport (TST) (Stohl et al., 2003). In this context, the term "mixing" does not only refer to irreversible exchange of air masses, but also to irreversible part of the transport in general, across the tropopause, e.g., caused by shear, turbulence, and wave–flow interactions. The relative importance of underlying PV altering physical processes is fascinating topic of research since last few decades and is mostly characterized by a large case-to-case variability (e.g., Shapiro, 1980; Appenzeller et al., 1996; Whiteway et al., 2003; Lee and Sprenger, 2025).

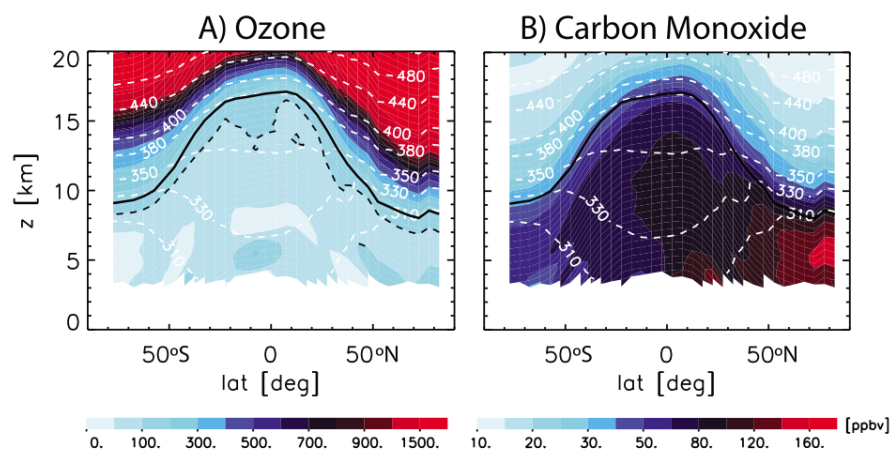


Figure 1.5: Schematic of seven year temporal and zonal average (2002–2008) of (a) ozone and (b) carbon monoxide for winter in the Ex-UTLS in tropopause relative coordinates, adapted from Gettelman et al. (2011). The thermal tropopause is indicated with thick black line. The dashed black line indicates the 100 ppbv ozone contour, whereas dashed white lines represent isentropes from 310 K (bottom) to 480 K (top). The distributions reveal strong horizontal and vertical tracer gradients across the tropopause in both species.

Potential vorticity is conserved for adiabatic and frictionless flow; however, observations indicate that STE is necessary to explain the distribution of trace species in the UTLS. Therefrom, transport across the tropopause can generally be grouped into two main categories:

(i) Adiabatic or quasi-isentropic eddy-driven exchange, in which air parcels are transported along isentropic surfaces that intersect the tropopause. This eddy-driven process leads to a gradual weakening of tracer and PV gradients through diffusive processes, particularly within the "middle world", a region defined by isentropic levels intersecting the tropopause (Gettelman et al., 2011).

(ii) Diabatic or cross-isentropic mixing, in which exchange occurs directly at the tropopause through non-conservative PV modification and diabatic processes. This results in the reassignment of air masses between the troposphere and stratosphere.

The relative importance of these two pathways strongly depends on the prevailing synoptic conditions. From Eq.1.4, it becomes apparent that in globally adiabatic ($\Theta = 0$) and frictionless ($\vec{F} = 0$) flow, PV is materially conserved quantity and an air parcels cannot cross PV-isosurface. The quasi-material nature of this dynamical transport barrier is reflected in PV-based tropopause definition. However, processes that do alter PV result in an exchange of air masses and chemical constituents including radioactive debris, water vapour, and ozone between the stratosphere and troposphere.

The UTLS is a region where several trace species including O_3 , N_2O or CO shows large vertical gradients (Figure 1.5). These gradients arise from regional and seasonal variations in strength of chemical source regions, chemical processing, photochemical production and removal, and transport and mixing processes, which results in characteristics lifetime, and thus, characteristics vertical profiles of individual trace gases. The transition from tropospheric to stratospheric trace gas mixing ratios at the tropopause contain information about the efficiency of the tropopause as a transport and mixing barrier and on the occurrence of STE.

A common method for analysing high resolution trace gas mixing ratio measurements is to correlate the time series of a trace species with main sources in the troposphere and sinks mainly in the stratosphere (e.g., N_2O or CO) with a characteristic stratospheric trace species, i.e. with main sources in the stratosphere and sinks in the troposphere (e.g., O_3) (Fischer et al., 2000). Such correlations reveal the degree of mixing and further helps to identify the transition region between the two atmospheric regimes.

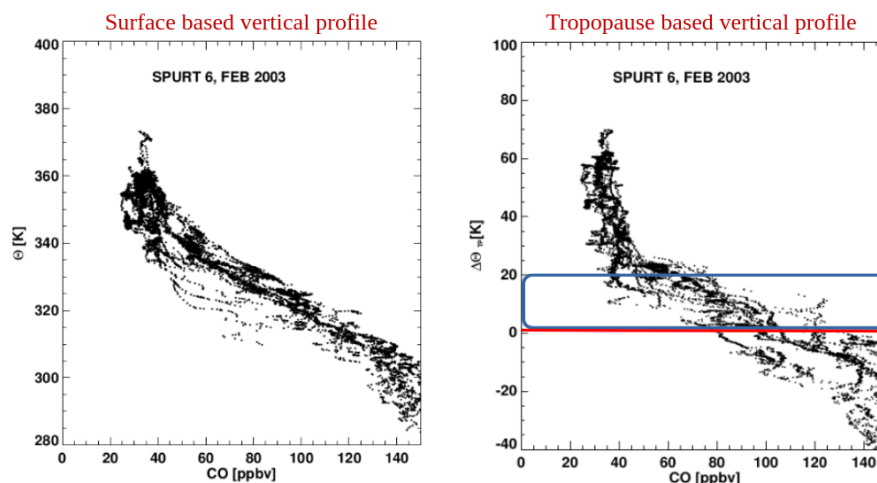


Figure 1.6: Vertical profile of CO obtained during SPURT 6 mission as function of (left) potential temperature and, (right) potential temperature relative to the local tropopause $\Delta\Theta$, adapted from Hoor et al. (2004). The distributions reveal more compact $\Delta\Theta$ profile and rather sharp change of the gradients of CO.

The extratropical transition layer (ExTL) is the region around the extratropical tropopause based on the vertical profiles of CO which show enhanced values of CO in the LMS (Hoor et al., 2002, 2004, see also Figure 1.6). The LMS is broadly defined as the region between the height of the extratropical and tropical tropopause (Figure 1.1). This LMS corresponds to the middle world, that allows quasi-isentropic exchange between the tropical troposphere and extratropical stratosphere (Holton et al., 1995). The

upper boundary of this layer is commonly used by the 380 K isentrope, that approximates the potential temperature of the lapse rate tropopause in the tropics, representing the height of the tropical tropopause (e.g., Appenzeller et al., 1996; Olsen et al., 2013; Wang and Fu, 2021; Weyland et al., 2025).

Moreover, the LMS encompasses the ExTL, which is characterized by changes in chemical tracer gradients and has been supported by trajectory-based studies (e.g., Hoor et al., 2004; Berthet et al., 2007; Hoor et al., 2010). Both the ExTL and LMS are regions with strong vertical gradients of chemical species which result from the different chemical environments of the stratosphere and troposphere. In the extratropics, quasi-isentropic transport plays a crucial role for the constituent exchange in the ExTL as has been shown by trajectory-based analyses (Berthet et al., 2007; Hoor et al., 2010) and by airborne observations (e.g., Hoor et al., 2004; Pan et al., 2004; Kunkel et al., 2019). Additionally, small-scale mixing events can locally affect tracer gradients, often linked to shear instabilities or convection (e.g., Whiteway et al., 2003; Lane et al., 2004; Zhang et al., 2015b; Lachnitt et al., 2023; Dörnbrack et al., 2025). This study focuses on processes in the entire LMS; accordingly, the analysis is not limited to the ExTL, and the term LMS is used throughout.

1.3.1 The tropopause inversion layer (TIL)

On sub-synoptic scales, GWs are well known to influence the temperature and wind field in the lower stratosphere, which consequently affects the static stability and vertical shear of the horizontal wind. In the UTLS, particularly within the ExTL, enhanced stratification and shear manifest as the tropopause inversion layer and the tropopause shear layer. Owing to their importance in the development of dynamical instabilities and wave propagation, these features are briefly introduced in the following.

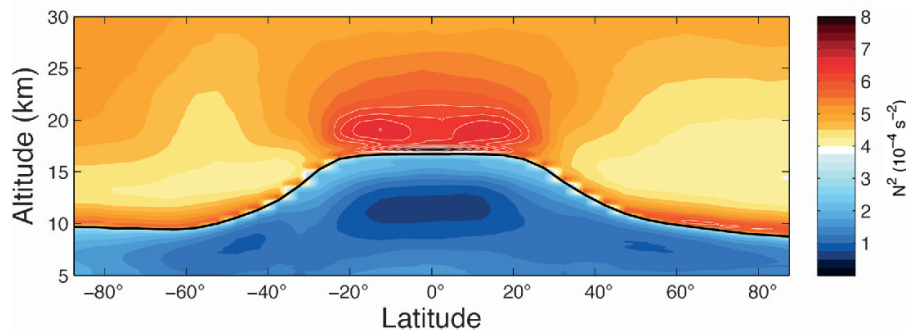


Figure 1.7: Vertical cross section of annual and zonal mean static stability calculated using the GPS temperature profiles from the CHAMP (Challenging Minisatellite Payload) satellite. The thick solid black line shows the annual and zonal mean thermal tropopause height. The thin white contours show the shading intervals for values $N^2 \geq 6 \times 10^{-4} \text{ s}^{-2}$. The annual mean is based on data averaged over April 2002–March 2008. Figure adapted from Grise et al. (2010). ©American Meteorological Society.

The definition of thermal tropopause is based on inversion of the vertical temperature gradient, as discussed in section 1.1. This temperature inversion is a well-established global climatological feature (Birner, 2006), which varies strongly in its strength and occurrence on large spectrum of spatiotemporal scales (Gettelman and Wang, 2015). The climatological maximum in the vertical temperature gradient $-\frac{\partial T}{\partial z}$ above the LRT as well as its seasonal variability have been discussed by Gettelman et al. (2011). Figure 1.7 shows the meridional section of static stability in tropopause-relative coordinates revealing that there is a maximum at the tropopause across all latitudes. In the the stratosphere with high $N^2 \approx 4 \times 10^{-4} \text{ s}^{-2}$ (e.g., Birner, 2006; Grise et al., 2010) and low in the troposphere $N^2 \approx 1 \times 10^{-4} \text{ s}^{-2}$.

This pattern is also reflected in Figure 1.8 that shows the vertical profile of N^2 relative to thermal tropopause. We see N^2 decreases below the tropopause (i.e., in the troposphere) and increases sharply just above it, and then gradually decreases again with height in the lower stratosphere.

The tropopause inversion layer (TIL) is commonly identified based on the resulting localized maximum in the vertical profile of the static stability N^2 (Birner et al., 2002) (see also Figures 1.8 and 1.2). The static stability defines the oscillation frequency of a vertically displaced air parcel in a stable background stratification (Eq. 1.1). The TIL represents a maximum in static stability and as such strongly damps vertical motion. The interrelation between TIL and previously mentioned ExTL, as inherent features within the LMS, is complex (e.g., Hegglin et al., 2009; Kunkel et al., 2016; Kaluza et al., 2019) and remains an active topic of research since last decade. This complexity arises from the broad spectrum of processes that are involved in the formation and maintenance of both the TIL and the ExTL on different temporal and spatial scales, as well as due to their bidirectional influence. The following paragraph shortly discusses the processes that are known to affect the evolution of the TIL.

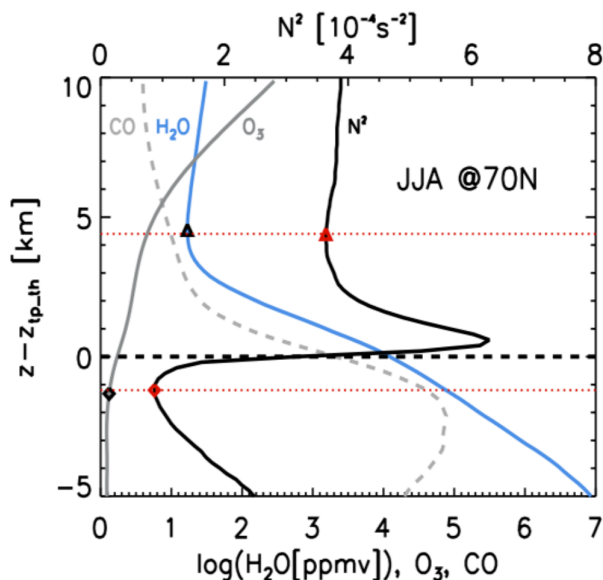


Figure 1.8: Vertical profiles of zonal mean N^2 (10^{-4} s^{-2} ; black), H_2O mixing ratio (ppmv; blue), O_3 (ppmv; solid grey) and CO (dashed grey; factor 20) relative to thermal tropopause for June-July-August (JJA) at 70° N , adapted from Hegglin et al. (2009).

The downwelling branch of the Brewer Dobson circulation during winter enhances lower stratospheric N^2 through a temporally lagged large-scale positive forcing (Birner, 2010). Sharp vertical gradients of H_2O and O_3 that maximizes near the tropopause (also called as hydropause and ozonopause, respectively) sharpen the vertical temperature profile across the tropopause on large scale due to dipole radiative forcing, where the seasonal and meridional variation in mixing ratios results in varying sharpening effects at the tropopause (Hegglin et al., 2009) (e.g., Figure 1.8). Water vapour gradients, in particular, might play a role in sustaining the TIL (Kunz et al., 2009). Consequently, the TIL is more pronounced during summer at high latitudes (Birner, 2006), consistent with enhanced radiative forcing and increased tropospheric moisture. Therefore, these processes substantially influence the large-scale seasonality of the TIL, i.e., the resulting tropopause sharpening mechanism. Specifically, the TIL often occurs in the regions of strong trace gas gradients.

1.3.2 The tropopause shear layer (TSL)

The vertical wind shear S^2 is defined as the squared vertical gradient of the horizontal wind components u and v (Wallace and Hobbs, 2006) and is given by:

$$S^2 = \left(\frac{\partial u}{\partial z} \right)^2 + \left(\frac{\partial v}{\partial z} \right)^2. \quad (1.5)$$

The pronounced shear is often occurs around the region of jet stream or at the jet exit region in the midlatitudes. The tropopause following maximum occurrence frequency of enhanced vertical wind shear is recently defined as tropopause shear layer (TSL, Kaluza et al., 2021) (see Figure 1.9). Here, regions of enhanced shear are defined as those where S^2 exceeds a threshold value S_t^2 , which corresponds to the 95th percentile of total S^2 values within a climatological dataset. That is to say, TSL is the region near the extratropical tropopause characterized by the maximum occurrence frequency of $S^2 \geq S_t^2$. This shear enhancement is also related to abundance of high static stability across the tropopause and can also lead to increased dynamic instability.

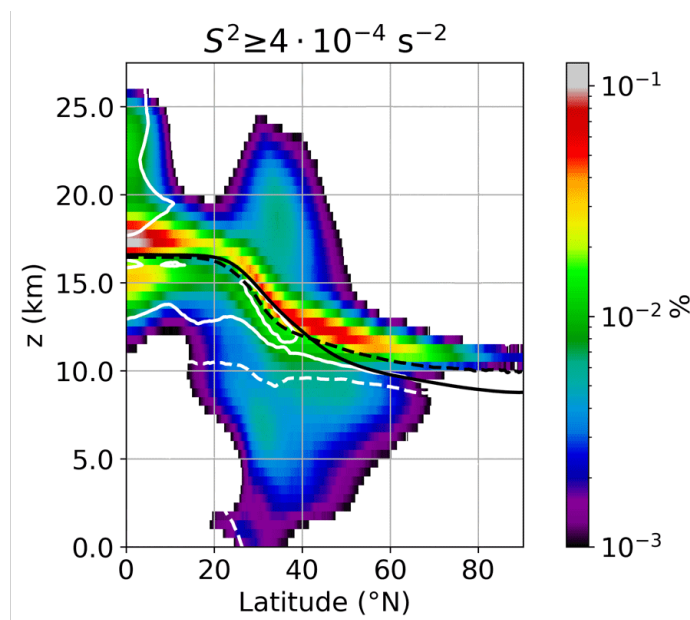


Figure 1.9: Occurrence frequency distribution of $S^2 \geq S_t^2$ with tropopause-based vertical coordinate system based on 10 year Northern hemispheric ERA5 climatology. The solid thick line shows mean lapse rate tropopause altitude. The occurrence frequencies are shown with logarithmic frequency contours, vertically binned with $\Delta z = 500$ m. Dashed thin black line indicates the effect of the cut-off of 1.5 km above orography. Solid (dotted) white line indicates where decreasing (increasing) horizontal winds with altitude constitute 75% of $S^2 \geq S_t^2$. Figure adapted from Kaluza et al. (2021).

The regions of enhanced shear are referred as those where S^2 exceeds a threshold value S_t^2 , which corresponds to the 95th percentile of total S^2 values within a climatological dataset. That is to say, the region near the extratropical tropopause characterized by the maximum occurrence frequency of $S^2 \geq S_t^2$, is related to the potential turbulence (Schäfler et al., 2023) and may impact troposphere-stratosphere exchange processes (Stohl et al., 2003, Figure 1.6). This statistical approach allows the identification of particularly strong shear events associated with tropopause disturbances. The mechanism behind the generation of vertical shear and further leading to the dynamic instability in the UTLS is discussed in subsequent sections.

Dynamical origin of vertical wind shear

Baroclinic instability is the primary dynamical mechanism governing synoptic-scale variability in the extratropics. Scale analysis of the physical forces involved indicates that the jet stream (large-scales)

particularly at midlatitudes can be approximated as a geostrophic wind. These geostrophic winds are driven primarily by a balance between the Coriolis force and the pressure gradient force. The geostrophic wind by definition is strictly horizontal and parallel to isolines of geopotential Φ and can be written as;

$$\vec{v}_g = \frac{1}{f} \vec{k} \times \vec{\nabla}_p \Phi \quad (1.6)$$

where f = Coriolis parameter, \vec{k} is the orthogonal unit vector in the vertical, $\vec{\nabla}_p$ is the horizontal gradient operator on an isobaric surface, and the geopotential Φ . Coriolis parameter f leads to a westerly wind in both hemispheres. Further, the pressure gradient force varies with altitude, due to baroclinicity of the atmosphere, which results in vertical shear of the geostrophic wind described by the "thermal wind" equation. Under the assumption of hydrostatic equilibrium, from the vertical derivative the geostrophic wind w.r.t. atmospheric pressure, the vertical shear of the geostrophic wind using Eq. 2.9 is written as;

$$\frac{\partial \vec{v}_g}{\partial \ln(p)} = -\frac{R_d}{f} \vec{k} \times \vec{\nabla}_p T. \quad (1.7)$$

Using, instead, a geometric altitude as vertical coordinate, the geostrophic wind is given by,

$$\frac{\partial \vec{v}_g}{\partial z} = \frac{g}{fT} \vec{k} \times \vec{\nabla}_h T. \quad (1.8)$$

The presence of significant vertical wind shear is a consequence of the existence of the baroclinic zone, such that $\frac{\partial \vec{v}_g}{\partial z} \neq 0$. More specifically, this means that either the strength of geostrophic wind or its direction or both vary with pressure altitude.

In general, the troposphere is warmer in the tropics and subtropics and cooler in the polar regions. Consequently, in both hemispheres, an increase in temperature towards the equator within the troposphere is associated with westerly winds in the upper troposphere, which are often concentrated in jets or jet stream. In the lower extratropical stratosphere, the temperature gradients are generally polewards rather than equatorward leading to negative wind shear. It follows that the jets have their maximum strength close to the tropopause.

(a) Occurrence of wind shear on large-scale: planetary to synoptic scale

The meridional temperature gradient extending from the equator to the poles exhibits local maxima that are shaped by large-scale dynamics and variations in heating. In the midlatitudes, these maxima are associated with baroclinic waves, cyclone and anticyclone activity, as well as localized jet streaks, notably the eddy-driven or polar-front jet (PFJ), which exhibits maximum wind speeds in the range of 250–300 hPa. The upper tropospheric front exhibits significant horizontal temperature gradients, accompanied by an increase in vertical wind shear in accordance with the thermal wind equation. Endlich and McLean (1965) observed a correlation between wind shear measured and that derived from thermal methods above the maximum wind speed level. However, the thermal wind equation neglect inertial forces, which may result in discrepancies in wind shear estimations, that are associated with flow curvature (Newton and Persson, 1962).

The climatological distribution of enhanced vertical shear reflects the occurrence of atmospheric processes that sharpen wind gradients and the ability of the tropopause region to sustain strong wind

shear. Early work by Birner et al. (2002) reported a pronounced S^2 peak just above the LRT from tropopause-relative radiosonde profiles at Munich, Germany, with maximum shear during winter and minimum during summer. Similar seasonal behavior was found by Zhang et al. (2015a) at Idaho. A broader set of radiosonde data analysis by Zhang et al. (2019) revealed a meridional dependence of enhanced shear occurrence, strongest in the tropics with bi-annual seasonality and S^2 mean maxima during JJA and DJF, while polar regions exhibit no pronounced S^2 maximum throughout the year. The equatorial summer shear enhancement is associated with the TEJ during the summer monsoon season (JJAS) (Sunilkumar et al., 2015).

The shear occurrence is influenced by jet streams dynamics at larger scales, and have proven effective for turbulence forecasting (Colson and Panofsky, 1965; Ellrod and Knapp, 1992). These atmospheric bands of the enhanced flow velocity or jet exhibit a synoptic to planetary scale extent, covering flow direction of up to several thousands of kilometers, with lateral shear zones of hundreds of kilometers and vertical shear zones spanning over several kilometers.

As a component of the Hadley circulation, the subtropical jet (STJ) functions at lower latitudes and higher altitudes (around 200 hPa), influenced by temperature gradients, the Coriolis force, and by the conservation of angular momentum during the poleward migration of air masses (Holton et al., 1995). STJ and PFJ exhibit a pronounced seasonality (Koch et al., 2006), with jet maxima peaks in winter (DJF) and minimize in summer (JJA). Oscillations such as the Madden-Julian oscillation (MJO, weekly to monthly timescales) and the El Niño Southern Oscillation (ENSO, yearly timescales) influence the Walker circulation and convective upwelling that define the equatorial region. The tropical easterly jet (TEJ), emerges as an inherent part of the East Asian summer monsoon circulation, is characterized by upper tropospheric easterlies with maximum wind speeds around 40 m s^{-1} located at about 150 hPa and is mostly centered above the Indian Ocean.

(b) Occurrence of wind shear on small-scale: sub-synoptic scale

The large-scale background wind shear provided by the planetary circulation and the jet streams is further modulated by sub-synoptic scale processes. In numerical data from the NCAR Whole Atmosphere Community Climate Model (WACCM), Liu (2017) conducted a spectral decomposition of wind shear features, which confirmed the significance of processes across a wide range of scales. On mesoscale, the processes of flow deformation, convergence, and differential temperature advection can lead to the development of frontal zones and an increase in wind shear, as described by the thermal wind equation (Ellrod and Knapp, 1992).

GWs strongly influence the dynamical and thermodynamical structure of the atmosphere, and plays important role in the generation of dynamic instabilities, particularly in the UTLS. The jet exit region of upper tropospheric streaks is a common source of GWs, as they are spontaneously emitted where the flow deviates from the geostrophic balance (O'sullivan and Dunkerton, 1995; Zülicke and Peters, 2006; Plougonven and Zhang, 2014; Kunkel et al., 2014). Fronts, convection and shear zones are another source of GWs which are common features of baroclinic wave development. By interacting with the background flow, GWs can amplify the strong vertical wind shear, often leading to the accumulation of static stability. Such interactions can give rise to the formation and maintenance of tropopause shear layer (Kaluza et al., 2021). This further leads to dynamical instabilities such as Kelvin-Helmholtz instability (KHI). Another possibility is GW breaking at critical levels where the phase speed of these waves

matches the background wind (e.g., Shapiro, 1978; Whiteway et al., 2004; Lane and Sharman, 2006) leads to reduction in static stability.

1.3.3 Dynamic instability and turbulence in the tropopause region

Initially, turbulence was introduced as a non-conservative process that can contribute to the overall STE, because it can materially alter the PV of an air parcel. The tropopause is defined based on a sudden increase in the static stability, and hence, the turbulence in this region is generally associated with dynamic instability within the stably stratified shear flow. Turbulent motions foster irreversible mixing of air masses, thus altering the chemical composition of the layer where it occurs. However, these turbulent motions in the extratropical tropopause region can substantially affect air traffic (Kim and Chun, 2011; Sharman and Pearson, 2017; Gultepe et al., 2019). In this regard, de Medeiros and Williams (2025) very recently studied long-term trends in jet stream behavior and its role in turbulence in context of climate change, where they indicated that, in future, air traffic might even be more affected by severe (clear-air) turbulence.

This study, however, focuses on large-scale dynamical proxies derived from the resolved variables to study the occurrence of small-scale processes rather than a direct quantification of turbulence. The employed datasets and model output do not resolve the small spatial and temporal scales at which turbulent motions occur. Accordingly, quantities such as the gradient Richardson number and turbulence indices are used as physically motivated proxies that identify dynamically unstable flow regimes favorable for turbulence generation. These indicators allow a statistical assessment of turbulence-prone conditions within the UTLS across the resolved scales. The following section gives an overview of flow conditions that favour the development of dynamic instabilities, from the planetary circulation down to small-scale wave perturbations, that leads to turbulence generation and ultimately, to the mixing.

(Gradient) Richardson number

According to linear wave theory, the dynamic stability of the flow can be derived based on the non-dimensional Richardson number Ri :

$$Ri = \frac{N^2}{S^2} \quad (1.9)$$

which is defined as the ratio between static stability and vertical wind shear of the horizontal wind. However, on large scales, the TIL is defined based on the local maximum static stability around an order of magnitude larger than the tropospheric values (refer section. 1.3.1). Thus, the gradient Richardson number criterion has two implications for the flow in the tropospheric region: first, exceptional vertical shear is necessary for the dynamic instability to emerge in the tropopause region, and second, an exceptional vertical shear can be sustained by the stably stratified flow before the onset of turbulent erosion of momentum gradients.

Dynamic instability in the stably stratified flow can occur when shear forces prevail that results in Ri below a critical threshold of $Ri_c = 0.25$. However, in studies using output from numerical models with comparable spatial resolutions, higher Ri thresholds are commonly used to identify regions prone to dynamic instabilities. More so, instabilities being a key prerequisite for mixing of air masses in the atmosphere, such as Kelvin–Helmholtz instability, can also be identified using Ri . For example, in this case the shear induced shift of a vertically displaced air parcel, such as due to wave perturbation, re-

sulting in local dynamic instability in an otherwise stably stratified flow with potential wave overturning and turbulent breakdown. The resulting effect on a background scalar field is commonly assumed to approximately follow the gradient diffusion hypothesis. This hypothesis states that the turbulent flux of the scalar ϕ is proportional to the mean scalar gradient, that ultimately satisfies the equation of diffusion given as;

$$\frac{\partial \phi}{\partial t} = K_\epsilon \frac{\partial^2 \phi}{\partial z^2} \quad (1.10)$$

with K_ϵ being the eddy diffusivity (unit: $\text{m}^2 \text{s}^{-1}$). Therefore, turbulence resulting from shear-induced dynamical instability acts as a diffusive transport process of heat and momentum that effectively erodes the underlying gradients of momentum and temperature. From a turbulence forecasting perspective, Ri is of interest due to its critical value, i.e. $Ri \geq Ri_c$ is sufficient condition for stability, where $Ri_c \sim \mathcal{O}(1)$. The influence of GW perturbations on Ri is also of importance because: previous studies indicate that GW motion can induce local reductions of Ri sufficient to occur instabilities in different parts of the wave.

Clear air turbulence (CAT)

Clear air turbulence is a type of turbulence occurring in the free atmosphere outside of convective activities and it is a concern for aviation safety. The turbulence can be initiated due to wave breaking at critical levels, that is regions where the background wind speed approaches the horizontal phase velocity of a propagating GWs (Dörnbrack, 1998). In the aviation sector, this issue has received substantial attention in the context of CAT, defined as turbulence occurring in cirrus clouds or in otherwise cloud-free conditions, and not in or adjacent to visible convective activity or thunderstorms (Ellrod et al., 2015; Sharman and Lane, 2016). The primary mechanism is shear-induced dynamic instability, and CAT has been identified to be largely a GW phenomenon (Sharman et al., 2012).

Previous studies have shown that CAT is often found in the UTLS region near jet streams, upper-level fronts, tropopause folds, etc., where strong wind shear and deformation are present. CAT is also found to be related to cross-tropopause exchange in case studies and hence influencing atmospheric composition. However, due to the intermittent nature of CAT and limited observational data, the understanding of CAT in relation to weather conditions favouring its occurrence and the impact of CAT on its surrounding environment is far from complete. With the introduction of the eddy dissipation rate (EDR) measurement on commercial aircraft, which indicates the intensity of turbulence, the number of observations for CAT increases significantly. This new dataset enable to examine the meteorological situations associated with the observed CAT events and categorize the events accordingly. However, it is yet to study the CAT in various weather systems, e.g. Rossby wave breaking, GW processes, tropopause folds, warm conveyor belt, and their dynamics near the tropopause, the relationship between CAT.

Although Ri captures dynamic instability, it may not fully represent turbulence under complex flow conditions. Recently developed Ellrod–Knapp turbulence indices provide empirical diagnostics specifically designed to identify CAT. CAT produced by vertical shear and frontogenesis is therefore examined in the upper troposphere near the core jet stream. To account for GW related contributions, shear under baroclinic flow conditions is analyzed and the Ellrod–Knapp Turbulence Index 1 (hereafter TI1) is applied (Ellrod and Knapp, 1992). TI1 consists of two key components: vertical shear and total flow deformation (DEF). TI1 has been shown to be capable of detecting 70 %–84 % of CAT occurrences (e.g.,

Ellrod and Knapp, 1992; Sharman and Pearson, 2017; Kim et al., 2018; Gultepe et al., 2019; Thompson and Schultz, 2021), making it a valuable complement to dynamically based measures. TI1 can be derived as

$$\text{TI1} = S \times \text{DEF} \quad (1.11)$$

The term DEF combines shearing Deformation (D_{SH}) and stretching Deformation (D_{ST}). In general, deformation is a property of a fluid that transforms a circular shaped area of a fluid to an elliptical shape. For example, the cols, troughs, and the exit region of jet stream. DEF can acts to strengthen upper-level frontal zones (Ellrod and Knapp, 1992). can be given as:

$$\text{DEF} = \sqrt{(D_{ST})^2 + (D_{ST})^2} = \sqrt{\left(\frac{\partial u}{\partial x} - \frac{\partial v}{\partial y}\right)^2 + \left(\frac{\partial v}{\partial x} + \frac{\partial u}{\partial y}\right)^2} \quad (1.12)$$

Another CAT diagnostics is the Ellrod-Knapp Turbulent Index 2 (TI2) which subtracts horizontal divergence from horizontal deformation before multiplying this difference by the vertical wind shear, and is given as;

$$\text{TI2} = S \times (\text{DEF} + \text{CVG}) \quad (1.13)$$

The term convergence (CVG) is the compaction of fluid caused by the confluence of streamline or the deceleration of the parcels, and can be derived using:

$$\text{CVG} = -\left(\frac{\partial u}{\partial x} + \frac{\partial v}{\partial y}\right) \quad (1.14)$$

At upper levels, CVG in the proximity of jet stream and tropopause induces strong subsidence, and in some cases, lead to turbulence. On the other hand, it can also contribute to frontogenesis and may generate GWs by disturbing the tropopause inversion. In this case, GWs thus may trigger mechanism for the development of KHI in that region. In this regard, simulations of midlatitude cyclones highlight the role of jet dynamics and GWs in CAT generation (Lane et al., 2004; Trier et al., 2020). However, forecasting CAT remains challenging due to its intermittent nature and small-scale motion (with turbulent eddies typically spanning horizontal scales of ~ 10 to 1000 m), compared to the resolution of current numerical weather prediction (NWP) models (Sharman et al., 2006, 2014; Sharman and Pearson, 2017). These motivates further investigation into GW-driven mixing, its contribution to the CAT and its influence on ExTL structure.

1.4 Current understanding of GWs in the UTLS region

In recent years, there has been growing interest in understanding the contribution of small-scale dynamics, specifically GWs, to STE and mixing in the UTLS (e.g., Luderer et al., 2007; Kunkel et al., 2019; Gisinger et al., 2020; Lachnitt et al., 2023; Dörnbrack et al., 2025). The UTLS is an intriguing region for GW studies, serves both as source and sink, due to its characteristics of jet streams, strong inhomogeneities in wind fields, horizontal temperature gradients, as well as abrupt changes in atmospheric stability. While horizontal temperature gradients influence the background wind structure and baroclinicity, vertical stability affects wave amplification and dissipation. These characteristics chiefly influence GW propagation and a potential source for GW dissipation. Regions of baroclinic instability and jet

streaks are often associated with enhanced GW activity, forming hotspots where GWs are frequently generated and interact with the background flow (Plougonven and Snyder, 2005; Zhang et al., 2015a). Consequently, the UTLS serves as an important source region for GWs, shaping their propagation and interaction with larger scale atmospheric processes.

Sources of GWs in the extratropical atmosphere can be manifold. Many GWs results from flow over topography (e.g., Durran, 1995; Lachnitt et al., 2023), while the GWs can also emerge above convective systems (e.g., Lane et al., 2001; Fritts and Alexander, 2003; Lane and Sharman, 2006; Alexander et al., 2010). Another important source are baroclinic waves with their jet and fronts (O’sullivan and Dunkerton, 1995; Plougonven and Zhang, 2014). In the extratropical atmosphere, this source is commonly associated with baroclinic waves, but still can be regarded as a less well understood source of GWs. Surface fronts and upper level jet streams associated with baroclinic wave development, generate GWs primarily through spontaneous imbalance, where deviations from geostrophic flow trigger GW emission (Plougonven and Zhang, 2014; Zhang et al., 2015b). Particularly, these GWs which are emitted along jet streaks and frontal zones propagate more horizontally and, while interacting with the background flow can foster the generation of shear and turbulence (e.g., Plougonven and Snyder, 2005; Zülicke and Peters, 2006; Trier et al., 2020; Kaluza et al., 2021). This source of GWs is particularly significant because baroclinic life cycles, which are quasi-periodic, being large-scale wave patterns in midlatitudes, are a persistent feature of extratropical atmosphere, with 4–8 distinct baroclinic waves typically evident (Hoskins et al., 1985). Ultimately, the GWs associated with baroclinic waves affect the tropopause structure and may significantly contribute to mixing in the UTLS. In particular, their contribution for shear occurrence in the UTLS has not been systematically studied despite the indications presented in recent years (e.g., Kunkel et al., 2014; Zhang et al., 2019; Kaluza et al., 2021).

The transport due to GWs in the atmosphere is driven by wave dissipation that limit their vertical propagation. As waves ascend into regions of decreasing density, conservation of wave action leads to a systematic amplification of perturbation amplitudes, increasing the likelihood of nonlinear effects and dynamical instability (Lindzen, 1981; Fritts and Alexander, 2003). Upon reaching saturation, further growth is inhibited and wave energy is removed through several mechanisms, such as critical-level absorption, radiative damping, wave–wave interactions (Broutman and Grimshaw, 1988; Sutherland, 2000, 2001), and shear or convectively induced instabilities that lead to wave breaking (Shapiro, 1978; Fritts and Alexander, 2003; Whiteway et al., 2004; Lane and Sharman, 2006). In fact, all waves experience breaking or dissipation before reaching their critical level (Dunkerton, 1997). These processes transfer momentum and energy to the background flow and modify the local wind and stability structure, thereby controlling the vertical extent and spatial distribution of GW activity. GWs also have an associated energy flux, so departures from conservative propagation will lead to energy dissipation and local heating of the atmosphere. If wave dissipation involves turbulence generation, then mixing and turbulent heat, momentum, and constituent transport will also occur. Key effects of GW dissipation that are believed to be necessary in global models are: (i) a body force on the background flow, important at the tropopause and throughout the middle atmosphere, and (ii) mixing effects on temperature and trace gas distributions, important in the upper stratosphere and above (Fritts and Alexander, 2003).

GWs further significantly influence tracer transport and mixing in the UTLS and may also lead to the generation of turbulence. One way is to enhance the strong vertical shear, which leads to dynamical instabilities such as Kelvin-Helmholtz instability, or another possibility is GW breaking at critical

levels where the phase speed of these waves matches the background wind (e.g., Shapiro, 1978; White-way et al., 2004; Lane and Sharman, 2006) leading to localized turbulent mixing. These processes are prominent in the ExTL, where turbulence facilitates tracer exchanges and cross-isentropic mixing (e.g., Hoor et al., 2004; Pan et al., 2006). This mixing layer, where the tracer-based tropopause indicates a blurred boundary between stratospheric and tropospheric air masses (Hegglin et al., 2009), is a direct consequence of STE and turbulent diffusion.

Observational studies including airborne measurements and radiosonde data, show that turbulence in the ExTL enhances the vertical mixing and redistribution of key chemical tracers, such as ozone and water vapor, as well as other radiatively active species, affecting UTLS composition and influencing radiative balance (Birner et al., 2002; Birner, 2006; Hoor et al., 2004; Zhang et al., 2015a; Heller et al., 2017). GWs modulate PV gradients near the tropopause and drive mixing via shear-induced instabilities (Kunkel et al., 2019; Spreitzer et al., 2019). This further suggest that GWs might play a role in enhancing mixing and modifying the structure of the mixing layer (e.g., Kunkel et al., 2019). High-resolution numerical simulations emphasize the role of GWs in enhancing wind shear and triggering instabilities, leading to efficient mixing in the UTLS (e.g., Spreitzer et al., 2019). Additionally, simulations of mid-latitude cyclones suggested the impact of tropospheric jet streak, wind speed, shear enhancement, and GWs on CAT occurrence, highlighting their interaction with wind shear profiles (Trier et al., 2020; Lane et al., 2004).

Evidence from the DEEPWAVE (Deep Propagating Gravity Wave Experiment) campaign has shown that orographic GWs can induce cross-isentropic mixing through turbulence (Lachnitt et al., 2023). This mixing led to irreversible changes in tracer distributions, providing direct proof of the role of GW-induced turbulence in shaping the UTLS composition. These findings underscore the coupling between GW dynamics and mixing processes, particularly within ExTL, where chemical gradients are sharpest and small-scale dynamics play a crucial role in vertical transport and mixing, further influencing large-scale atmospheric processes.

Regarding CAT, very recent study by Lee and Sprenger (2025) suggested that if GWs are involved, they may propagate and perturb the environmental conditions further away from the sources, acting as non-local causes of clear-air turbulence, for instance, when the perturbed regions become unstable and create conditions favorable for Kelvin-Helmholtz instability. Nonetheless, it is suggested that for better predictions of turbulent motion, a more concise analysis of the potential processes leading to turbulence are required. Yet, the question remains whether GWs play a role in development of CAT or whether there is a link between GWs and CAT on larger as well as smaller (spatial and temporal) scales.

1.5 Scientific hypotheses, research questions and outlook

This study was motivated by the wide range of research studies as discussed in Chapter 1 above, given potential for enhance shear occurrence in the vicinity of GW activity, including Shapiro (1976, 1978); Whiteway et al. (2003); Kunkel et al. (2014, 2019); Kaluza et al. (2021). However, to our knowledge an explicit description of an interaction between TSL and GWs, as well as the ExTL, has not yet been presented. Podglajen et al. (2017) suggests that occurrence of tropopause following strong shear layer could be influence by enhanced GW activity associated with deep convection as convection is the major source for GW generation in the tropics through several forcing mechanisms (Müller et al. (2018), and references therein). Kunkel et al. (2019) illustrates the mechanisms facilitating shear-induced mixing within a stably stratified region, focusing on the dynamics that drive mixing and exchange across the tropopause within the ridge of a baroclinic wave. Kaluza et al. (2021) suggested that the role of additional processes like GWs propagation, refraction, and momentum deposition at the tropopause should be investigated in context to the TSL. However, beyond this there was no significant mechanism provided on how this interaction might work.

Hence, the overarching goal of the present study is to elucidate the contribution of small-scales, mainly GWs, and to assess whether such processes play a substantial role, alongwith the fundamental processes and mechanisms that govern the formation of tropopause shear layer and thereby to the maintenance of extratropical transition layer, including idealized modeling, comprehensive modeling with ICON frameworks supported by reanalysis and IFS forecast data, and in situ measurements. In addition to this, the seasonal variation of GWs role in TSL and their indirect effect to large scale circulation patterns have also been studied. Moreover, the present study also investigates the impact of GWs on the local tracer mixing and GWs relevance to the onset of CAT.

The research questions and hypotheses of the present study are as follows:

(a) Quantify the influence of GWs alongwith physical processes on the shear generation in idealized framework

Initially, some ideas from previous studies are used to better understand the role of GWs associated with baroclinic life cycles to the generation of shear and consequent turbulence in the LMS. This analysis is conducted in the framework of idealized baroclinic life cycle experiments of varying complexity with the ICOSahedral Non-hydrostatic (ICON) model.

1. How does the ICON model resolve GWs in idealized baroclinic life cycle simulations, and where do these GWs emerge relative to the tropopause location?
2. Are these GWs associated with instabilities in the LMS, which could lead to mixing?

Hypotheses:

- The emergence and evolution of GWs in baroclinic life-cycle simulations conducted with the ICON model could depend on model resolution and tropospheric forcing. When the model grid spacing is sufficiently fine to resolve mesoscale processes, GWs are expected to form preferentially in the baroclinic flow near the tropopause, where they interact with the background flow and modulate vertical shear across the tropopause.
- The presence of latent heating fosters GW activity and hence can also play a role in shear generation near the tropopause, thereby increasing the probability of dynamic instabilities and turbulent

mixing in the LMS.

(b) Test the hypothesis using in-situ measurement, modern reanalysis, forecast and ICON simulations for realistic case study

This study investigate the contribution of GWs to tropopause following shear enhancement and impact of GWs on the distribution of trace species in the LMS during an extratropical cyclone over the North Atlantic using airborne in-situ observations, ERA5 reanalysis data as well as IFS and ICON forecast data.

1. Whether measured trace species show signatures of small-scale mixing in regions of enhanced static stability in the lower stratosphere ?
2. Are these GW-induced shear layers linked to reduced stability and turbulent mixing? Can the results from the idealized world transferred to a situation over the North Atlantic? Are these GWs responsible for CAT occurrence?
3. How well do different models capture these processes during the observed tracer mixing event? How much does ERA5 differ from high resolution IFS and ICON forecasts?

Hypotheses:

- GWs can amplify vertical shear near the tropopause in the extratropical UTLS by interacting with the background flow, thereby promoting dynamically unstable regions that favor turbulence and mixing. GWs might also contribute to the development of clear air turbulence at the cruising altitude. The contribution and representation of GWs can vary depending on background flow, model spatiotemporal resolution, dynamics and physical processes including convection, moisture and latent heat release.

(c) Examine the annual cycle of GWs and tropopause shear layer over the North Atlantic

This study focuses on the spatial and temporal co-occurrence of GWs and of vertical shear and turbulence in the extratropical LMS over the North Atlantic region.

1. Is there a any relation in an annual cycle of characteristics of GWs, shear, and turbulence occurrences and variability over the North Atlantic in the LMS?
2. Does the GWs and GW-induced shear also play a role in the development of (clear-air) turbulence in the UTLS? Is the diagnosed GWs contribution be attributed to the ExTL dynamics and thereby to the large-scale processes?

Hypotheses:

- GWs can be one of the significant contributor to the formation of TSL, with their impact on instability and turbulence varying seasonally in response to large-scale circulation and tropopause structure. Stronger GW activity, especially under winter baroclinic conditions, can amplify shear and promote turbulent mixing in the ExTL, which can link small-scale wave dynamics to variability on a larger-scale in the atmosphere.

Outlook of the thesis

This thesis examines GWs in a cascade of processes across scales: starting from idealized baroclinic life cycles to realistic extratropical cyclone case study and ending with reanalysis data covering annual cycle to identify the geographical and seasonal patterns of small-scale GWs, GW-induced shear and tropopause shear layer, and investigate processes down to mesoscale in different dynamic situation.

The thesis is structured as follows:

In Chapter 2, the model configuration, overview of the idealized experiments and the procedure to separate GW scale features is described alongwith the datasets used in this study.

In Chapter 3, a series of baroclinic life cycle experiments with the ICOSahedral Non-hydrostatic model (ICON) is presented in order to study the impact of GWs on the occurrence of vertical wind shear and consequent potential turbulence, an indicator for turbulent mixing in the LMS. The occurrence of GWs and shear are discussed in context of varying model resolution as well physics parameterization processes in this part. The important role of moist tropospheric dynamics is identified to foster the GW activity and its relevance to shear enhancement in the lower stratosphere which gives rise to the potential for dynamic instability is discussed.

In Chapter 4, an evidence is presented which illustrates the role of GWs and of GW-induced shear as a mechanism for the occurrence of turbulence and exchange of air masses with different chemical composition in the lower stratosphere over the North Atlantic during a life cycle of an extratropical cyclone. This is further extended by the validation of these results with airborne in-situ measurements, supported by reanalysis and forecast datasets and to the relevance of GW-induced shear with onset of CAT.

In contrast to the chapters before, where instantaneous GW-induced shear events were examined, Chapter 5 focuses on the spatial and temporal co-occurrence of GWs and of vertical shear and turbulence in the extratropical lowermost stratosphere. The distinct hotspots of GW activity via zonal GW forcings and absolute momentum fluxes are identified and their particular characteristics associated with tropopause shear layer such as their geographical distribution and seasonal cycle are discussed. Special attention is given to the intra-monthly variability of occurrence of TSL and the quantification of mixing in the North Atlantic lowermost stratosphere. Chapter 6 comprises a summary of the key findings of this work, as well as an outlook on open questions for future research that arise from these results.

2 Atmospheric model, data and methodology

Objective

This chapter provides a general overview of the ICON model first, followed by a description of the ECMWF Integrated Forecasting System. It aims to present an overview of the hydrostatic and non-hydrostatic dynamical core of models, as well as essential tools, and algorithms that are frequently used throughout this work. It also outlines methods used to compute resolved GW momentum fluxes as well as turbulence diagnostics.

2.1 Atmospheric model ICON-NWP

The Icosahedral Non-hydrostatic (ICON) general circulation atmospheric model used here in its numerical weather prediction mode (ICON-NWP) and is part of the unified modeling framework developed in Germany. This framework employs a single model system across different scales in time and space. The non-hydrostatic dynamical core of ICON can be applied over a broad range of scales, for example approximately 100 km to 100 m, and is able to explicitly represent convective processes.

In addition to the global NWP configuration used in this study, ICON is also available in a climate configuration, in a coupled chemistry–aerosol mode (ICON-ART), and in limited-area (ICON-LAM) and large-eddy (ICON-LEM) configurations. All ICON configurations are based on the same dynamical core (Zängl et al., 2015). This hierarchical modeling framework enables parameterizations to be evaluated from a very small-scale (e.g., turbulence-resolving; ~ 100 m) LEM simulations to the global-scale. The work presented herein will focus on idealized as well as real case simulations with the global and nested setup of ICON-NWP. The following section briefly describe the ICON model itself alongwith the experimental setup used during this work.

2.1.1 Model description

This section provides a brief overview of the ICON-NWP configuration. The dynamical core used in ICON is described in detail by Zängl et al. (2015). The tutorial for working with the ICON Model is available on <https://www.icon-model.org>. The ICON source code is provided under an institutional license granted by the German Weather Service (DWD), and the current version is available from the DKRZ GitLab repository.

Icosahedral grid of ICON

One of the key features of ICON is its icosahedral grid, formed by mapping an icosahedron onto the sphere, which yields 20 nearly equilateral spherical triangular faces (see Figure 2.1a). Each edge of the initial triangular faces is first subdivided into n segments, and connecting the new vertices produces

Table 2.1: Commonly used ICON resolutions in R_nB_k notation.

Grid nomenclature	$\overline{\Delta x}$ (km)
R02B04	157.8
R02B05	78.9
R02B06	39.5
R02B07	19.7
R03B07	13.2
R03B08	6.5
R03B09	3.3

n^2 smaller spherical triangles within each parent triangle. Subsequently, the grid is refined through k successive edge bisections. The resolution of the resulting icosahedral mesh is denoted by R_nB_k . For a specified model resolution, the total number of grid cells n_c is given by:

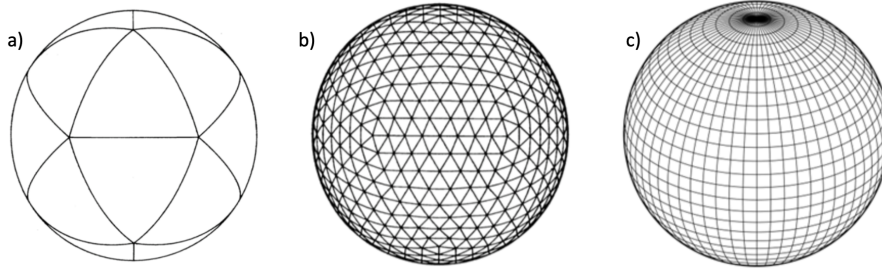


Figure 2.1: Illustration of (a) an icosahedron mapped onto the sphere, (b) the corresponding global ICON grid at **R2B2** resolution, and (c) regular latitude–longitude grid for comparison.

$$n_c = 20n^24^k. \quad (2.1)$$

The average cell area $\overline{\Delta A}$ is determined by the total grid-cell count n_c and the Earth's radius $r_e = 6.371229 \times 10^6$ m:

$$\overline{\Delta A} = \frac{4\pi r_e^2}{n_c}, \quad (2.2)$$

Using Eq. 2.1 and 2.2, the mean horizontal grid resolution $\overline{\Delta x}$ is then given by:

$$\overline{\Delta x} = \sqrt{\overline{\Delta A}} = \sqrt{\frac{\pi}{5} \frac{r_e}{n2^k}}. \quad (2.3)$$

The quantities defined above for commonly used ICON resolutions are summarized in Table 2.1. In particular, the total number of cells and the corresponding mean grid spacing enable a comparison with the more widely used Gaussian latitude-longitude grid. The present study applies ICON resolution from R02B05 to R03B09, corresponding to grid spacings of approximately 78.9 to 3.3 km. For operational global numerical weather prediction, the German Weather Service (DWD) uses the R03B07 resolution, which provides a average resolution of about 13.2 km.

Vertical grid

Like most atmospheric modeling systems, the vertical coordinate system in ICON is chosen to be a terrain following system. In contrast to commonly used pressure-based vertical coordinates, ICON employs a height-based vertical coordinate with Lorenz-type staggering. In this framework, vertical velocity is defined at half levels, whereas the remaining prognostic variables are at full levels. ICON can be run with different number of vertical levels, extending from approximately 20 m (lowermost level) above the surface to about 75 km altitude (uppermost level). Following (Leuenberger et al., 2010), ICON uses a smooth level vertical (SLEVE) coordinate, which allows a more rapid transition to smooth levels in the UTLS. This study employs configurations with 40, 100, and 200 vertical levels while keeping the domain height constant at 35 km in altitude. These levels correspond to approximate vertical grid spacings of about 900, 300, and 100 m, respectively, in the UTLS.

2.1.2 Physical parameterization schemes

The atmospheric physics module of ICON comprises a multitude of schemes designed to depict diabatic and turbulent processes at the subgrid-scale and their influence on the resolved circulation. In idealized simulations, aim is to investigate the impact of certain physical processes on GWs. In particular, focus is to examine the impact of latent heating and turbulence on the GWs and, ultimately, the emergence of shear and dynamic instability in the LMS. To accomplish this, a minimal set of physical parameterizations that reliably represent these processes are included. Moreover, for comprehensive ICON-NWP simulations, processes that occur on scales too small to be resolved directly are parameterized and such processes includes radiation schemes for longwave and shortwave radiation, a cloud-cover parameterization, a packages of mass-flux due to shallow and deep convection. These parameterizations are kept constant in different ICON experiments discussed in Chapter 5. A detailed description of such diabatic processes formulation are given in Prill et al. (2020). The schemes used in this study are briefly outlined in the following.

(a) Turbulence: vertical transfer and diffusion

The moist turbulence scheme TURBDIFF (TURBulent DIFFusion) developed by Raschendorfer (2001) is used, which emphasizes the distinction between turbulence and potential non-turbulent components of the subgrid-scale energy spectrum. This distinction introduces additional scale interaction terms in the prognostic TKE equation, accounting for extra shear production of TKE driven by non-turbulent subgrid-scale flow structures. This scheme can also amplify the intensity of turbulent vertical mixing. Three-dimensional turbulent effects are neglected which is a valid approximation for simulations on the mesoscale, which means that horizontal homogeneity is assumed. Therefore, the Boussinesq approximation is taken into account while parameterizing only vertical turbulent fluxes. Furthermore, the vertical change in specific humidity (q_v) and cloud water (q_c), as well as vertical shear of the horizontal wind components, have a substantial impact on the TKE budget equation. In the case of moist simulations, TURBDIFF includes processes related to saturation adjustment, which leads to latent heating and impacts the overall energy budget

(b) Cloud microphysics and latent heat release

In ICON, cloud microphysics parameterization uses a closed set of equations to calculate the formation and evolution of condensed water in the atmosphere. Latent heating can occur as part of the microphysics scheme, chiefly via the saturation adjustment and the convection scheme which leads to convective precipitation. The saturation adjustment process converts any supersaturation into cloud water or ice, releasing latent heat and thus influencing atmospheric stability. Notably, the employment of saturation adjustment leads to latent heating, which impacts the overall energy budget. This excess energy significantly influences the dynamics of the atmosphere, marking a significant difference from the dry simulations where such effects are absent. The present study used a single-moment microphysics scheme (Seifert, 2008). This scheme predicts specific humidity along with the specific mass content of four hydrometeor categories: cloud water, rainwater, cloud ice, and snow. This study focuses on understanding the effect of microphysics on dynamics and, specifically, the associated latent heat release of the large-scale clouds on GWs, excluding the convective scheme, which would necessitate a more intricate configuration, including radiation and surface fluxes.

(c) Subgrid scale orographic drag

Depending on its source mechanism, the GW drag can be typically partitioned into orographic and non-orographic components. In ICON, both are represented within the slow-physics parameterization framework (that is with larger time stepping) but are treated separately. We first describe the orographic drag in this section, followed by the non-orographic component in the subsequent section.

The orographic GW drag in ICON is parameterized within the subgrid-scale orography (SSO) drag scheme, following Lott and Miller (1997). This scheme was implemented to increase the surface drag in order to reduce the surface-pressure biases, such as highs that are too high and lows that are too low. With sufficiently high SSO, low level flow becomes partially blocked. As a consequence, drag develops along mountain flanks and GWs are generated as the upper portion of the flow is forced over the orography. The non-dimensional height H_n (i.e., of the subgrid scale mountain), representing the inverse Froude number Fr , is defined as:

$$H_n = Fr^{-1} = \frac{NH}{|U|}, \quad (2.4)$$

with N = Brunt-Väisälä frequency (Eq. 1.1), the maximum height of the mountain H , and the wind speed $|U|$.

The orographic input fields required for the SSO scheme are derived from the GLOBE (Global Land One-km Base elevation Project) dataset, that has a resolution of ~ 1 km (Hastings et al., 1999). The SSO parameterization includes four tunable parameters: (i) the critical Froude number, (ii) the low level wake drag constant, (iii) the GW drag constant, and (iv) the critical Richardson number.

The critical Froude number (Fr_c) has a default value of 0.4 and governs the likelihood of low-level flow blocking. Larger Fr_c values promote more frequent blocking, whereas smaller Fr_c values favour flow passing over the orography. Hence, a reduction of Fr_c also decreases the excitation of orographic GWs. The low level wake and GW drag constants are directly proportional to the magnitudes of the SSO drag and the orographic GW drag, with default values of 1.5 and 0.075, respectively. At last, the Ri_c controls the onset of the GW breaking and has a default value of 0.25. An increase in Ri_c number leads to the reduction of the altitude at which GWs tend to break and exert drag or deposit momentum.

(d) Non-orographic gravity wave drag

GWs generated by synoptic-scale flow can have horizontal and vertical wavelengths smaller than the model grid spacing and therefore must be represented through parameterization. In addition, non-orographic gravity waves exert a substantial influence on the middle and upper atmosphere and play an important role in shaping stratospheric circulation (Polichtchouk et al., 2018b). In ICON, the non-orographic GW drag parameterization follows the formulations of Warner and McIntyre (1996); Scinocca (2003), and is documented in Orr et al. (2010). The scheme prescribes vertical fluxes of horizontal momentum at a launch level in the UT, and represents a statistical mean of all sources of upward-propagating GWs. The vertically integrated momentum-flux magnitude across the GW spectrum is assumed to be constant and is expressed as:

$$\rho F(\cos\varphi_i, \sin\varphi_i)|_{z=z_0} = \rho F_0(\cos\varphi_i, \sin\varphi_i) = \overline{\rho w' |v'_h|}(\cos\varphi_i, \sin\varphi_i)_{z=z_0}, \quad (2.5)$$

where ρ denotes air density, z_0 the launch level. The azimuthal angle φ_i is the element of four horizontal directions of horizontal momentum sampled by the scheme. The perturbation velocities w' and v'_h are the GW-borne fluctuations of the vertical and horizontal wind components, respectively. The overline denotes the spatial averaging over one grid cell. The reference momentum-flux magnitude $\rho_0 F_0$ is controlled by the tunable parameter, with a default value of 0.0025. Using the spectral distribution of ρF at the launch level (Eq. 2.5) together with the local atmospheric state, the ρF can be integrated in the vertical. The resulting drag exerted on the horizontal flow is obtained from the vertical divergence of this momentum flux.

$$\left(\frac{\partial v_h}{\partial t}\right)_{drag} = \left[\frac{\partial(u, v)}{\partial t}\right]_{drag} = -\frac{1}{\rho} \cdot \frac{\partial(\overline{\rho F}_{zonal}, \overline{\rho F}_{meridional})}{\partial z}. \quad (2.6)$$

In this formulation $\overline{(\cdot)}$ denotes the integration over the GW spectrum. The resulting drag becomes non-zero at altitudes where GWs undergo breaking.

Both the orographic and non-orographic drag contributions are constrained by a height-dependent threshold in order to prevent numerical instabilities associated with too strong increase of the wind magnitude. The associated processes are treated as irreversible and thus acts as a source of heat.

(e) Convection

The convection scheme in ICON for both shallow and deep convection is based on a mass-flux scheme, where the entrainment and detrainment include contributions from turbulent and organized part. The implemented scheme for cumulus convection in ICON represents a branch of the Tiedtke-Bechtold convection scheme that is used in the IFS model. As such the shallow convection is parametrized using a mass-flux convection scheme (Tiedtke, 1989; Bechtold et al., 2008, 2014; ECMWF, 2017). Similar to the operational IFS scheme it contains an improved convective available potential energy closure for deep convection (Bechtold et al., 2014) in order to improve the representation of the diurnal cycle of convection over land.

The full convection parameterization is generally applied at horizontal grid spacings coarser than about 5 km, with resolution-dependent adjustments introduced for grid spacings below ~ 20 km. For convection-permitting resolutions ($\sim 1-3$ km), the largest convective clouds can be explicitly resolved by the model, and the parameterized treatment of deep and mid-level convection can be turned off.

(f) Radiation

Radiation is treated using ecRad scheme (Hogan and Bozzo, 2018), which is implemented in ICON by (Rieger et al., 2019), includes the Rapid Radiative Transfer Model (RRTM, Müller et al., 2016) as well as a radiative solver that calculates the propagation of radiation through the optical medium (Prill et al., 2020). It considers only upwelling and downwelling radiation, due to which the optical properties are integrated for all angles within the hemisphere, reducing the optical parameters that are required for optical depth, single factor albedo and symmetry factor, for example, of scattering. Radiative heating and cooling are computed from the radiative fluxes which then feeds back into dynamics and physics.

2.1.3 Calculation of potential vorticity on the ICON Grid

This section shortly describes the calculation of PV on the ICON grid (see also Selz, 2019). In a nonhydrostatic model, a vertical coordinate in terms of pressure does not make sense since it cannot be taken for granted that the pressure is monotonously decreasing with increasing altitude. In ICON the choice is a height based coordinate system that follows the terrain and consequently, the top and bottom triangle faces are inclined with respect to the tangent plane on a sphere. Hence, the exact altitude of each grid box depends on the geographical position on the globe.

To calculate PV on the ICON grid, Ertel (1942) or Eq. 1.2 is transformed to spherical coordinates, locally rotated to the edge-coordinate system of the grid and finally transformed to a generalized vertical coordinate system.

$$PV = \frac{1}{\rho} (\nabla \times \mathbf{v}_a) \cdot \nabla \theta, \quad (2.7)$$

where ρ denotes air density, f the Coriolis parameter, \mathbf{v}_a the three-dimensional absolute wind and $\nabla \theta$ the vertical gradient of potential temperature Θ . The absolute wind $\mathbf{v} = (u, v, w)$ is the sum of the wind relative to rotating Earth and velocity of the rotation itself, i.e., $\mathbf{v}_r = \boldsymbol{\Omega} \times \mathbf{r}$. Using $f = \nabla \times (\boldsymbol{\Omega} \times \mathbf{r}) = 2\boldsymbol{\Omega}$, Eq. 2.7 becomes:

$$PV = \frac{1}{\rho} (\nabla \times \mathbf{v} + \mathbf{f}) \cdot \nabla \theta. \quad (2.8)$$

Also note that the PV field from model output is three-dimensional. It can be written on the original model levels as well as can be interpolated to z , p and Θ levels.

2.2 The ECMWF integrated forecast system

The numerical weather prediction data used in chapter 4 and 5 are produced with the ECMWF's Integrated Forecast System (IFS), which represents one of the most advanced operational atmospheric modeling systems currently available. The IFS utilizes a *hydrostatic* dynamical core combined with semi-implicit and semi-Lagrangian numerical schemes. Fast processes, such as GWs, are treated implicitly to enhance numerical stability. The model formulation involves a spectral-grid point transformation: the governing equations are solved in spectral space, while advection and physical parameterizations are computed on the grid. Vertically, the atmosphere is discretized using hybrid pressure-sigma coordinates. Subgrid scale processes that cannot be explicitly resolved are represented through parameterization schemes, including radiation, cloud microphysics, moist convection, turbulent exchanges of heat, moisture, and momentum, as well as both orographic and non-orographic gravity wave drag (ECMWF,

2016b). The following section briefly describes the physical parameterization schemes implemented in the IFS model version used for the analysed in this thesis.

(a) Turbulence

The turbulent diffusion scheme represents the vertical exchange of heat, momentum and moisture through sub-grid scale turbulence. The vertical turbulent transport is treated differently in the surface layer and above. The turbulence parameterization in IFS is formulated through prognostic tendency equations that describe the temporal evolution of the horizontal momentum components (u , v), temperature (T), and moisture variables (q , q_l , q_i for vapour, liquid, and ice). These tendencies represent the effects of unresolved vertical turbulent mixing and are expressed as diffusive fluxes that depend on the local vertical gradients $\partial\phi/\partial z$ and an associated exchange coefficient K_ϕ ($\text{m}^2 \text{s}^{-1}$), where ϕ denotes the quantities affected by the parametrization scheme (u, v, T, q).

The choice of the turbulence closure that is applied depends on the height above the surface as well as on the local stratification. Near the surface, mixing is represented by a first-order K -diffusion approach based on Monin-Obukhov similarity theory, while in convective boundary layers this formulation is extended by an eddy-diffusivity mass flux scheme that accounts for both local K -diffusion and non-local eddy mass transport through the boundary layer (Köhler et al., 2011).

In the free atmosphere, the scheme differentiates between unstable layers ($N^2 < 0$) where the exchange coefficient K_ϕ is determined according to Monin-Obukhov similarity theory, and stably stratified conditions ($N^2 > 0$) where K_ϕ is calculated based on a revised Louis scheme (Louis et al., 1982). In this formulation, K_ϕ depends on the vertical gradients of the prognostic variables and on a characteristic mixing length, and is further modulated by stability functions that vary with the gradient Richardson number. These functions reduce turbulent mixing with increasing stability but allow weak residual diffusion even for large Ri , thereby gradually eroding strong shear and temperature gradients. Since the present study focuses on shear-induced turbulence near the tropopause, this stable-regime parameterization is of particular relevance.

(b) Clouds and large-scale precipitation

Cloud and large-scale precipitation processes in the IFS are represented through a dedicated micro-physical parameterization that accounts for phase changes and interactions among different hydrometeor species. The scheme describes processes such as condensation, deposition, evaporation, collection, melting, and freezing, thereby enabling the exchange of mass between vapour, liquid, and frozen phases. It provides prognostic equations for multiple condensate categories, including cloud liquid water, cloud ice, snow, and rainwater content, as well as for a subgrid fractional cloud cover (Tiedtke, 1989; Forbes and Tompkins, 2011; Forbes and Ahlgrimm, 2014). The formulation also permits occurrence of supersaturation with respect to ice and mixed-phase clouds. The thermodynamic impact of phase transitions is incorporated through latent heating effects, in the form of $\partial T/\partial t$, a temperature tendency term.

(c) Subgrid-scale orographic drag

The model further accounts for the effects of unresolved GWs on the mean flow through parameterizations of both orographic and non-orographic GW drag. Subgrid-scale orographic drag implemented as a turbulence induced momentum sink in the lower troposphere due to the non-resolved orography (<5 km) (Beljaars et al., 2004), as well as GW drag due to absorption and reflection of vertically propagating GWs and a blocked flow drag due to the immediate blocking of the unresolved orography itself (Lott and Miller, 1997). The resulting drag is incorporated as additional momentum tendency terms for the horizontal wind components in the turbulence scheme.

(d) Non-orographic gravity wave drag

Non-orographic GW drag parametrization scheme implements the effect of non-resolved GWs generated by processes such as deep convection, frontal systems, and shear zones. The scheme emits a globally uniform m^3 spectrum, with m being the vertical wave number, of non-resolved GW upwards from the UT, with drag being applied to mean flow when wave instability due to critical layers or reduced air density and non-linear dissipation occurs (Orr et al., 2010). The impact is ultimately implemented as tendency terms $\partial\phi/\partial t$ resulting from the divergence of the wave momentum flux, where ϕ stands for the horizontal wind components (u, v) and the temperature (T).

(e) Convection

Moist convection is represented using an advanced mass-flux parameterization based on the original scheme of Tiedtke (1989). The formulation introduces additional tendency terms in the prognostic equations for heat, moisture, momentum, and chemical tracers to account for subgrid-scale convective transport. The scheme uses different approaches for different cloud type: deep convection is linked to the removal of convective available potential energy, mid-level convection incorporates the influence of the large-scale vertical motion, and shallow convection is constrained by the moist static energy budget. The parameterization further includes a simplified microphysical scheme to represent cloud formation and precipitation processes. This convection scheme is an vital factor concerning the representation of static stability and vertical shear in the tropopause, as they influence the momentum and heat budget in outflow regions of deep convection through heat and momentum transport as well as through energy conversion.

(f) Radiation

Radiative transfer in the IFS is represented by separate treatments of shortwave and longwave fluxes, which are incorporated into the thermodynamic equation as temperature tendency terms of the form $\partial T/\partial t = f(\partial F/\partial p)$, where F denotes the net vertical radiative flux. Thus, heating or cooling rates are determined by the vertical divergence of the radiative energy flux. Radiative tendencies are particularly relevant in the UTLS and near the tropopause, where strong vertical gradients in radiatively active trace gases and the presence of high-reaching clouds substantially modify the local thermal structure. The radiation scheme uses prognostic model fields, including temperature, humidity, and cloud properties,

together with prescribed climatologies of aerosols and trace gases that contribute significantly to radiative forcing. The implementation is based on the Rapid Radiative Transfer Model (RRTM) framework, while cloud-radiation interactions are treated using cloud properties provided by the microphysics parameterization combined with a Monte Carlo Independent Column Approximation (McICA) to account for subgrid-scale cloud variability. In the long wave spectrum, radiative transfer includes absorption by H₂O, CO, O₃, methane CH₄, N₂O, and selected chlorofluorocarbons, and is computed across multiple spectral bands spanning $\approx 10\text{--}3250\text{ cm}^{-1}$. The shortwave component additionally considers molecular oxygen absorption and covers a broader spectral range extending to about $50\,000\text{ cm}^{-1}$.

2.3 Vertical derivatives and representation of GWs in models

Hydrostatic equilibrium refers to an atmospheric state in which the (upward directed) pressure gradient force is balanced by the (nearly downward directed) gravitational pull of the Earth, such that vertical acceleration is neglected. This hydrostatic equilibrium can be written as

$$\frac{\partial p}{\partial z} = -\rho g \quad (2.9)$$

This balance is essential for maintaining the Earth's atmosphere, which is, on average, very close to hydrostatic equilibrium. For large-scale atmospheric motions resolved at grid spacings of order 10 km, as in current operational models, the hydrostatic approximation is well satisfied. However, the processes with small horizontal scales are not in hydrostatic equilibrium. In pressure coordinates, vertical motion is represented by the pressure vertical velocity $\omega = \partial p / \partial t$, which describes the Lagrangian rate of pressure change of an air parcel. Negative values correspond to ascent and positive values to subsidence. In hydrostatic models such as ERA5 and IFS, ω is diagnosed directly from the continuity equation and therefore constitutes the native representation of vertical motion. The geometric vertical velocity is then calculated using;

$$w = -\frac{\omega}{\rho g}. \quad (2.10)$$

On the other side, non-hydrostatic (Full Euler) formulation retains the full vertical momentum equation considering vertical acceleration term,

$$\frac{Dw}{Dt} = -\frac{1}{\rho} \frac{\partial p}{\partial z} - g \quad (2.11)$$

allowing explicit vertical accelerations and buoyancy-driven motions. Non-hydrostatic effects become significant when the horizontal and vertical scales of motion are comparable. In atmospheric models, this regime typically occurs for phenomena with horizontal scales of order 10 km that are resolved with grid intervals of order 2 km. Therefore the high-resolution models used nowadays by the weather services are formulated as non-hydrostatic models, such as ICON, while global climate models with coarser horizontal resolution can use the hydrostatic assumption.

An example Figure 2.2 provides a comparison between hydrostatic and non-hydrostatic model behavior is the propagation of orographically forced GWs in presence of vertical shear. The configuration considers airflow over a 100 m high ridge in a stably stratified atmosphere with constant Brunt–Väisälä frequency. The background wind increases linearly from 10 m s^{-1} at the surface to 35 m s^{-1} at the

tropopause and remain uniform above. A reference solution obtained by the state-of-the-art model EULAG (Eulerian/semi-Lagrangian fluid solver, Prusa et al., 2008) (Figure 2.2a) shows trapped GWs that propagate predominantly horizontally. Corresponding simulations with the IFS are shown for the non-hydrostatic and hydrostatic configurations (Figures 2.2b and 2.2c). The hydrostatic formulation produces vertically propagating mountain GWs, whereas the non-hydrostatic configuration correctly reproduces the trapped, horizontally propagating wave pattern seen in the reference solution.

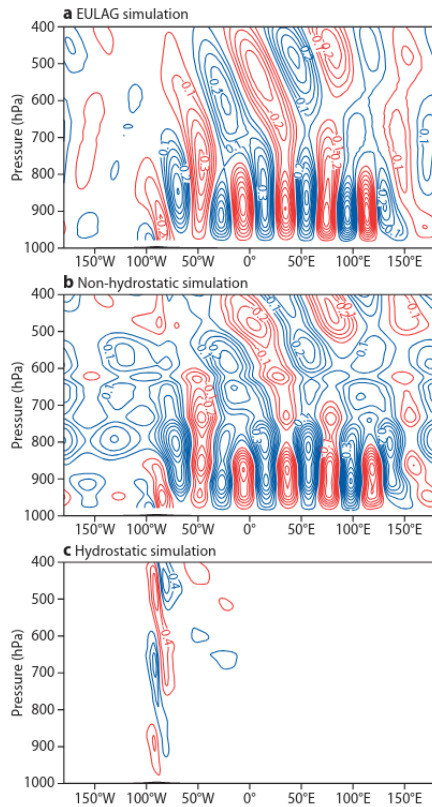


Figure 2.2: Vertical cross-section of vertical velocity at the equator comparing (a) the non-hydrostatic EULAG simulation with (b) non-hydrostatic and (c) hydrostatic IFS simulations for a linearly-sheared flow past a quasi-two-dimensional obstacle at the equator on the reduced-size sphere. The atmosphere is vertically-stratified and there is a zonal flow of 10 m s^{-1} impinging on the mountain near the surface, increasing linearly to 35 m s^{-1} at 10.5 km (or approximately 687 hPa) and constant above. Contour interval is 0.05 m s^{-1} ; blue/red lines denote positive/negative contours.

Figure adapted from Wedi and Malardel (2010).

In the present study, ICON employs a pure non-hydrostatic dynamical core, while IFS are based on hydrostatic formulations combined with semi-implicit and semi-Lagrangian numerical schemes. However, it should be noted that the differences in horizontal and vertical resolution, numerical discretization, and physical parameterizations influence the representation of small-scale GWs. In particular, the accuracy of diagnosed quantities that depend on vertical derivatives, e.g., S^2 , N^2 , and PV, are sensitive to the vertical grid spacing and the numerical formulation of the governing equations. Consequently, variations in GW properties, shear, and thus, turbulence diagnostics between ICON, ERA5, and IFS should not be interpreted solely as physical differences, but also as a consequence of their distinct numerical resolution and model dynamics.

2.4 Datasets

(a) ERA5 reanalysis data

In Chapter 4, as a reference for the zonal and meridional wind components, ERA5 the most recent reanalysis produced by the European Center for Medium-Range Weather Forecasts 5th generation (ECMWF, Hersbach et al., 2020) is used. It is based on 4D-Var data assimilation and model forecast in Cy41r2 cy-

cle of the ECMWF Integrated Forecasting System model. Here, the ERA5 reanalysis fields are analyzed on a regular 0.25° latitude-longitude grid, native vertical hybrid sigma-pressure levels, and one hourly time resolution (Hersbach et al., 2020). The ERA5 reanalysis is based on the IFS version with TL639 spectral truncation about $\Delta x \approx 31$ km horizontal grid spacing. Specifically, the native hourly zonal wind data provided on model levels with pressure-based vertical coordinates in the stratosphere is used.

ERA5 also features a finer vertical resolution, with 137 model levels extending up to 0.01 hPa, makes it particularly adept to capture GWs with vertical wavelengths down to ~ 1 – 2 km. To reduce spurious wave reflections and improve numerical stability, ERA5 incorporates advanced model treatments such as sponge layers and hyper diffusion. These features contribute to its ability to simulate large-scale wave dynamics, including GWs with wavelengths exceeding 400 km (Stephan and Mariaccia, 2021). Given these characteristics, ERA5 serves as a robust reference dataset, particularly useful for evaluating subgrid-scale wind shear in the UTLS. In this study, horizontal wind components were retrieved on model levels and converted to altitude levels using geopotential height, temperature, and humidity fields.

It should be taken into consideration that the increasing vertical grid spacing with increasing altitude in the native coordinates may result in a potential bias towards larger values of vertical wind shear at lower altitudes. However, in the UTLS region, the vertical grid spacing increases from around 300 m at 5 km altitude up to around 400 m at 20 km altitude (e.g., Hoffmann et al., 2019). Thus, the resolution bias unlikely contributes substantially to the results here.

(b) IFS forecast

Further the ECMWF Integrated Forecasting System IFS cycle Cy43r3 data as a high resolution companion of the ERA5 reanalysis dataset on regular 0.25° and 0.1° latitude-longitude grid with 1 hourly temporal resolution is used. Also this data is of interest because it is a version very close to the version used for ERA5. The operational IFS employs a Tco1279 spectral truncation and an associated O1280 octahedral grid which results in an $\Delta x \approx 9$ km grid spacing in the horizontal and incorporates 137 vertical levels, derived from the operational analysis data. This IFS data has almost the same dynamical core and physical package as ERA5 which allows to study the effect of higher horizontal resolution on the representation of shear and GWs. We use the operational forecast from 23 September 2017, 00:00 UTC, with hourly resolution for the first 24 hours.

(c) ICON simulations

Furthermore, ICON simulation data for WISE case is used from Schwenk and Miltenberger (2024). This allows us to study the representation of the same situation in model with different dynamical core and physics package as well as in three different resolutions from roughly the resolution in IFS data to almost convection permitting resolution. The atmospheric evolution for this case was simulated using the high resolution ICON modeling framework (version 2.6.2; Zängl et al., 2014) over the North Atlantic Ocean to fill the data gaps when validating the WISE observations and ECMWF product results.

The simulation run was initialized with the operational ICON global analysis at 00:00 UTC on 20 September 2017, shortly before the cyclone developed, and ran for 96 hours, ending at 00:00 UTC on 24 September 2017. The global ICON model simulation at R03B07 grid (~ 13 km) with a 120 s time step, was nested twice with R03B08 (~ 6.5 km) and R03B09 (~ 3.3 km) grids with 60 s and 30 s time steps, respectively. Nonetheless, we focus mainly on the largest domain that covers the North Atlantic

and the research flight region. For the dataset intercomparison, the focus is initially on the simulation of larger domain that covers the North Atlantic and the research flight region.

The spatial resolution of innermost nested domain is chosen such that it permits convection. In the global domain, convection is parameterized using the Tiedtke–Bechtold convection scheme (Tiedtke, 1989; Bechtold et al., 2008). In the higher-resolution nested domains, only shallow convection is parameterized. The non-orographic GW drag (Orr et al., 2010), sub-grid scale orographic drag (Lott and Miller, 1997) and turbulence (Raschendorfer, 2001) are parameterized using the standard schemes used in ICON. Radiation is treated using the Rapid Radiative Transfer Model. Cloud microphysical processes are computed with the two-moment microphysics scheme (Seifert and Beheng, 2005), which gives the specific mass mixing ratios of six hydrometeor species including cloud water, rainwater, cloud ice, snow flakes, graupel grains and hailstones. This model configuration enables a detailed representation of the region of interest, i.e., different sources of GWs including convection and baroclinic instability.

Table 2.2: Physics parameterization schemes used for ICON_NWP simulations used in Chapter 4.

Domain	ICON grid, Δt (s)
DOM01	R03B07, 120
DOM02	R03B08, 60
DOM03	R03B09, 30
Physics	Schemes used
Convection	Tiedtke–Bechtold convection scheme (DOM01) only shallow convection (DOM02, DOM03)
Non-orographic gravity wave drag	Orr et al. (2010)
Sub-grid scale orographic drag	Lott and Miller (1997)
Turbulence	Raschendorfer (2001)
Radiation	Rapid Radiative Transfer Model
Cloud microphysics	two-moment microphysics (Seifert, 2008)

2.5 Analysis Methods

This section outlines the analysis methods applied throughout this study, such as methods used to separate small-scale features, derive GW momentum fluxes, identify mixing events through tracer correlations, and compute turbulence diagnostics.

2.5.1 Gravity wave momentum flux

One of the key properties of GWs is their ability to transport horizontal momentum vertically, then depositing it into the mean flow upon breaking.

The vertical flux of horizontal momentum, termed as momentum flux, is an important coupling mechanism between the lower layers of the atmosphere, i.e., the troposphere, stratosphere and mesosphere. In the case of ascending waves, decreasing density with altitude means that even low levels of tropospheric momentum flux can have far-reaching effects on the circulation of the middle atmosphere if they are transported and deposited by GWs. For GWs propagating against the mean flow in the horizontal direc-

tion, this exerts an acceleration, in other term usually a “drag” force, upon circulation.

GW momentum flux is a vector quantity, and can be defined in terms of zonal, meridional and vertical wind perturbations u' , v' , and w' (e.g., Fritts and Alexander, 2003) as:

$$(F_x, F_y) = \bar{\rho} (\overline{u'w'}, \overline{v'w'}). \quad (2.12)$$

where $\bar{\rho}$ is the mean background density, F_x and F_y are momentum flux in the zonal and meridional directions respectively. The units momentum flux are force per unit area, i.e. Pascals.

Procedure to obtain resolved GW momentum flux

Here, we discuss the step by step methods used to isolate small-scale GW features from the large-scale flow patterns.

In order to quantify the GW perturbations from synoptic-scale structures, we use a hybrid approach that combines both a dynamical and a statistical approach to separate large- and small-scale components of the flow. The selection of this hybrid approach is motivated by its ability to effectively capture the patterns of small-scale GWs (Wei et al., 2022; Zhang et al., 2025). This criterion is based on both the scale and structural characteristics of the perturbations. The frequency and wavelength of these perturbations are also critical identifiers of GW-scales, distinguishing them from other atmospheric phenomena.

In a dynamical method to isolate GW signals we follow the approach used in Wei et al. (2022). Specifically, we extract the divergent components of the horizontal wind field using the Helmholtz decomposition technique, prior to applying any spatial filtering or smoothing.

The Helmholtz theorem allows a horizontal vector field $\vec{v} = (u, v)$ to be decomposed into an irrotational (divergent) component and a solenoidal (rotational) component as:

$$\vec{v} = \nabla\phi + \nabla \times \psi, \quad (2.13)$$

where ϕ is the scalar velocity potential and ψ is the stream function. The divergent component $\vec{v}_{\text{div}} = \nabla\phi$ captures unbalanced, compressible motions and is dynamically associated with GW activity.

To obtain ϕ , we solve the Poisson equation derived from the divergence of \vec{v} :

$$\nabla \cdot \vec{v} = \nabla^2\phi. \quad (2.14)$$

This is solved numerically in spectral space under the assumption of periodic lateral boundary conditions. Once ϕ is obtained, the divergent wind components are calculated as:

$$u_{\text{div}} = \frac{\partial\phi}{\partial x}, \quad v_{\text{div}} = \frac{\partial\phi}{\partial y}. \quad (2.15)$$

After extracting the divergent wind components, the spectral filtering is applied to retain only small-scale fluctuations. For the so-called statistical approach, a filter in spectral space using a one-dimensional zonal FFT over the full domain is applied. As part of GW-scale processes understanding, we focus particularly on small-scales, excluding any with wavenumber from 0 to 20 and considering the covariance

only from zonal wavenumbers 21 and higher, i.e.

$$u' = u_{\text{div}} - (u_{\text{div}})_{k \leq k_s}, \quad (2.16)$$

where $k_s=20$ is the wavenumber cutoff that splits respective quantities into a large-scale and small-scale components. The latter is the perturbation from synoptic-scale structures and is from now on denoted with primes ('). Note here that the sensitivity tests with k_s values of ± 4 showed no significant variation in the resulting primed quantities. An example of the deviation of small-scale from large-scale flow is given in Figure 2.3. This two-step process, Helmholtz decomposition followed by spatial filtering, ensures that the GW zonal (F_x) and meridional (F_y) momentum fluxes are computed using flow components that are both dynamically relevant and spectrally separated from the background state. The GW momentum flux components are then computed using:

$$F_x = \overline{\rho u' w'}, \quad (2.17)$$

$$F_y = \overline{\rho v' w'}, \quad (2.18)$$

where ρ is the air density, w' is the perturbation vertical velocity, and u', v' representing the quantities retrieved from $u_{\text{div}}, v_{\text{div}}$, i.e., are the spectrally filtered divergent components of the horizontal wind. The

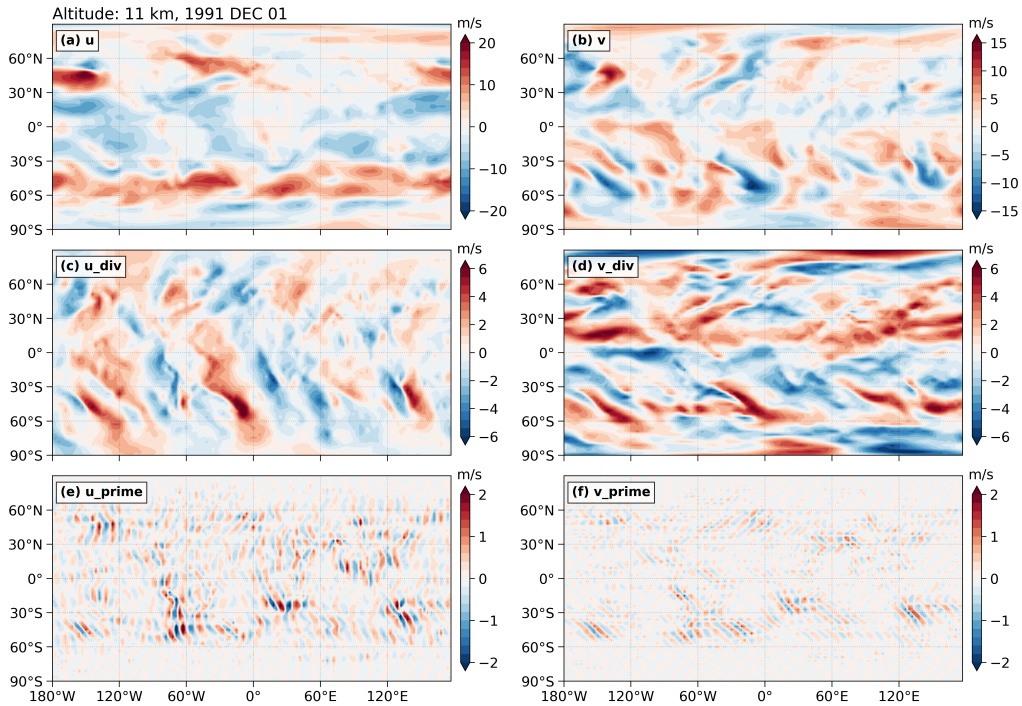


Figure 2.3: Example of small-scale deviations from the large-scale flow in an MS_GWaM (Multi-Scale Gravity Wave Model) simulation at 11 km altitude. Panels (a, b) show the distribution of total horizontal wind components (u and v), while panel (c, d) presents the decomposed divergent (u_{div} and v_{div}) wind components gained after using Helmholtz decomposition technique. Panels (e, f) show the perturbation components (u' and v') byproduct after the spectral filtering applied to the u_{div} and v_{div} components.

absolute momentum flux (AMF or |GWMF|) is then computed from perturbation fields as follows:

$$|\text{GWMF}| = \text{AMF} = \sqrt{F_x^2 + F_y^2} = \rho \sqrt{(u'w')^2 + (v'w')^2} \quad (2.19)$$

where ρ is the mean density, and u' , v' , and w' are the zonal, meridional, and vertical velocity perturbations, respectively. Higher frequency GWs that are found directly above their source of origin generally carry much larger momentum fluxes higher and faster to the middle atmosphere than low-frequency counterparts. In the real atmosphere, typical values for GW momentum fluxes can range from a few ones to a few hundreds of millipascals (mPa). Note that absolute momentum flux values are shown as a base-10 logarithm of flux magnitude throughout the analysis.

The overline denotes the perturbation products, i.e., $\overline{u'w'}$ and $\overline{v'w'}$ are computed using a low-pass filtering of the quadratic quantities which uses the same Gaussian spectral filter as in Kruse and Smith (2015). This filtering is to ensure that the flux estimates are physically meaningful, as direct pointwise computation of these second-order terms without low-pass filtering or areal averaging would not appropriately capture the wave-induced momentum transport (Wei et al., 2022).

Although this approach follows the commonly used GW scale separation methods as in Lehmann et al. (2012); Wei et al. (2016); Stephan et al. (2019); Strube et al. (2020); Gupta et al. (2021); Wei et al. (2022), despite different cutoff wavenumber used, it is previously been applied to the stratospheric region. To the authors knowledge, there is no particular method, particularly within a modeling framework, that specifically separates the GW signals targeting the UTLS region. As the focus of this work is more on the lowermost branch of stratosphere, we emphasize that our hybrid approach is well justified in the UTLS as well. This approach enables a more physically consistent identification of GW signals, ensuring that both the dynamical (divergent) and spectral (small-scale) properties of GWs are taken into account.

2.5.2 Extraction of GW parameters in observations

The first step is to remove the background from the measured data. The background removal procedure is essential in GW analysis techniques and may even result in somewhat biased outcomes. This is due to the fact that most analytical techniques depends on amplitude of fluctuations that persists after the background removal to deduce wave energy. The horizontal wind components $u(t)$ and $v(t)$ were decomposed into background and perturbation parts as:

$$u(t) = \bar{u}(t) + u'(t), \quad v(t) = \bar{v}(t) + v'(t)$$

where, $\bar{u}(t), \bar{v}(t)$ represent the background wind. A Butterworth band-pass filter can be used to isolate the amplitude response within selected frequency or period ranges of interest from a given time series (Butterworth et al., 1930). Following that, low-frequency mesoscale perturbations $u'(t), v'(t)$ were isolated by applying a 4th order Butterworth band pass filter within the 2-10 minute period:

$$u'(t), v'(t) = \text{Butterworth}_{\text{band}}(u(t), v(t); 2-10 \text{ min})$$

These filtered components were then used to construct hodographs and assess GW properties. More specifically, fluctuations u', v' are analyzed with our automated hodograph method. Next paragraph follows the more detailed description on the hodograph method used in this study. The outcomes from this procedure is demonstrated in Chapter 4 for zonal and meridional wind, respectively.

Note that due to distinct sampling frequencies and noise characteristics, separate filtering methods were applied to flight and model datasets to optimally isolate GW related perturbations.

Hodograph method to identify GWs in observation

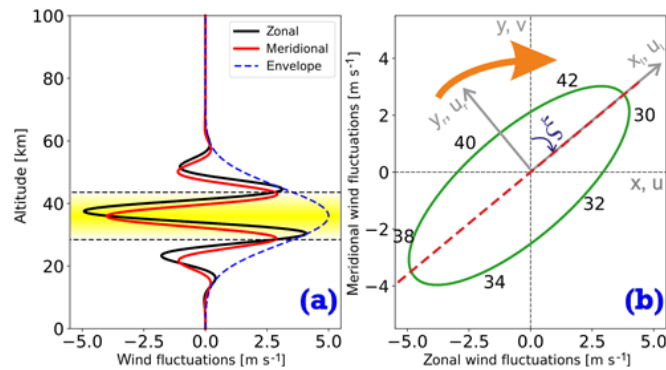


Figure 2.4: Schematic of the hodograph method, adapted from Strelnikova et al. (2020). The altitude profile of horizontal velocity fluctuations (a), the colored are marks the altitude range of one wavelength where wave amplitude is most significant. The corresponding hodograph ellipse of GW horizontal velocity variations (u' and v') from the marked region in (a) is shown in panel (b). Dashed line shows major axis of ellipse depicting propagation direction of the wave, number around ellipse shows altitude.

Hodographs, which depict the variation of horizontal wind disturbance vectors in velocity space, typically show an elliptical shape in presence of inertia GWs (Hirota and Niki, 1986). The schematic for the hodograph method is given in Figure 2.4. Given the high resolution of the measurements, the hodograph techniques can be utilized to identify the presence of inertia GWs and its characteristics (e.g. Guest et al., 2000; Lane et al., 2004; Yoshida et al., 2024).

For the identification of GW signatures from the observations/measurements during WISE RF05, we opted to use hodograph technique. Although, hodographs can be drawn from vertical profiles at a time, given that limited altitude level data, in our analysis a single hodograph is drawn using profiles at multiple times at one flight altitude (e.g., as in Gomes et al., 2025). Also, it is important to note the phase relation between u' and v' . For a zonally propagating wave, the horizontal perturbation velocities are 90° out of phase. As the wave propagates upwards, the horizontal wave vector rotates cyclonically, in the Northern Hemisphere, resulting a "spiral" hodograph (see Guest et al., 2000, and references therein). This behavior will be discussed in Chapter 4 where we discuss observations of GWs from the in-situ measurement.

2.5.3 Mixing diagnostics through trace gas correlations

The well-known method to analyse the effect of transport on the development of air mass composition in the UTLS is intercomparison of two tracer species (Fischer et al., 2000; Hoor et al., 2002, 2004; Pan et al., 2006). This method helps to analyse the transport and mixing across troposphere-to-stratosphere and vice versa. A fundamental distinction must be made between timescales of transport processes under consideration of the underlying dynamical processes. These range from the study of stratospheric circulation, which occurs over several years, to the examination of mixing processes, e.g., near the tropopause, that occur on time scales of weeks and are relevant for short-lived species with different characteristics. The mixing ratios of trace gases at a given location in the atmosphere are generally controlled by their sources and sinks, chemical lifetimes, and the characteristic transport time scales. The use of tracer correlation allows the analysis of mixing, e.g., the irreversible exchange and/or mixing

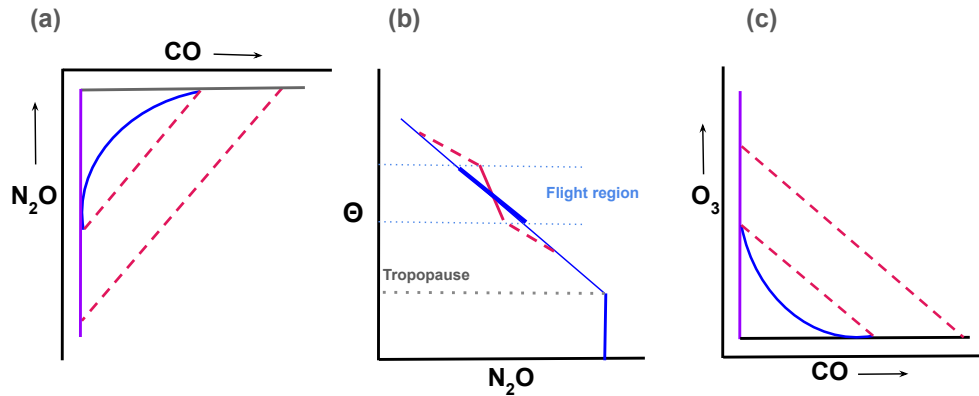


Figure 2.5: Schematic of tracer-tracer correlation (a) N_2O – CO and (c) O_3 – CO , and (b) vertical profile of N_2O with Θ in vertical. The purple, black axis lines in (a) and (c) form the “L” shape characteristic of conditions without mixing. The two straight red dashed lines in in (a) and (c) represent rapid, isentropic exchange and thus irreversible mixing between the troposphere and stratosphere, that are also seen in the vertical profile in (b). The curved blue line indicates incomplete or slow mixing, during which stratospheric CO has been chemically degraded.

of species that exhibit a vertical gradient. This approach allows the impact of reversible processes, such as transport or advection, to be distinguished from mixing in the sense of irreversible trace gas exchange.

Trace gases can be classified based on their chemical lifetime, i.e., whether they have a long (several months to years), such as N_2O , O_3 or CH_4 (methane), or a short (days to a few weeks), such as CO or SO_2 (sulfur dioxide), chemical lifetime compared to the timescale of transport. Note that a quasi-constant tracer values in the complementary reservoirs are a key to form the idealized L-shape (like CO and N_2O). Deviations from this can be assigned to irreversible species exchange as a result of mixing. When air masses with different compositions mix rapidly (on timescales shorter than chemical degradation), a straight mixing line connecting the two reservoirs establishes itself in the correlation (Hoor et al., 2002; Pan et al., 2004; Müller et al., 2016). This is shown by the two dashed red lines in Figure 2.5. Such mixing lines appear when correlations involve trace gases that have contrasting background concentrations defined in one of the respective reservoirs, for example in troposphere or stratosphere. Once mixing is complete, the trace gas mixing ratios become homogenized, meaning that the presence of a linear mixing line reflects incomplete or ongoing mixing. Over longer period, or if the chemical lifetime is shorter than the timescale of the mixture, as well as due to mixing with other air masses, the originally straight mixing lines disappear again. As a result, a curved shape emerges (blue line in Figure 2.5). A change in the curve shape therefore also a direct consequence of increased mixing in relation to the chemical timescale. This means that in the O_3 – CO correlation, the curvature is less pronounced when mixing is more efficient (Figure 2.5a, c). The mixing process itself affects both trace gases. When mixing is complete, only one point can be seen on the correlation.

Mixing lines are direct indication of influence of mixing processes on trace gas distributions. They enable the identification and analysis of exchange processes between chemically distinct reservoirs, such as the troposphere and stratosphere, as well as between air inside and outside the polar vortex. As discussed earlier, they can also be used to diagnose irreversible mixing on short time scales ranging from

days to a few weeks (Fischer et al., 2000; Hoor et al., 2002; Zahn et al., 2000; Pan et al., 2004). If multiple mixing lines appear within a correlation, they can be clearly linked to specific periods, indicating different mixing events, and to locations representing distinct reservoirs. Correlations such as O_3 -CO, N_2O -CO and O_3 - H_2O are commonly applied in studies of trace gas transport and distributions in tropopause fold regions to distinguish between tropospheric and stratospheric air, and to examine the mixing occurring within these folds (e.g., Fischer et al., 2000; Zahn et al., 2000; Pan et al., 2006; Gettelman et al., 2011; Woiwode et al., 2018; Kunkel et al., 2019; Lachnitt et al., 2023; Dörnbrack et al., 2025).

As an alternative to O_3 , the N_2O mixing ratio can be used in trace gas correlations because it has a well-defined background value in the troposphere. Although its weak gradient near the tropopause requires high measurement precision, N_2O behaves as a conservative tracer in the UTLS. Unlike O_3 , it is not affected by chemical reactions in this region, ensuring that the correlation is not influenced by chemical processes. Moreover, linear mixing lines can also be used to infer the original composition of air masses (Hoor et al., 2002). This requires knowledge of the mixing ratios at the tropopause. Using tracers such as O_3 or N_2O makes it possible to determine the tropospheric entrance value of other species, such as CO (Hoor et al., 2004; Müller et al., 2016).

More so, there is a monotonic relation between CO, N_2O and potential temperature Θ . The mixing ratios of N_2O and CO should decrease as an air mass becomes more stratospheric, whereas potential temperature should simultaneously increase. However, if there are deviations from such fixed relation, they can be linked to recent mixing (e.g., Kunkel et al., 2019; Lachnitt et al., 2023). This approach is further used in Chapter 4 for the identification of small-scale mixing of trace gas measurements taken during WISE campaign.

2.5.4 Calculations of turbulence diagnostics

In general, the vertical wind shear can be calculated based on the gradients of zonal and meridional wind components u, v as given in Eq. 1.5. Considering the focus is on small-scale dynamics, we reformulate this shear as vertical shear perturbations $S^{2'}$ induced by GWs and derived it according to:

$$S^{2'} = \left(\frac{\partial u'}{\partial z} \right)^2 + \left(\frac{\partial v'}{\partial z} \right)^2. \quad (2.20)$$

Here, the u' and v' are wind fluctuations from the background flow calculated from the method mentioned in section 2.5.1. Turbulence diagnostics and their constituents are computed as outlined in section 1.3.3. The potential turbulence regions are identified via two meteorological parameters: the gradient Richardson number Ri and the Ellord turbulence indices, TI1 and TI2.

Note that, Ri is derived using total horizontal wind components as described in Eq. 1.9. Regions with $Ri \leq 0.25$ are theoretically considered to be dynamically unstable and prone to KHI. In contrast, when using a value from resolved model quantities, the criterion is slightly weaker, i.e., Ri in the order of 1 is the criterion for the potential KHI.

We resort empirical diagnostic for CAT based on the Ellord-Knapp Turbulent Index (TI1) to the small-scale (Ellrod and Knapp, 1992) that combines vertical wind shear perturbations and the total flow defor-

mation. The TI1 used here is mainly to assess the regions of potential CAT, calculated using;

$$TI1 = S' \times DEF = \left(\left(\frac{\partial u'}{\partial z} \right)^2 + \left(\frac{\partial v'}{\partial z} \right)^2 \right)^{1/2} \times \left(\left(\frac{\partial u'}{\partial x} - \frac{\partial v'}{\partial y} \right)^2 + \left(\frac{\partial v'}{\partial x} + \frac{\partial u'}{\partial y} \right)^2 \right)^{1/2} \quad (2.21)$$

The TI2 additionally considers horizontal convergent flow related to the development of upper-level frontal zones, and is derived as;

$$\begin{aligned} TI2 &= S' \times (DEF + CVG) \\ &= \left(\left(\frac{\partial u'}{\partial z} \right)^2 + \left(\frac{\partial v'}{\partial z} \right)^2 \right)^{1/2} \\ &\quad \times \left[\left(\left(\frac{\partial u'}{\partial x} - \frac{\partial v'}{\partial y} \right)^2 + \left(\frac{\partial v'}{\partial x} + \frac{\partial u'}{\partial y} \right)^2 \right)^{1/2} - \left(\frac{\partial u'}{\partial x} + \frac{\partial v'}{\partial y} \right) \right] \end{aligned} \quad (2.22)$$

where S' is the magnitude of vertical wind shear perturbations (Eq. 2.20). Here, the DEF and CVG are retained from the zonal and meridional wind perturbations. Thus, both TI1 and TI2 are likewise based mainly on the small-scales that are comparable to GW features.

3 Contribution of gravity waves to vertical shear in baroclinic life cycle experiments

Objective

The objective of this chapter is to investigate whether GWs contribute to the generation of shear in the formula of grid spacing sensitivity as well as varying physical processes including turbulence, saturation adjustment only, cloud microphysics and a set of different physics complexities.

*This chapter is published as a research article in journal Atmospheric chemistry and physics as: **Umbarkar, M. and Kunkel, D., 2025: Contribution of gravity waves to shear in the extratropical lowermost stratosphere: insights from idealized baroclinic life cycle experiments, Atmospheric chemistry and Physics, 25, 10159–10182, <https://doi.org/10.5194/acp-25-10159-2025>.***

A way to approach baroclinic life cycles and processes within is to use an idealized numerical representation of small-scale GWs. In fact, several studies used idealized setups to study GWs within baroclinic life cycles. In a series of experiments, O'sullivan and Dunkerton (1995) were the first to show that GWs, more precisely inertia GWs, emerge in dry adiabatic baroclinic life cycles in regions of the jet stream. However, they did not analyze their role for shear or turbulence generation. Wei and Zhang (2014) studied the effect of additional moisture in the setup on the appearance of the GWs. Although they show that the convectively generated GWs emerge much earlier in fast-growing moist baroclinic wave, their role in the subsequent mixing was not explored. Kunkel et al. (2014) show that GW from baroclinic waves can alter the tropopause structure and generate an environment prone to mixing and STE. However, they did not systematically study the role of GWs on shear generation and the consequences for turbulence occurrence.

In this chapter, some ideas from previous studies are used to better understand the role of GWs associated with baroclinic life cycles to the generation of vertical shear and potential turbulence in the LMS. This is conducted within the framework of idealized baroclinic life cycle experiments of varying complexity using the ICON model. Specifically, the following questions are addressed:

- *How does the ICON model resolve GWs in an idealized baroclinic life cycle simulations, and where do these GWs emerge relative to the tropopause location?*
- *Are these GWs associated with instabilities in the LMS, which could lead to turbulence and mixing?*

This chapter is structured as follows to address these questions: the model configuration is initially introduced, and an overview of the experiments used in this study is provided. Section 3.2 presents a thorough analysis of the evolution of baroclinic life cycles and the spatial resolution sensitivity experiments, with the GWs appearance therein. Then, we take a closer look at some GW events. Section 3.3 discusses the occurrence of shear and turbulence in the LMS and their relation to the small-scale GWs in different baroclinic life cycles. Further comprehensive analysis of the possible contribution of GWs

in the generation of TSL is provided in section 3.4. Finally, the outcomes from the idealistic approach are summarized in section 3.6.

3.1 Idealized baroclinic life cycle experiments: ICON model setup

Idealized baroclinic life cycle (BLC) provide a simplified yet effective framework for investigating dynamics of baroclinic waves in the extratropical atmosphere. These simulations, first explored by (O'sullivan and Dunkerton, 1995), have been instrumental in understanding the fundamental processes of wave growth, nonlinear evolution, and their interactions with mean flow. By isolating factors like thermal gradients, wind shear, and stratification, idealized BLC experiments simplify the study of complex atmospheric interactions. A key aspect lies in their use to study GW generation, propagation and feedback on UTLS. Studies by Plougonven and Zhang (2014); Plougonven and Snyder (2007) and Kim et al. (2003) demonstrated that GWs are spontaneously generated in regions of jet streaks and frontal imbalances during baroclinic wave evolution, with their characteristics closely tied to the structural evolution of the parental wave. These waves propagate into stratosphere, influencing vertical wind gradient by the means of wind shear, turbulence and static stability (Plougonven et al., 2008; Wei and Zhang, 2014). The work of Wirth and Szabo (2007) and Kunkel et al. (2014) further highlighted how GWs generated in idealized BLCs interact with tropopause dynamics, inducing shear and contributing to mixing processes in the UTLS. Given their controlled conditions and ability to isolate key physical processes, idealized BLC experiments are particularly well-suited for investigating GW formation and their broader impact on the UTLS structure.

Adiabatic model configuration

The baroclinic life cycle experiments in an idealized configuration of the non-hydrostatic ICON model (Zängl et al., 2015) are conducted. Firstly, the dynamical core of ICON is used to simulate the dry adiabatic experiments. In this study, the ICON model is set up over the global domain, from the surface up to a height of 35 km. ICON uses the icosahedral triangular grid that provides nearly homogeneous coverage of the globe, alleviating numerical stability concerns caused by the so-called "pole problem" on traditional latitude-longitude grids. To mitigate the reflection of upward propagating waves back into the computational domain, the sponge covers the upper 13 kilometers of the model domain. Free slip boundary conditions are applied at the surface in ICON, assuming zero tangential wind velocity, representing smooth flow over the surface without friction.

The ICON model effectively simulates atmospheric dynamics by numerically solving the fully compressible, non-hydrostatic Navier-Stokes equations. The time integration of ICON combines the Matsuno scheme and the Heun scheme (also known as the trapezoidal scheme), commonly known as the predictor-corrector scheme (Zängl et al., 2015). Numerical hyper-diffusion is used to reduce the impact of inherently produced grid-scale checkerboard error patterns on numerical simulations. In the dry dynamical experiments, we exclude the topography and moisture, which eliminates the possibility of the generation of GWs by topography or diabatic heating. Thus, the GWs in this simulations are generated internally.

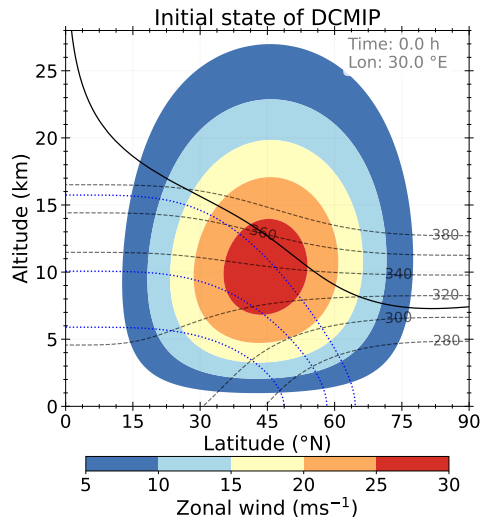


Figure 3.1: Zonally symmetric balanced initial conditions at 30° E longitude: zonal wind \bar{u} (shaded contours, 5 m s^{-1} spacing), potential temperature $\bar{\Theta}$ (solid black lines, 15 K spacing, starting with 280 K in the lower right corner) and specific humidity q_v for values 0.002, 0.02, 0.05, 0.2, 0.5, 1.0 g kg^{-1} (dotted lines, from bottom to top), the thick dashed line marks the location of dynamical tropopause, defined as the 3.5 pvu potential vorticity isosurface.

3.1.1 Initial background state: DCMIP testcase

For initial state, the setup proposed in the Dynamical Core Model Intercomparison Project (DCMIP2016, Ullrich et al., 2017) test case is followed. The initial state is composed of a zonally symmetric background state, which is in thermal wind balance and a perturbation to trigger a faster baroclinic wave evolution. The background state is initiated globally, while introducing the perturbation only in the Northern Hemispheric UTLS. Consequently, a baroclinic wave will only emerge in the Northern Hemisphere within a period of about 15 days. Thus, hereafter, the focus is only on the atmospheric state of the Northern Hemisphere.

Figure 3.1 shows the initial background state for zonal wind, potential temperature, potential vorticity, and specific humidity. In DCMIP, a weak, Gaussian-shaped wind perturbation is introduced at the center of the model domain, which points to the location (20° E, 40° N) at the altitude of the tropopause. The mid-latitude jets at 45° N/S are centered slightly below the tropopause, with the horizontal mean surface temperature of $T = 288$ K. Moreover, the zonal wind is derived under the thermal wind balance. A moist variant of the dry dynamical test is considered here to understand the impact of moisture feedback on the development of the wave. The moisture field is only initially available for simulations including moisture.

The DCMIP case with the zonal wind perturbation leads to a life cycle resembling a case known as life cycle type 1 (Thorncroft et al., 1993). This type shows the development of a stratospheric streamer along with anti-cyclonic wave breaking. The DCMIP stream function case leads to a different evolution, which has some resemblance to the life cycle type 2 described in Thorncroft et al. (1993). Both cases will be discussed in result section in the following since the two solutions provide some coverage of the life cycles observed in the real atmosphere.

Table 3.1: Summary of idealized DCMIP experiments performed using ICON

*MOIST: only saturation adjustment, CMP: saturation adjustment + bulk microphysics scheme

Dry adiabatic simulations		
Experiments	Short Description (with ICON grid)	Δx (\approx in km), Δz (model levels)
REF _{wind}	wind perturbation with R02B07	20, 100 (\sim 300 m)
REF _{stream}	stream perturbation with R02B07	20, 100
HRES _{stream}	stream perturbation with R03B07	13, 100
HRES _{wind}	wind perturbation with R03B07	13, 100
MRES _{wind}	wind perturbation with R02B06	40, 100
MRES _{stream}	stream perturbation with R02B06	40, 100
MRES40 _{wind}	wind perturbation with R02B06 on 40 levels	40, 40 (\sim 900 m)
MRES40 _{stream}	stream perturbation with R02B06 on 40 levels	40, 40
LRES _{wind}	wind perturbation with R02B05 on 40 levels	80, 40
LRES _{stream}	stream perturbation with R02B05 on 40 levels	80, 40
Simulations with physical forcing		
Experiments	Short Description	Schemes used
REF _{wind} MOIST	Wind perturbation with moisture	saturation adjustment
REF _{wind} TURB	Wind perturbation, turbulence	Raschendofer
REF _{wind} CMP	Wind perturbation, cloud microphysics	single moment
REF _{wind} TURB CMP	Wind perturbation, turbulence and cloud microphysics	Raschendofer + single moment
REF _{wind} TURB MOIST	Turbulence with moisture	Raschendofer
REF _{stream} MOIST	Stream perturbation with moisture	saturation adjustment
REF _{stream} TURB	Stream perturbation, turbulence	Raschendofer
REF _{stream} CMP	Stream perturbation, cloud microphysics	single moment
REF _{stream} TURB CMP	Stream perturbation, turbulence and cloud microphysics	Raschendofer + single moment
REF _{stream} TURB MOIST	Turbulence with moisture	Raschendofer

3.1.2 Dry and moist baroclinic life cycle experiments

In total, the results from 20 different baroclinic life cycle experiments (see Table 3.1) will be discussed in this chapter. The life cycles vary in their initial state, the model resolution, or through the addition of physical processes. Ten simulations with a dry adiabatic setup, five each for the two initial states, *wind* and *stream* (see Table 3.1) are conducted. In these simulations, the underlying horizontal grids are varied from 13 km (R03B07; ICON grid) to 80 km (R02B05). The number of vertical levels changed between 40 and 100 while keeping the domain height constant at 35 km altitude. These levels resulted in roughly 900 m or 300 m grid spacing in the UTLS. The simulations with 20 km horizontal grid spacing and 100 vertical levels will be regarded as our reference simulation (REF), for which the majority of the physics-added simulations are conducted. The other simulations are either denoted as high (HRES), medium (MRES), or low (LRES) simulations. This setup strategy allow to further study the emergence of GWs, shear, and potential turbulent regions in our simulations.

In the next step, sensitivity experiments focusing on non-conservative processes, including either turbulence parameterization (further denoted as TURB) or cloud microphysics (CMP) are performed. For both initial states, we study the effect of moisture and, particularly, the effect of latent heat release on the GW, shear, and turbulence appearance. Two simulations only used the saturation adjustment scheme of the model to mainly study this latent heat feedback (MOIST). Additionally, we run two more simulations with a simple cloud microphysics scheme to address potential additional effects. We note here that the MOIST simulations have been carried out for all resolutions used in the dry adiabatic setup.

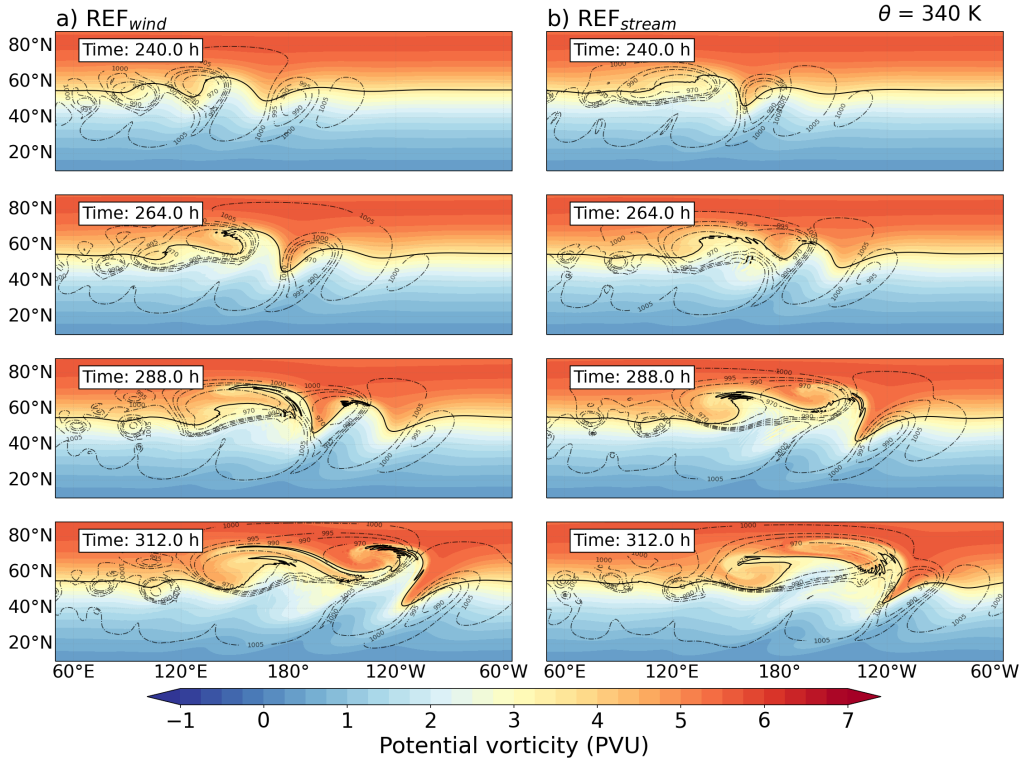


Figure 3.2: The evolution of the baroclinic life cycle for the (a) REF_{wind} and (b) $\text{REF}_{\text{stream}}$ simulation. Horizontal cross sections of potential vorticity at 340 K isentropic surface and surface pressure (dashed contours) over the Northern Hemisphere after 240, 264, 288 and 312 h of model integration. The solid black line represents the 3.5 PVU, regarded as a dynamical tropopause.

However, since the general difference between dry and moist simulations is very similar, independent of the resolution, only the results for the REF cases are shown and discussed further.

In order to determine whether the turbulence parameterization affects the appearance of GWs, shear, and turbulence in our simulations, two REF simulations are performed with the turbulence parameterization turned on (TURB). Finally, we run four REF simulations with combinations of *wind*, *stream*, TURB, MOIST, and CMP to address the combined effects of these parameterizations and initial states. More details about the simulations are given in Table 3.1.

3.2 The DCMIP baroclinic wave development and the occurrence of GWs

3.2.1 Baroclinic wave evolution and gravity wave appearance in the reference simulations

We start this section with a brief introduction of the main features of the baroclinic life cycle. First, we show the evolution of the baroclinic wave using isentropic potential vorticity for the two reference simulations. We then discuss the occurrence of GWs that emerge during the various stages of life cycles.

Figure 3.2 provides an overview of the synoptic evolution of the baroclinic wave for two dry adiabatic reference simulations between 240 h and 312 h after the simulation start. As will be shown later, this is the time period most interesting for our GW, shear, and turbulence analysis. The REF_{wind} and $\text{REF}_{\text{stream}}$ simulation features the same general characteristics of the life cycle as described in Ullrich et al. (2014) and covers initial growth and rapid development of the baroclinic disturbance. The extra-

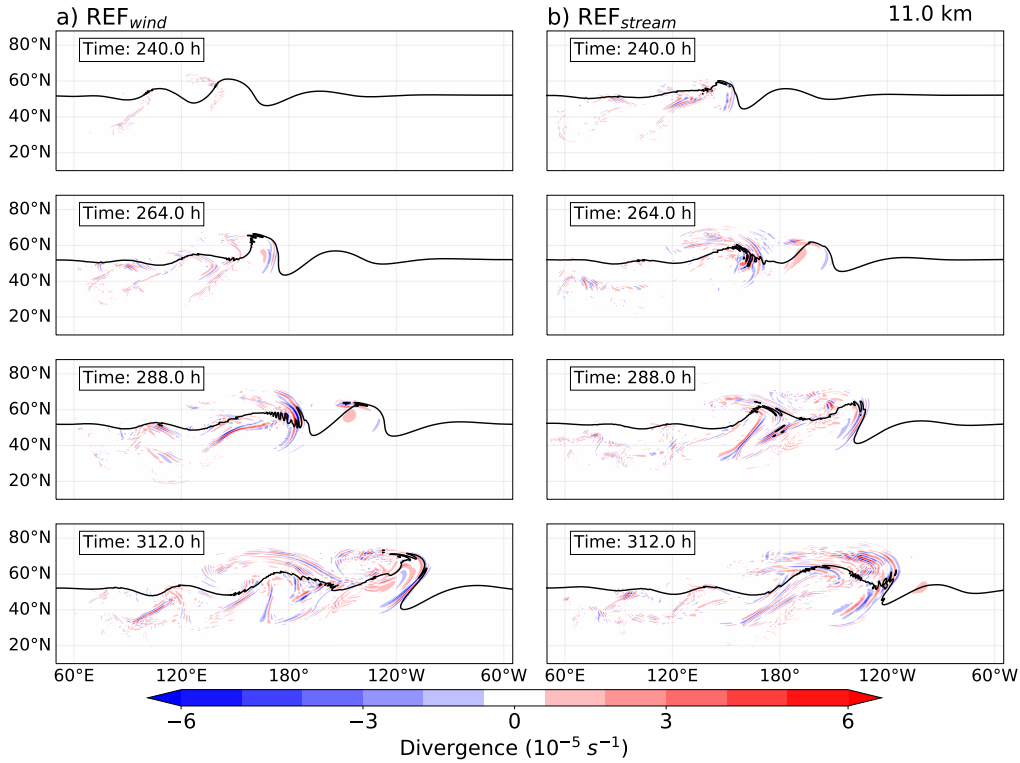


Figure 3.3: The evolution of the GWs for the (a) REF_{wind} and (b) $\text{REF}_{\text{stream}}$ simulation. Horizontal cross sections of horizontal divergence at 11 km altitude over the Northern Hemisphere after 240 h, 264 h, 288 h and 312 h of model integration time, respectively. The solid black line represents the dynamical tropopause.

tropical dynamical tropopause is defined in our simulations as the 3.5 PVU isoline ($1 \text{ PVU} = 1 \times 10^{-6} \text{ K m}^2 \text{ kg}^{-1} \text{ s}^{-1}$), following a commonly used definition in the literature (e.g., Hoerling et al., 1991; Erler and Wirth, 2011), and is highlighted by the black line in Figure 3.2. Our life cycle evolves rather slowly, with the first signs of a substantially growing wave after 192 h. We consider this beneficial for two reasons: first, we can regard our results more conservatively since a slow evolution correlates with less GW emission; second, we think that numerical, spurious features occur less with a slower evolution.

As the time series highlights, both REF_{wind} and $\text{REF}_{\text{stream}}$ baroclinic waves grow to substantial amplitudes, showing tropospheric and stratospheric intrusions, a PV streamer, and secondary cyclogenesis. PV streamers are identified as the high PV trough downstream of the anticyclonic wave breaking. Differences are observed in the size of the PV streamer and the strength of the tropospheric and stratospheric intrusions. Both life cycles exhibit baroclinic wave breaking. Despite their dry adiabatic nature, there are signs of PV non-conservation in the region of the steep PV gradients, potentially associated with numerical diffusion. Figure 3.3 shows the divergence of the horizontal wind components and illustrates regions where GWs are present in two dry adiabatic reference simulations at various time steps at an altitude of 11 km. This altitude is close to the altitude of the jet stream core (see Figure 3.1), thus representing well the situation of the tropopause region along the LMS and is taken as a representative height for further discussion. As evident in Figure 3.3, alternating signals in the horizontal divergence mark the presence of GWs in both reference simulations from 240 h onward. Wave activity was not prominent before the indicated simulation time (i.e., 240 h) but horizontal divergence fields highlight the emergence and subsequent intensification of wave-induced features thereafter. The GWs have their source of imbalances in the synoptic flow and propagate into the UTLS during life cycles. The wavelength of

this wave mode can be deduced from the peaks in the divergent field. In many cases, the horizontal wavelength is on the order of a hundred kilometers which is similar to wavelengths of inertia GWs.

A prominent sign of a GW emerges first after 240 h in the REF_{wind} simulation around 140° E. At 264 h, this feature is evident on the tropospheric side of the jet in the ridge around 170° E. Interestingly, the GW crosses the tropopause into the LMS (after 288 h) and spreads out in the stratosphere over the course of the next 24 h. The GW signatures are typically observed in the jet exit region and over the northwards reaching ridges of the baroclinic wave, especially in regions characterized by pronounced PV gradients with larger amplitudes (Plougonven and Snyder, 2005, 2007; Plougonven and Zhang, 2014). The jet stream in the UTLS partially excites the waves, indicating that both the surface front and the upper tropospheric jet-front system contribute as sources of these small-scale waves. This indicates that the background flow significantly influences the wave characteristics during their propagation. The larger spectrum of GWs was observed after 312 h when the baroclinic wave undergoes breaking. The GW characteristics adhere to the phases of baroclinic wave development. This aligns well with the fact that the growth rate of flow imbalance correlates with the growth rate of baroclinic waves, which, in turn, strongly correlates with the frequency of GWs.

REF_{stream} experiment (Figure 3.3b) reveals comparable temporal evolution of GWs but with slight variations in the location of GW development. The prominent signatures and the curl-up feature were noticed one day prior to the REF_{wind}, resulting in the earlier appearance of GW modes. Three strong GW packets appear after 288 h, moving poleward and towards the west. The remarkable feature here is that the wave modes develop clockwise, representing the clockwise evolution of baroclinic waves. After 312 h, the REF_{stream} BLC undergoes cyclonic breaking in the LMS. Overall, this cyclonic wave breaking of baroclinic instability with stream perturbation resembles an LC2 type life cycle (Thorncroft et al., 1993). Even though the baroclinic wave in this form evolves quite swiftly, the wave breaking occurs later than in REF_{wind}. During the intensifying stage of BLC, features like substantial stratospheric intrusion and tropospheric wrap-up, along with the PV streamers in the horizontal divergence field, hint towards the potential turbulence in the LS and could lead to STE.

3.2.2 GW occurrence: impact of horizontal and vertical grid spacing

This section aim to answer how GWs emerge in low and high-resolution simulations and how the occurrence, location, and properties of GWs are influenced by the horizontal and vertical grid spacing in the UTLS.

In the first step, we aim to assess the resolution dependence for which we use all of our dry adiabatic simulations with differing spatial resolutions. In general, the evolution of the baroclinic wave is similar across all dry simulations. While the large-scale structure remains consistent, mesoscale differences and slight variations in the exact location of the trough are evident. These are general features observed across all simulations, independent of the perturbation function. As a result, GW activity tends to emerge in similar regions among all dry simulations. Figure 3.4 illustrates the distribution of horizontal divergence at 11 km altitude after 288 h for the respective simulations, highlighting these similarities. In the wind perturbation simulations, this is the region of the baroclinic wave ridge (see around 180° E after 288 h at 11 km) and above the trailing surface cold front. Other hotspots for GWs are evident, particularly upstream of the jet core, where the baroclinic wave induces strong vertical motion, and downstream near the tropopause, where GWs propagate along the sharp PV gradient of the streamer.

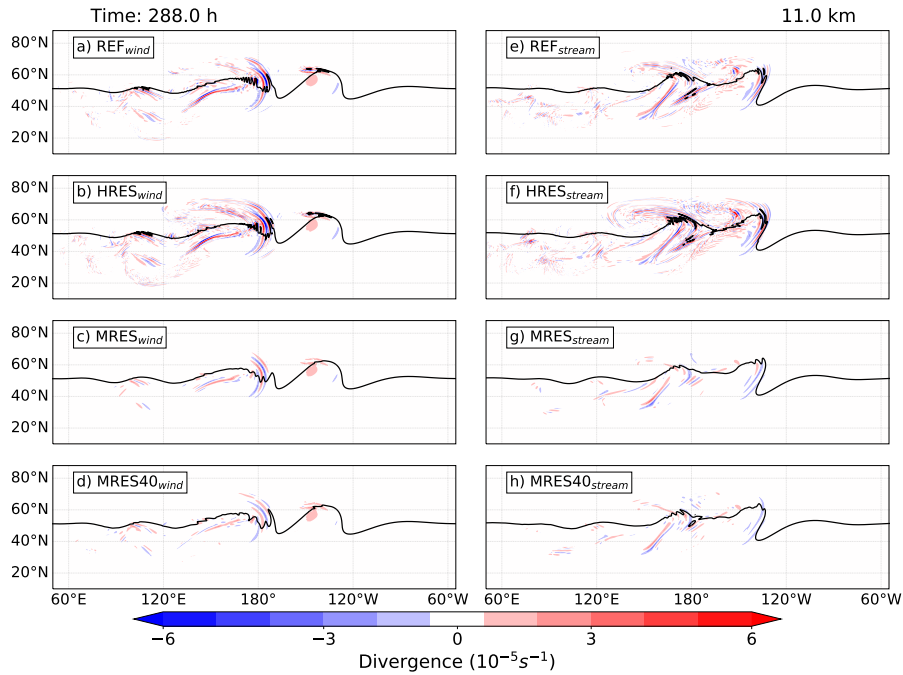


Figure 3.4: Evolution of GWs for simulations with varying grid spacings. Panels (a-d) represent simulations with wind perturbations for experiments REF, HRES, MRES, and MRES40, respectively, while panels (e-f) show simulations with stream perturbations for the same configurations. The figure displays the distribution of the horizontal divergence field at 11 km altitude over the Northern Hemisphere after 288 h of model integration.

Similar regions can be identified in the simulations with the stream function perturbation.

Besides these similarities, there are notable differences which can, of course, be expected. We noticed minimal differences in GW representation when varying vertical resolution between 40 and 100 levels, with 100 levels adequately capturing the GW spectrum and their key features. The higher the model resolution, the more of the GW spectrum is resolved, compare e.g., the horizontal divergence field between REF, HRES, MRES and LRES simulations. An example of wind perturbation is the region north to surface cold front with more GW signals in the high-resolution simulations, which is virtually absent in coarser resolution i.e. LRES_{stream}. Henceforth, we exclude the LRES simulations as they did not exhibit significant indication of GWs. A second notable difference is the amplitude of the divergent signal, which is larger in the high-resolution cases, aligning with previous findings that high resolution better captures GWs signals and their propagation (Zhang, 2004; Plougonven and Snyder, 2005). There is minor sensitivity of medium-scale waves to enhanced horizontal resolution, implying that they are being adequately resolved in REF and HRES simulations. These results support earlier studies showing that increased resolution enhances the ability to capture fine-scale GW structure and dynamics while medium scale remains relatively insensitive (Plougonven et al., 2003; Kunkel et al., 2016).

3.2.3 Evolution of BLC: the latent heat release

As for the latent heat release, we use relative humidity at 850 hPa as a quasi-proxy for latent heat release. Figure 3.5 shows the evolution of surface pressure and surface potential temperature for the dry REF, MOIST, and TURB MOIST simulation from 192 h to 264 h of model run. For MOIST simulations, relative humidity at 850 hPa is shown. In the MOIST cases, the onset of frontogenesis around 192 h is accompanied by progressive humidification in the warm sector of the developing cyclone. Relative

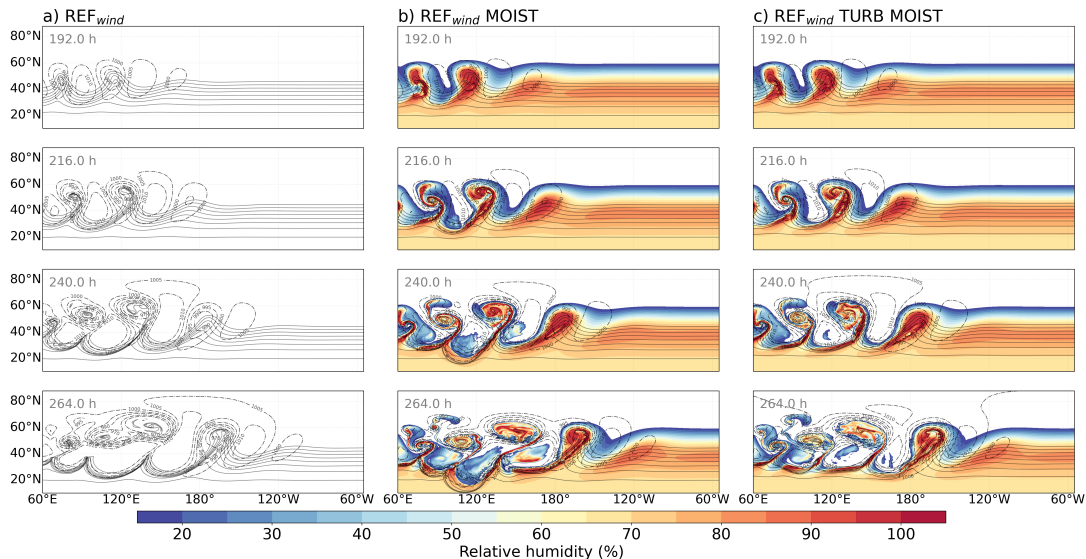


Figure 3.5: Time evolution from 192 h to 264 h, of surface pressure (dashed contours), surface potential temperature (solid contours, every 5 K), and (for the moist simulation only) relative humidity at 850 hPa (colored, %). (a) REF_{wind} , (b) REF_{wind} MOIST and (c) REF_{wind} TURB MOIST simulations.

humidity values rise to above 80%, with localized saturation ($\geq 90\%$) along and ahead of the warm front, indicative of sustained lifting and associated condensation processes. After 216 h, as the cyclone matures and enters the frontal fracture stage, the structural differences between dry and moist simulations become more evident. The bent-back segment of the warm front in the MOIST simulation exhibits elevated relative humidity alongside intensified horizontal temperature gradients. This spatial alignment reflects dynamically consistent latent heating, contributing to stronger pressure gradients and the development of a low-level wind maximum. At this point, the central sea level pressure in the MOIST runs falls below 965 hPa, compared to ~ 970 hPa in the REF simulation. After 240 h, relative humidity values in the primary cyclone remain elevated across both warm and cold frontal regions, suggesting ongoing moist processes. Importantly, the downstream cyclone in MOIST also shows relative humidity exceeding 90% in its core, despite forming later in the BLC implying that in-situ latent heating plays a key role in its intensification. While the primary baroclinic wave evolution remains largely controlled by dry dynamics in the early stages, the differences in cyclone intensity, frontal structure, and secondary cyclone development in the moist runs point to the substantial dynamical role of latent heating.

More details on the impact of this latent heat release and inclusion of water component in the model, have been discussed in the following section where the impact of included physical processes are discussed.

3.2.4 GW occurrence: impact of non-conservative processes

In this section, the impact of physical processes on the evolution of the baroclinic waves and the occurrence of GWs is explored. For this, we compare the reference simulations with simulations including (1) latent heat feedback, i.e., MOIST, (2) a parameterization for cloud microphysics, i.e., CMP, (3) a parameterization for turbulence, i.e. TURB, (4) a combination of the parameterizations for cloud microphysics and turbulence, i.e., TURB CMP, and (5) turbulence parameterization with moisture, i.e., TURB MOIST.

The experiments investigate the influence of moisture on GW patterns within baroclinic waves, using

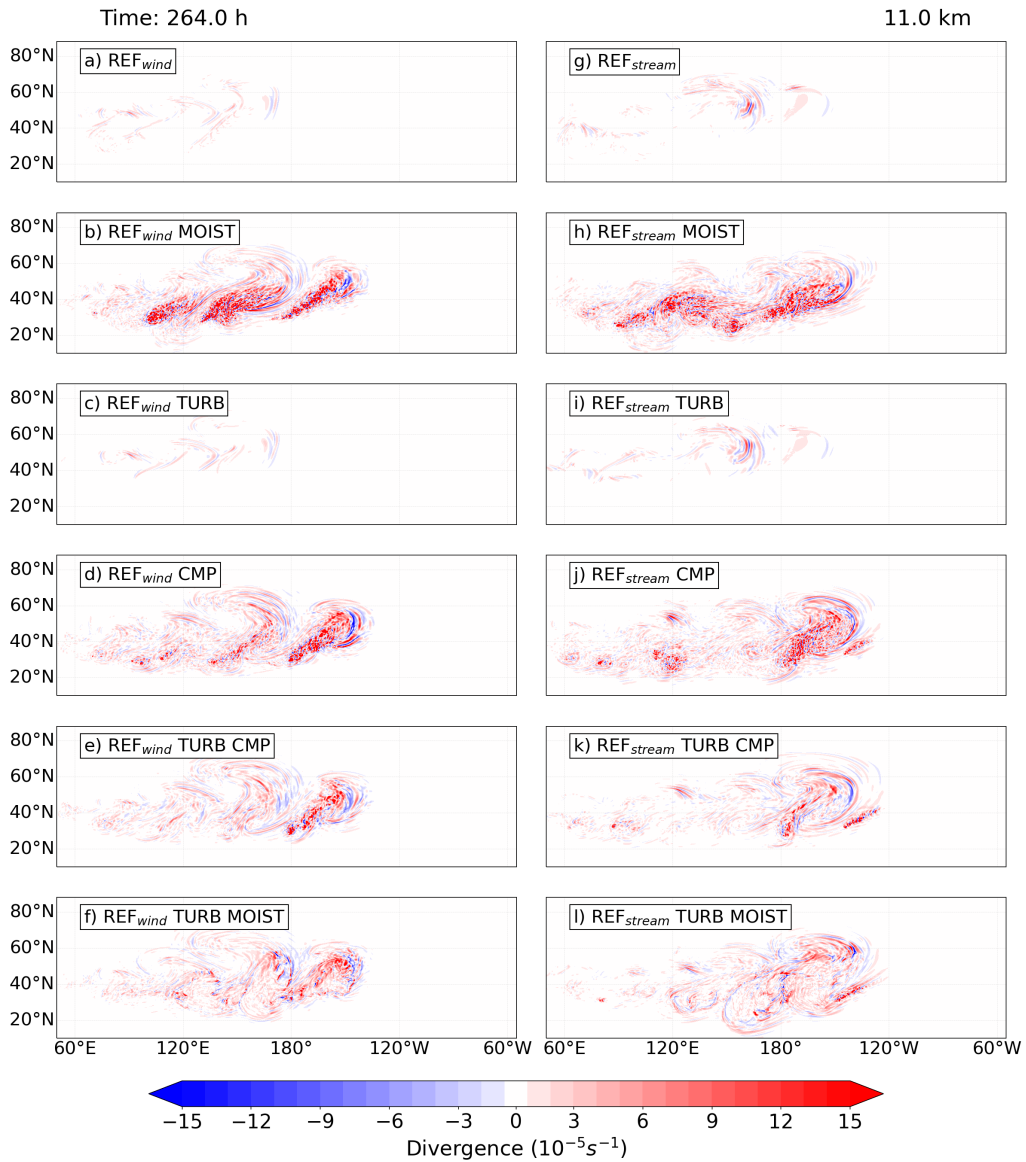


Figure 3.6: As in Figure 3.4 but after 264 h for the simulations with varying physical processes. Top panel (a, g) represents the corresponding reference simulations.

both wind and stream perturbations. Figure 3.6 shows the 11 km horizontal divergence distribution at 264 h, highlighting the evolution of baroclinic waves and showcasing various GW modes during different stages of baroclinic wave development. Specifically, Figure 3.6a captures the baroclinic structures in the REF_{wind} experiment, corresponding to the conditions in Figure 3.6b REF_{stream} . Moist cases (Figure 3.6b, h) indicate noisy horizontal divergence, inconsistent with the patterns observed in REF experiments. The MOIST simulation shows that baroclinic wave growth begins earlier than in the dry case, likely due to the release of latent heat being an additional energy source from moisture. Noticeable differences in the horizontal divergence pattern appear across the MOIST runs at this stage despite the initial moisture content being similar. The emergence of wave-like features before the appearance of the main GW pattern suggests spontaneous emission influenced by moisture. As a result, significant GWs are detected near large-scale structures. In conditions with moisture and saturation adjustment, the introduction of weak convective instability allows dry dynamic GW modes to prevail. Nonetheless, small-scale

features indicative of GWs in the LS reveal consistent GW activity throughout the evolution of moist baroclinic wave, which may warrant further analysis. Overall, the development of simulated moist baroclinic waves is qualitatively similar to the life cycles described by Wei and Zhang (2014) and Wei et al. (2016). However, isolating small-scale features from the large-scale dynamics in moist scenarios remains challenging, requiring additional steps to understand their impact on mixing.

We now move our discussion to assess the impact of bulk microphysics and turbulence parameterization on the development and characteristics of GWs. These experiments are conducted using the same spatial resolution as in the REF experiment. In the TURB simulations (Figure 3.6c, i), the GW signature appears weaker, which could be due to the tendency of turbulence to reduce strong vertical gradients. Although turbulence acts against the effects of dry dynamics, the GW features observed in TURB are similar to the REF experiment. In the CMP experiment (Figure 3.6d, j), similar horizontal divergence patterns as in MOIST experiments are observed around 180° W/E, explaining that the latent heat release drives these patterns. The GW patterns in the LMS indicate that moisture inclusion leads to stronger updrafts, accelerating the evolution of the GW life cycle. Processes originating from lower tropospheric levels significantly influence GW activity, and similar effects are noted in experiments with saturation adjustment, i.e., MOIST, confirming that latent heat release, rather than microphysical processes, is responsible for the observed effect. Figures 3.6e, k and 3.6f, l display the TURB CMP and TURB MOIST cases, respectively, for both initial states. After 264 h of model integration, similar structures of GWs are observed in these experiments, with minor variations in GW characteristics. Specifically, GWs are more prominent in the TURB MOIST case, while the TURB CMP shows differences in GW locations, with more subsequent GW modes emerging. The TURB CMP closely resembles the REF_{wind} CMP, suggesting that microphysical processes play a more dominant role than turbulence. Overall, distinct variations in GW patterns across all physics experiments are evident at this stage of the life cycle.

Taken together, in all MOIST physics experiments, latent heat release, a consequence of condensation, enhances vertical motions in the tropospheric region, which extend to the UTLS, creating a sharp vertical gradients in stability and moisture. The air masses above are already in the sinking motion, exhibiting enhanced upward motions. The processes in MOIST experiments differ fundamentally from those in dry scenarios, leading to significant variations in GW emergence in the LS. The rapid, small-scale lifting processes associated with these upward motions drive the faster evolution of the GW life cycle, resulting in earlier wave breaking compared to the dry case. This demonstrates that incorporating moisture in the model accelerates GW evolution due to the enhanced upward motions caused by latent heat release throughout the life cycle. Nevertheless, the physical processes leading to GW occurrence seem to be similar in LC1 and LC2.

3.2.5 GW occurrence: connection with vertical shear

Our primary goal is to analyse the connection between GW occurrence in baroclinic life cycles and their potential to contribute to the formation of the shear layer above the tropopause and potential mixing. We have shown that GWs emerge under various initial states, grid resolutions, and process complexities. Before we dive deeper into the analysis of shear and turbulence in these simulations, we want to briefly highlight the spatial and temporal connection between the occurrence of GWs and enhanced small-scale vertical shear. For this, we again focus on the dry reference simulations.

The location of the GWs is analyzed via two metrics: the vertical wind perturbations w' and the

absolute momentum flux. The latter is a momentum flux of the sub-synoptic scales, which we refer to as a first proxy for the momentum flux due to GWs (hereafter GWMF). We use w' instead of horizontal divergence because they are interconnected, and w' is directly linked to the GWMF. As all the other prime quantities, w' here represents a filtered quantity. To quantify the GW perturbations from synoptic-scale structures, we used a hybrid approach following Wei et al. (2022) that combines both dynamical and statistical approach to separate large and small-scale components of the flow. More details can be found in section 2.5.1.

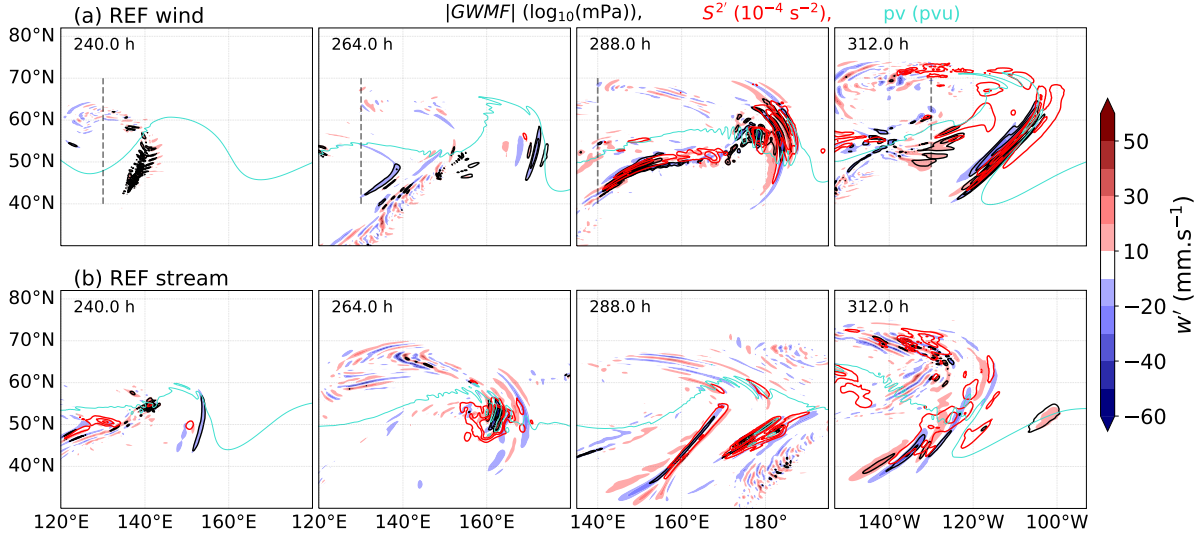


Figure 3.7: Horizontal evolution of 11 km perturbation vertical velocity w' in mm s^{-1} from 240 h to 312 h of model integration for REF_{wind} and $\text{REF}_{\text{stream}}$ experiment. The absolute GW momentum flux (1.0, 1.5 and 2.0 in $\log_{10}(\text{mPa})$; black) and vertical wind shear perturbations S^2 (1.0, 2.5, 4.0 in 10^{-4} s^{-2} ; red) from the spectral domain. The turquoise lines denote the 11 km dynamical tropopause where potential vorticity equals 3.5 PVU.

Figure 3.7 shows the temporal evolution of GW packets reconstructed from the spectral domains at 11 km altitude for REF_{wind} and $\text{REF}_{\text{stream}}$. Velocity perturbations initially emerge above the low-level trough with small magnitudes, which then gradually intensify and form the organized GW structure in the eastern trough (see also Figure 3.2, between 120° E and 100° W). These GW packets are identified by their horizontal wavelength ($\sim 100 \text{ km}$). We find alternating regions of upward and downward vertical velocity perturbations in the LS, which often results from emerging GWs from the updrafts but is also present in the regions of eastward propagating GWs. More so, an increase in small-scale shear is observed near GWs above lifted air masses reaching up to the tropopause. Vertical wind shear is primarily attributed to two major sources in our setup: the jet dynamics and the GWs. The small-scale shear location relative to the phase of low-level baroclinic waves remains consistent with GWs throughout the simulation. Notably, maxima of S^2 occur above the tropopause, overlapping significantly with the regions of peak GWMF. This alignment implies a potential interaction between GWs and small-scale shear, suggesting that energy/momentum transfer due to GWs may contribute to and/or be influenced by the small-scale vertical shear in the LS. The remarkable overlap of GW and small-scale shear occurrence motivates a deeper look at the link between these two features and ultimately on potential turbulence occurrence.

3.3 Shear and turbulence diagnostics in the LMS

3.3.1 Static stability and vertical wind shear

In the following, our discussion centers around the investigation of the role of GW in the generating shear, which could lead to turbulence in the LMS. On sub-synoptic scales, GWs are well known to influence the temperature and wind field in the LS, which consequently affects the static stability and vertical shear of the horizontal wind (Kunkel et al., 2014; Kaluza et al., 2019). Thus, GWs play a role in the formation of the TIL (Birner, 2006; Kunkel et al., 2014; Zhang et al., 2019) and may also play a role in the formation and maintenance of TSL (Kaluza et al., 2021). We focus our analysis on strong wind shear and static stability, with emphasis on GW-induced shear and potential turbulence in the LMS.

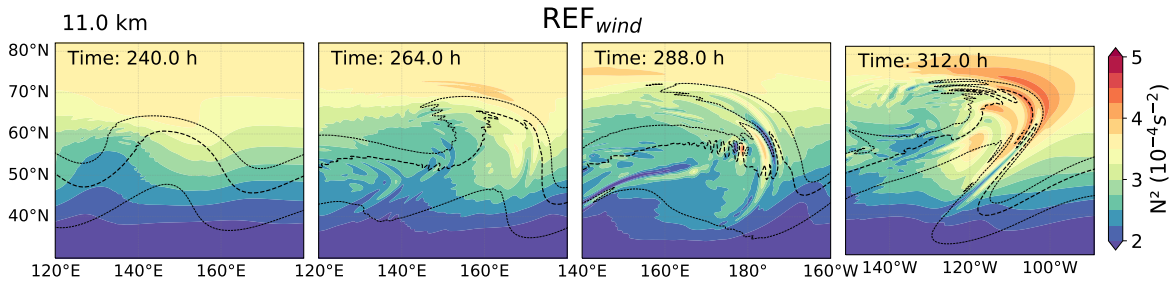


Figure 3.8: Horizontal evolution of static stability N^2 at 11 km from 240 h to 312 h of model integration for REF_{wind} experiment. The dashed black lines denote the 11 km dynamical tropopause where PV equals 3.5 PVU.

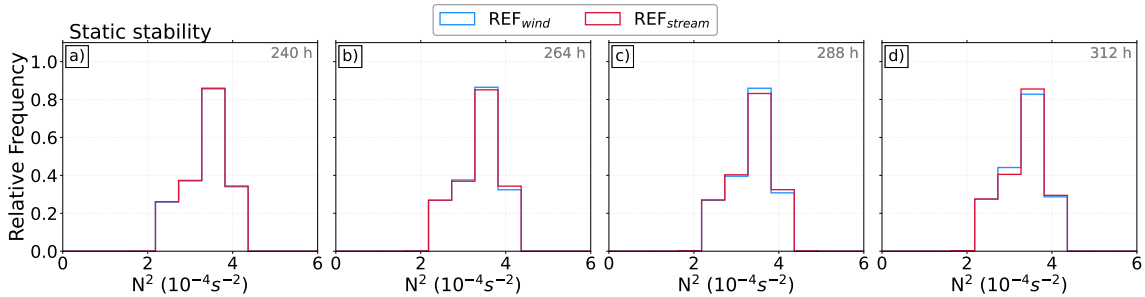


Figure 3.9: The temporal evolution of PDFs of static stability, N^2 in the LMS for dry reference experiments.

In our BLC setup, vertical shear arises from two main sources: the evolving jet structure and GWs. The vertical wind shear is primarily associated with the baroclinic jet, while small-scale vertical shear is mainly induced by large-amplitude GWs generated due to imbalances associated with jet-front system during baroclinic wave development. With our setup, we omit GWs from convection and from flow over topography; thus, the emerging GWs are a result of the baroclinic jet-front systems (e.g. Plougonven and Snyder, 2007).

Instabilities are a key prerequisite for mixing of air masses in the atmosphere. This section focuses on shear-driven instabilities such as Kelvin-Helmholtz instability, which can be diagnosed using the gradient Richardson number Ri , as given in Eq. 1.9, and is defined as the ratio of static stability to vertical shear of the horizontal wind (S^2), with the gravitational acceleration g , and the zonal and meridional wind components u and v . Note here that Ri is computed using the full vertical shear S^2 , to initially assess turbulence-prone regions throughout the large-scale baroclinic flow. In contrast to static or con-

vective instability, diagnosed via negative squared Brunt-Väisälä frequency, KHI is a hydrodynamic or dynamic instability, which requires a weaker criterion to be fulfilled for the flow to become unstable. Theoretical considerations require that Ri falls below a critical Richardson number, which is commonly set to $Ri_c = 0.25$. However, in studies using output from numerical models with comparable spatial resolution, higher Richardson number thresholds are commonly used to identify regions prone to dynamic instabilities. Following this, we regard regions of low Richardson numbers, i.e., $Ri \leq 1$, as being prone to turbulent mixing (Kunkel et al., 2019; Kaluza et al., 2021).

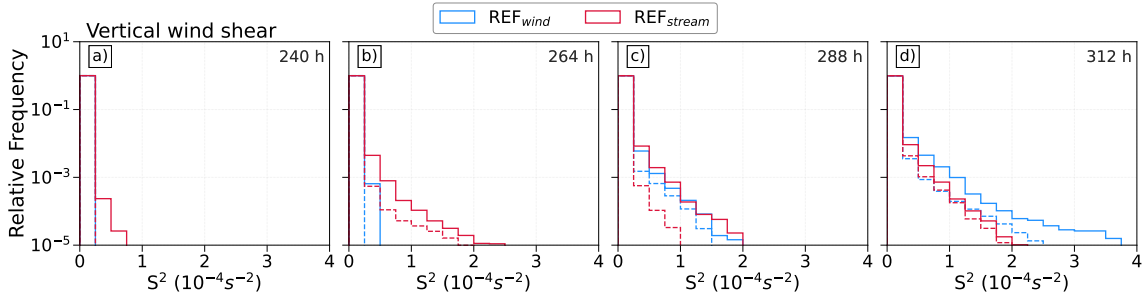


Figure 3.10: The temporal evolution of PDFs of vertical wind shear, S^2 in the LMS for dry reference experiments. The dashed histograms represents shear perturbations $S^{2'}$ from spectral domain for the respective REF simulations.

In our analysis of shear and turbulence, we initially focus on the LMS. The lower boundary of LMS is defined here by the 3.5 PVU dynamical tropopause whereas the 380 K isentropic level serves as an upper boundary, which corresponds to the height of the tropical lapse rate tropopause (e.g., Holton et al., 1995; Shepherd, 2007). This is the region in the extratropics where the mixing layer resides (e.g., Hoor et al., 2004). The distribution of N^2 at 11 km altitude is shown in Figure 3.8 together with PV isolines of 2, 3.5 and 4 PVU. This indicates the temporal evolution of N^2 , of which the extent increases as the baroclinic wave grows. Figure 3.10 shows the distribution of probability density functions (PDFs) of N^2 , S^2 and $S^{2'}$ in the LMS. Here, $S^{2'}$ denotes small-scale shear derived as deviations from the background vertical shear. We focus on the time with significant GW activity, i.e., from 240 h onward in the dry reference simulations (refer section 3.2.1). Here, two important implications become evident: (i) the distribution of static stability is relatively constant with time and with perturbation method (Figure 3.9) and, (ii) the distribution of S^2 in Figure 3.10a-d shows temporal variation in the positive tail of the distribution, whereas $S^{2'}$ majorly follows the trend of S^2 . There is an increase in the occurrence of S^2 maxima with time, particularly during the strong GW activity. Although the changes in S^2 PDFs differ between the two perturbation methods, both exhibit a similar overall behavior. Notably, the increase in S^2 and $S^{2'}$ is temporally aligned with the occurrence of GWs in the simulations. Under the assumption that $S^{2'}$ is strongly influenced by GW activity, this, in turn, indicates a substantial contribution of GW to the generation of the largest shear values. This also reveals that the major part of S^2 in the LMS resembles the small-scale shear.

An analysis of N^2 , S^2 and $S^{2'}$ PDFs for our sensitivity experiments with respect to grid spacing (Figure 3.11a-c) and physical forcing (Figure 3.11d-f) further hints at the dominant role of GWs in the generation of the largest shear values. While the distribution of N^2 in the LMS shows comparable distributions among the sensitivity simulations (Figure 3.11a, d), notable differences between the simulations arise for S^2 (Figure 3.11b, e) as well as $S^{2'}$ (Figure 3.11c, f). These differences can be summarized as follows: the finer grid spacing leads to more enhanced shear values, where the moist dynamical processes dras-

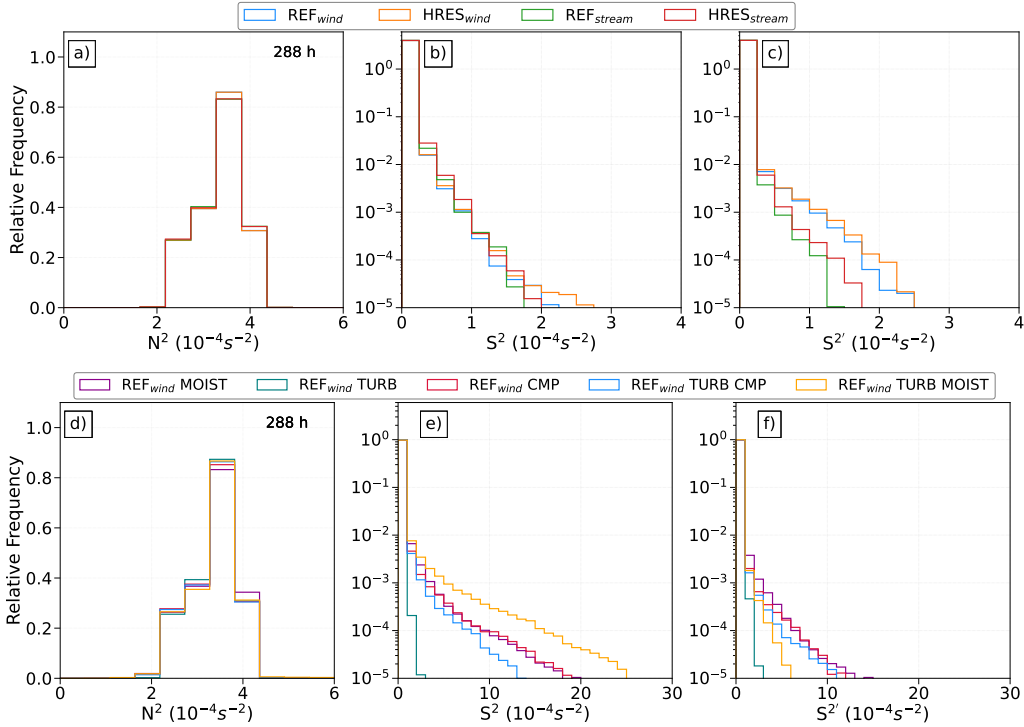


Figure 3.11: Temporal evolution of relative occurrence frequency distribution of N^2 (a, d), S^2 (b, e) and $S^{2'}$ (c, f) in the LMS over the Northern Hemisphere. Upper panel (a, b, c) represents grid spacing sensitivity experiments. Lower panel (d, e, f) represents physics sensitivity experiments performed using wind perturbation function. LMS is defined as the region between 3.5 PVU, a dynamical tropopause and 380 K isentropic surface.

tically enhance the maximum shear values. However, the intense S^2 observed in TURB MOIST results in relatively fewer $S^{2'}$ occurrences in the spectral domain, likely due to enhanced turbulence indicated by turbulent kinetic energy (TKE), which suppresses small-scale variability in shear. These findings align with our observations of GW appearance discussed in section 3.2.2 and 3.2.4, further supporting the hypothesis that GWs play a key role in generating the largest shear values in the LMS in our BLC experiments.

To better understand the physical mechanism behind GWs contribution, we consider the vertical propagation behavior of GWs in a strongly stratified environment. The enhanced shear in the LMS is plausibly linked to the presence of upward-propagating GWs. As these waves cross the tropopause, the strong vertical gradient in buoyancy frequency could lead to a shortening of the vertical wavelength of GWs. This, in turn, increases the vertical gradients of horizontal wind perturbations and thereby enhances local vertical wind shear. This interpretation is consistent with the theoretical framework described in Wei and Zhang (2015).

3.3.2 Dynamic instability and turbulence

On smaller scales and in instantaneous considerations, we observed significant general co-location of enhanced GW activity and enhanced S^2 and $S^{2'}$ occurrences in the LMS. Now we move our discussion to the potential occurrence of turbulence in the LMS and additionally discuss the relation between N^2 , S^2 , $S^{2'}$ and Ri using a two-dimensional density function (following Figure 14 in Kaluza et al., 2021). Turbulence is a rare event under general atmospheric conditions (Sharman et al., 2012; Dörnbrack et al.,

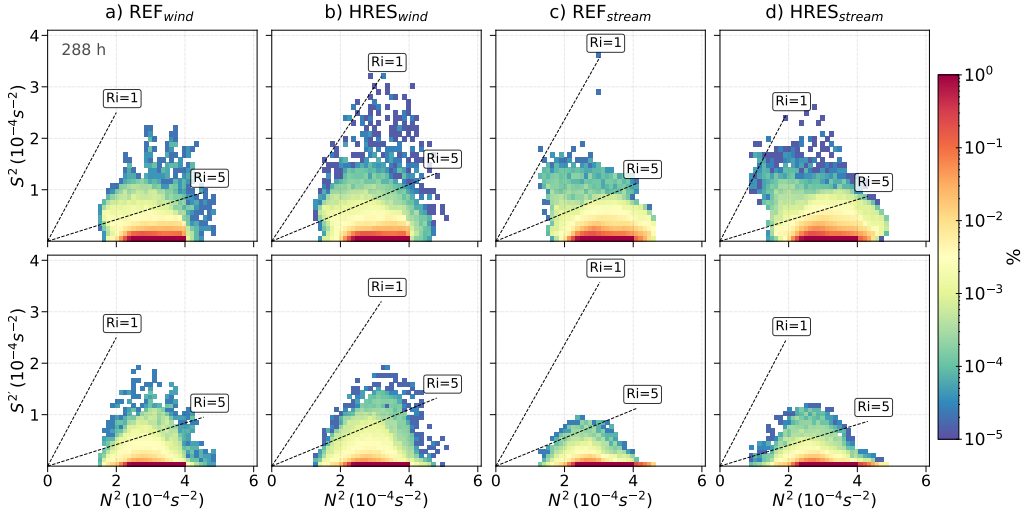


Figure 3.12: Relative occurrence frequency distribution of N^2 - S^2 (upper panel) and N^2 - $S^{2'}$ (lower panel) pair plot after 288 h for simulations with varying grid sensitivity over Northern Hemisphere in the LMS. Logarithmic occurrence frequency color scale is applied. Dashed lines indicates the gradient Richardson numbers.

2022), even in the LMS, and is even rarer than enhanced vertical shear. As such, only a few data points are expected to exhibit small-scale turbulence. This becomes evident when using two-dimensional probability density distributions with the axes being the N^2 and the vertical shear proxies, i.e., S^2 or $S^{2'}$. The color shows the relative frequency of N^2 and S^2 values in the LMS with respect to Ri (Figure 3.12). We also added black dashed lines to mark values for Ri . For $Ri \leq 5$, an indication of potential for the occurrence of dynamic instability is given to identify regions with enhanced potential for turbulence, considering previous studies (e.g., Lane et al., 2003; Olsen et al., 2013; Wang and Fu, 2021; Kunkel et al., 2019; Kaluza et al., 2021) and accounting for resolution-dependent effects (e.g., Shao et al., 2023). This threshold ensures consistent comparison across different grid spacings from 13 to 80 km, where small Ri values close to 1 are less likely, particularly in the LS (Kaluza et al., 2022). The most unstable and/or potential turbulent regions are still captured using a more conservative threshold of $0 \leq Ri \leq 1$. Note that only data points in the LMS are considered for this analysis. Thus, we only analyze the turbulence and enhanced shear occurrence above the local 3.5 PVU dynamical tropopause and below 380 K. We also note that we focus on individual time steps and compare the PDFs for various simulations, which again helps to highlight the differences among the simulations.

We start again with the dry adiabatic reference experiments and their high-resolution companions (REF and HRES, see Figure 3.12). The results show that turbulence and enhanced shear are rare events with few grid volumes falling between $0 \leq Ri \leq 1$. For *wind* perturbations, HRES produces more regions of enhanced S^2 and tends to exhibit slightly more turbulence-prone areas compared to REF simulation, highlighting the stronger influence of higher resolution in capturing these features. In contrast, *stream* perturbations show greater similarity between HRES and REF, with only marginally enhanced total as well as small-scale shear and turbulence occurrences in HRES. Overall, S^2 and $S^{2'}$ show only minimal differences in the values but with the same magnitude, indicating that smaller scales contribute substantially to the total shear occurrence. HRES captures finer details and shows slightly more enhanced shear and turbulence than REF, as expected, with smaller scales contributing significantly to these enhanced values and low Ri occurrence. The dynamically stable LMS persists throughout most of the simulation,

with a brief indication of potential turbulence during wave propagation and/or breaking. This indicates that the dry experiments exhibit evidence of potential dynamical instability in the LMS, with GWs as a potential contributor to turbulence generation.

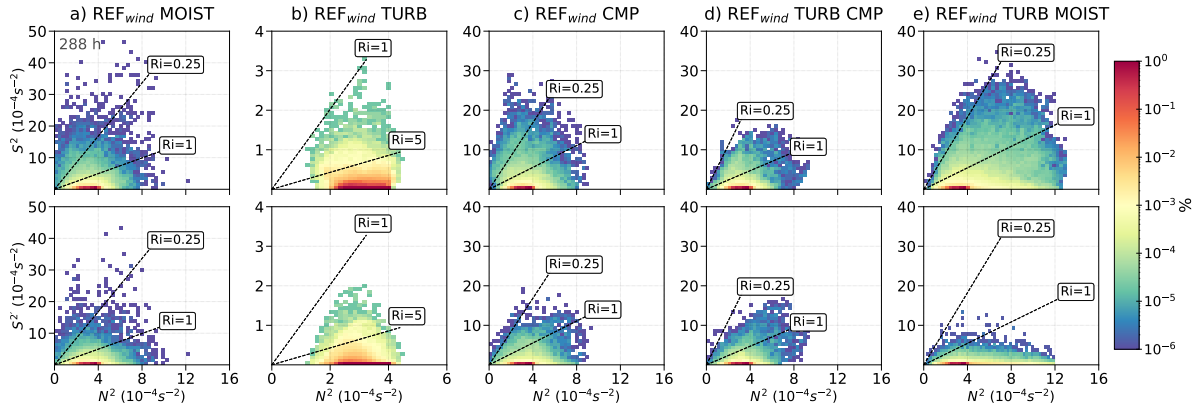


Figure 3.13: As in Figure 3.12 but after 288 h for the REF_{wind} simulations with varying physical processes.

Figure 3.13 continues to demonstrate the temporal evolution of N^2 – S^2 pairs with Ri in sensitivity experiments with physical processes. The observed latent heating, i.e., REF_{wind} MOIST (Figure 3.13a), is shown to increase the occurrence of enhanced shear in the LMS. The N^2 – S^2 (upper panel) and N^2 – $S^{2'}$ (lower panel) show in all cases with moisture that Richardson numbers below 1/4 occur. The shear values reach up to ten times higher than in the dry cases, as also evident in Figures 3.10 and 3.11, which show consistently lower shear values in the dry simulations compared to the moist cases. Thus, moist processes in the troposphere seem to be eminently important for the occurrence of dynamic instability in the LMS. At least to the point that moist processes substantially increase the probability of an instability to form. In contrast, the inclusion of TURB reduces this probability again. The case of REF_{wind} TURB still shows more occurrence of low Ri than the corresponding dry case, but TKE can also be produced. The shear, in a way, also contributes to the enhanced values of TKE and might thus explain its enhancements and vice versa. REF_{wind} CMP and MOIST shows strong $S^{2'}$ values dynamically correlate with the larger N^2 in the vicinity of $0 \leq Ri \leq 5$, indicating strong signatures of dynamic shear instability.

Shear instability occurs when the vertical shear is large enough to overcome the tendency of stratified flow to remain stratified, and then KHI and vortexes form. These instabilities generally resulted from strong temperature gradient and wind shear induced by GWs (Fritts and Alexander, 2003). REF_{wind} TURB CMP mirrors the behavior of REF_{wind} CMP. Noticeable here in REF_{wind} TURB MOIST is the appearance of lower Ri attributed to latent heat release as discussed in the section 3.2.4. The turbulence counteracts the effects of dry dynamics, which enhance the lower stratospheric static stability (Koch et al., 2005).

Moreover, due to the tendency of turbulence to reduce the strong vertical gradients, a lower vertical shear is expected in this case. However, the TURB MOIST case shows much less potential turbulence from the small-scales, even compared to its companion simulation CMP TURB. It is remarkable that in this case the N^2 – S^2 distribution differs substantially from the N^2 – $S^{2'}$ distribution. Thus, much of the potential turbulence in TURB MOIST is evident on larger scales. To further demonstrate this, the vertical distribution of TKE is found to be enhanced by a factor of 50 in TURB MOIST compared to TURB CMP and TURB (Figure 3.14). There are two sources for the generation of TKE: first, the vertical

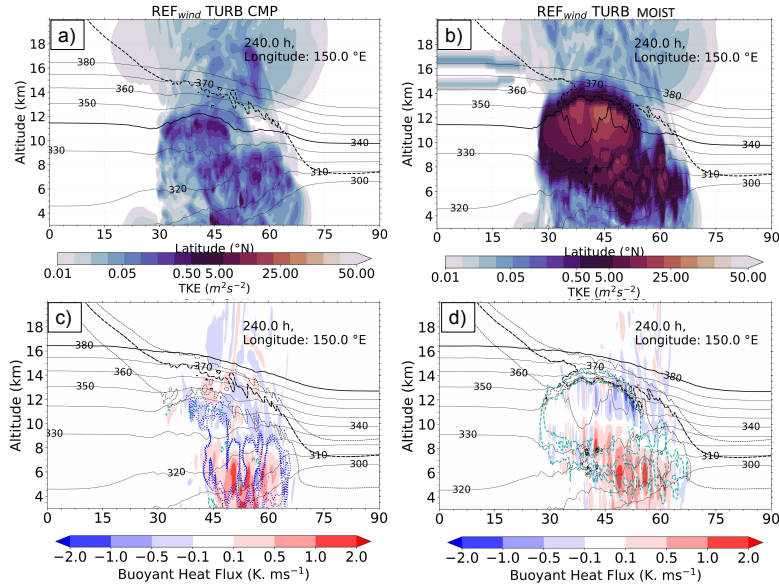


Figure 3.14: Vertical cross section of (a, b) turbulent kinetic energy (TKE, in $\text{m}^2 \text{s}^{-2}$) and (c, d) buoyant heat flux (BHF, in $\text{K m}^2 \text{s}^{-1}$) for simulations $\text{REF}_{\text{wind}} \text{ TURB CMP}$ & $\text{REF}_{\text{wind}} \text{ TURB MOIST}$. The green lines in c and d indicate maximum TKE with cloud ice content (q_c , in kg kg^{-1}) in blue.

shear, and, secondly, the vertical gradient of total moisture, which can consequently lead to buoyant heat flux (Doms et al., 2011). Although the vertical shear (both small- and large-scale) was observed to be similar in all turbulence included cases, the subsequent buoyant heat flux in TURB MOIST shows positive and negative values at the region of larger TKE values (Figure 3.14b, d) around tropopause, most probably related to Rossby waves, as it is linked to large-scale flow features rather than small-scale GW activity. Thus, $N^2-S^{2'}$ spectrum shows a drastic decrease in grid volumes associated with low Ri . Ultimately, there is the existence of a large overlap between enhanced small-scale shear and low Ri as well as GW activity. Altogether, the occurrence of low Ri is primarily driven by shear induced by large-amplitude GWs, as evidenced by localized regions of strong small-scale wind shear despite moderate background shear. This is further supported by the similarity in the distributions of S^2 and $S^{2'}$ in the LMS, particularly in the upper tail of the PDFs (as shown in Figure 3.11b, e and c–f).

This relation further explored through the inclusion of the small-scale momentum flux (Figures 3.15 and 3.16). If small-scales play a major role in the shear and turbulence generation, then we expect a positive correlation between $S^{2'}$ and absolute momentum flux in case of turbulence occurrence. This positive correlation is confirmed when we filter the data of our simulations for potential turbulence, i.e., $0 \leq Ri \leq 5$ in the LMS. This can be interpreted as an indication of the small-scales contributing substantially to the occurrence of strong large-scale as well as small-scale shear and potential turbulence. This relation is evident in the dry simulations, also across the various sensitivity experiments (see Figure 3.15 for the RES and HRES experiments), as well as for the sensitivity simulations with physics (see Figure 3.16). Note here that the results are not strongly dependent on the wavenumber used to separate the background from the small scales.

Overall, our results from $N^2-S^{2'}$ and GW momentum flux–vertical shear perturbations strongly highlight the important role of GWs in determining potential turbulence in the LMS. Consequently, they might also play a vital role in turbulent mixing of trace species in this region and thus in the formation of the extratropical transition layer (Hoor et al., 2004; Pan et al., 2006). Because the potential turbulence

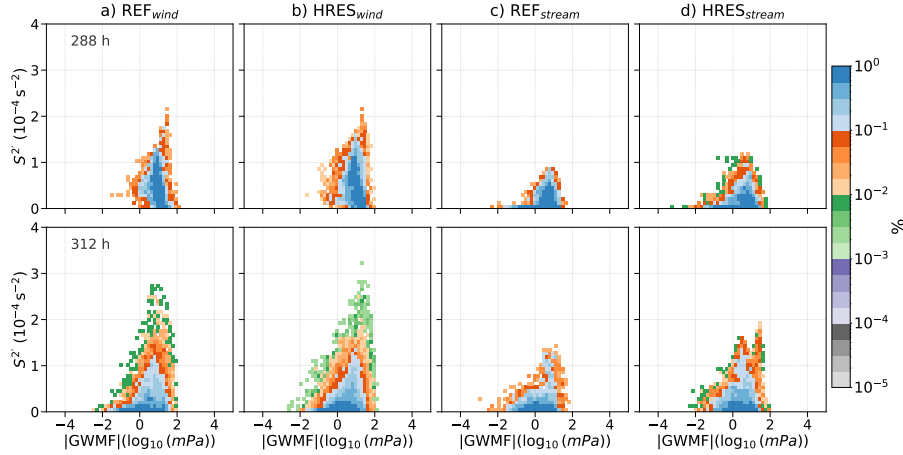


Figure 3.15: Relative occurrence frequency or probability density distribution of absolute momentum flux due to GWs–vertical shear perturbations S^2 pair in the LMS for $Ri \leq 5$ after 288 h (upper panel) and 312 h (lower panel) for simulations with grid spacing sensitivity. Normalized counts of PDFs distribution is shown where logarithmic occurrence frequency color scale is applied.

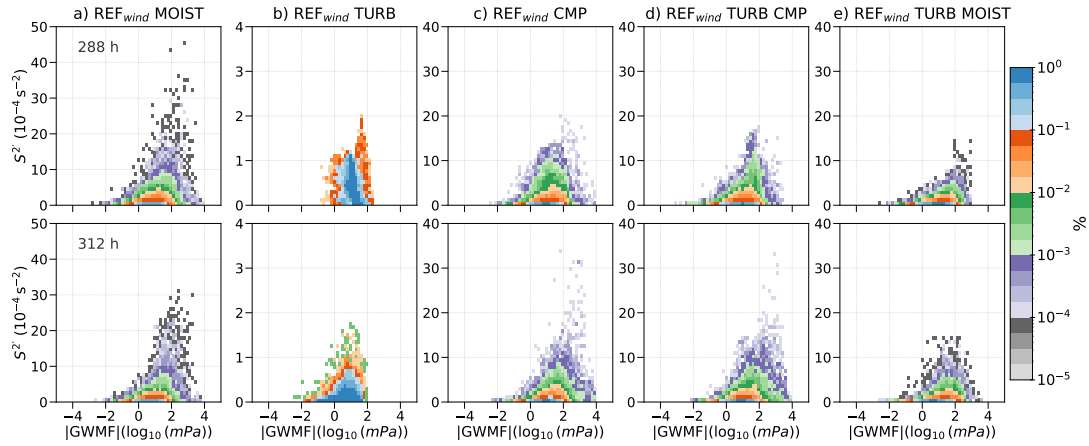


Figure 3.16: As in Figure 3.15 but for simulations with physical processes sensitivity. Normalized counts of PDFs distribution is shown where logarithmic occurrence frequency color scale is applied.

occurrence is strongly linked to enhanced shear, we will explore in the next section in more detail the role of the small-scale dynamics in the formation of the shear layer above tropopause.

3.4 Vertical distribution of shear and associated GW signatures

Until now, the discussion has centered on enhanced shear generation, as well as the potential for turbulence occurrence and consequent mixing. In this section, we shift our focus to the occurrence of the TSL in the extratropics and its potential association with GWs in the LMS. The TSL has been defined via an exceeding a defined threshold value of vertical wind shear. In Kaluza et al. (2021), the authors calculated the occurrence frequency of such shear exceeding a defined threshold in the tropopause-following coordinate over a ten-year data set for the Northern Hemisphere. Here, we adopt this approach for our data but do the analysis on an instantaneous time step. Our goal is to show that the occurrence frequencies of enhanced vertical wind shear are temporally aligned with the presence of GW in the LMS. Note that in this case, the total shear S^2 derived from the full wind components is used. In contrast to Kaluza et al. (2021), here, we start from a state with no TSL, which allows us to analyze the temporal evolution of

the shear in the LMS. We follow the steps outlined in Kaluza et al. (2021) with some adaptations for our simulations.

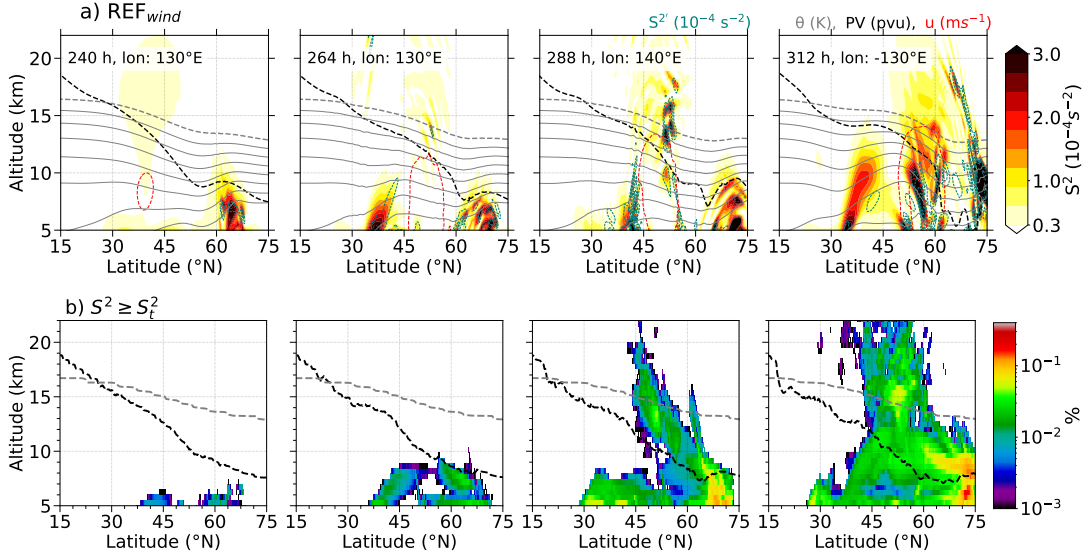


Figure 3.17: The temporal evolution of (a) vertical cross section of shear through the identified regions of GWs from time 240 h onward for REF_{wind} simulation with S^2 (dashed green), potential temperature (grey), zonal wind (30 ms⁻¹, red) and dynamical tropopause (black) and (b) the respective Northern hemispheric occurrence frequency distribution of grid volumes that exhibit $S^2 \geq S_t^2$. Logarithmic frequency contour, vertically binned in $dz=500$ m is applied. The zonal mean value of 3.5 PVU in the PV field (dashed black line), and the zonal mean value of 380 K in the potential temperature field (grey dashed line) is overlaid.

The identification of the TSL requires the definition of a threshold value for S^2 . We follow the method used by Kaluza et al. (2021) with adaptation to our BLCs. In particular, the threshold value is selected based on the criterion that $S^2 \geq S_t^2$ is typically unsustainable under the average tropospheric static stability ($\overline{N_{trop}^2}$), which results in low Ri and conditions favorable for potential turbulence. Following this, and the average tropospheric static stability $\overline{N_{trop}^2} \approx 2 \times 10^{-4} \text{ s}^{-2}$ for simulations incorporating physical processes, we use a threshold value $S_t^2 = 2 \times 10^{-4} \text{ s}^{-2}$, consistent with Kaluza et al. (2021), where latent heating enhances GW activity and shear occurrences. In contrast, dry simulations exhibit much lower mean tropospheric static stability value $0.1 \times 10^{-4} \text{ s}^{-2}$ due to the prescribed temperature profile of the idealized setup. To adequately capture the full range of dynamically relevant shear in these weakly stable conditions, we adopt a lower threshold of $0.3 \times 10^{-4} \text{ s}^{-2}$. This value is supported by sensitivity tests, which showed that increasing the threshold (e.g., $1 \times 10^{-4} \text{ s}^{-2}$) significantly reduced the frequency of identified shear occurrences but did not change the overall distribution patterns. Thus, for dry experiments, the chosen threshold accounts for inherently low shear occurrences and ensures the full spectrum of shear is captured. Therefore, our selected thresholds reflect the underlying differences in static stability and shear environments between dry and moist simulations while maintaining consistency with an established physically based criterion. Note, these values are much lower than the threshold defined in Kaluza et al. (2021), which is mainly rooted in the idealized setup compared to a fully comprehensive reanalysis system.

Figure 3.17a demonstrates the temporal evolution of vertical cross section of shear S^2 , zonal wind u , PV and potential temperature. The corresponding wave signals at 11 km altitude are indicated by a dashed line in Figure 3.7a. Notably, the region of S^2 is strongly affected by a small-scale wave pattern

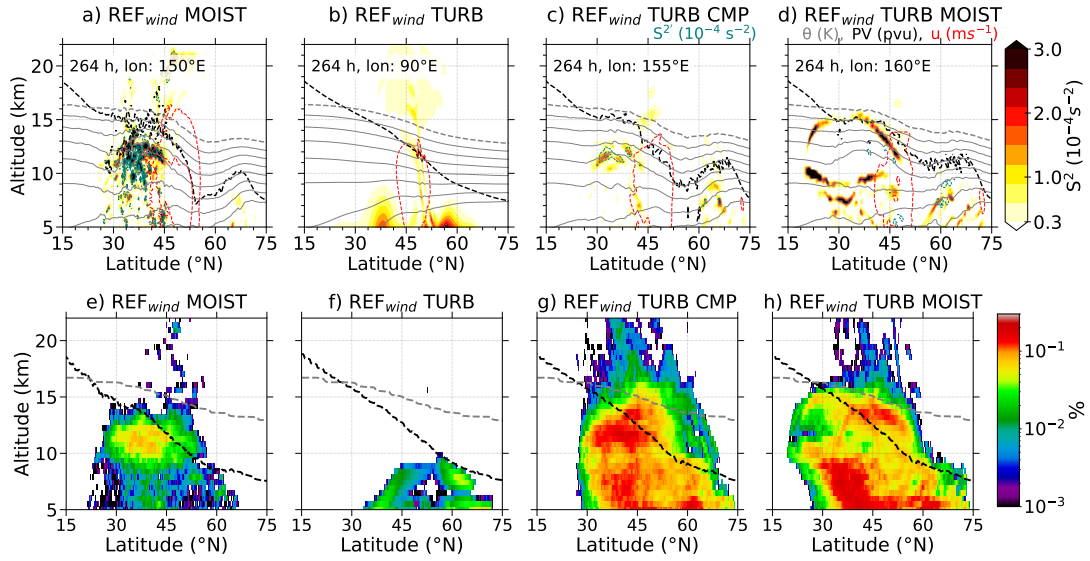


Figure 3.18: Vertical cross section of shear (a-d) through the identified regions of GWs at 264 h REF_{wind} simulations with physical processes sensitivity and the respective Northern Hemispheric occurrence frequency distribution of grid volumes that exhibit $S^2 \geq S_t^2$ (e-h). Logarithmic frequency contour, vertically binned in $dz=500$ m is applied. The zonal mean dynamical tropopause altitude is indicated by the dashed black line and tropical tropopause (380 K isentrope) by grey dashed line.

related to an upward propagating GW, evident in the potential temperature and PV isolines. Meanwhile, the spatiotemporal overlap of GW signatures and S^2 , particularly after 288 h, indicates that GW is an important, if not the major, source of the enhanced values of shear occurrence in the LMS. Figure 3.17b shows the temporal evolution of relative occurrence frequency counted in zonal direction for vertical wind shear $S^2 \geq S_t^2$ on a logarithmic color scale for the Northern Hemisphere, with the geometric altitude as the vertical coordinate. Figure 3.17b reveals regions of distinct occurrence frequency located in UTLS: one in the mid-latitudes between 40–55° N and the second one between 60–75° N above the dynamical tropopause in the extratropics. The progression of enhanced shear over time, with significant enhancement in the LMS, appears to follow the occurrence of the GW in the BLC and is tightly linked to the breaking of the synoptic-scale wave. We note here that the REF_{stream} simulation exhibits a similar pattern. As discussed in section 3.2.5 and in the paragraph above, the growing GW trains amplify S^2 maxima and induce shear in the extratropics, with upward propagating GWs inducing pronounced shear in the vicinity of the tropopause and the LMS. This overlap between the pronounced shear occurrence and GW activity through the LS strongly proposes that GWs are the source of enhanced shear generation in the LMS.

Furthermore, an analysis of TSL occurrence across sensitivity experiments, including grid spacing and physical forcing (as shown in Figure 3.18), also suggests that GWs play a dominant role in generating enhanced vertical shear. For the simulations with moisture and turbulence parameterization, we see a similar temporal evolution of the vertical shear in the UTLS. Major differences are related to the TURB CMP and TURB MOIST showing firm $S^2 \geq S_t^2$ occurrences due to contributions from sub-synoptic features and enhanced turbulent processes. Here, the vertical shear distribution broadens with altitude, shifting toward higher values, with the peak shear predominantly concentrated in the extratropical UT (Figure 3.18). This peak shear occurrence just below the tropopause, as noted by Kaluza et al. (2022), aligns with the sharp unimodal turbulence distribution. The observed collocation of shear generated by

GWs and peak shear occurrence in the UT reveals the substantial contribution from small-scale features, particularly GWs, along with moist tropospheric dynamics.

Overall, these findings support the hypothesis that GWs could contribute to enhanced shear occurrence, and hence, to the formation of TSL in the extratropical LMS. Broadly speaking, our results hint that GWs play a pivotal role in shaping TSL dynamics, and consequently, may contribute to the formation and maintenance of ExTL.

3.5 Testcase Intercomparison with JABW BLC experiments

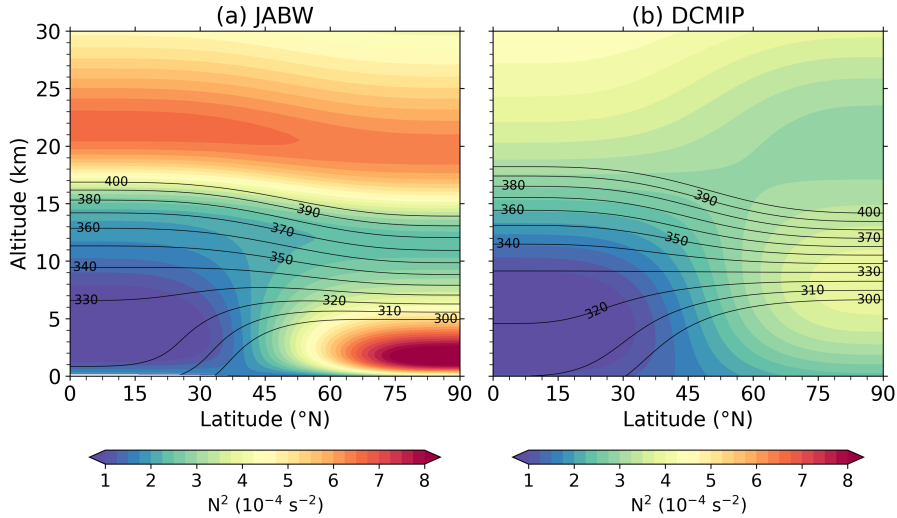


Figure 3.19: Initial background state of (a) JABW and (b) DCMIP test case, shaded contours represent static stability at 30° E longitude with potential temperature Θ (solid black lines, 10 K spacing, starting with 280 K in the lower right corner).

Besides the DCMIP experiments, note here that we also conducted all simulations discussed in the paragraphs above for a third initial state, following Jablonowski and Williamson (2006). The DCMIP *wind* and the Jablonowski test case have strong similarities, both leading to a life cycle that resembles the life cycle type 1 (Thorncroft et al., 1993, LC1,) while the DCMIP *stream* instead shows a life cycle development of type 2 (LC2). To clarify the commonalities and differences in GWs role to shear generation in the LMS, intercomparisons were made between DCMIP_{wind} and standard Jablonowski-Williamson test case with and without physics. Despite slight initial state differences, such as the absence of a vertical temperature inversion in DCMIP_{wind}, both cases exhibited similar baroclinic wave evolution and GW characteristics in the UTLS. The distribution of initial static stability is shown in Figure 3.19 for both cases. The distribution varies in both cases: (i) in JABW, the high static stability is observed at lower levels below 5 km around $60\text{--}75^\circ$ N and (ii) however, DCMIP shows equatorial belt with the weak static stability. The prior then leads to the generation of strong GW activity, i.e., the propagation of GWs at the lateral time steps. Nonetheless, despite the different initial conditions, the results leads to the same conclusion in terms of the contribution of GWs in the generation of shear and potential turbulence in the LMS. These findings suggest that our approach is robust and can reproduce small-scale GW behavior effectively, even with slight initial state variations.

3.6 Synthesis

3.6.1 Discussion and summary

GW permitting idealized baroclinic life cycle experiments using ICON have been performed in order to understand the role of GWs in the generation of shear and thereby understanding their contribution to TSL in the extratropics. To clarify the common features and differences of GWs and their role in shear generation in the LMS, intercomparisons of test cases were made between DCMIP_{wind} and standard JABW with and without physics. Our results show that the DCMIP_{wind} configuration captures key dynamic characteristics of Earth's atmosphere with a comparable level of accuracy to the standard JABW baroclinic wave test case. Despite slight differences in the initial states, such as the absence of a vertical temperature inversion in DCMIP_{wind}, both cases reveal similar evolution patterns in baroclinic waves and GW characteristics in the UTLS. The distribution of static stability and shear in both cases supports consistent conclusion in terms of GW contribution to the vertical shear and turbulence development in the LMS. These findings suggest that our approach is robust and can reproduce small-scale GW behaviors effectively, even with slight initial state variations.

The GWs observed in the BLC experiments in an idealized environment concludes that:

1. GWs appearance highly dependent on the grid spacing. Therefore, it is necessity to properly simulate GWs and turbulence generated from baroclinic waves considering suitable higher spatial resolution. Besides this, using DCMIP in both form of wind and stream perturbations i.e. LC1 and LC2 type (Thorncroft et al., 1993) gives similar evolution of GWLC and leads to same conclusion in terms of role of GWs in shear and potential turbulence generation in the UTLS.
2. Faster evolution of BLC and variations in extent of GWs observed with employed physical forcing. GW occurrence and thus shear and turbulence occurrence in the LMS dictates significant impact of moist processes from the troposphere.
This results are quite robust for different model setting in terms of spatial and temporal resolution and physics parameterizations. Thus gives further confidence that GW breaking may be relevance for TSL. At the same time, the relevance of small-scale GWs are also observed.
3. GWs are one of the important source for the shear generation thereby plays crucial role for turbulence occurrence in the LMS. It is also found that GWs play crucial role in momentum transfer into the LS as upward moving maximum GWMF occurrences collocate with zonal shear occurrences particularly in the LMS.
4. The GWs shows significant correlation with enhanced zonal shear occurrence in the LMS. However, TSL might have a noticeable intersection with the large-scale forcing for tropopause regions that are susceptible to turbulent STE. This, however, needs thorough further investigation. The limitations of the numerical models used are an important factor to consider.

Regarding 3, the drastic shear enhancement in diabatic experiments are due to the moisture. The air masses lifted from moist, lower tropospheric regions fosters the GW activity in the LS and leads to the shear enhancement in the LMS. In general, turbulence parameterization are not designed to reproduce GW generation associated with shear, which can be a reason for the low GW activity at LMS in the

model. Further research using GWs and convection permitting simulations would be interesting to assess the impact of GWs on turbulence.

In conclusion, various aspects hint that GWs can be a key factor for the shear enhancement in the extratropics which leads to turbulent mixing in the LMS. Thus, GWs might play crucial role in the formation of the ExTL. These results suggest that during the prediction of CAT, GW should not be neglected as they play a major role in the unforeseen turbulence occurrence.

3.6.2 Limitations and uncertainties

Despite the results gained in this study, idealized numerical experiments of baroclinic waves, and in particular the representation of GWs in such simulations, have certain limitations. While the appearance of GWs and their effect on shear are tightly coupled to the model resolution, the findings of this study might be regarded as a lower estimate of the effect of GWs on shear generation. Also note that this study specifically focuses on GWs generated by jet-front systems during baroclinic wave evolution. GWs from other sources, such as orography and convection, are not considered, as their adequate representation would require different model configuration and substantially higher resolution which are beyond the scope of this study. Nonetheless, our idealized setup allows a controlled investigation of the effect of GWs emitted within baroclinic disturbance while isolating their role from other processes.

Notwithstanding, the limitations that the results have been described only for the ICON NWP mode, the validation of ICON model we made here supports the results from COSMO and Weather Research and Forecasting model (WRF) models, and the effectiveness of the model for various studies on GW in the middle atmosphere. Performing multi-year simulations could produce a better picture of climatological dataset of small-scale GWs in the whole UTLS. Such a dataset, validated by long term observations, would be a useful guideline for the source contributing to the TSL. On the other hand, validation of these results using orographic and non-orographic GW parameterizations might help to thoroughly explain the role of GWs in STE and mixing in the LMS. Furthermore, GW interactions with middle atmospheric flow are impacted by lateral propagation, especially in significantly disrupted flows as sudden stratospheric warming (Song et al., 2020; Gupta et al., 2021; Stephan et al., 2020). Related to that, Okui et al. (2024) very recently demonstrated that the pattern of sudden stratospheric warming preconditioning represents a common fluctuation in zonal-mean zonal winds within the stratosphere and mesosphere, rather than a unique or isolated occurrence. This opens a door to further explore how these common patterns with respect to sub-grid scale GWs influence the UTLS, particularly their role in shaping vertical shear and transport processes in the ExTL.

4 Evidence of GW-induced shear and mixing in the North Atlantic baroclinic environment

Objective

The objective of this chapter is to validate the findings from Chapter 3 in real case scenario using airborne in situ measurements, supported by ERA5 reanalysis, IFS forecast data and sensitivities using higher resolution ICON simulations. Here, we extend the analysis further to understand whether GW-induced shear are of any relevance to clear air turbulence at the flight cruising altitude.

*This chapter is an adaptation of research article that is currently in review to the journal Atmospheric chemistry and physics as: **Umbarkar, M., Kunkel D., Miltenberger A., Lachnitt H.-C., Kaluza T., Schwenk C., and Hoor, P., 2025: Evidence of gravity wave contribution to vertical shear and mixing in the lower stratosphere: a WISE case study, Atmospheric chemistry and Physics, Copernicus, <https://doi.org/10.5194/egusphere-2025-5142>.***

The overarching goal of this chapter is to investigate the contribution of GWs to wind shear enhancement above the tropopause within the ExUTLS over the North Atlantic region during an extratropical cyclone, as revealed by the idealized baroclinic life cycle experiments in Chapter 3. First, the synoptic situation during the flight period followed by an evidence of observed recent air mass mixing during a flight of the Wave-driven Isentropic Exchange (WISE) mission is described. Second, whether this mixing event is related to enhanced shear and GW activity is investigated. Third, discussion then shifts to the differences among ERA5 and IFS in their capabilities to simulate this event and represent the associated GW-induced turbulent mixing in the UTLS. The latter is related to the question of whether ERA5 is well enough resolved to study GWs, shear and mixing in the UTLS in case studies, and thus potentially also in a climatological context. This investigation is further extended in order to understand whether instabilities triggered by GW-induced shear has any relevance to the development of CAT. Finally, the analysis is extended with sensitivity experiments performed using ICON, the non-hydrostatic environment.

This chapter aims to offer new observational insights into the GW-induced shear and its relevance to TSL over the North Atlantic by analyzing selected research flight from the WISE campaign, which was primarily based in Shannon, Ireland. The central goal of the mission was to investigate the link between the TIL and the ExTL, as previous work suggested a potential connection between STE processes and the presence of the TIL. We further enhanced our understanding by exploring potential role of small-scales in the formation of mixing layer which occurred through the shear enhancement due to GWs in the extratropical UTLS. Section 4.2 presents the analysis of research flight number 05 (hereafter denoted as **RF05**). Specifically, aim is to address the following research questions:

1. *Whether measured trace species show signatures of small-scale mixing in regions of enhanced static stability in the lower stratosphere?*
2. *How well do different models capture these processes during the observed tracer mixing event? How much does ERA5 differ from high resolution IFS and ICON forecasts?*
3. *Are these GW-induced shear layers linked to reduced stability and turbulent mixing? Can the results from the idealized world transferred to a situation over the North Atlantic? Are these GWs responsible for CAT occurrence?*

4.1 The 2017 Wave-driven ISentropic Exchange (WISE) campaign

The WISE airborne measurement campaign was conducted in September and October 2017, with a key objective of studying the TIL, particularly its development during baroclinic life cycles in the North Atlantic storm track region. It was motivated by earlier studies suggesting that various processes influence the formation and persistence of the TIL, which occurs across broad spectrum of spatial and temporal scales. While the TIL has been widely explored using idealized numerical models (Kunkel et al., 2014, 2016), most research has concentrated on its climatological characteristics. Fewer studies have examined the specific mechanisms responsible for the enhanced static stability in the LS (e.g. Kunkel et al., 2019). In autumn 2017, the WISE mission was conducted using the German High Altitude Long (HALO) research aircraft, operating from Oberpfaffenhofen, Germany, and Shannon, Ireland. The main target of this campaign was to study the relation between lower stratospheric static stability and cross tropopause exchange in the extratropics. In this case study, specific focus is on the RF05 that took place on 23rd September 2017 starting at 08:09 to 17:04 UTC with the goal to investigate the dynamical and chemical structure of the atmosphere in the vicinity of tropopause during the wave breaking event.

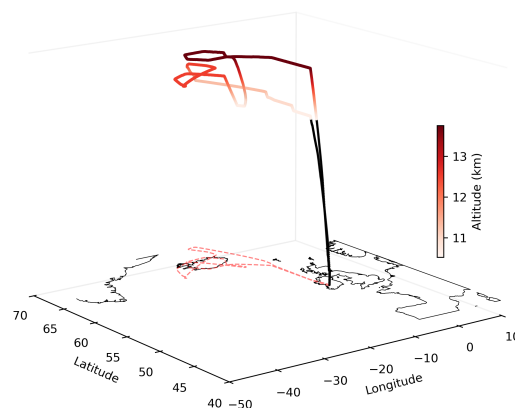


Figure 4.1: Flight pattern of WISE research flight 05. Color code indicates flight altitude, red dashed line shows surface projection of the flight path.

In situ measurements

During the WISE campaign, HALO was outfitted with a specialized suite of instruments for in situ and remote sensing. This study utilizes in situ measurements of CO, N₂O as well as state parameters such as temperature, pressure and three dimensional wind vector. The state parameters were measured with Basic HALO Measurement and Sensor System (BAHAMAS). The system is integrated into the aircraft and includes a data acquisition unit along with sensors designed for fundamental meteorological and aerodynamic measurements. All atmospheric sensors operate at a base frequency of 100 Hz, with data typically processed at 10 Hz. The pressure measurements have an accuracy of approximately ± 0.3 hPa, and the static temperature measurements are accurate within ± 0.5 K. The uncertainty in wind measurements is primarily determined by the accuracies of the pressure and airflow sensors. The system interfaces with various aircraft subsystems, such as the inertial reference unit and the air data computer, to monitor aircraft state parameters (Krautstrunk and Giez, 2012; Kunkel et al., 2019).

CO and N₂O data have been obtained using the University of Mainz Airborne Quantum Cascade Laser Spectrometer (UMAQS). The instrument is based on direct absorption spectroscopy using a continuous-wave quantum cascade laser with a sweep rate of 2 kHz (Müller et al., 2015). For the WISE campaign the total drift-corrected uncertainty was determined to be 0.94 ppbv for CO and 0.18 ppbv for N₂O.

Mainly, the major goal of the RF05 was on whether the trace species show specific signatures of irreversible mixing in regions of enhanced static stability in the LS. The flight was planned in the ridge of a synoptic-scale baroclinic wave which evolved during the previous days over the North Atlantic at the edge of large-scale trough. The observed irreversible mixing event is further elaborated with regard to the regions of GW-induced shear enhancement.

4.2 Observation of GW-induced mixing in a baroclinic wave over Iceland during WISE RF05

The selected RF05 aimed at the survey of the tropopause region during a pronounced baroclinic wave breaking process over the North Atlantic in late September. The following subsections first describe the meteorological situation and flow features derived from modeled outputs, followed by illustration of the research flight as well as the measurements taken. Then troposphere-stratosphere trace gas exchange put into the context of the dynamic structure of the tropopause region derived from the ERA5 reanalyses, IFS forecast and ICON simulations mentioned in Chapter 2.

4.2.1 Synoptic situation on 23 September 2017 over the North Atlantic

First, the atmospheric conditions in the UTLS at 11:00 UTC over the North Atlantic region on September 23, 2017, are described in detail, which serve as the focus of our case study. For the estimation of STE, the quantitative information is required about the transport of mass and properties between these regions. For this, either the isobaric or isentropic surface or much more often the surface of equal values of the Ertel PV (isertelic surface, Eq. 1.2) is used.

The isentropic distribution of potential vorticity on 340 K in Figure 4.2a–c illustrates the meteorological situation during WISE RF05 across ERA5, IFS and ICON, respectively. This synoptic situation over the North Atlantic is dominated by the strong meridional excursion of the sub-tropical air masses far north in a region from Iberian peninsula over Great Britain upto Iceland (Figure 4.2a). West of this tropospheric streamer there is a trough structure which is quite coherent, while east of this, there is

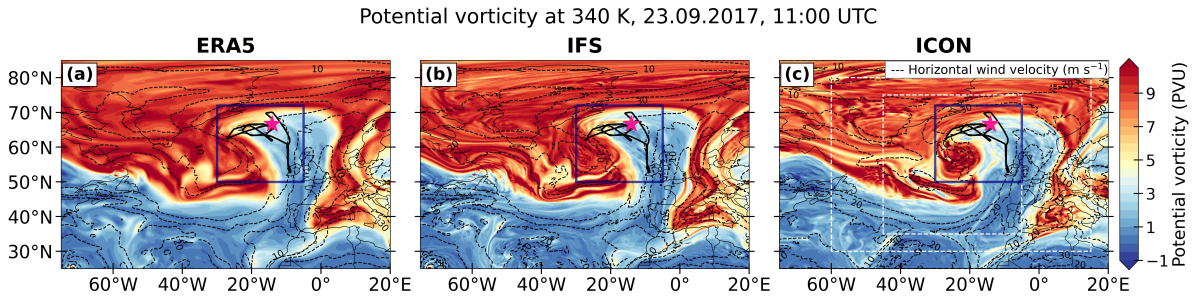


Figure 4.2: Snapshot of the atmosphere at 11:00 UTC on 23 September 2017 using ERA5 potential vorticity (PVU) and horizontal wind velocity (m s^{-1}). The two nested domain boundaries are set for the reference. Through potential vorticity contours one can clearly see the prominent tropopause fold and pv streamers. The star denotes the flight location at this time.

trough structure which seems to be more mixed in terms of isentropic PV. These features contribute to air mass mixing, especially in areas where PV contours appear filamented, indicating potential transport across the tropopause and ultimately, signals towards the STE processes.

The flight trajectory was such that the flight started from the Shannon towards Iceland where a hexagon was flown as well as a dive was performed before returning to Shannon (Figure 4.1). From Figure 4.2, the PV distribution shows that the flight took place to a large degree in the region where subtropical air masses, around 11–13 km, moved polewards while some parts of the flight track also reached across the PV gradient into the LS. The region of the strong PV gradient shows the location of the jet stream, which acts as a barrier between tropospheric and stratospheric air masses. On the large-scale, all three dataset show similar patterns in terms of the overall PV distribution. Moreover, smaller-scale ripple-like structures in the PV field around 20° W and 65° N could signify wave activity, which are often generated near jet streams or strong dynamical forcing regions, as reported for the case of WISE RF07 by Kunkel et al. (2019). Such small-scale wave like structures in the PV field in the transition region between tropospheric and stratospheric air masses could already hint towards the presence of GW activity associated with mixing of air masses. The observational data from WISE RF05 is further explored in the following section.

4.2.2 Identification of small-scale mixing in the LMS

4.2.3 Identification of flight segments affected by turbulence

To identify regions and periods of potential small-scale mixing above the tropopause, we examine the time series of measured and modeled quantities during WISE RF05. Figure 4.3 shows a comparison of in situ measured atmospheric state parameters including chemical tracers and potential temperature (Figure 4.3a) as well as the dynamical tropopause altitude and instability parameters (Figure 4.3b) from the ERA5 reanalysis data that was interpolated in time and space onto the flight path. The general agreement promotes a synergistic analysis that relies on in situ measurements together with model and forecast data. It is essential to incorporate model data because of the absence of three-dimensional measurements and the consequent lack in measured gradient-based quantities, such as static stability and vertical wind shear. It should be noted, however, that the interpolated model-derived numbers are still an estimate due to the model's limited temporal and spatial resolution, as well as its ability to realistically resolve key physical processes.

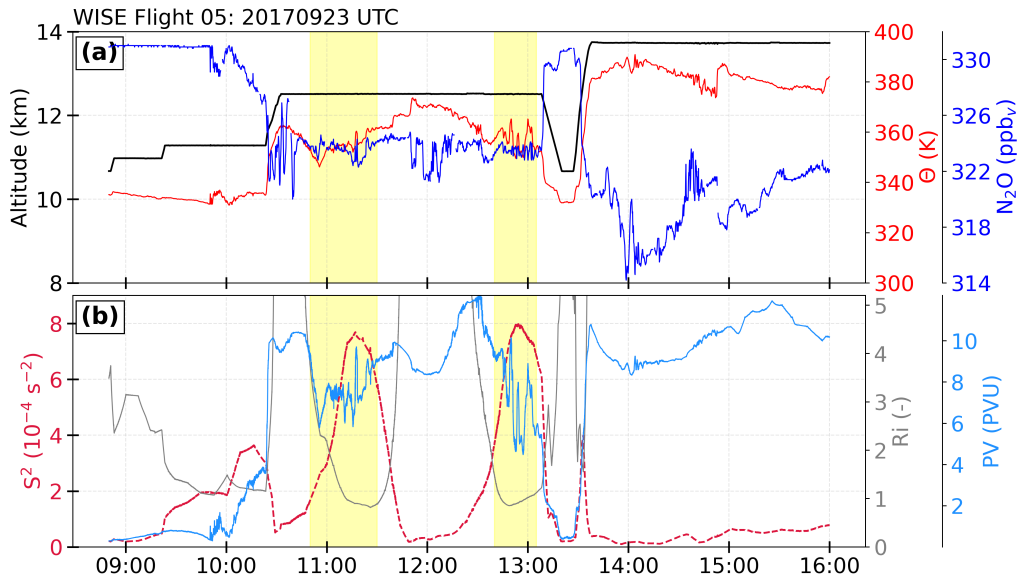


Figure 4.3: Time series of measured (a) N_2O (blue), Θ (red), and (b) ERA5 vertical shear, potential vorticity (navy) and gradient Richardson Ri interpolated on flight track. The black line denotes the flight altitude. Light yellow boxes indicate the flight section for the detailed mixing analysis. The corresponding altitude track is shown in Figure 4.2.

Except for a dive between 13:00 UTC and 14:00 UTC the flight path was designed to ascend with time. Initially, the flight was in the troposphere, indicated by constant N_2O values, low Θ and low PV values. Around 10:00 UTC the flight path crosses the tropopause, also evident in smaller N_2O values. The leg between 10:30 UTC and 13:05 UTC at ~ 12.5 km altitude shows interesting time periods in terms of increased potential for mixing. First, the N_2O , PV and potential temperature time series show time periods of enhanced small-scale variability. Second, the Ri (and S^2) deduced from ERA5 shows very low (high) values on the order of 1 ($\geq 4 \times 10^{-4} s^{-2}$), indicative for the plausible presence of a dynamic instability. Especially, three distinct periods mainly 10:45–11:30, 12:40–13:05 and 14:00–15:00 UTC show rapid variations in N_2O (~ 320 – 330 ppbv to ~ 316 – 320 ppbv) and Θ (~ 340 K). Out of which, first two periods show the shear maxima and Ri reduction indicative of potential turbulence during the flight. In a next step, tracer-tracer correlations are used to conduct a more in-depth investigation of these times and events.

4.2.4 Trace gas observations, tracer-tracer correlation and small-scale mixing

The behavior of tracer-tracer correlation between N_2O , CO and Θ is further analysed for individual segments between 10:45–13:05 UTC for the identification of small-scale mixing. We use trace gases highlighting a tropospheric origin on the one side, i.e., CO, and trace species indicative of stratospheric air masses, i.e., N_2O on the other side. Similarly, we can use H_2O and O_3 .

The vertical profile of CO and N_2O with potential temperature is shown in Figure 4.4a, b for the whole flight (grey colored). The colored data point indicates the period from 10:45 to 13:05 UTC, which is the time period bounded by the two yellow marked regions in Figure 4.3. The corresponding tracer-tracer correlation between CO and N_2O mixing ratio for the whole flight (Figure 4.4c) shows the commonly expected behavior, i.e., the troposphere is characterized by a pronounced CO variability on potential temperature variability. Moreover, the color scale in Figure 4.4c reveals the consecutive

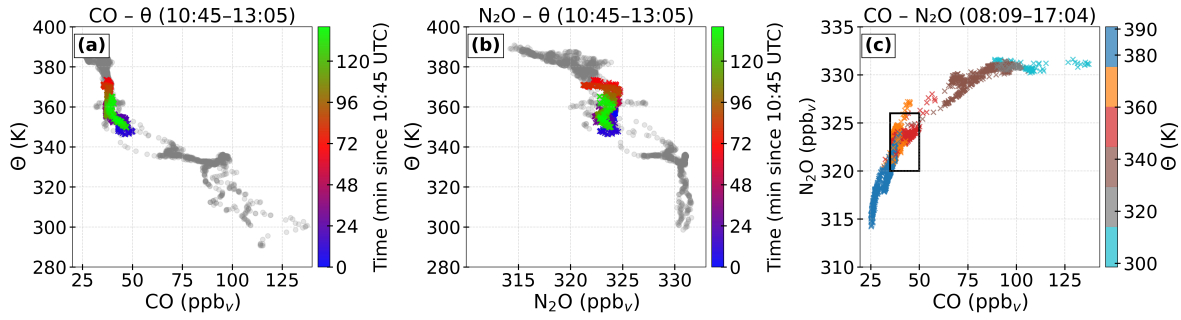


Figure 4.4: Vertical profile of (a) CO and (b) N_2O and tracer-tracer correlation of the mixing ratios of (c) N_2O and CO that were measured during WISE RF05.

alternation between low Θ (large CO/ N_2O) and high Θ (low CO or N_2O), indicating the impact of small-scale wave patterns on tracer abundance. The negative deviations from tropospheric background mixing ratios in N_2O can only be explained by irreversible mixing with stratospheric air masses. The further thorough investigation of this local mixing event is presented in next part.

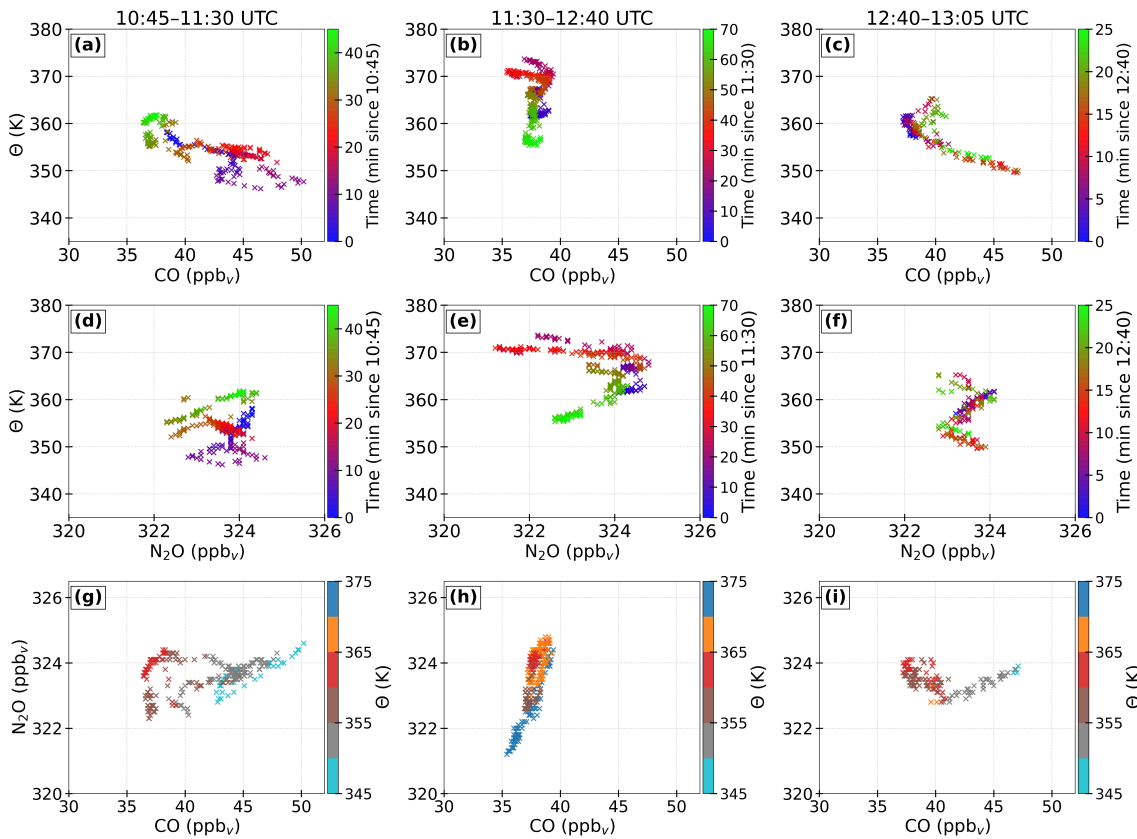


Figure 4.5: Vertical profile of CO (a–c) and N_2O (d–f), and tracer-tracer correlation of the mixing ratios of N_2O and CO that were measured during WISE RF05 for time periods between 10:45–11:30 UTC (left), 11:30–12:40 UTC (middle) and 12:40–13:05 UTC (right), color-coded with potential temperature.

Tracer-tracer correlations of CO and N_2O measurements along the WISE RF05 are shown as a function of time (based on selected time windows) and potential temperature (Figure 4.5), focusing on time windows between 10:45 and 13:05 UTC that are identified in section 4.2.3 above, which signifies potential turbulence and mixing. Under background conditions CO, N_2O and Θ typically exhibit monotonic relation such that mixing ratios of CO and N_2O should decrease as an air mass becomes more strato-

spheric, whereas potential temperature should simultaneously increase (see also section 2.5.3). As such we expect to have the fixed tri-variate correlation between these quantities in the lower stratosphere. If, however, the CO and N₂O values vary significantly along the isentropic surface, this is a clear indication of quasi-isentropic mixing of tracers in the LS.

For further inspection, the correlation is separated into three time periods: (i) 10:45–11:30 UTC, (ii) 11:30–12:40 UTC and (iii) 12:40–13:05 UTC. If turbulence occurred in the region of strong tracer gradients at the region where measurements were taken, it should have affected the composition of trace gases. Both CO and N₂O exhibit vertical gradients in the LS (Figure 4.5a-f). HALO was initially at the LS during the selected period with low values of CO and N₂O. This location is particularly sensitive to mixing because small perturbations can significantly alter tracer abundances. The vertical profile of tracers reveal that air masses with low N₂O and CO are of stratospheric origin, while higher values indicate tropospheric influence. The gradual transition between these regimes, occurring between potential temperatures of 350–360 K, marks the mixing zone.

Further CO–N₂O correlation on the selected time periods results in some interesting findings. The first shorter time period exhibits two branches which are interconnected with a mixing line (at around N₂O ~ 324 ppbv, Θ ~ 359 K) (Figure 4.5g). In the second time period, one branch is evident which shows rather Θ values spread over the entire branch, meaning that no fixed relation between Θ and the tracer is evident although CO and N₂O show a compact positive correlation (Figure 4.5h). In the third time period almost all data points reside in a very small domain in the correlation space with potential temperature values varying strongly over this domain (Figure 4.5i). All of these findings are potential indications that these air masses have been subject to a process which breaks the relation between CO, N₂O, and Θ ; one potential process which can lead these correlations is mixing. It is interesting to note that the first and third time periods show indications of recent mixing, where the ERA5 analysis shows indications of recent turbulence occurrences (Figure 4.3b). Meanwhile, the second time period appears closer to the equilibrated background CO–N₂O relation. This could indicate that the first and third event have been subject to more local recent mixing, while the air mass in between has been mixed some time ago.

Power spectral density

Further analyses of the occurrence of turbulence is performed by means of power spectral densities (PSD) of basic state parameters which in general allows to investigate how much energy is present in particular spatial scale, and indicates the type of turbulence that affects the considered domain. In general, a line that follows slope of -3 indicate the geostrophic turbulence, whereas a slope linen of -5/3 indicate signs of mesoscale turbulence. The latter often characterizes three-dimensional isotropic turbulence, that is the dynamic processes on or below the mesoscale affecting the flow.

Figure 4.6 shows PSDs of w and Θ (a, b) as well as N₂O and CO (c, d). The w shows the slope of -3 for the smaller wavelengths i.e., longer frequency (<0.8 Hz), in agreement with Lachnitt et al. (2023), for wavelength <10 km. For higher frequencies (shorter wavelengths), the increase of PSD 0.5 Hz for w would be consistent with the potential source of turbulent energy. Overall, the w and Θ spectra follows the slope close to $k = -5/3$, can be related to three dimensional isotropic turbulence. This is an indication of dynamic processes on or below the mesoscale affect the flow. Whereas N₂O and CO also has overall slope of -5/3 for intermediate frequencies i.e., for smaller wavelengths. In N₂O spectra,

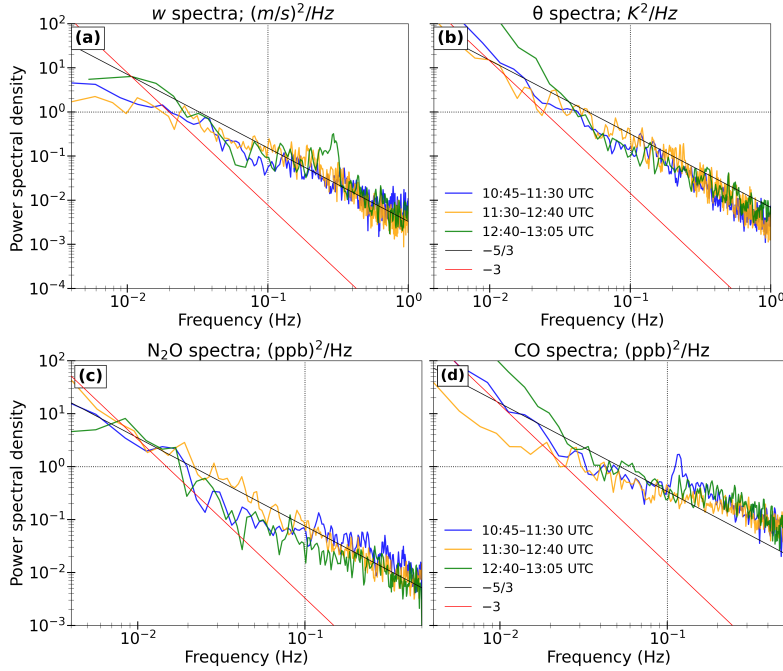


Figure 4.6: Power spectral density of (a, b) w and Θ from BAHAMAS and (c, d) of N_2O and CO measured during WISE RF05 zoom in for the shaded yellow regions of Figure 4.3. Black solid lines are introduced for better comparability. The black and red reference lines have slopes of $5/3$ and 3 .

the small transition between slopes observed around 10^{-2} Hz (follow the green and blue lines), where the slopes of w indicates turbulent energy source, and here, the N_2O hints the turbulent behavior of small-scales, e.g., those related to GWs, might be substantial to explain the dynamics in the LS.

4.2.5 Observation based estimate of GW related mixing

Are these mixing processes influenced by the small-scale GWs in the LS? The above results do not permit a definitive answer to that question, but they do permit an exploration of whether they may be important or whether they are negligible. To investigate their potential impact on the turbulent mixing, we further attempted to provide an observational evidence on whether we see GWs signatures from measurements. The close spacings of the measurements shown in Figure 4.3 allows the detailed mesoscale structures of the jet/front to be elucidated, including low Ri , and possible coherent phase structures of GWs (Figure 4.7). Nonetheless, the resolution of in situ measurements is too large to properly sample waves with horizontal wavelengths of ~ 100 km in hourly model output data. However, the height of flight is enough to identify coherent phase lines and/or mixing lines in the LS.

Figure 4.7 show a comparison of in situ measured atmospheric state parameters, i.e. the horizontal wind components u , v (a) and their perturbation products u' and v' (b). The large scale wind and temperature features are resolved in the model, like the pronounced meridional wind peak of the jet streak that is crossed several times. Panel (b) displays the perturbation components (u' and v'), capture higher-frequency variations, which are indicative of small-scale dynamical processes such as GW activity, shear instabilities, or turbulence. Intervals with enhanced perturbation amplitudes correspond to episodes of intensified wind variability, which are of particular interest for diagnosing GW–shear interactions and their potential role in mixing. The combination of background and perturbation wind time series provides a framework for linking the observed small-scale variability to larger-scale flow

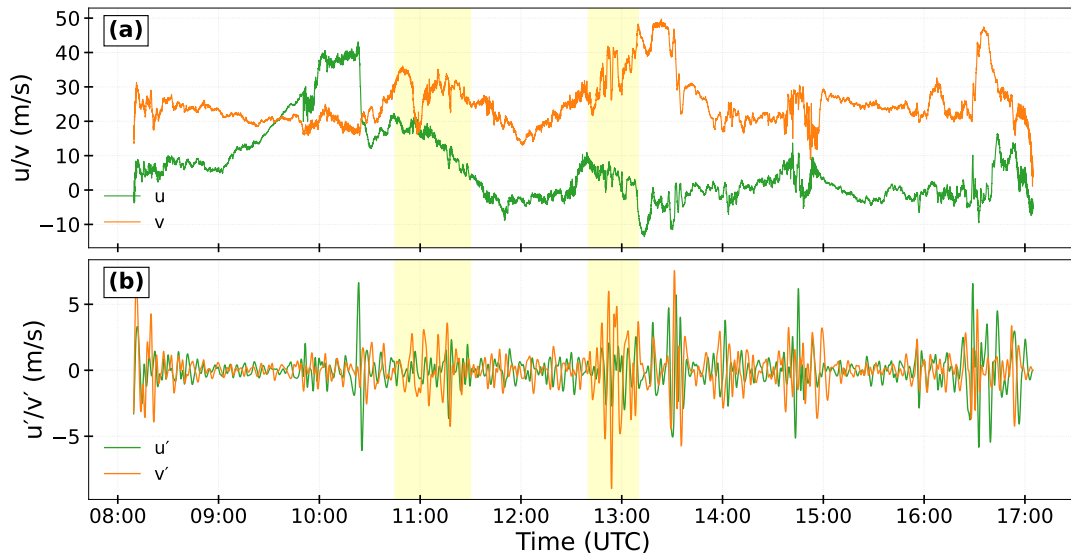


Figure 4.7: Time series of (a) zonal (u , ms^{-1} ; green) and meridional (v , ms^{-1} ; orange) wind component from HALO for WISE RF05, whereas panel (b) shows perturbation of u and v obtained from Butterworth filter for the whole flight period. The shaded yellow regions highlight period of interest same as Figure 4.3.

conditions, thereby enabling an assessment of the dynamical environment in which wave–mean flow interactions occur. In the following, we look whether there are GW signatures during RF05 observations.

Although, hodographs can be drawn from vertical profile at a time, given that limited altitude level data, in our analysis a single hodograph is drawn using profiles at multiple times at one flight altitude, as in (Gomes et al., 2025). Figure 4.8 shows example hodographs for the period and region of interest where the mixing has been observed. Note that, as discussed in section 2.5.2, to isolate wind perturbations associated with GWs from the background wind, horizontal wind components (u , v) along the flight track were bandpass filtered using a 4th order Butterworth filter. The filter was applied to remove both large-scale trends and high-frequency noise, retaining signals within a 2–10 minute period range. The resulting perturbations (u' , v') were then used to construct hodographs and assess wave properties from the in situ measurements. Due to distinct sampling frequencies and noise characteristics, different filtering methods were applied to observations and model output datasets to optimally isolate GW related perturbations.

Linear theory of GWs in a uniform background flow predicts that one vertical wavelength of an inertia GW traces an elliptical perturbation hodograph (as described in Guest et al., 2000; Plougonven et al., 2003; Yoshida et al., 2024), which rotates anticyclonically (cyclonically) for an upward (downward) propagating wave. This technique has some limitations in terms of condition with strong background wind shear and hence only suitable for a part of the wave spectrum with low-frequency, long-wave limit (Plougonven et al., 2003). This technique is applied at temporal series of u' , v' at ~ 12.5 km flight altitude. The respective time series shown in Figure 4.8a and 4.8c. Of these two selective periods, representing multiple ellipses, only few periods show clear evidence of anticyclonically rotating hodographs, i.e., the red colors in Figure 4.8b, d. A well-defined elliptical pattern is evident in Figure 4.8b, indicating the presence of upward-propagating GWs. In contrast, such a signature is less apparent in Figure 4.8d. Based on this, we focus our subsequent GW–induced shear analysis around 11:00 UTC, where the wave activity appears most pronounced. Moreover, these profiles gives a estimates of horizontal and vertical wavelength that are similar to those determined from the models. The range of horizontal wavelength

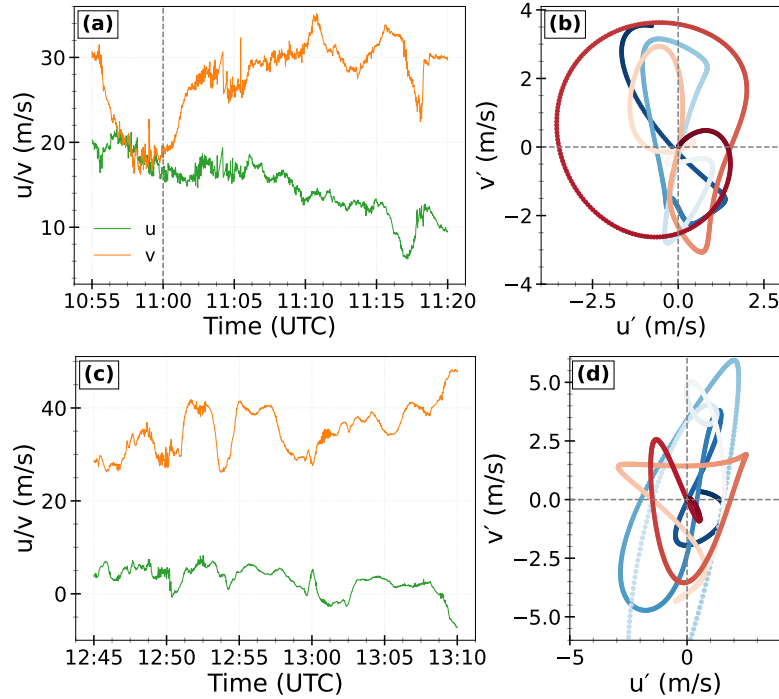


Figure 4.8: Time series (a, c) of zonal (u, ms^{-1} ; (green) and meridional (v, ms^{-1} ; orange) wind component measured during WISE RF05 zoom in for the shaded yellow regions of Figure 4.3. Perturbation hodographs for the corresponding flight period on left are shown in panel (c) and (d).

estimated is of 30-150 km. Also, the limited altitude region, as the aircraft is flown consistently at singular altitude level, means that only one or two vertical wavelengths are sampled, which adds some uncertainty to the analysis.

Nonetheless, this further motivates an in-depth analysis to understand whether GWs and GW-induced shear responsible for observed turbulence and mixing. The following section delves more into this analysis, with the central aim to determine whether the findings from the idealized cases are also evident in the real-world atmosphere using two different modeling approaches: first, the investigation based on ECMWF, the hydrostatic dynamical core, is presented in section 4.3; and second, the ICON sensitivity experiments, i.e., nonhydrostatic dynamical core, are examined in section 4.4.

4.3 Analysis of GWs and turbulence occurrence: ECMWF perspective (Part I)

4.3.1 GW appearance and shear in different datasets

From here onward, the discussion centered on the modeling perspective of the aforementioned analyses. Basically, analysis is based on model data from ECMWF's ERA5 reanalysis and IFS forecast. One of the major goal is to first analyse similarities and differences in the occurrence of GWs in these datasets. Note that the comparison is shown only for the selective flight flow region, i.e., the domain between 50°N - 72°N and 5°W - 30°W . The analysis domain is shown in Figure 4.9.

First, the comparison of the divergence between the two datasets is shown to identify location and strength of potential GW signatures in the LMS. The alternating signatures of divergence-convergence representing GWs features observed at the location of tropopause fold and/or jet streak or exit region. The dominant GWs activity over the Iceland and along the flight track can be identified by eye in the

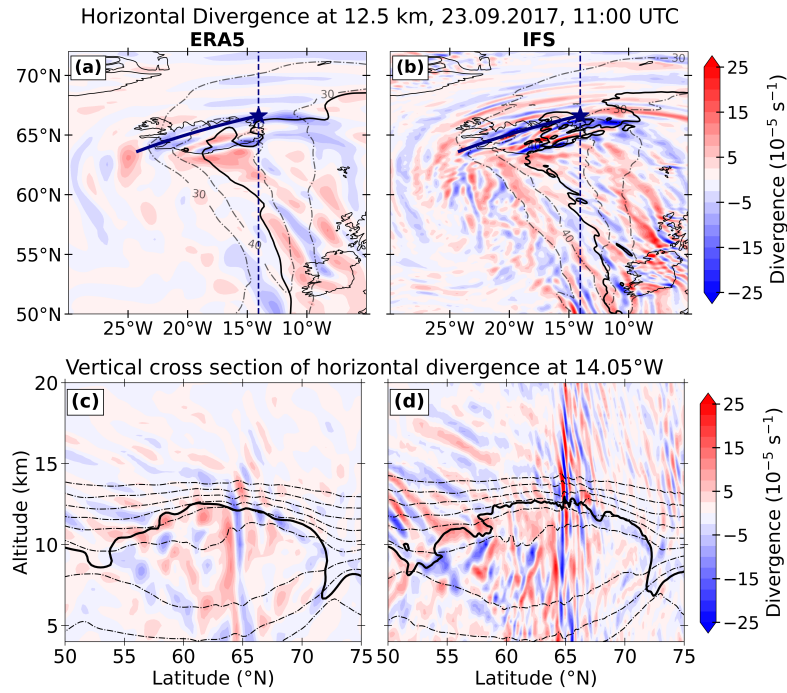


Figure 4.9: Distribution of horizontal divergence at 12.5 km altitude for (a) ERA5 and (b) IFS datasets. The dashed lines in upper panel represent corresponding horizontal wind speed for values greater than 30 ms^{-1} . The RF05 flight path from 10:55 UTC to 11:45 UTC is indicated in blue, HALO location at 11:00 UTC shown by blue star. The corresponding vertical cross sections of divergence at 14.05° W is shown in lower panel (c-d). The solid black line represent the 3.5 PVU as a dynamical tropopause whereas dashed lines in lower panel represent the potential temperature starting from 280 K (bottom) to 380 K (top) with 10 K increments.

Figures 4.9a-b between 60° N – 72° N . Moreover, IFS shows prominent, though small magnitude GWs over the region of northeastern highlands of Iceland, features that are not clearly captured in ERA5. Notably, this region lies along the flight path where signatures of mixing are observed. It appears that the nominal resolution largely controls the magnitude of the GW fluctuations in the reanalyses. The corresponding vertical cross sections at 14.05° W representing the approximate flight location at 11:00 UTC (marked by the dashed line) are shown in Figure 4.9c, d.

Note again that, following a commonly used PV based tropopause definition in the literature, the 3.5 PVU isosurface is used as the extratropical dynamical tropopause. In Figure 4.9c–d, the thick solid line indicates the dynamical tropopause altitude, however, the GW activity influence this. This means that the undulations in these tropopause field are identified as the signatures of upward propagating GWs. This waves further propagate vertically with large amplitudes through the LS. In ERA5, the observed packet propagates only a short horizontal distance, while spanning vertically up to $\sim 17.5 \text{ km}$ in altitude (Figure 4.9c), suggesting a low ground-based phase speed and a narrower vertical wavelength. IFS, in fact, resolves finer horizontal structures and larger amplitudes with a notably shorter vertical wavelength of $\sim 2\text{--}3 \text{ km}$ (Figure 4.9d). Moreover, the horizontal wavelength is visibly shorter in the IFS than that of ERA5. Overall, much more fine-scale signals are observed in IFS and rather lower in ERA5, indicates that the GWs characteristics, especially horizontal details are strongly influenced by the spatial resolution. Other minor differences include the GW signatures around the tropopause and in the PV field. Of interest is the fact that ERA5 despite its much lower horizontal resolution, is able to capture the appearance of GWs in the LMS. The large amplitude wave signatures pointing towards the strong

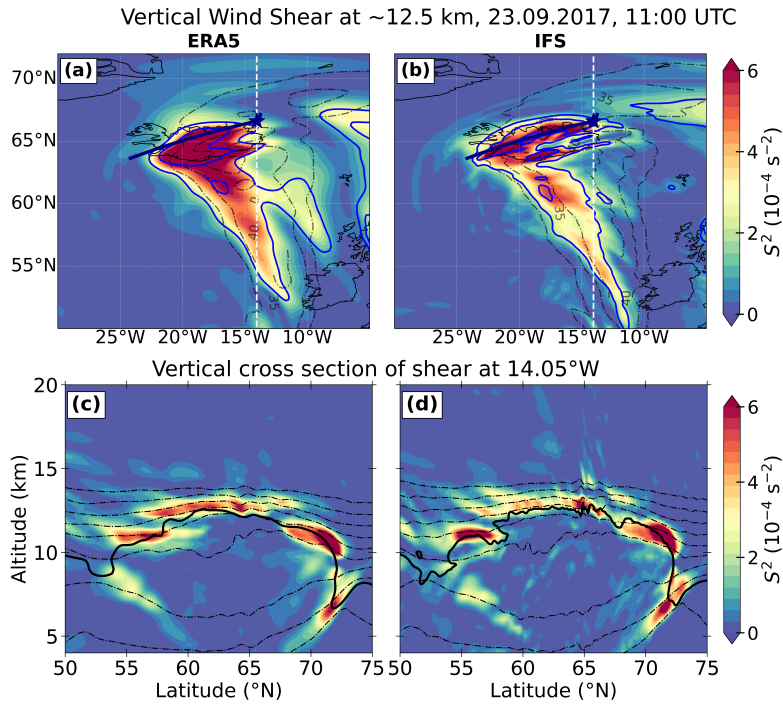


Figure 4.10: Distribution of vertical wind shear at 12.5 km altitude for (a) ERA5 and (b) IFS. The dashed black lines in upper panel presents the horizontal wind speed for values greater than 30 m s^{-1} , 3.5 PVU isoline in magenta and solid lines represent the $Ri < 1$ (black) and $Ri = 1.25$ (grey) at 12.5 km altitude. The star marker indicates the position of flight at 11:00 UTC. The corresponding vertical cross sections of vertical shear at 14.05° W is shown in lower panel (c-d). The solid line in lower panel represents the 3.5 PVU as a dynamical tropopause whereas dashed lines represents the potential temperature starting from 280 K (bottom) to 380 K (top) with 10 K increments.

upward motions across the tropopause, which could of interest to further understand the vertical shear in this region. In the subsequent section, the discussion shift towards the shear occurrence in the vicinity of GWs activity.

The distribution of vertical shear in Figure 4.10a-b indicate significant vertical shear north of 60° N , in the vicinity of GW activity identified in the previous paragraph, i.e., around 65° N and 15° W . As discussed in the paragraph above, IFS shows much more signs of GW activity across the tropopause region and in the LMS, being the interesting region to further study the GWs role to shear enhancement. Moreover, the jet location in Figure 4.10a-b (grey dashed) and 3.5 PVU dynamical tropopause in Figure 4.10c-d (black dashed) featuring the tropopause fold, holds important piece of information about the jet disturbances being one of the source region of high shear abundance in this region.

Furthermore, the vertical distribution of shear in ERA5 (Figure 4.10c) shows the maximum shear abundance in the ridge and along the tropopause fold with maximum values reaching up to $6 \times 10^{-4} \text{ s}^{-2}$. The maxima in the ridge (around 62° N) is in the proximity of GWs which in turn could affect the shear values there. These shear maxima is observed near the regions of GWs likely above the lifted air masses reaching up to the tropopause and beyond in the ERA5. While the IFS shows very similar pattern of S^2 with maxima having similar values as ERA5, the spatial scale of maxima is smaller around the ridge.

Particularly, in the UTLS, the jet-stream on larger scales and GW on smaller scales contribute significantly to the generation of shear. In principle, all two shows countable though not significant, colocation of shear with GW patterns and also at the tropopause fold region (Figure 4.10c-d) and thus the shear

location related to the phase of GWs modes remain consistent among all datasets. Overall, GWs that propagate upwards across tropopause indicate the spatiotemporal co-occurrence of GWs and vertical wind shear at different locations in the extratropics.

However, this required further investigation to understand whether the small-scale and vertically propagating GWs observed in ERA5 are of relevance to the shear generation across the tropopause. As discussed in Chapter 3, one possible explanation for this could be that vertically propagating, large amplitude, high vertical (less horizontal) wavelength GWs could lead to enhanced upward motion and hence to this higher shear just above the tropopause in the ExUTLS. This hint that GWs may contribute (or influenced) partially to the vertical shear generation in the LS. On the other hand, the maximum shear in locations other than GW activity, likely generated from the large-scale components including the jet stream. This further motivates a deeper look at the significance of small-scale GWs to high wind shear, and subsequently to the potential turbulence occurrence.

4.3.2 Occurrence of potential turbulence in the LMS

The co-location of shear and GWs identified earlier hint that GW-induced shear may lead to a considerable dynamic instability and influence the turbulent mixing the most. This allow the in-depth investigation of small-scale behavior of GWs in the LMS. Here, we discuss the potential of dynamic instability associated with GWs in the LMS, as well as the relation between the occurrences of GWs and shear perturbations in terms of 2D histograms.

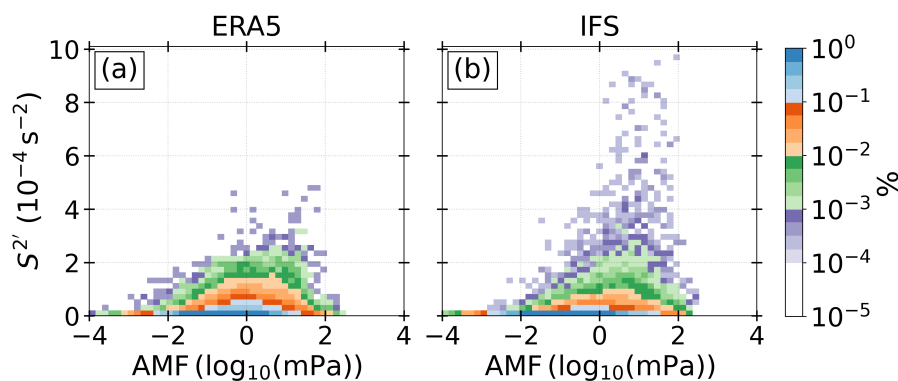


Figure 4.11: Relative occurrence frequency distribution of AMF– S' shear perturbations pair in the LMS for $0 \leq Ri \leq 1$ for (a) ERA5 and (b) IFS. Normalized counts of PDFs distribution is shown. Logarithmic occurrence frequency color scale is applied.

Based on the findings of Chapter 3, if smaller scales play a major role, a positive correlation is expected between absolute small-scale momentum flux and shear perturbations in terms of turbulence occurrence in the LMS. Qualitatively, there is a positive correlation between shear abundances and GWs in the LMS in all two datasets (Figure 4.11). This result supports previous analysis based on idealistic studies in terms of GWs related to the shear and subsequent turbulence (Umbarkar and Kunkel, 2025). Here, we expect ERA5 reanalysis to resolve the vertical shear in the UTLS similar to the operational IFS data (Kaluza et al., 2019, 2021).

As discussed previously in section 4.3.1, ERA5 represents the resolved fine-scale structures of the GWs, and as such shows the positive correlation between AMF and shear fluctuations (Figure 4.11). However, high resolution IFS shows more pronounced S' and AMF likely due to finer resolution as

well as at least well represented GWs in the UTLS than in ERA5. ERA5 rather shows less occurrences of maximum shear than IFS, could be due to its coarser horizontal resolution, which might lead to the limited representation of (partially resolved) GW spectrum in the UTLS.

Combining all these information pinpoints the crucial role of GW-induced shear to the potential turbulence occurrence, and subsequently representing the important role of GWs to transporting the momentum across the tropopause.

4.3.3 GWs as a probable cause for CAT

The connection between GWs and CAT is further investigated with specific focus on GW-induced shear that lead to potential dynamic instability. One previously suggested impact from inertial instability is that any associated inertia GWs could lead to CAT when these waves breaks (Knox, 1997). Previously, Thompson and Schultz (2021) showed the emission of inertia GWs, following the release of inertial instability, instigate light–moderate occurrences of CAT around the unstable region using idealized model simulations. This case study widen our analysis by looking at both the broader upstream flow patterns and the small-scale disturbances, mainly GWs, that contribute to the development of dynamical instability and potentially to the CAT in the LS region.

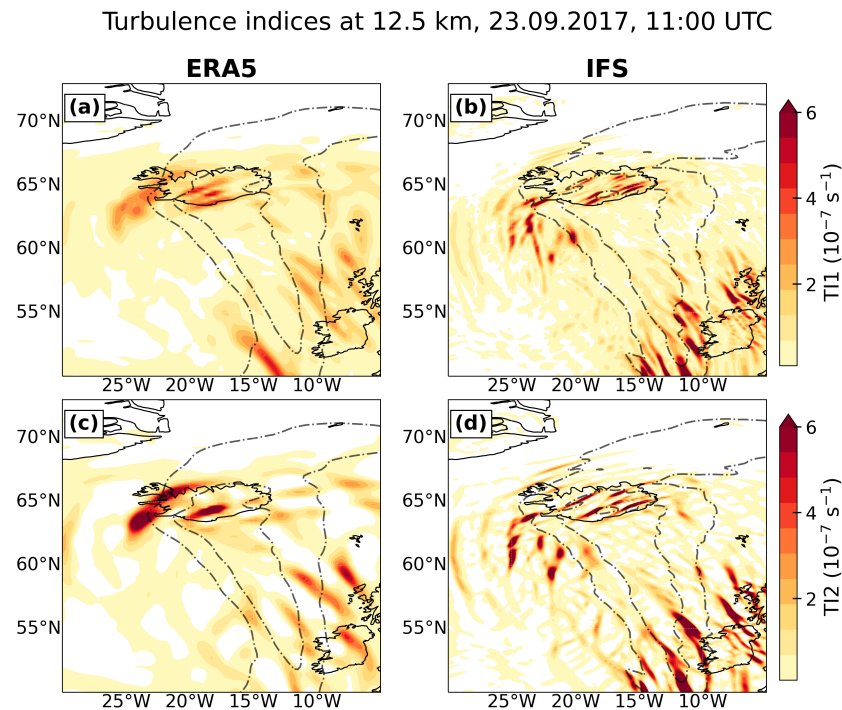


Figure 4.12: Distribution of turbulent indices TI1 (upper panel) and TI2 (lower panel) at 12.5 km altitude for ERA5 (a, c) and IFS (b, d). The dashed black lines indicate horizontal wind speeds exceeding 30 m s^{-1} .

The turbulence doesn't develop as a single continuous area, but in sporadic pockets of light to moderate intensity that persists for few minutes around the periphery of unstable region (Sharman et al., 2006, see also Figure 4.12). While ERA5 data have an hourly resolution and may limit the representation of such short lived events, the observed structure suggest the conditions conducive to their occurrence, albeit with reduced intensity. As the GWs propagate upward through the tropopause, the wave perturbations significantly modify the local Ri . Subsequently along the phase lines of GWs there appeared bands of increased TI1 and TI2 (Figure 4.12). Also, it is noted that some turbulence occurred in the regions of upper level divergence (Figures 4.9). In these case, the enhanced turbulence, especially the CAT, was

generated mostly due to the small-scale GWs and it is proposed that such mechanism contributed to the turbulence encountered during the flight.

Based on the analysis of TI1, as a proxy for CAT, from ERA5 and IFS zonal and meridional wind perturbations, we find several regions where CAT develops simultaneously across the tropopause. Given that the current study focus on the occurrence frequency of CAT in the UTLS likely near the upper level jet stream, we choose the 95th percentile value of the total occurrences as the thresholds of each CAT index for light-moderate intensity level followed by Lee et al. (2019, 2022). Figure 4.13 illustrates the frequency distribution of CAT indices over the LMS. The 95th percentile is computed from the PDF distribution of CAT index values across all datasets under LMS filtering constraints. The resulting TI1 threshold values for ERA5 and IFS are $1.0 \times 10^{-7} \text{ s}^{-1}$ and $2.01 \times 10^{-7} \text{ s}^{-1}$, respectively. There are only minor difference in the threshold observed across datasets. In addition to this, the additional GW related turbulent index TI2, gained from the inclusion of convergent flow, applies the same threshold selection criterion as TI1, where the resulting thresholds are $1.0 \times 10^{-7} \text{ s}^{-1}$ and $2.28 \times 10^{-7} \text{ s}^{-1}$ for ERA5 and IFS, respectively.

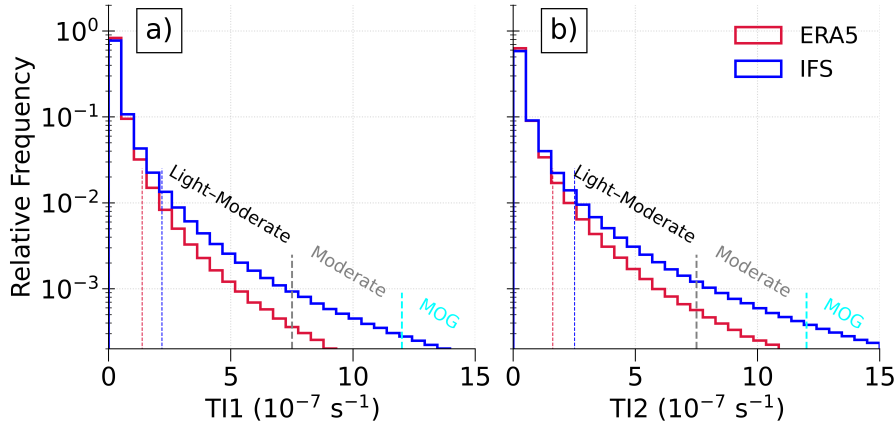


Figure 4.13: Relative occurrence frequency distribution of (a) TI1 and (b) TI2 for ERA5 and IFS in the LMS. Corresponding to histogram, colored dashed lines indicate threshold retrieved as the 95th percentile over the LMS domain distribution that is considered as threshold for light moderate category. Grey and aqua lines represent the threshold for moderate ($7.5\text{--}12 \times 10^{-7} \text{ s}^{-1}$) and moderate to greater (MOG; $>12 \times 10^{-7} \text{ s}^{-1}$) intensity CAT, respectively.

Collating all turbulence occurrence across the datasets, as seen in Figure 4.13a, most of the occurrences fall into light–moderate category, with some occurrences of moderate intensity ($7.5\text{--}12 \times 10^{-7} \text{ s}^{-1}$) are also found which are more pronounced in the IFS, but virtually absent in ERA5. The calculation of TI2 index includes the convergence term and thus a more direct relation to GW dynamics in order to understand the direct relationship between GWs and CAT. Nonetheless, the MOG intensity ($>12 \times 10^{-7} \text{ s}^{-1}$) CAT in TI1 with slightly less occurrences are found to be strong in the positive tail of the TI2 (Figure 4.13b). Furthermore, the more pronounced moderate-level CAT with TI2 (Figure 4.13b), suggests a probable contribution of GWs to CAT development. One possible explanation for this could be that GWs over Iceland observed in the IFS leading to the maximum shear perturbations as well as TI1 and TI2 which could further induces strong potential for instability, and ultimately causes development of CAT in the subsequent region.

Figure 4.14 show joint PDFs of TI1-AMF (upper panel) and TI2-AMF (lower panel) pairs in the LMS domain. As discussed above, if the subgrid or small-scales plays a major role, the positive relation

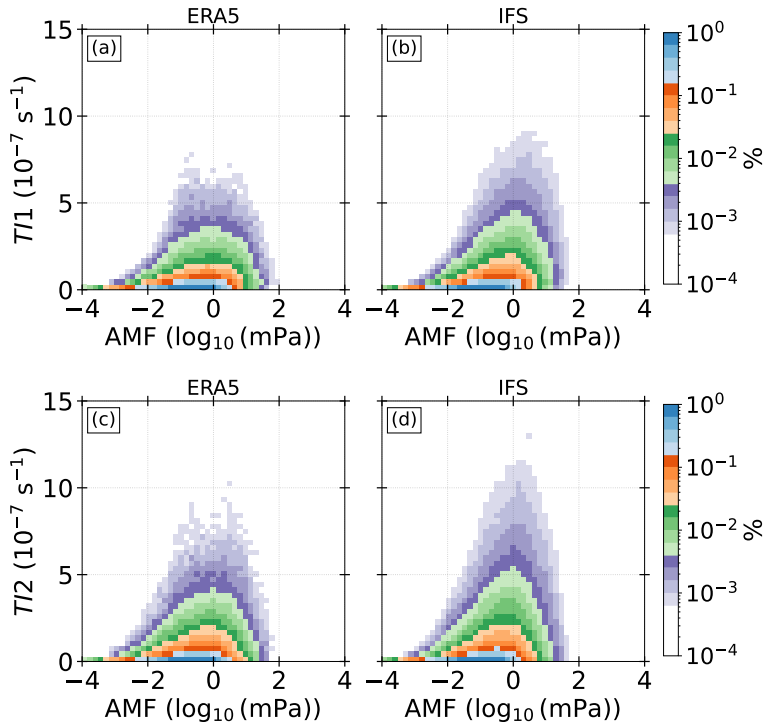


Figure 4.14: Relative occurrence frequency distribution of (a-b) TI1 and (c-d) TI2 and AMF pair in the LMS for ERA5 and IFS datasets. Normalized occurrence frequencies of the joint PDFs are shown in a logarithmic color scale.

between AMF and turbulent indices is expected. In-depth investigation of this relation in the LMS depict the positive correlation between occurrence frequencies of these two quantities. There are smaller values for TI1/TI2 in ERA5. In contrast, IFS shows slightly higher abundance of TI1 and AMF above the threshold, indicating occurrence of light to moderate level CAT. When looking at the TI2, while ERA5 shows slightly less occurrence in this case, its maxima reaches around MOG intensity in IFS (Figure 4.14c, d). Therefore, based on the relation between AMF and small-scale shear enhancement as discussed in the previous section, it is now confirm that LMS is susceptible to CAT caused by GW-induced shear as well. Overall, the pronounced co-occurrences of GW momentum flux and turbulent indices at smaller scale indicate that GWs are of relevance to the CAT development in the LMS.

Altogether, these findings support the hypothesis that subgrid or small-scale GWs contribute substantially to the enhanced shear formation, the development of high intensity CAT, and hence, consequently could contribute to shaping the ExTL dynamics.

In conclusion, the results obtained in Chapter 3 from the idealized cases are also evident in the "real" world in terms of modeling perspectives. As of now, the discussion in this chapter centered around the role of GWs in the occurrence of strong shear in the LMS, and whether (clear-air) turbulence occur in the region of the GW-induced shear across available datasets from ECMWF, that uses hydrostatic dynamical core in combination with semi-implicit and semi-Lagrangian numerical schemes. It is yet to investigate whether this findings are also true in the real world that uses non-hydrostatic dynamical core. Based on this, the subsequent section discusses the analysis performed using ICON simulations for this case from Schwenk and Miltenberger (2024) with different physics package as well as in three different nominal resolutions.

4.4 Analysis of GWs and turbulence occurrence: ICON perspective (Part II)

4.4.1 Occurrence of GW and shear in the lower stratosphere

The dynamical situation previously examined using ECMWF data is further evaluated in this section using ICON simulations with varying horizontal resolutions and physics parameterization schemes. More details about the simulations and physical parametrization schemes used for this simulations are given in Table 2.2.

Figure 4.15 presents the distribution of horizontal divergence at 12.5 km altitude. The pronounced GWs activity over the northeastern Icelandic highlands is evident across all domains (Figures 4.15a–c), with enhanced GW signatures between 60° N– 72° N, particularly over and to the east of Iceland along the flight track. The ICON simulation with $\Delta x \approx 3.3$ km captures GW activity across the analysis domain with moderate wave activity in the northwestern sector (Figure 4.15c), albeit with large amplitude small-scale wave features. It should however noted that, the shallow convection schemes used for the later two experiments, i.e., for $\Delta x \approx 6.5$ and $\Delta x \approx 3.3$, could resolve more finer scale signatures upon accounting for convective processes, and hence also being responsible for the convectively generated GWs.

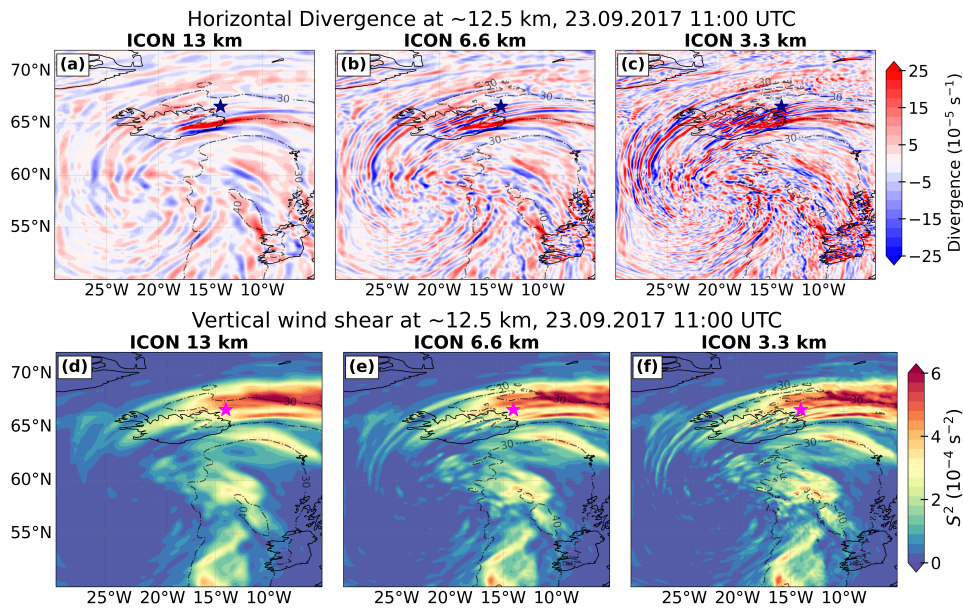


Figure 4.15: Distribution of horizontal divergence (upper panel) and vertical wind shear (lower panel) at 12.5 km altitude for ICON 13 km, 6.5 km and 3.3 km resolution nested simulations overlaid with flight location at 11:00 UTC shown by star. The dashed line represent corresponding horizontal wind speed for values greater than 30 ms^{-1} .

The corresponding horizontal distribution of vertical shear (Figure 4.15d–f), shows higher shear abundance in the vicinity of GW activity identified earlier at around 65° N and 15° W. Here again, the $\Delta x \approx 3.3$ km resolution reveals high shear values and is collocated with pronounced GW activity across the tropopause region and in the lower stratosphere. It should however noted that, enhanced GW activity in higher resolution experiments likely originated from convective sources, and thereby could lead to the higher shear abundance across the tropopause. Moreover, these overall behavior indicate that both horizontal and temporal resolution substantially influence the magnitude and representation of GW fluctuations in the forecasts, consistent with the findings presented in section 4.3.

4.4.2 Diagnostics of potential turbulence and CAT in the LMS

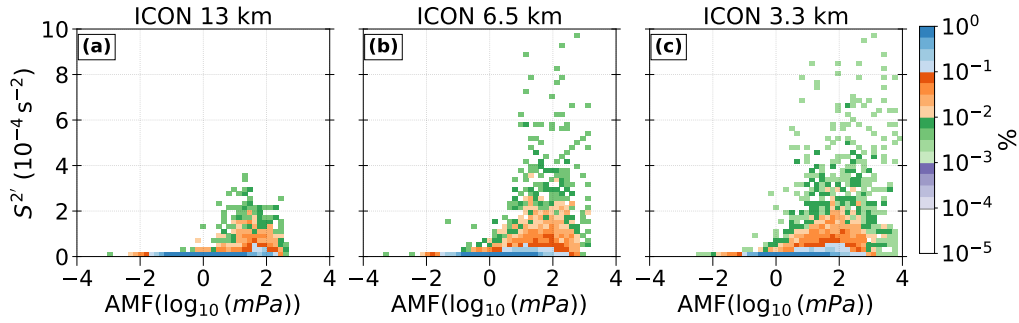


Figure 4.16: Relative occurrence frequency distribution of absolute momentum flux due to GWs-vertical shear perturbations pair in the LMS for $0 \leq Ri \leq 1$ for ICON 13 km, 6.5 km and 3.3 km resolution nested simulations at 11:00 UTC. Normalized counts of PDFs distribution is shown. Logarithmic occurrence frequency color scale is applied.

To further investigate the previously identified close relationship between momentum flux and shear perturbations in the context of turbulence occurrence within the LMS, both AMF and S^2 quantities are masked for the regions in the LMS where potential turbulence $0 \leq Ri \leq 1$ could occur. A closer examination reveals that enhanced shear occurrences are predominantly associated with AMF values on the order of 10^1 – 10^3 , i.e., corresponding to a range from a few to a few hundreds of millipascals (see Figure 4.16). Also, from the experiment with $\Delta x \approx 3.3$ km, it is clear that the frequency of co-occurrence of GWs and enhanced shear increases with finer horizontal resolution (Figure 4.16c). Nonetheless, the positive relation is evident across all simulations. As anticipated, this behavior is consistent with the results presented in section 4.3 and aligns with findings from idealized studies demonstrating that GW-induced perturbations plays a role in enhancement of shear, and thereby preconditioning the flow for shear-driven instabilities and subsequent turbulence generation.

To this point, the results obtained from the vertical shear and absolute GW momentum flux gives potential for turbulence occurrence. In particular, it could be possible that the identified shear and small-scale structures are primarily associated with the synoptic-scale flow rather than directly linked to (clear-air) turbulence. While the preceding interpretation relies on the previous studies, this issue can be addressed more directly by examining the relationship between CAT indices at smaller scales and GW momentum fluxes.

For this reason, we here shortly discuss the spatiotemporal resolution and processes parametrization effects on the probable occurrences of CAT. The wave perturbations significantly modify the background flow as GWs propagate upward through the tropopause. Following that, along the phase lines of GWs, there are apparent bands of enhanced TI1 (Figure 4.17a–c) and TI2 (Figure 4.17d–f), that are seen in the region of GW packets at 12.5 km altitude in Figure 4.15. This bands are more prominent in $\Delta x \approx 3.3$ km (Figure 4.17c, f) followed by $\Delta x \approx 6.5$ km (Figure 4.17b, e). That is to say, the higher resolution ICON simulations with nesting revealed that localized volumes of enhanced resolved and subgrid, small-scale turbulence formed in the bands of high TI1 and TI2. The more resolved small-scale structures, i.e., the appearance of such patches could be attributed to a strong correlation between the AMF (i.e., the zonal wind and vertical velocity perturbations (u' , w') and small-scale shear during turbulent episodes discussed above. This relation is further explored in the following paragraph.

The relative occurrence frequency distribution of TI1 (a) and TI2 (b) for three ICON nested do-

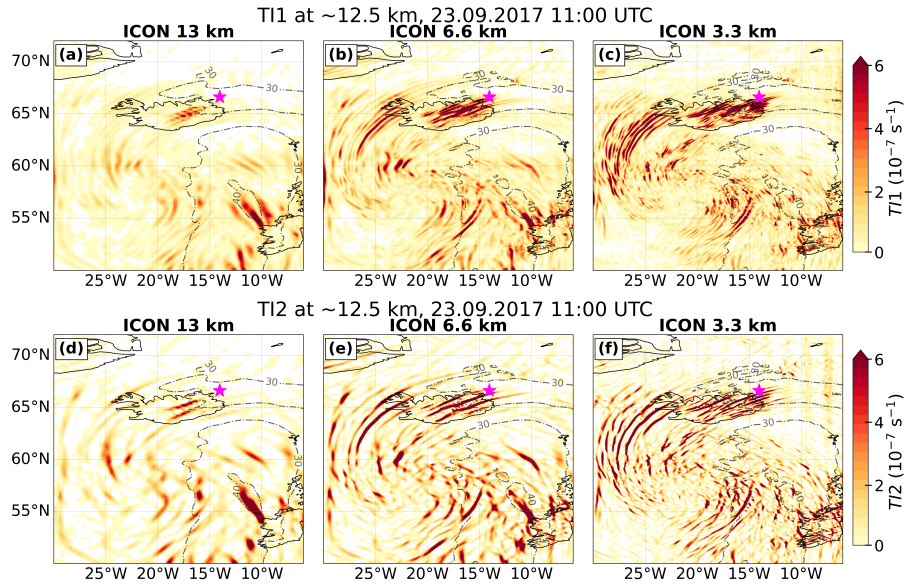


Figure 4.17: Distribution of turbulence indices T11 (upper panel) and T12 (lower panel) at 12.5 km altitude for ICON 13 km, 6.5 km and 3.3 km resolution nested simulations. The dashed line represent corresponding horizontal wind speed for values greater than 30 ms⁻¹.

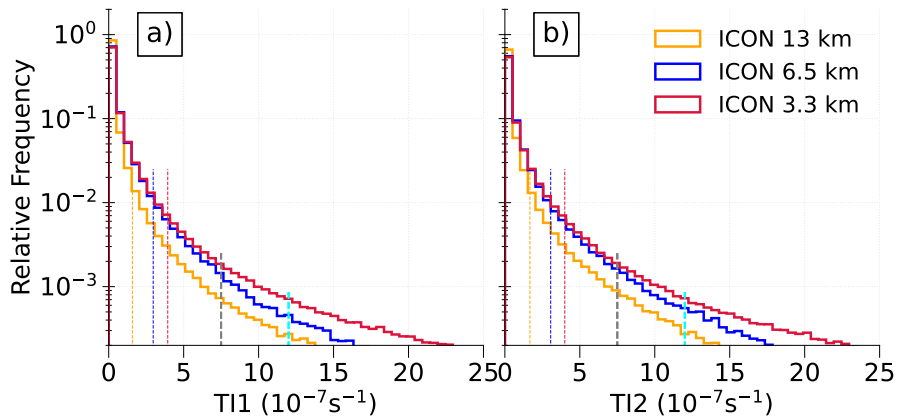


Figure 4.18: Relative occurrence frequency distribution of (a) T11 and (b) T12 for three ICON nested domains in the LMS. Corresponding to histogram, colored dashed lines indicate threshold retrieved as the 95th percentile over the LMS domain distribution that is considered as threshold for light moderate category. Grey and aqua lines represent the threshold for moderate ($7.5-12 \times 10^{-7} \text{ s}^{-1}$) and moderate to greater ($>12 \times 10^{-7} \text{ s}^{-1}$) intensity CAT, respectively.

mains in the LMS is shown in Figure 4.18. The threshold criterion is based on 95th percentile for each case in the LMS and is same as in section 4.3. Based on this, the resulting TI1 threshold values for simulations with $\Delta x \approx 13$ km, $\Delta x \approx 6.5$ km, and $\Delta x \approx 3.3$ km are $1.5 \times 10^{-7} \text{ s}^{-1}$, $3.21 \times 10^{-7} \text{ s}^{-1}$, and $4.03 \times 10^{-7} \text{ s}^{-1}$, respectively; and for TI2, the resultant threshold values are $1.72 \times 10^{-7} \text{ s}^{-1}$, $3.75 \times 10^{-7} \text{ s}^{-1}$, and $4.31 \times 10^{-7} \text{ s}^{-1}$, respectively. For the comparison across dataset and following the previous studies (e.g., Thompson and Schultz, 2021), the threshold values are kept common for moderate ($7.5\text{--}12 \times 10^{-7} \text{ s}^{-1}$) and MOG ($>12 \times 10^{-7} \text{ s}^{-1}$) categories. Figure 4.18 shows the threshold values for both TI1 and TI2 increases with finer resolution.

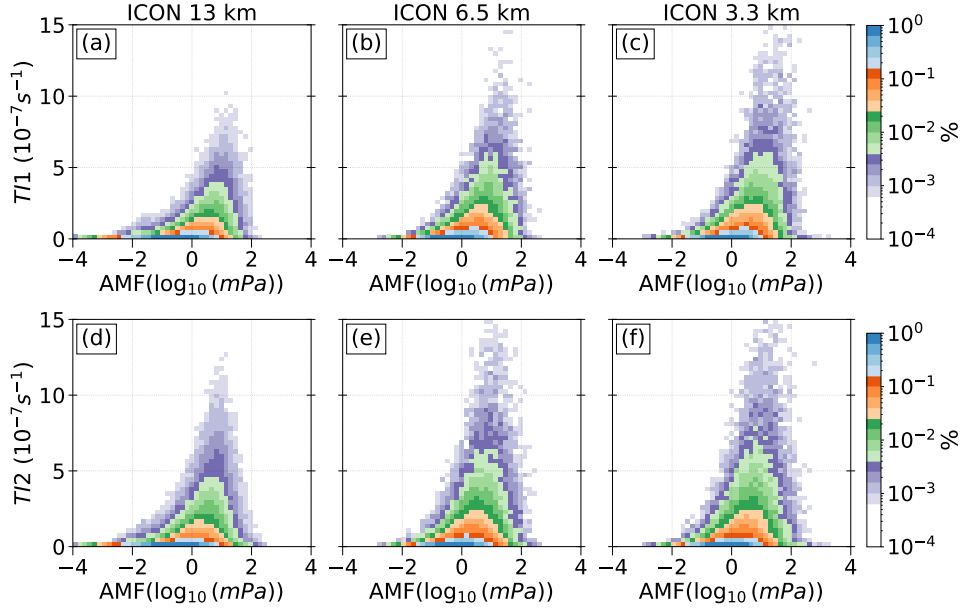


Figure 4.19: Frequency (%) distribution of absolute momentum flux–turbulent indices TI1 (a-c), TI2 (d-f) in pairs over the LMS for ICON 13 km, 6.5 km and 3.3 km resolution nested simulations at 11:00 UTC. Normalized counts of PDFs distribution is shown. Logarithmic occurrence frequency color scale is applied.

From Figure 4.18, it is observed that the occurrence frequency of MOG intensity CAT increases with finer spatiotemporal resolution. This is also evident in the joint histograms of TI1 – AMF and TI2 – AMF pairs in the LMS domain (Figure 4.19), also across the various sensitivity experiments. One possible explanation for this could be the strong GW activity that is originated from the convective source in higher resolution experiments, being responsible for the amplification of shear, highlighting the fact that vertically propagating GWs, and mainly GW-induced shear, could play a significant role not only in the generation of CAT, but also in its dynamics and evolution. This suggests that improved representation of GW-like small-scale structures at higher resolution could give more accurate prediction of such turbulence events.

Combining the information gain from the analysis based on both hydrostatic and non-hydrostatic dynamical simulations/ datasets, the overall outcomes suggests that the representation of small-scale GWs and the computation of turbulence related fields such as TI1, TI2 are quite sensitive to the spatial and temporal resolution, to the existence of high quality data (such as the ICON 3.3 km and 6.5 km data available for this study), as well as to the physical process considered therein.

4.5 Synthesis

4.5.1 Summary

Chapter 3 describe the potential impact and role of GWs to the occurrence of vertical shear above the tropopause, within the ridges of baroclinic waves that were examined using the idealized environment. The GW appear to be closely linked to generation of shear in the extratropical UTLS and the analysis of relevant physical processes revealed the importance of moist tropospheric dynamics to the enhanced GW-induced shear and turbulent mixing within the LMS. Chapter 4 aimed at a more comprehensive analysis of relation between GWs, strong vertical wind shear and potential (clear-air) turbulence occurrence during the WISE airborne measurement campaign.

To approach this, a case study based on the atmospheric state over the North Atlantic during an episode of the airborne mission WISE is presented. The airborne measurements are complemented by outputs of three gridded model data sets: ECMWF's ERA5 reanalysis and IFS forecast, and ICON forecast data, and evaluated based on various methods such as time series analysis of trace species, tracer-tracer correlations, hodographs and spectral analysis. Therefore, the following summary will refer to both the analysis based on observations and the model perspectives. The key outcomes from the analysis of GW-induced shear and mixing based on WISE case study are as follows:

- WISE RF05 observations show mixed air masses in the vicinity of vertical shear and GW occurrence. Tracer-tracer correlations of CO and N₂O mixing ratios revealed the occurrence of mixed air masses indicative of quasi-isentropic mixing. Vertical profiles of these trace gases showed that these mixed air masses resided in the LMS between 345 K and 375 K. Further analysis revealed that the mixing might be in relation to GWs and that the mixing occurred very recently in regions of persistently low Ri and enhanced vertical wind shear.
- The dynamical situation is very similarly represented in ECMWF ERA5 and IFS data, where both differ slightly mainly in the representation of mesoscale features that are mainly attributed to the varying underlying resolution. Larger differences between the ERA5 and IFS appear in the representation of vertical shear and Ri , and the turbulence indices TI1 and TI2. Despite its coarser horizontal resolution, ERA5 captures upward propagating large-amplitude GWs, which further affect the vertical gradients of the wind components and then leads to shear generation. However, it shows slightly less vertical shear occurrences than high-resolution IFS data, likely due to insufficient or partial (resolved) representation of GWs in the UTLS.
- Compared with its predecessors, ERA5 although at ~ 31 km captures a larger portion of GW spectrum providing valuable information on the spectral characteristics of GWs and is therefore suitable for long term analysis of GW-induced shear, at least over the North Atlantic.
- Using ICON, the nonhydrostatic dynamical core, the impact of model grid spacing and physical processes including convection on the GW emergence and the generation of shear is examined. Overall, ICON with grid spacing range from 13 km to 3.3 km, all captures fine scale structures of large-amplitude GWs. However, the appearance of GWs, shear and turbulence indices are highly dependent on the model grid spacing. Further investigation of GWs and shear reveals the similar positive correlation between the absolute momentum flux and shear that is observed in Chapter 3.

Taken together, these behavior can be regarded as a well resolved GW spectra with finer, km-scale resolution.

- Turbulence prone GW-induced enhanced shear highly correlates with appearance of envelopes (or packets) of small-scale GWs of ~ 100 km of wavelength in the LMS with the same characteristics. Spectral function detects downscale energy transfer from small-scale GWs that intensifies shear near ~ 340 K, thereby creating conditions conducive to the generation of (clear-air) turbulence.
- The diagnosed turbulent regions display strongly banded structures associated with GWs and GW-induced shear, parallel to the upper-level front, that is closely linked to baroclinic activity and associated tropopause variability (Kaluza et al., 2021). On one side, ERA5 and IFS indicate widespread potential for the occurrence of dynamic instability. Regarding CAT indices, ERA5 shows signatures of moderate intensity CAT in the LMS associated with strong GW activity, with IFS mimic this pattern rather with slightly higher intensity. On the other side, ICON shows slightly weaker shear perturbations but rather higher GW momentum flux at low Ri . The strong GW activity that is originated most probably from the convective source in higher resolution ICON experiments, resulting in the shear enhancement. This indicate the fact that vertically propagating GWs, and mainly GW-induced shear, could play a significant role not only in the generation of CAT, but also in its dynamics and evolution.

In summary, the present study confirms the findings from idealized world from Chapter 3 and hints at the role of GW-induced shear as a key parameter for the formation of tropopause shear layer (Kaluza et al., 2021) on the basis of observations, reanalysis and forecast data, and revealed that GW-induced shear is key mechanism for the potential occurrence of clear air turbulence in the extratropical lowermost stratosphere. As such these processes may play a crucial role in the formation and maintenance of extratropical tropopause transition layer, alongside other processes such as convective injection. Alongwith the vital role of GWs in enhancing shear, this case study also hint at ERA5 capturing both GW spectra and its contribution to shear and turbulence, making it suitable for long-term studies over the North Atlantic.

4.5.2 Implications and future research

The implications of the results presented are as follows. The baroclinic waves dominate the large-scale flow in the midlatitude, and play a crucial role in concerning the cross-tropopause diabatic exchange of air masses between the troposphere and the stratosphere. The GWs, a dynamical feature of these baroclinic life cycles are potential contributors to STE and mixing in the LMS. Also, turbulence has been identified to contribute significantly to the overall STE budget, particularly within the baroclinic waves (Spreitzer et al., 2019). However, the role of small-scale processes such as GWs contributing to mixing process has gained less attention in this context, where the exact magnitude and representation of these processes remain sensitive to model resolution and the treatment of subgrid-scale GW processes, particularly in parameterized frameworks. This continues to be an area of active research and debate in both modeling (e.g., Plougonven and Zhang, 2014; Stephan et al., 2019) and observational (e.g., Geller et al., 2013; Jewtoukoff et al., 2015) studies. This is justified by a deeper investigation of GWs in relation to the cross-isentropic mixing, strong shear and dynamic instability, as well as turbulence.

The relation between small-scale GW momentum flux has long been used as a reliable index for

GW analysis (Plougonven et al., 2003, 2017; Lachnitt et al., 2023; Umbarkar and Kunkel, 2025), hinting towards the possibility for the active role of GWs in producing shear hotspots and thereby to the subsequent mixing in the LMS. However, further research should address the seasonal and geographical variability of small-scale, GW-induced shear over the multi-latitude region.

Empirical turbulence diagnostics computed from the operational forecasts constitutes an important piece of information for the turbulence prediction, while our results emphasize the added value of perturbation-based measures at GW scales. Nevertheless, our results suggest the need for additional diagnostic methods that explicitly account for the degree of imbalance, such as direct detection of GW-induced shear-turbulence, likely proposed by Koch and Caracena (2002), given the role of GWs in preconditioning the environment for shear instability. In addition, we show that the representation of small-scale GWs and turbulence metrics is quite sensitive to the model resolution, and the availability of high-quality data, for instance, finer ICON simulations demonstrate the potential value of high-resolution datasets. This points to the importance of complementary diagnostics that specifically target small-scale processes. Future work should also involve large eddy simulations that would provide more natural setting for the turbulence investigation.

One sees that our results can also serve a way to judge parameterizations in climate models and wave forcing in high-resolution models. However, the similarities and differences we find here are certainly model, resolution and parameterization dependent. While ICON demonstrates skill in reproducing observed GW flux patterns, questions remain as to whether resolved GW amplitudes in the extratropics are fully converged across resolutions, and how parameterized sources interact with the resolved spectrum. To a certain extent, this is supported by the fact that high-resolution simulations have not yet converged when it comes to GWs in the extratropics (Polichtchouk et al., 2023; Gupta et al., 2024), and there is substantial evidence that at least for convective waves, the amplitude in high-resolution models is highly sensitive to model formulation at least in the stratosphere (Stephan et al., 2022).

5 Co-occurrence of gravity waves, vertical wind shear and turbulence over the North Atlantic

Objective

The work presented in this chapter is based on an investigation of co-occurrence and co-variability of resolved GW momentum fluxes and vertical shear in the North Atlantic region using ERA5 reanalysis data. Here, we discuss the vertical and seasonal distribution of GWs, vertical shear and GW-induced shear in the LMS, as well as turbulence indices. The aim is to examine how resolved GWs in ERA5 relate to or influence the occurrence and maintenance of the TSL.

*This chapter has been submitted to the journal *Weather and Climate dynamics* as: **Umbarkar, M., Kunkel, D., and Achatz, U., 2026: Co-occurrence of gravity waves, vertical wind shear and turbulence in the lowermost stratosphere over the North Atlantic, *Weather and Climate dynamics, Copernicus*, <https://doi.org/10.5194/egusphere-2026-413>.***

5.1 Background

GWs critically influence the atmospheric predictability from subseasonal to seasonal timescales and climate variability. Chapter 3 and 4 showed the systematic co-occurrence of strong vertical shear and GW momentum flux in close vicinity of local dynamical tropopause. This chapter presents the statistical based study of the geographical, seasonal and altitudinal variations of GWs and vertical shear derived from ERA5 reanalysis and its role in generating turbulence over the North Atlantic (hereafter NA) LMS.

Despite advancements, current climate models still lack sufficient horizontal resolution to explicitly simulate the mesoscale and smaller-scale GWs. Thus, the main effect of unresolved GW on the large-scale circulation remains to be parameterize if they are to be included (e.g., Kim et al., 2003; Jewtoukoff et al., 2015). Very recently the study from Banerjee et al. (2025) hint that both oblique GW propagation and GW–turbulence interactions play an important role in transport and mixing processes in the middle atmosphere and it should therefore be accounted for subgrid-scale parameterizations, although further observational constraints are still needed. Current state-of-the-art reanalysis data, especially the ERA5 reanalysis offer relatively fine temporal and spatial resolution, and resolve central features of the GW spectrum, despite the issues discussed before (e.g., Podglajen et al., 2020; Kaluza et al., 2021; Gupta et al., 2024). ERA5 is able to resolve GWs with wavelengths of a few hundred kilometers and longer (Gupta et al., 2024), thereby contributing to its ability to simulate large- as well as small-scale wave dynamics.

TSL occurrence, although being a global feature, is dependent on different dynamic sources spanning from planetary to synoptic to sub-synoptic scales. In midlatitude, the strong shear emerges mainly

in the storm track region over the NA and in the Northeast Pacific, at above-average tropopause altitudes within ridges of baroclinic waves. The subsequent analysis, further expands the key findings from chapters above and generalizes them for all seasons in the annual average and the NA LMS.

Overarching goal is to address the question of whether the GWs sharpen or smoothen the near tropopause gradients and whether they play a role in shear enhancement above the local tropopause. For this purpose, ERA5 reanalysis data over the NA region, i.e., 35° N–60° N, 60° W–0° W, starting from March 2017 up to February 2018 is used to assess the seasonal variability of GWs and TSL. Here, we use ECMWF data at night 00:00 UTC. The analysis region spans from 5 km above the orography up to level 37, corresponding to ~25 km altitude, thereby excluding the planetary boundary layer as well as the enhanced shear region in the mesosphere–lower thermosphere (Liu, 2017). The statistical evaluation is performed in a tropopause-relative framework which is mandatory to preserve the outlined sharp gradients in the UTLS when averaging profiles with different tropopause altitudes (Birner, 2006). The specific research questions addressed in this chapter are as follows :

1. *Is there any relation in an annual cycle of characteristics of GWs, shear, and turbulence occurrences and variability over the North Atlantic in the LMS?*
2. *Does the influence of GWs induced shear affect the TSL dynamics under different scenarios? Does the GWs and GW-induced shear also play a role in the development of (clear-air) turbulence in the UTLS?*

5.1.1 Theory and computation of resolved GW-forcing in ERA5

GW carry momentum vertically in the form of vertical fluxes e.g. $\overline{u'w'}$, $\overline{v'w'}$. That means, when waves propagate upwards, their vertical flux of momentum converge. For GWs, the term $-\overline{u'w'}_p$ in the vertical component of EP flux is most important, and is evaluated here via its vertical derivative with altitude. This term is also important to understand the direct GW contribution to mean flow forcing. Although, it cannot connect to shear directly, this zonal GW forcing provide an estimate whether GWs accelerate or decelerate the mean wind fields, which is closely related to the occurrence of strong shear.

To quantify the role of GWs in driving the mean flow and contributing to turbulence generation, we adopt the Transformed Eulerian Mean (TEM) framework, in which the zonal mean zonal wind equation is expressed as (Andrews et al., 1987):

$$\frac{\partial \bar{u}}{\partial t} = \bar{v}^* \left[f - \frac{1}{a \cos \varphi} \frac{\partial}{\partial \varphi} (\bar{u} \cos \varphi) \right] - \bar{w}^* \frac{\partial \bar{u}}{\partial z} + \frac{1}{\rho_0 a \cos \varphi} \nabla \cdot \mathbf{F} + X, \quad (5.1)$$

where \bar{u} is the zonal-mean zonal wind, (\bar{v}^*, \bar{w}^*) are the residual mean meridional and vertical velocities, ρ_0 is the background density, \mathbf{F} is the Eliassen–Palm flux vector, and X represents external forcings such as friction. The vertical component of the Eliassen–Palm flux divergence, known as the vertical momentum flux convergence (VMFC), is given by:

$$\text{VMFC} = -\frac{1}{\rho_0} \frac{\partial F_z}{\partial z} = -\frac{\partial}{\partial z} (\overline{u'w'}). \quad (5.2)$$

The term $-\frac{\partial}{\partial z} (\overline{u'w'})$ within the total Eliassen–Palm flux divergence includes the net forcing of the mean flow by the resolved wave fluxes due to GWs (Fritts and Alexander, 2003). Here, followed by (Gupta

et al., 2021), we reformulate this term to estimate the wave forcing due to resolved GWs by considering the covariance only from zonal wavenumbers $k_x = 21$ and higher as:

$$\text{VMFC} \triangleq -\frac{\partial}{\partial z} (\overline{u'w'}) (k_x \geq 21) \quad (5.3)$$

This term captures the effect of vertical momentum transport by GWs on the mean flow. In our analysis, VMFC is computed using the perturbation winds extracted after Helmholtz decomposition and spectral filtering to isolate the divergent wave motions as described in section 2.5.1.

5.1.2 Synoptic situation over the Northern Hemisphere on 11 September 2017

One of the motivation for the selected year is, as noted in Kaluza et al. (2021), 2017 is one of the years with the most pronounced shear occurrences over the NA in their dataset. We focus not on the long-term trend but on the annual variability and how it relates to the occurrence of GWs. Moreover, it has been suggested that the occurrence of strong vertical wind shear near the tropopause could be influenced by enhanced GW activity associated with deep convection (Podglajen et al., 2017), as convection is the major source for GW generation in the tropics through several forcing mechanisms (Müller et al., 2018, and references therein). The metrics are introduced first with a selected time step in September 2017 before extending the analysis to longer periods, starting with the synoptic situation to provide a large-scale context.

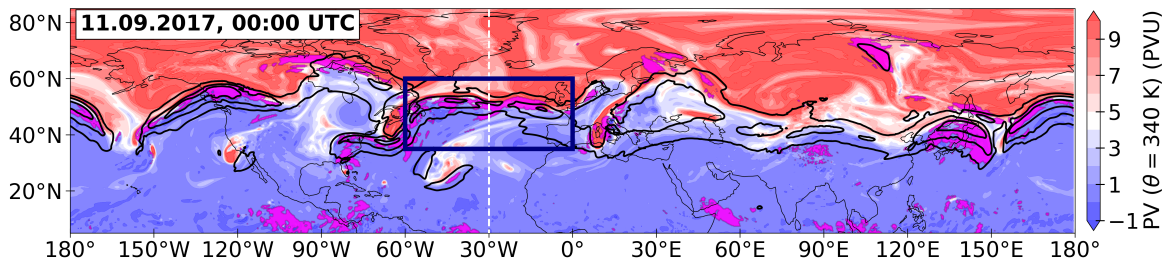


Figure 5.1: Potential vorticity at 340 K isentropic surface over the Northern Hemisphere on 11 September 2017, 00:00 UTC. The solid black lines represents the horizontal wind beginning at 30 m s^{-1} in steps of 15 m s^{-1} at 200 hPa pressure surface. Magenta shaded areas represent regions of $S^2 \geq S_t^2$ where $S_t^2 = 4 \times 10^{-4} \text{ s}^{-2}$, between 3.5 PVU dynamical tropopause and 1 km above. (Adapted from Kaluza et al. (2021) Figure 01).

Figure 5.1 presents a snapshot of the Northern Hemispheric PV distribution on the 340 K isentropic surface for 11 September 2017, 00:00 UTC, together with maxima of horizontal wind speed at 200 hPa. A distinct feature is the pronounced tropopause break and its close link to jet streaks in the upper-level flow. Over the Asian continent extending into the western Pacific, the PV structure exhibits a sharp meridional gradient that coincides with a coherent subtropical jet. Toward the western sector, the PV gradient becomes weaker and organizes into a sequence of likely Rossby or GW patterns generated via baroclinic flow and each associated with jet streaks occurring at different latitudes.

The mechanism behind the relevance of vertically propagating GWs to the shear generation across the tropopause have been discussed in Chapters 3 and 4. It is suggested that the GWs with large amplitudes locally modulate the N^2 in the LMS (Kunkel et al., 2014; Zhang et al., 2019), thereby can deform the flow, resulting in enhanced upward motions. This reduction in N^2 which in turn also allows to accumulate vertical shear in this region. Based on case studies, it is inferred that the GWs that propagate

upwards show a spatial and temporal co-location with vertical wind shear. Yet, the question remains whether we see a similar link on larger (spatial and temporal) scales.

5.2 Annual cycle of GWs, vertical shear and turbulence indices over the North Atlantic

5.2.1 Occurrence of strong vertical wind shear in a tropopause-relative framework

At midlatitudes, the occurrence of enhanced tropopause based vertical wind shear is linked to the jet streaks of PFJ and therefore to the associated baroclinic waves patterns. The TSL analysis steps on the vertical distribution of vertical shear from Kaluza et al. (2021) is repeated for a whole year dataset using daily ERA5 fields over the NA. The monthly vertical distribution of $S^2 \geq S_t^2$ over the NA is presented first, followed by the seasonality in the tropopause region.

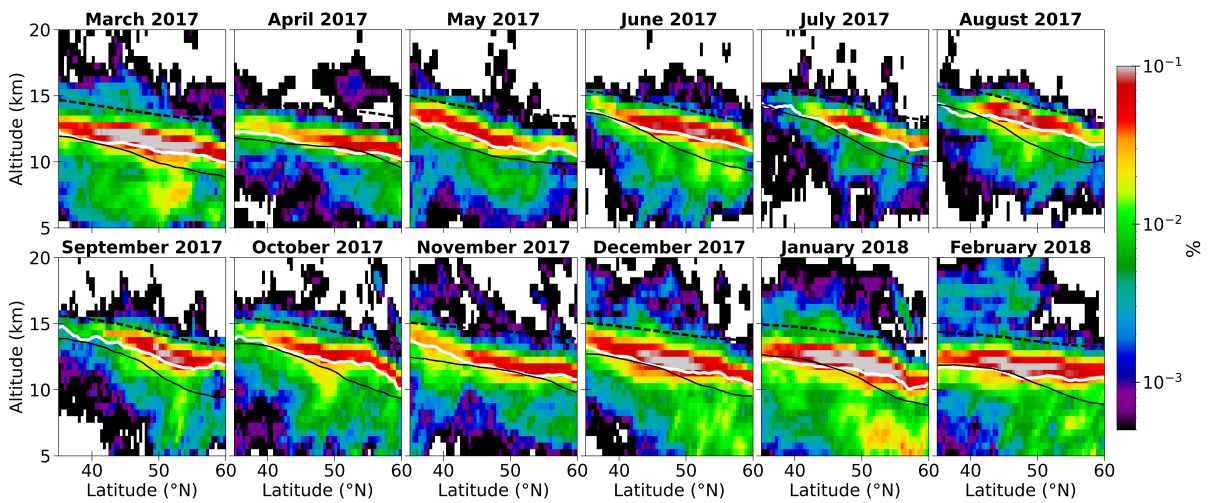


Figure 5.2: Occurrence frequency distribution of (a) $S^2 \geq S_t^2$ from March 2017 to February 2018. The occurrence frequencies are shown with logarithmic frequency contours, displaying the data in bins of sizes $\Delta y = 0.4^\circ$ and $\Delta z = 500\text{m}$. The zonal-mean dynamical tropopause (3.5 PVU isosurface; black solid line) and the zonal-mean 380 K isentropic surface of potential temperature (black dashed line) are overlaid.

Figure 5.2 shows the the monthly temporal and zonal average occurrence frequency for strong vertical shear with the geometric altitude as the vertical coordinate, along with the mean tropopause altitude and 380 K isentropic surface for the same time period and region. The colors represent the relative frequency of occurrence on a logarithmic scale, highlighting the regions where intense shear is most frequently observed.

The annual cycle of TSL reveals the meridional regions of exceptional occurrence frequencies located in the UTLS region covering the $35\text{--}60^\circ\text{N}$ and midlatitudes. The distinct occurrence frequency maxima of strong S^2 are apparent in the midlatitudes between $45\text{--}55^\circ\text{N}$ mainly in the close vicinity of the tropopause and are related to the position of upper-tropospheric jet features. The tropopause-based vertical coordinate centers the occurrence frequency maxima in a distinct layer above the dynamical tropopause, where the horizontal distribution of this layer spans all over NA and exhibits occurrence frequencies on the order of 1–10 % over a vertical range between 1–3 km. Note that the thickness of these shear layers varies across months.

In general, the vertical and meridional extent of this maxima exhibits a pronounced seasonal cycle: during boreal winter months (DJF), the region of enhanced S^2 strengthens and extends equatorward

and downward, while during summer (JJA), it weakens and shifts poleward and upward toward the LS. This evolution is consistent with the seasonal migration and intensity changes of the subtropical and polar-front jets.

Overall, this suggests the role of large-scale wave dynamics, particularly the polar jet streaks within ridges of baroclinic waves, which are known to exhibit distinct wind shear in the midlatitude tropopause region (Kunkel et al., 2019; Kaluza et al., 2019). Although the clustering of $S^2 \geq S_t^2$ agrees with the dynamic stability criterion, as well as the thermal wind associated with the baroclinicity at upper-tropospheric fronts, the significance of processes related to the occurrence of the TSL still remains to be quantified. The influence of large-scale jet dynamics on the intensity of TSL is further discussed in the following paragraph.

Meteorological state over the North Atlantic lowermost stratosphere

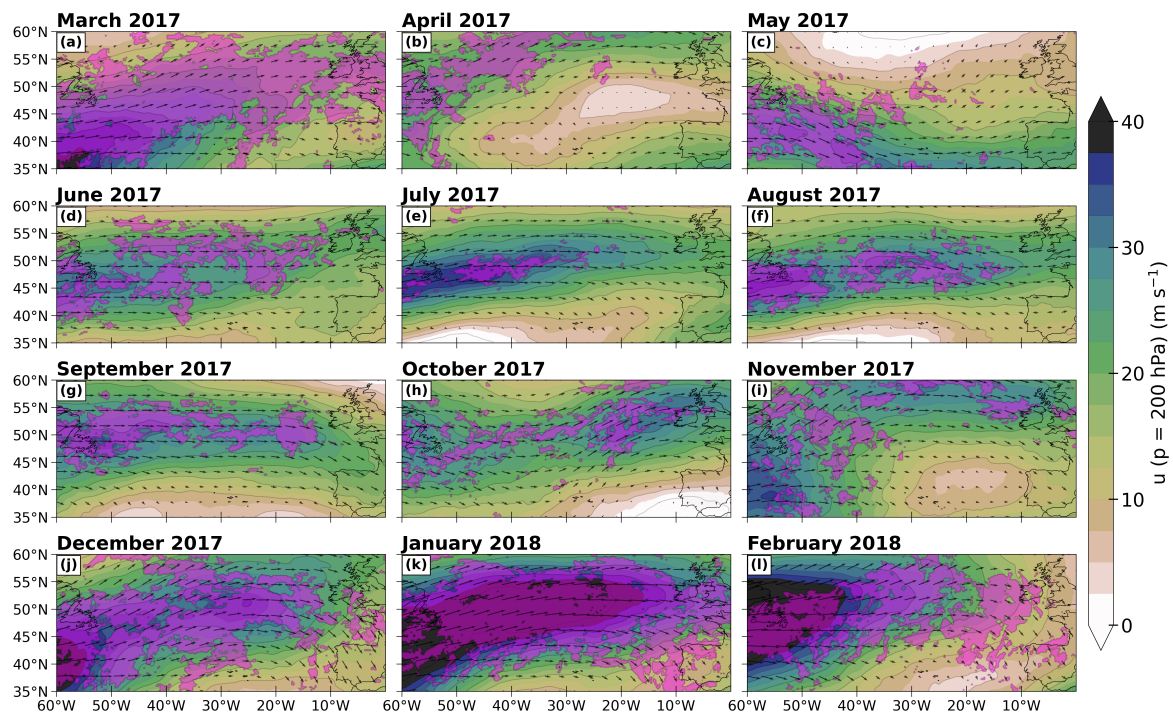


Figure 5.3: The 200-hPa monthly mean zonal wind (shaded; m s^{-1}) and horizontal wind vectors (arrows) over the North Atlantic from March 2017 to February 2018. Magenta shaded areas represent monthly mean occurrences of strong vertical wind shear $S^2 \geq S_t^2$ between 3.5 PVU dynamical tropopause and 1.5 km above.

Figure 5.3 shows the monthly mean zonal wind and horizontal wind together with the regions of strong shear between the dynamical tropopause and 1.5 km above over the NA. The jet stream reaches its maximum strength in winter (December-January), with core speed exceeding 50 m s^{-1} . During these months, the jet axis is displaced farthest south, typically located between $35\text{--}45^\circ \text{ N}$ over western and central NA. In contrast, from June to August the jet structure weakens and shifts northward, with the core positioned around $45\text{--}55^\circ \text{ N}$. The seasonal displacement is accompanied by a broadening of the jet entrance and exit regions.

Throughout the year, a clear coherent band of strong wind shear is apparent mainly near the jet core, where each region can be attributed to a planetary circulation feature. This band also migrates meridionally with the jet: southward and more intense in winter and early spring, and weaker and

positioned farther north in the summer. The pronounced shear occurs along the climatological storm track regions (Shaw et al., 2016), where shear maxima extend zonally from eastern North America across central NA into western Europe. In addition to this large-scale jet related shear structure, several small-scale shear patches appear sporadically and can be associated with transient synoptic systems such as extratropical cyclones, warm conveyor belts, stratospheric cut-offs, and localized GW activity embedded within the baroclinic flow.

Especially during winter, the wind systems described above align closely with the meridional band of frequent occurrences of strong vertical wind shear near the tropopause (Figure 5.2). At midlatitudes, this tropopause region is exposed to strong shear arises within the Rossby-wave jet streaks and along the cyclonically curled-up ridges associated with breaking baroclinic waves (Kaluza et al., 2019, 2021). The latter is frequently exposed to enhanced GW activity and hence, hints at their link to the formation of the TSL due to their bi-directional interaction with the thermal stratification gradients. Therefore, following section 5.2.2 discuss the relevance of GW-induced momentum fluxes to the observed shear layers.

Vertical wind shear in the LMS

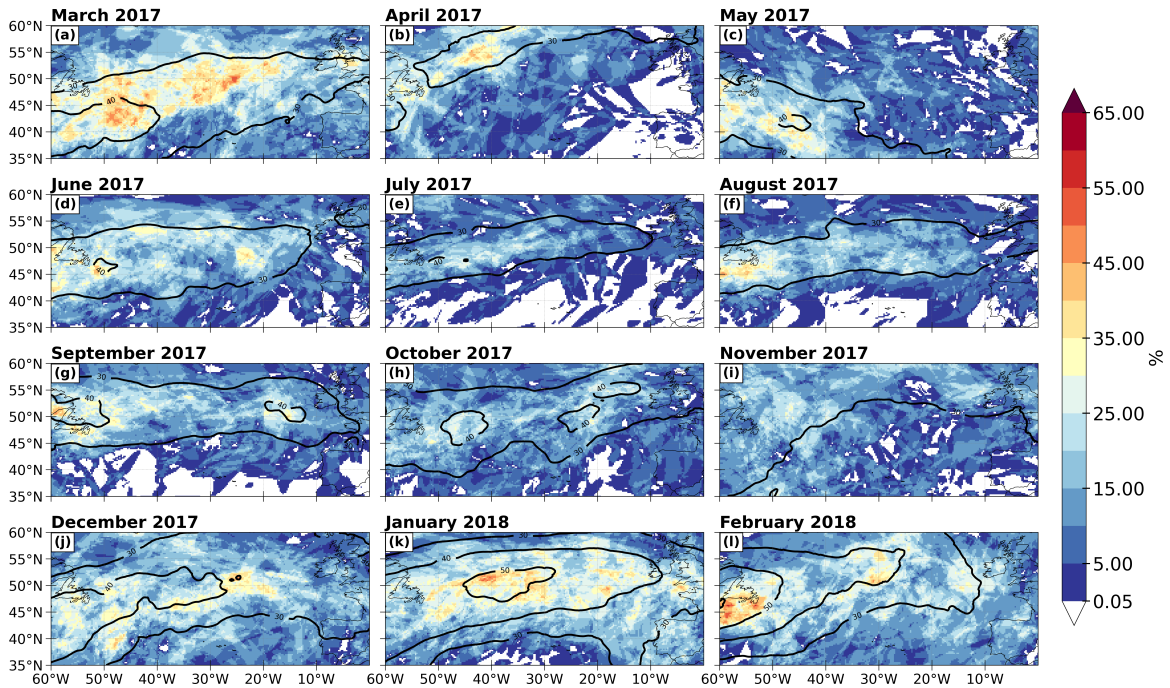


Figure 5.4: Occurrence frequency distribution of $S^2 \geq S_t^2$ over the LMS in the NA from March 2017 to February 2018. The solid black lines represents the horizontal wind $>30 \text{ ms}^{-1}$ at 11 km altitude.

Returning to the initial point of the analysis, the geographical distribution of vertical shear S^2 exceeding the threshold S_t^2 that is located between the dynamical tropopause and 380 K isentropic surface is indicated in Figure 5.4. For that, how often $S^2 \geq S_t^2$ criterion is met at each grid point is counted during all time steps for each month. The resulting distribution reveals a distinct annual cycle of these quasi-horizontal occurrence frequencies of strong shear over the NA lower stratosphere.

It becomes evident that NA exhibits several coherent hotspots of high shear encounters (Figure 5.4). In particular, the most extensive occurrences are apparent during winter (DJF), where a dominant shear maximum emerges southwest of Ireland and another, more zonally oriented maximum stretches from

Newfoundland across central NA. These regions align closely with the jet-core region, reflecting increased baroclinicity and intensified jet activity in the cold season. In contrast, summer months (Figure 5.4b-d) show weaker and more spatially confined shear, consistent with the poleward shift and weakening of the PFJ. Autumn (Figure 5.4g-i) months display a gradual re-intensification of shear along the developing jet, and are associated with the seasonal strengthening of the storm-track region.

At midlatitudes, the high shear occurrences are most pronounced during winter and are associated with jet streaks of the eddy-driven jet, with maxima centered between 40° N– 55° N and around 60° W– 30° W. Overall, the strong shear exhibits a distinct seasonality over NA. The recurrent occurrence of enhanced tropopause-based vertical shear could be further linked to the jet streaks of the PFJ and consequently, to the associated baroclinic wave patterns. Thus, the intra-annual variability of strong vertical shear reflects largely the variability of the jet stream.

5.2.2 GW momentum flux in a tropopause-relative framework

The persistent alignment of enhanced S^2 with the tropopause and jet regions suggest that UTLS is a dynamically active zone characterized by the dynamical instabilities and mixing processes i.e., frequent interactions between large- and small-scale motions. Such enhanced shear layers often emerge in response to Rossby wave breaking and jet streak dynamics and can be further modulated by smaller-scale processes such as GWs activity including their propagation.

Nevertheless, the question whether GWs are of any relevance to the formation and maintenance of these extratropical shear layers, or are merely a passive response to the background flow variability remain. This section discuss the relevance of GW-induced momentum fluxes to the maintenance of the observed shear maxima above the tropopause.

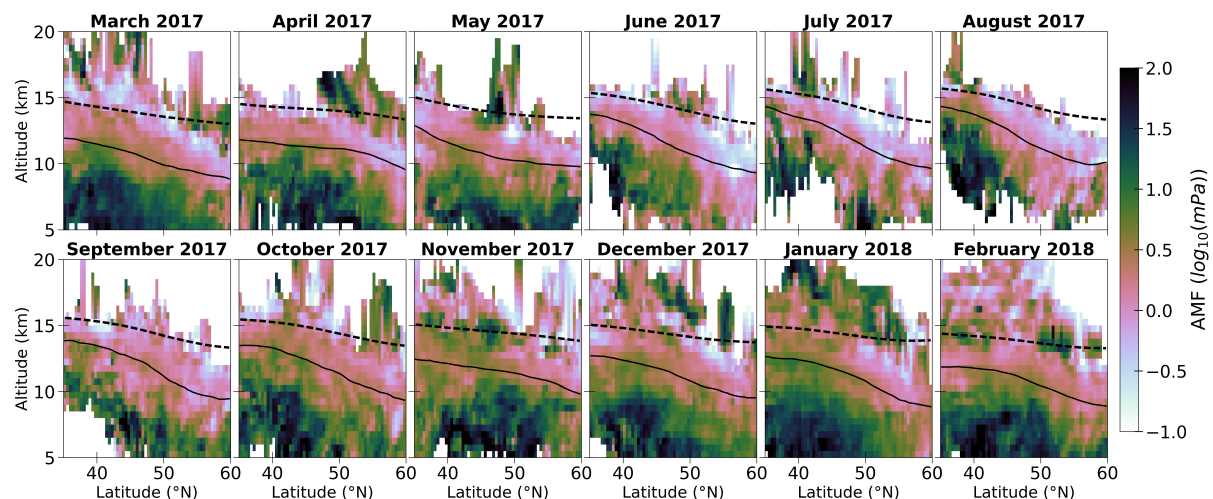


Figure 5.5: Zonal mean resolved GW absolute momentum flux (AMF, $\log_{10}(\text{mPa})$) conditioned on regions where $S^2 \geq S_t^2$ from March 2017 to February 2018. The data is shown in bins of sizes $\Delta y = 0.4^\circ$ and $\Delta z = 500\text{m}$. The zonal-mean dynamical tropopause (3.5 PVU isosurface; black solid line) and the zonal-mean 380 K isentrope of potential temperature (black dashed line) are overlaid.

The relation between GWs and TSL is assessed by the tropopause-relative vertical distribution of monthly mean AMF in the vicinity of higher occurrences of strong wind shear $S^2 \geq S_t^2$ (Figure 5.5). In general, shorter GWs that propagate more vertically carry or deposit larger momentum flux. From the analysis of vertical distribution of AMF, several hotspots of intense GW activity become evident over

the NA, which seem to fit the enhanced high shear hotspots identified in the previous section.

The tropopause-based vertical structure of AMF reveals three prominent features: (i) the upper tropospheric enhanced AMF hints at intense upward propagating GW activity (around $\sim 5\text{--}10$ km), but could also be related to the other small-scale processes such as convection or processes within clouds (e.g., in-cloud dynamics), (ii) the areas of distinct maxima with strong AMF abundance in the close vicinity of the tropopause, and (iii) pronounced vertical gradients in the upper branch of the LMS. These patterns demonstrate that shear hotspots systematically co-locate with regions of strong GW activity, with substantial AMF transport both across the tropopause and within the LMS.

During boreal winter, AMF exhibits a broader and stronger spectrum, characterized by higher AMF deposition in the vicinity of higher S^2 and sharp vertical gradient upward towards the LS. This indicates the strong GW activity, especially around $40\text{--}50^\circ$ N near $11\text{--}14$ km altitude. In contrast, summer features finer small-scale flux structures and steep vertical gradients throughout the UTLS, likely associated (at least partly) with non-orographic GWs. However, AMF magnitudes are substantially reduced and remain confined to lower altitudes, consistent with weaker shear and reduced wave propagation into the LS.

Altogether, the spatial and seasonal co-location of elevated AMF with strong shear hints at the plausible role of GWs in the formation of shear layers above tropopause and in modulating UTLS dynamics over the NA throughout the annual cycle.

5.2.3 Turbulence diagnostics in a tropopause-relative framework

The GWs and in particular their relation to the TSL owe their potential importance to the fact that both features majorly influence dynamics in the LMS. If small-scale processes play a role in the formation of shear layers, their contribution is also expected to be relevant for the generation of turbulence, given that vertical shear is one of the key precursors for turbulence in the UTLS. In addition to that, the strong horizontal deformation has usually been linked to upper-level frontogenesis, may also be an indication of the influence of GWs generated due to flow imbalance (Knox et al., 2008), which could ultimately lead to the development of CAT. Related to that, further discussion focus on analysis of potential occurrence of turbulence due to small-scales in the NA domain.

Figure 5.6 presents the extension of previous analysis in the form of occurrence of $0 \leq Ri \leq 1$ in tropopause-based vertical coordinate system, i.e., highlighting region susceptible to potential dynamic instability. The overall vertical distribution of subcritical Ri occurrences shows that these low Richardson numbers occur most commonly in the upper troposphere during all months. However, the occurrence frequency shows a clear annual cycle: low Ri values are most frequent from November to March while they show lower occurrences during the most other months. Interestingly, there are smaller hotspots of enhanced occurrence frequency during June, August and September which could be related to specific dynamical events, for example the hurricane season was quite active during 2017.

Another interesting feature is that low Ri occurrences in the LMS occur more often during winter and as such the potential for turbulence occurrences is enhanced during the winter months compared to that of summer months. However, this is no longer the case in the upper part of the LMS. As discussed in Kaluza et al. (2022), this could be related either to model-based Ri values underrepresenting the occurrence of low Ri at subgrid scales, or to a systematic underestimation of vertical shear near the tropopause that stem from the IFS, resulting in rather conservative estimates of the occurrence frequency

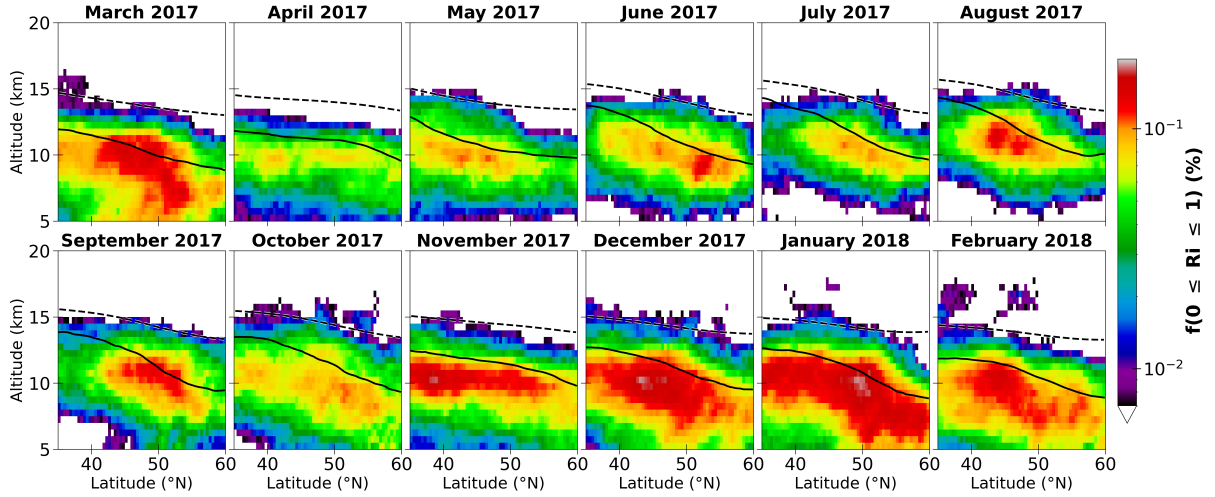


Figure 5.6: Monthly occurrence frequency distribution of $0 \leq Ri \leq 1$ with tropopause-based vertical coordinate system from March 2017 to February 2018. The occurrence frequencies are shown with logarithmic frequency contours, displaying the data in bins of sizes $\Delta y = 0.4^\circ$ and $\Delta z = 500$ m. The zonal mean dynamical tropopause (3.5 PVU isosurface; black solid line) and the zonal mean 380 K isentrope of potential temperature (black dashed line) are overlaid.

with regard to shear instabilities in this region (Schäfler et al., 2020). This overall annual pattern is consistent with the TSL occurrence discussed in section 5.2.1, and hence, could further linked to GW activity (section 5.2.2). To further understand the GWs role to potential turbulence occurrence, we resort to the vertical distribution of empirical turbulence indices (Ellrod and Knapp, 1992) in the following.

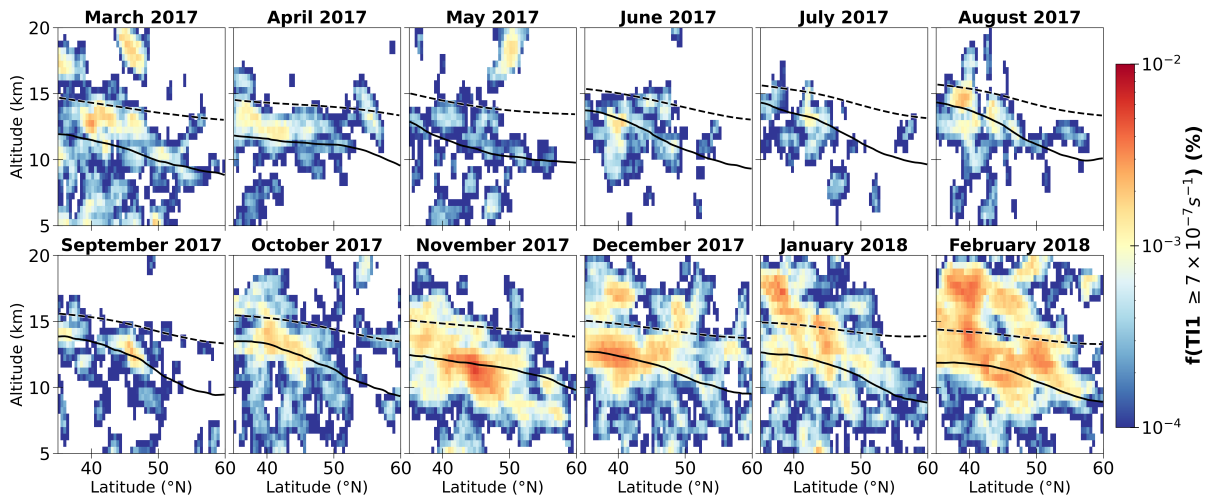


Figure 5.7: Monthly occurrence frequency distribution of $TI1 \geq 7 \times 10^{-7} s^{-1}$ from March 2017 to February 2018. The occurrence frequencies are shown with logarithmic frequency contours, displaying the data in bins of sizes $\Delta y = 0.4^\circ$ and $\Delta z = 500$ m, along with the zonal mean dynamical tropopause (3.5 PVU isosurface; black solid line), and the zonal mean 380 K isentrope of potential temperature (black dashed line).

The occurrence frequency of turbulence diagnostics TI1 (Figure 5.7) and TI2 (Figure 5.8) is evaluated in tropopause-relative vertical coordinates, which provide a more dynamically coherent representation of turbulence occurrence relative to the tropopause height. We start here with occurrences of TI1 exceeding the threshold value, $7 \times 10^{-7} s^{-1}$, which corresponds to moderate-intensity CAT. Since the spatial and temporal patterns of climatological indices are weakly sensitive to the choice of thresholds,

the main focus in the remainder is not on the absolute values of turbulence frequencies, but rather on their spatial and monthly patterns. It is important to note that turbulence rarely develops as a single continuous area; instead, it appears in sporadic, short-lived pockets around the periphery of unstable regions (Sharman et al., 2006). Meanwhile, ERA5 data have an hourly resolution, and as our analysis relies on daily single-time-step fields, it may limit the representation of such short-lived events. Henceforth, the observed structure might suggest the conditions conducive to their occurrence, albeit with reduced intensity.

The monthly distributions of TI1 (Figure 5.7) show that turbulence occurrences cluster in the vicinity of the LMS throughout the year, with enhanced frequencies evident between 40° N and 55° N, broadly following the latitude band of the midlatitude jet. The most pronounced occurrences appear during late autumn and winter (NDJF), particularly around 10–13 km altitude, indicating an increased likelihood of small-scale induced turbulence during these months. In contrast, summer (JJA) exhibits substantially reduced TI1 occurrences, consistent with weaker vertical shear and likely related to the reduced GW activity.

It should, however, be noted that neither Ri nor TI1 are solely defined by S^2 . On the sub-synoptic scale, the flow deformation, convergence and differential temperature advection can result in frontal zones with the associated wind shear according to the thermal wind relation (Ellrod and Knapp, 1992). In fact, in our analysis, these processes are the major influences of GW activity. In particular, if GWs are involved, they may propagate and perturb the environmental conditions further away from the sources, acting as non-local causes of CAT, for instance, when the perturbed regions become unstable and create conditions favorable for KHI. We note that this is key for the potential occurrence of CAT, as highly transient yet frequent mixing processes in the extratropical LMS. Here, the seasonal pattern suggests that regions of enhanced turbulence activity align closely with the altitudes and latitudes featured by frequent strong shear layers that occur under the influence of GW activity in the LMS.

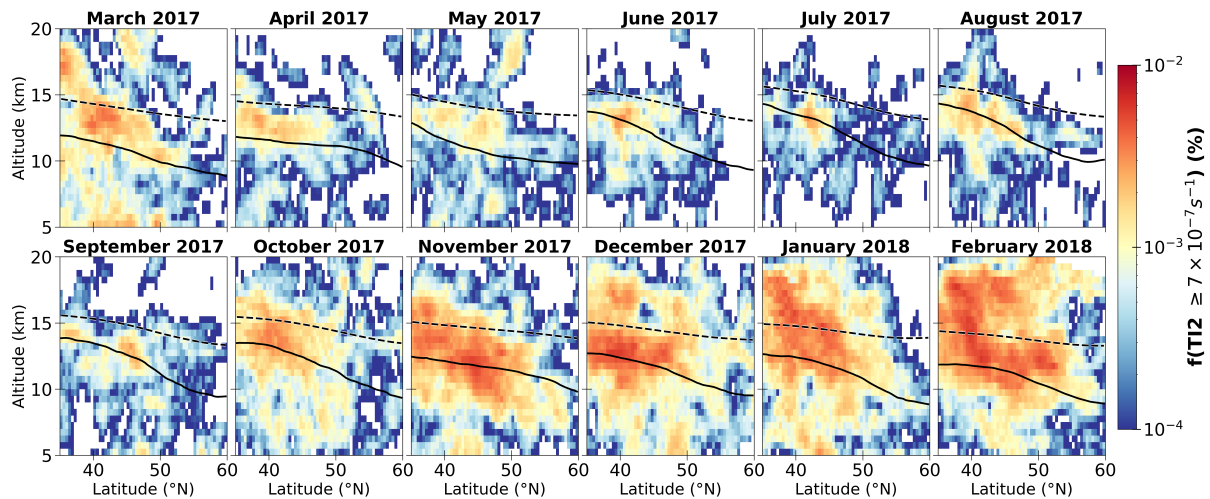


Figure 5.8: As in Figure 5.7 but for TI2.

The distribution of TI2 which gives a more direct relation to GW dynamics (Figure 5.8) represents maximum abundance of TI2 mostly in LMS and are tightly aligned with the tropopause. These are also regions that exhibit sharp AMF gradients as well as high GW intensity and has a certain resemblance to the annual cycle of the GW discussed in the section before. Thus, this co-location hints at such a

link between small-scale structures, including GW-induced turbulent activity and tropopause dynamics. The elevated wintertime occurrence remains pronounced, but the vertical extent of enhanced TI2 is more sharply confined than TI1, emphasizing that most TI2 events occur within ± 2 km of the tropopause. The close alignment of TI2 occurrence with the tropopause surface and its strong wintertime enhancement strongly suggest that GW propagation across the UTLS plays a key role in shaping turbulence occurrence across the tropopause.

Moreover, associated with the region of most intense turbulence related shear are the patches of increased CAT occurrences. These intense CAT occurrences show that after some strong shear occur, the moderate intensity CAT occurred at, far north and upwards the shear layers. In addition, as expected, the GW momentum fluxes consistently exhibit enhanced small-scale vertical gradients in the vicinity of strong shear and turbulence potential (see also section 5.2.2). Overall, the higher vertical gradients of AMF are evident in the regions where there are pronounced shear and indications of (clear-air) turbulence. Combining all this information suggests the substantial contribution of small-scales, mainly GWs, to the formation of TSL and consequently to the turbulence hotspots.

In principle, this findings demonstrate that there is a quasi-permanent layer of high shear occurrences, i.e., TSL, that has a close resemblance to the annual cycle of the GWs as well as GW-induced CAT potential. Nevertheless, the question remains whether GWs modulate the formation and maintenance of the extratropical shear layers or are merely a passive response to the background flow variability. This will be further addressed in-depth in section 5.3.

5.3 Lower stratospheric hotspot of zonal GW forcing and momentum fluxes

This section presents detailed investigation of GW activity in terms of zonal GW forcing over NA. Figure 5.9 shows maps of GW vertical convergence of momentum flux at dynamical tropopause and 1.5 km above the tropopause height in NA as a function of month, along with monthly mean horizontal wind speed. The monthly mean patterns of VMFC reveal a pronounced seasonal variability. The dominance of GWs occur during winter (DJF; Figure 5.9j-l) over the northeastern side of the American highlands and their downstream oceanic regions, while weaker magnitudes are found during summer (JJA). In general, the VMFC distribution is not zonally uniform, but rather with maxima concentrated along the jet-stream region and minima over the subtropical Atlantic.

The spatial distribution of VMFC can be related to distinct GW source mechanisms that vary seasonally. During winter months, the enhanced fluxes over the northeastern American continent and adjacent ocean are likely driven by strong surface winds and/or orographic forcing along steep terrain. In contrast, during summer, the weaker and patchier GW activity around $20\text{--}30^\circ$ W and near the Iberian Peninsula (Figure 5.9e) likely reflects orographic generation of GWs in association with strong surface winds such as katabatic winds (Watanabe et al., 2006). Similar localized enhancements also appear in June and September, suggesting intermittent wave propagation under favorable synoptic conditions.

From a dynamical perspective, the sign and structure of VMFC provide the direction of GW momentum transfer. According to linear theory, the direction of the horizontal momentum flux vector is the same as that of wavenumber vector of GWs if they propagate energy upward. At the LMS, VMFC is negative in most of the regions where the zonal winds are easterly in most of the regions at this level. Thus, the dominance of this feature is consistent with GWs that propagate upwards in easterly wind flow, at which the magnitude of negative values is maximized around the jet streak region. This suggest

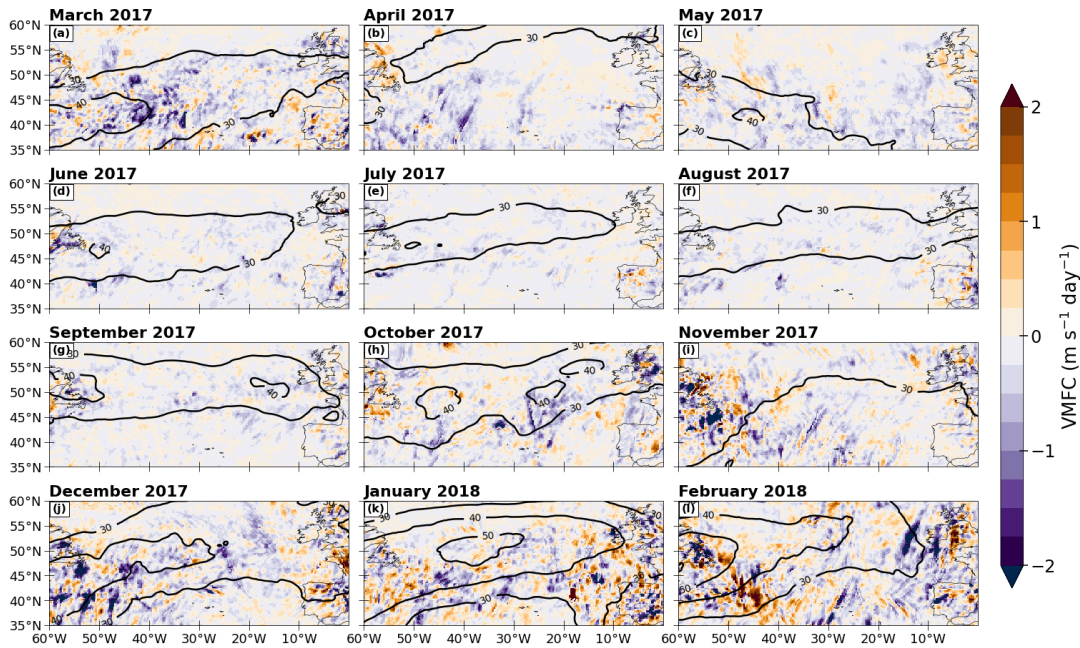


Figure 5.9: Monthly occurrence frequency distribution of VMFC (in $\text{m s}^{-1} \text{day}^{-1}$) between dynamical tropopause and 1.5 km above in the North Atlantic from March 2017 to February 2018. The solid black lines represents the horizontal wind $>30 \text{ m s}^{-1}$ at 11 km altitude.

that GWs generated upstream deposit their momentum in a horizontal region far from their origin.

The monthly distribution of GW momentum flux at the dynamical tropopause and 1.5 km above the tropopause height over the NA is shown in Figure 5.10. The distribution of AMF reveal similar spatial patterns to those seen in momentum flux convergence, with the largest magnitudes co-located with the subtropical and polar-front jet regions. While the absolute amount of momentum flux for convective GWs changes little over season, GWs generated by storms and mountain waves might show large day-to-day variability, which has a strong influence also on the inter-hemispheric fluxes (Preusse et al., 2014). The GW momentum flux exhibits a clear seasonal cycle, with enhanced values during winter and reduced activity in summer. Peak magnitudes exceed $1.5 \log_{10}(\text{mPa})$ and are collocated with the STJ and PFJ regions, particularly on the western and central NA, consistent with enhanced generation and propagation of GW in baroclinically active regions. This alignment suggests that upper-tropospheric jets act as key wave sources and/or waveguides.

During summer, reduced AMF is evident over most of the domain, with localized maxima persisting near the jet axis, indicative of weaker baroclinic forcing but still active wave sources associated with subtropical jet dynamics. In winter, stronger and broader maxima correspond to intensified PFJ activity and storm-track variability. This pattern highlights a robust seasonal modulation of GWs activity closely tied to the upper-tropospheric jet.

Overall, the observed transition from localized summer maxima to broad winter enhancements reflects the seasonal strengthening and poleward displacement of the upper-tropospheric jet system, which governs both the generation and vertical propagation of GWs. This emphasizes the dominant role of large-scale jet dynamics and orographic forcing in shaping the spatial and temporal variability of GW-driven momentum transport over the NA. Moreover, the enhanced GW momentum flux signatures have been identified in the same regions. Also, the convergence of vertical momentum flux provides a peak GW forcing upto $2 \text{ m s}^{-1} \text{day}^{-1}$ around $40\text{--}50^\circ \text{N}$ are the regions of pronounced shear.

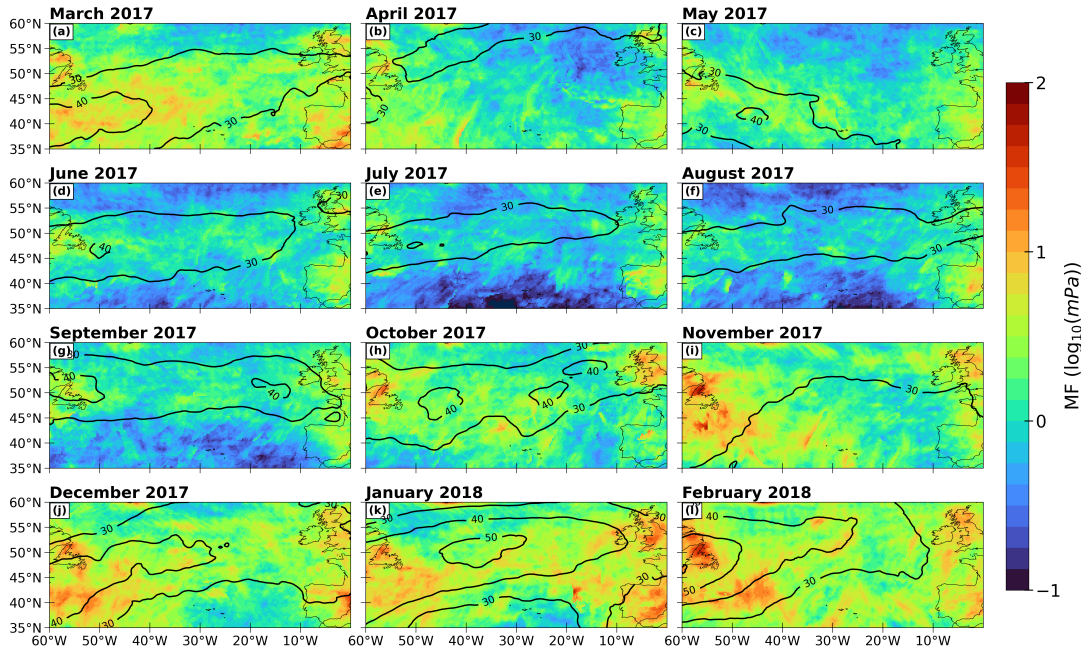


Figure 5.10: Same as Figure 5.9 but for the distribution of GW absolute momentum flux (in $\log_{10}(\text{mPa})$).

Altogether, the regions of strong shear identified earlier shows a spatiotemporal co-location with intense GW activity also on a larger spatial and temporal scales, suggests that GWs contribute to conditions that favor enhanced shear encounters. In addition, momentum deposition associated with GW breaking could further intensify this shear generation.

5.4 GW perturbations and shear prone to potential turbulence in the LMS: Coincidental or correlated?

In the previous discussion, significant co-location of intense GW activity and enhanced S^2 was identified in the LS at smaller spatio-temporal scales. In this section, discussion now focus on the potential occurrence of turbulence in the LMS and the relation between N^2 , S^2 and Ri examined using a two-dimensional PDFs. Here, a threshold of $0 \leq Ri \leq 1$ is adopted to identify regions with enhanced potential for turbulence, following previous studies (e.g., Lane et al., 2003; Olsen et al., 2013; Wang and Fu, 2021; Kaluza et al., 2021) and accounting for resolution-dependent effects (e.g., Shao et al., 2023), to capture the most unstable and/or potential turbulent regions. Note that only data points in the LMS are considered for this analysis, and the focus is again on monthly distributions of metrics, which again helps to highlight the differences among the intra-seasonal variations.

Variability of shear and static stability in the LMS

The monthly distribution of occurrence frequencies of N^2 and the vertical shear S^2 in the LMS over the NA is shown in Figure 5.11 from March 2017 to February 2018. The distribution reveals that the majority of occurrences are concentrated in regimes where N^2 exceeds S^2 . This dominance of N^2 reflects the presence of the TIL, a sharp layer of enhanced stability just above the thermal tropopause (Birner, 2006). The TIL acts as a convectively stable region that inhibits vertical mixing and support the persistence of strong potential vorticity gradients across the tropopause (Kunkel et al., 2019). The

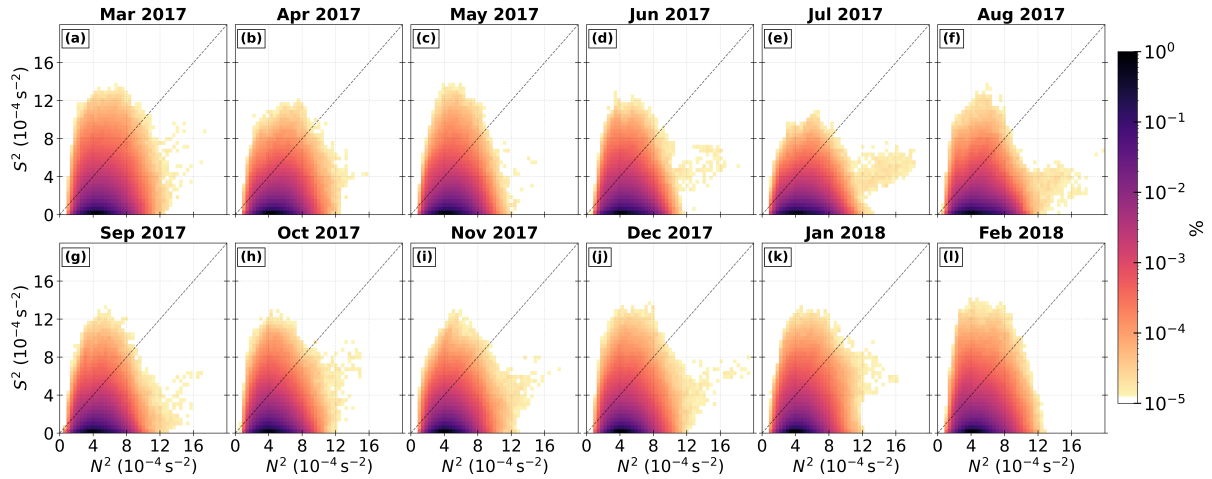


Figure 5.11: Relative occurrence frequency distribution of N^2 - S^2 pairs from March 2017 to February 2018. The occurrence frequencies are shown with logarithmic frequency contours. The black dashed line represent the $Ri=1$.

systematic shift in the tail of the distributions suggests that there could be impact of GW processes during winter that likely contributes to stronger vertical shear near the tropopause, increasing the likelihood of dynamical instabilities and potential turbulence generation in the extratropical LMS.

The enhanced shear and reduced Ri during winter imply stronger potential for dynamic instability and higher likelihood of shear-induced turbulent mixing, whereas summer months are dominated by a more stable TIL signature with less GW influence.

It is important to note that higher shear alone does not translate into the occurrence of turbulence and mixing. Hence, one need to assess whether turbulence also occurs in the region of enhanced shear occurrences. Since turbulence is a rare event under general atmospheric conditions (Sharman et al., 2012; Dörnbrack et al., 2022), even in the LMS, only a few data points are expected to exhibit potential for dynamic instability. This becomes evident in joint PDFs of N^2 and S^2 which reveals an indication of the occurrence of potential turbulence in the LMS with respect to Ri (Figure 5.11). We here observed substantial values of S^2 maximum is attributed to the low Ri .

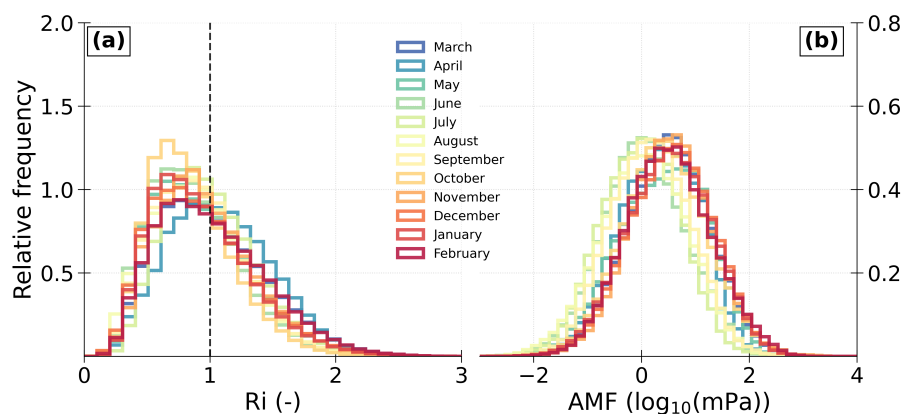


Figure 5.12: Relative occurrence frequency distribution of (a) Ri in the vicinity of $S^2 \geq S_r^2$ and (b) the logarithm of absolute momentum flux conditioned on $S^2 \geq S_r^2$ associated with $0 \leq Ri \leq 1$ displayed in panel (a) in the LMS from March 2017 (blue) to February 2018 (red). The black dashed line in (a) represent the $Ri=1$.

The corresponding relative frequency distribution of Ri is shown in Figure 5.12. The distribution peaks at $Ri=0.7$ are largely associated with vertical shear $S^2 \geq 4 \times 10^{-4} \text{ s}^{-2}$ and span over a broad spec-

trum of larger Ri of value up to 2 in the LMS. This further agrees with the Kaluza et al. (2021), suggesting that LMS is mostly dynamically unstable in the presence of strong vertical shear. In addition, the question remains whether these strong shear occurrences in the vicinity of low Ri are attributed to GWs. The occurrence of AMF in the vicinity of $S^2 \geq S_t^2$ that is associated with $Ri \leq 1$ (Figure 5.12b) shows higher positive AMF in winter and slightly less in summer months. This enhanced GW activity in terms of AMF reveals that GWs, along with other small-scale features, contribute to at least part of the pronounced shear that causes potential turbulence occurrence in the LMS. Yet, in this case, how much of the GWs contribute to shear and turbulence generation in the LMS remains unclear. This will be briefly addressed in the following paragraphs.

GWs, GW-induced shear and shear prone to potential turbulence occurrence

At this point, the results obtained from the wind shear and mean state of GW fields could be questioned: what if the shear and small-scale features concerned, for instance GWs, are only tied to the synoptic feature, such as flow imbalances, but not to the turbulence occurrence? That is a similar pattern will be obtained, if we randomly pick regions that show the collocation, regardless of whether the location is turbulent or not. On one hand, the justification given above relies on the previous studies, but it can also be answered with the correlation between shear perturbations and GW fluxes or forcings. On the other hand, it should, however, be considered that the interaction between mesoscale GWs and synoptic-scale is a typical multiscale problem that needs a bit more extensive treatment.

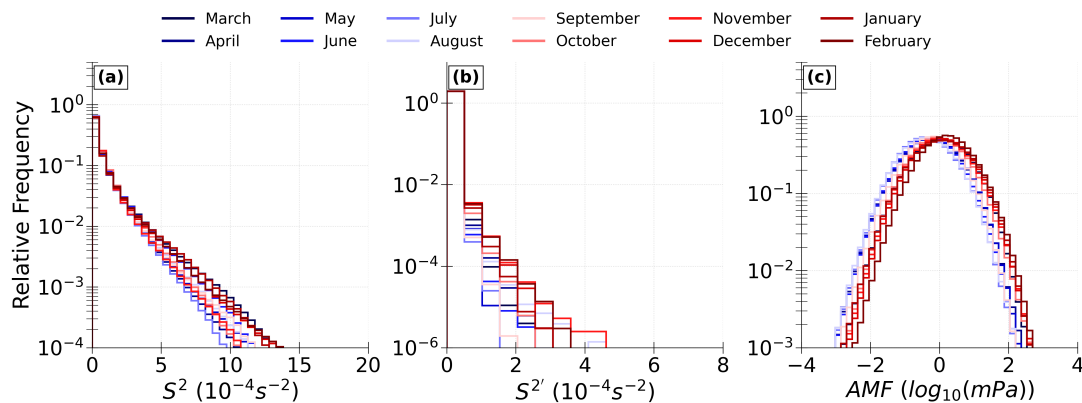


Figure 5.13: Relative frequency distribution of (a) S^2 , (b) $S^{2'}$ and (c) absolute GW momentum flux over the LMS from March 2017 to February 2018.

As the main focus here is on the GWs contribution to turbulent shear, the relation between GWs and shear, as well as GW-induced shear in the LMS has given a priority hereafter. For this we calculate the shear and shear fluctuations in the LMS for each month in the entire year. The distribution of shear and shear fluctuations in the LMS for each month in the entire year is shown in Figure 5.13. Both large-scale and small-scale shear indicate that the largest shear values are rare events; however, as noted before, the largest shear values occur during the winter months. During the summer months, the largest shear values have lesser occurrences. As expected based on its derivation, the occurrence frequencies of $S^{2'}$ are much smaller than those of S^2 . We note again that we regard $S^{2'}$ as a proxy for the behavior of the smallest scales which are resolved by ERA5 and to estimate whether these small-scales behave differently than the large-scales.

The distribution of momentum flux (Figure 5.13c) shows temporal variation in the higher occurrences of the distribution, where the distinct separation between the higher AMF occurrences are evident in September-February (autumn and winter) months and the relatively lower occurrences in March-August (spring and summer) months. There is an increase in the occurrence of S^2 maxima, particularly during the intense GW activity. Under the assumption that S^2 is strongly under the influence of GW activity, this, in turn, suggests a possible contribution of GWs to the generation of the largest shear values.

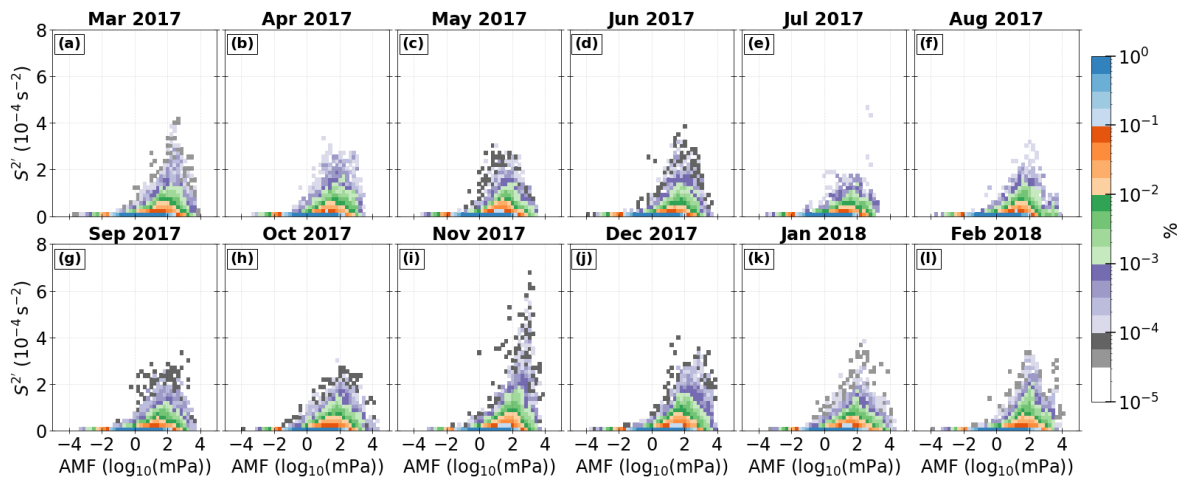


Figure 5.14: Relative occurrence frequency distribution of AMF due to GWs and shear perturbations pair in the LMS for $0 \leq Ri \leq 1$ over the NA from March 2017 to February 2018. Normalized counts of PDFs distribution with the logarithmic occurrence frequency color scale is shown.

Figure 5.14 explores this relation through the joint PDFs of AMF and S^2 in the vicinity of turbulence. Likely observed in idealized and real-case scenarios in chapters 3 and 4, a positive correlation between S^2 and AMF in case of turbulence occurrence is anticipated if GWs play a role in the shear and turbulence generation. Monthly distribution of data points of S^2 and AMF in the vicinity of $0 \leq Ri \leq 1$ shown in Figure 5.14, indicate the positive correlation between these two quantities. The higher (lower) abundance of this relation is observed in the winter (summer) months. In all months, there is positive correlation in a sense that larger values of S^2 occur preferentially during larger AMF. Notably, the distribution of AMF is mostly shifted toward larger values in the proximity of potential turbulence, with maxima occurring on the order of 10^1 to 10^3 mPa, while the corresponding non-turbulent distribution of AMF in Figure 5.13c is more centered around 0. In contrast, there is higher positive correlation observed in November, which could stem from the convectively generated intense GW activity, likely associated with storm track region coming from the Atlantic Northeast (region of eastern North America).

Combining all this information, we interpret this as an indication that the small-scales and, here in particular, the GWs contribute substantially to the occurrence of strong shear perturbations and potential turbulence in the LMS.

Finally, it is important to assess whether zonal GW forcing is related to the shear enhancement during the turbulent episodes or is merely a coincidence in the LMS. This relevance is further explored through the joint PDFs of VMFC and S^2 in the LMS (Figure 5.15). Due to the fact that upward-propagating GWs deposit their momentum in the subsequent region and thereby enhance local vertical wind gradients, the higher co-occurrences of both parameters in the vicinity of turbulent region where momentum-

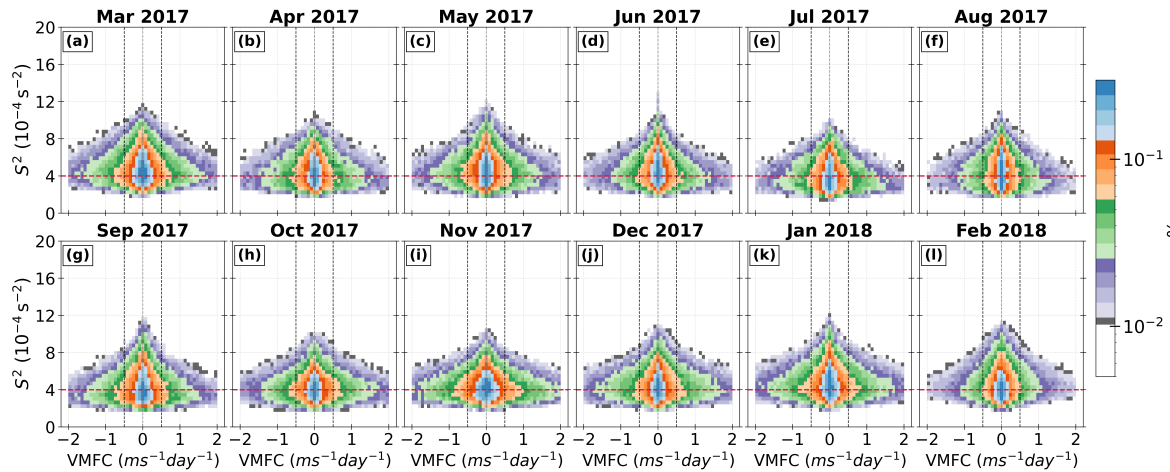


Figure 5.15: Same as Figure 5.14 but for VMFC vs. vertical shear S^2 . Dashed white line indicate $S^2=S_t^2$. Vertical dashed lines mark the ± 0.5 range for readability.

flux convergence occurs are expected. Figure 5.15 confirmed this interrelation via: in all months, the distributions narrow toward larger shear and simultaneously shift toward more negative VMFC values (purple and green colors), results in a unimodal distribution which peaks around $\sim 12 \times 10^{-4} \text{ s}^{-2}$ vertical shear. Specifically, the distribution of VMFC, exceeding the range of $\pm 0.5 \text{ ms}^{-1} \text{ day}^{-1}$, broadens during winter months mainly with higher occurrences (see red colors), indicating that the strongest shear occurrences preferentially coincide with regions of enhanced upward momentum flux convergence. In contrast, this distribution is narrowest for summer months where profiles are rarely found outside the range of $\pm 0.5 \text{ ms}^{-1} \text{ day}^{-1}$. This coupling is most pronounced during winter, when baroclinic activity and jet strength peak, leading to both higher shear values and more intense GW forcing (see also discussion in section 5.3). In summer, the relationship remains detectable but is rather weaker and confined to lower shear values. Interestingly, the previously noted strong linkage between shear perturbations and AMF in November is reaffirmed here: VMFC– S^2 pairs show that the large GW forcing aligns with the upper tail of the shear spectrum. This confirms that the intense shear observed during this month is not merely a product of jet imbalances but is mostly dynamically reinforced by active GW forcing linked to baroclinically unstable background flow.

In conclusion, this relation provides compelling evidence that small-scale GWs play an active role in amplifying vertical wind shear in the LMS and contribute to the seasonal modulation of dynamical instability and turbulence susceptibility in the extratropical UTLS.

5.5 Summary

The objective of Chapter 5 was a comprehensive analysis on the role of ERA5-resolved GWs in modulation and/or formation of strong vertical wind shear above the tropopause and their contribution to potential turbulence in the NA lowermost stratosphere. This was motivated by the results from Chapters 3 and 4 concerning the GWs contribution to occurrence of enhanced shear above tropopause within ridges of breaking baroclinic waves and in the vicinity of large amplitude upward propagating GWs. This is further explored using the annual daily NA ERA5 fields as a comprehensive state-of-the-art representation of the atmospheric state. The key points of the link between strong vertical wind shear and the GWs processes are as follows:

- Using the high-resolution ERA5 reanalysis, which at least partially simulates the GW spectrum in the UTLS; GWs, GW-induced shear, and the occurrence of the tropopause shear layer is analyzed over the NA domain. Our results demonstrate that there is a quasi-permanent layer of high shear occurrences just above the elevated tropopause, which has formerly been framed as the TSL (Kaluza et al., 2021). This TSL shows an annual cycle with maximum values during winter and minimum values during summer. The geographical mapping of the TSL revealed distinctly separate regions of preferred occurrence, which can be linked to small-scale GW activity associated with jet-front systems in baroclinic waves in the extratropics.
- The analysis of GW momentum fluxes and turbulence diagnostics (TI1/TI2) on tropopause-relative vertical coordinate reveals the distinct seasonality of both parameters and also holds an important piece of information: (i) the GW fluxes exhibit intense GW activity during the formation of shear layers, and have sharp gradients in the vicinity of strong shear, and (ii) the turbulence diagnostics show strong occurrences just above the tropopause and mainly in the LMS, collocated with enhanced vertical shear layers as well as regions with intense GW activity.
- Furthermore, the TSL is located near regions of pronounced GW momentum flux above the extratropical tropopause. As such, the TSL may be regarded as a key indicator for nonlinear wave-mean-flow interaction and, consequently, of momentum deposition (Zhang et al., 2019; Bense, 2019; Kaluza et al., 2021). Further investigation of vertical profiles of the wind shear and TI1/TI2 revealed that these turbulent layers are generated at least partly by GW-induced shear above a tropospheric jet.

Overall, this analysis presents a step towards a better understanding of GW-scale processes influencing the dynamical structure of transition region between the troposphere and stratosphere, and above, i.e., the LMS in the extratropics. For the extratropics, the analysis is confirmed and extended the central results from Chapter 4, i.e., the strong shear co-occurs in the regions of intense GW activity within the ridges of baroclinic wave, and thus a region that is also associated to evolution of TIL and in the proximity of potential turbulence occurrence. The GWs processes can have several implications in the LMS:

- GWs in the LMS are predominantly concentrated along the flanks of the upper-tropospheric jet, with a pronounced seasonal cycle. GW fluxes and associated shear are strongest in winter and weakest in summer, consistent with previous climatological analyses (e.g., Kaluza et al., 2021). This seasonality reflects enhanced baroclinic activity and GW generation during winter, with stronger vertical propagation into the UT through the LMS and above.
- The relative contribution of GWs to shear generation is found to be notable, especially in the winter in the LS, where the convergence of vertical momentum provides a peak forcing of up to $2 \text{ m s}^{-1} \text{ day}^{-1}$ in the midlatitude between $45\text{-}55^\circ \text{ N}$. The strong vertical gradients in static stability near the tropopause make the UTLS particularly sensitive to GW forcing. The estimated peak momentum flux associated with the most intense shear and turbulence is on the order of $\sim 10^2 \text{ mPa}$. This also reveals the presence of moderate upward propagating GWs through the LMS, producing vertical shear of $\sim 10^{-4} \text{ s}^{-2}$ magnitude, thereby triggering local instabilities.
- Regions of enhanced GW momentum flux converge with zones of intensified vertical shear, particularly in the vicinity of the tropopause. A clear positive correlation is found between GW-induced

shear and absolute GW momentum flux, indicating that small-scale GWs are closely linked to the occurrence of dynamically unstable shear layers. This suggests that GWs act as an important mechanism in the formation of tropopause-following shear layers, which in turn contribute to the conditions conducive for CAT generation.

In summary, the ERA5 reanalysis data at least partially resolves GWs allowing evaluation of small-scale GWs contribution to the climatological tropopause shear layer. The quasi-climatological patterns of GW activity and shear highlight that resolved GWs in ERA5 contribute substantially to the climatological structure of the TSL and could further be related to the formation of the extratropical transition layer. The fact that TI2 occurrence strongly aligns with the tropopause shear layers suggests a dynamically consistent link between GW propagation, shear amplification, and (clear-air) turbulence onset in the LS. Moreover, high resolution ERA5 reanalysis forms a natural bridge between observations and free running climate models, can be used to estimate the zonal forcings of such GWs and can help assess their role in the CAT which is major concern in aviation safety.

6 Conclusion, outlook and recommendations

6.1 Conclusion

This thesis focuses on understanding the impact of small-scale dynamics on UTLS transport and mixing, has taken a novel approach by studying the relation between GWs and shear from a day-to-day, synoptic-scale point of view, starting from idealized baroclinic life cycles (Chapter 3) to a comprehensive extratropical cyclone case study (Chapter 4), and extending to quasi-climatology and planetary scales analyses based on reanalysis data (Chapter 5). The quantification of the modulation and enhancement of the tropopause shear layer (TSL) by small-scale processes represents a significant step forward in understanding the mechanisms that lead to the formation and maintenance of shear layers and the existence of the extratropical transition layer (ExTL). Overall, this work revisits and refines the hypothesis by Kaluza et al. (2021), and sets a new paradigm about how gravity waves (GWs) constitute an important source for the formation of the TSL as well as for the onset of (clear-air) turbulence in the UTLS. A short overview of the three main topics discussed in this thesis is provided, and the results achieved during the doctoral work are presented chapter-wise, followed by a discussion of the open research questions relevant to each topic.

In Chapter 3, a series of baroclinic life cycle experiments with the ICOSahedral Non-hydrostatic model is presented to study the impact of GWs on the occurrence of vertical wind shear and consequent potential turbulence, an indicator for mixing in the LMS. Dry adiabatic simulations with varying spatial resolution reveal that the spatiotemporal occurrence of GWs depends on model grid spacing and is closely linked to shear and turbulence generation. Further process understanding is gained from experiments incorporating physical processes like latent heating, (vertical) turbulence, and cloud microphysics. Physical processes, such as moisture and latent heat release in the troposphere, significantly influence the extent and occurrence of GWs, and thus, shear and turbulence occurrence in the LMS.

On one hand, introduction of water related physics in simulations revealed that latent heat release and its effect on the overall evolution of the baroclinic wave enhances GWs near the tropopause, leading to substantial shear enhancement in the lower stratosphere. The faster evolution of the baroclinic wave, along with stronger upward motions, substantially affects the presence of GWs in the LMS in terms of number, magnitude, and growth rate. On the other hand, turbulence parameterization has a lesser effect on the overall evolution without moisture, while it dampens the effect of latent heat release in moist simulations.

Another implication of Chapter 3 is that it supports the hypothesis that grid spacing sensitivity is mainly influenced by horizontally propagating GWs with large horizontal wavelengths, which dominate the horizontal derivatives of momentum fluxes, while upward-propagating large-amplitude GWs contribute predominantly to the vertical derivatives of the wind components. This, in turn, leads to much higher shear values and lower Richardson numbers, i.e., more regions prone to become dynamically unstable. Ultimately, this highlights the role of tropospheric dynamics for the potential mixing of air masses due to small-scale dynamics in the LMS.

The results gain above based on idealized studies of the GW-scale cascade process in Chapter 3 are further put in context of a more realistic environment. The main focus of Chapter 4 is to determine

whether the findings from the idealized cases are also evident in the "real" world, or in terms of modeling perspective whether comprehensive models including all parameterizations will result in the same findings as the idealized cases. The airborne in situ observations are used to show that there are GWs in the domain of interest, then three models with different dynamical core are used to determine whether there is a relation between GWs and shear and thereby to the potential turbulence occurrence.

During WISE research flight RF05, the flight path was designed to ascend with time, and the airplane approached the lower stratosphere from the troposphere above the ridge of late stage baroclinic wave that was related to the intense surface cyclone. According to ERA5 and IFS forecast fields, the airplane crossed the region of strong shear layer that was located closely above tropopause and in the proximity of GWs signatures. Moreover, the tracer observations as well as model simulations reveal fine scale structures around the tropopause which are embedded in a region influenced by the inertia GWs, warm conveyor belt ascent and mesoscale modifications of the tropopause structure. The GWs propagate through highly sheared flow above the jet stream maximum, perturbing background wind shear and static stability, and thereby creating conditions conducive to turbulent mixing in the LMS. Thus, the model predicted Ri of the order of 1.

Tracer-tracer correlations of in situ measured CO and N₂O revealed the occurrence of mixed air masses in the form of quasi-isentropic mixing in this region along with small-scale wave like perturbations in the trace gas mixing ratios and the measured potential temperature. These processes took place on scales below the IFS resolution capability. Important fact is that these irreversible mixing and resultant turbulence in the LMS is took place in the vicinity of GW activity as confirmed by the hodograph analysis and power spectral densities indicative of mesoscale turbulence.

In-depth inspection of these processes in different model datasets, the observed significant correlation between GW-induced momentum flux and enhanced shear perturbations confirms the role of GWs in driving potential turbulence and facilitating trace gas exchange in the LMS. Further analysis of empirical turbulence diagnostics computed from the operational forecasts constitutes an important piece of information for the turbulence prediction, which suggests that GWs produce shear that leads to the occurrence of CAT. Turbulence was generated as the GWs perturbed the background wind shear and static stability, promoting the development of bands of reduced Ri , conducive to the generation of KHI and CAT. This analysis suggest the value of GWs to CAT, but also suggest that other algorithms should be developed to account for the degree of imbalance, such as direct detection of inertia GW-induced shear-turbulence, likely proposed by Koch and Caracena (2002), since GWs appear to play an important role in modifying the environment to be more susceptible to shearing instability.

Overall, the results in Chapter 4 broaden our understanding from the idealized results in Chapter 3. For WISE RF05, the GWs processes and GW-induced shear are identified as a key driver for generation of shear, and hence to the modulation of TSL (Kaluza et al., 2021) on the basis of observations, reanalysis and forecast data. We note that GW-induced shear is key for the onset of CAT, and a prerequisite for the potential for dynamic instability and shear induced turbulent mixing above the tropopause. As a consequence, the small-scale mixing processes identified based on the case studies (e.g., Kunkel et al. (2019) and Chapter 4) most potentially contributes substantially to STE in the extratropics. One of the main reason for the significance of frequently occurring small-scale mixing within the LMS is the fact that the GWs are predominant flow feature within the baroclinic flow in the UTLS, with 4-8 baroclinic waves being present in midlatitude zone all the time.

The potential for turbulence and mixing presented in Chapter 3 and 4, is ultimately the consequence of shear and GW-induced shear of the horizontal wind. This is a prerequisite to Chapter 5, as it allows to see the results of Kaluza et al. (2021) in a new light, focusing more on the role of resolved small-scale processes. Although it is known that the strong shear occur above the tropopause region and of which the climatological view was noted previously by Kaluza et al. (2021). However, no explicit representation of annual behavior for such shear occurrence is yet noted. This gap is now closed by the detail investigation of TSL from daily ERA5 data over the singular year in the North Atlantic along with the analysis of GWs influence on its formation and maintenance. The subset of strong vertical wind shear spectrum associated with turbulence is analyzed in terms of vertical, geographical, and seasonal occurrence frequency distribution. Applying a threshold criterion similar to Kaluza et al. (2021), showed that regions of strong shear are most dominantly present in the layer above the extratropical dynamical tropopause. TSL, being a global feature, its occurrence is dependent on different dynamic sources spanning from planetary to synoptic to sub-synoptic scales (Kaluza et al., 2021). Similar to the ExTL, a chemically defined mixing layer, the occurrence of TSL is limited to the first $\sim 2-3$ kms above the local tropopause.

One of the key results of Chapter 5 is that TSL exhibits a pronounced seasonal cycle with maximum values during winter and minimum values during summer. Subsequent analysis of GW momentum fluxes and turbulence diagnostics in a tropopause-relative coordinate system reveals the distinct seasonality of both parameters. The annual pattern of GW momentum fluxes suggests intense GW activity during the formation of shear layers, and have sharp gradients in the vicinity of strong shear. This region, in fact, also characterized by an abundance of turbulent layers across the tropopause and mainly in the upper troposphere. This tendency towards dynamic instability is governed by the strong vertical shear, and thus, the dynamical processes responsible for its occurrence.

Another important outcome of Chapter 5 is that the relative contribution of small-scale GWs to strong shear is found to be substantial, especially in the North Atlantic winter LMS, where vertical momentum flux convergence provides a peak GW forcing up to $-2 \text{ ms}^{-1} \text{ day}^{-1}$ around 45° N at and just above the tropopause. Moreover, the prominent vertical propagation in the wintertime midlatitudes substantially contributes to the formation of belts of GW activity as evident by GW momentum fluxes and thereby leads to the enhanced shear in the LMS. The quasi-climatological patterns of GW activity and shear in Chapter 5 hint that resolved GWs in ERA5 contribute substantially to the climatological structure of the TSL and could further be related to the formation of the ExTL. However, the GWs excited from tropical convection (Müller et al., 2018) could also contribute to the formation of the TSL (Podglajen et al., 2017), and its occurrence in this region vice versa likely influences the spectrum of vertically propagating GWs (Lane, 2021), which has not been within the scope of this study, and seek further investigation.

Apart from the GWs contribution to shear, many questions remain about the GW momentum fluxes and their probability distributions, some of which could be addressed by further analysis on large eddy simulations of individual events in different geographical regions. Relating the momentum fluxes to the phase speeds could also provide a more direct interpretation on a relationship that is commonly used in the parameterizations (e.g., Alexander and Dunkerton, 1999). Moreover, the shear based on GW propagation through the tropopause and lowermost stratosphere have been discussed so far (e.g., Fritts and Alexander, 2003; Kunkel et al., 2019; Kaluza et al., 2021; Umbarkar and Kunkel, 2025; Umbarkar

et al., 2025), yet the effect of GW dissipation on the shear instability remains to be understood. Also, intermittency of GW must be taken into account when extrapolating regional turbulence occurrences to the global statistics in order to properly describe the systems. More case studies based on the in situ observations as well as the climatological view like the one presented in this study might help to better understand the impact of GWs on the energy budget and the turbulent transport in the atmosphere.

Combining all this information, the resulting picture presented by a synthesis of our findings in one cascade of processes across scales: starting with inertia GWs associated with the flow imbalance, proceeding through the generation of enhanced shear mechanism, with excitation of shear instabilities at the small-scales where potential turbulence was generated and ending with the energy-momentum transfer in the vertical. Overall, the analysis highlights GW-induced shear as a key driver of UTLS transport and mixing, as well as a source of high-risk CAT occurrences, meriting further investigation into its prevalence in the geographic location and its potential implications for both climate processes, particularly the redistribution of H₂O and O₃ and their associated radiative forcing, and aviation forecasting.

In summary, the results of this thesis provide physical evidence for the formation of the tropopause shear layer and the ExTL. The latter has first been identified as a global feature on the basis of chemical species only. This thesis provides evidence that the occurrence of GWs and induced turbulence are an essential part for the formation of the ExTL.

6.2 Open questions

- While the idealized study specifically focuses on GWs generated by jet-front systems that emerge during baroclinic wave evolution, starting from the dry dynamics into perspective to results from model simulations with minor changes, i.e., inclusion of moisture to include latent heating and inclusion of turbulence, it does not account for other important GW sources such as orography and convection. Accurately representing these additional sources would require different model configurations, substantially higher spatial resolution, and the inclusion of comprehensive physical parameterizations, e.g., for clouds, radiation, and turbulence.
- As Kaluza et al. (2021, 2022) showed, the TSL occurrence across the tropopause depends on its location and vertical extent of the tropopause altitude. This study has all the required tools to reproduce the analysis for longer timescales with respect to small-scale processes and to investigate the robustness of the results found by Kaluza et al. (2021). Furthermore, it would be interesting to see whether the characteristics of GWs generated from different sources (as well as during various extreme events such as thunderstorms and extratropical cyclones) has any influence on the associated mixing and STE, and whether a merely very steep tropopause, that is not necessary folded, has similar impact on the lower boundary of the TSL.
- The similarities and differences identified in this study are strongly influenced by model configuration, spatiotemporal resolution, and parameterization schemes. A key question is to what extent the resolved GW amplitudes in the extratropics are converged across different resolutions, and how parameterized GW sources interact with the resolved spectrum to shape shear and turbulence structures.
- Existing empirical CAT diagnostics offer valuable operational information but may not fully

capture GW-related processes. Further research should focus on recently developed diagnostic methods such as dissipation due to turbulent mixing (DISS) that includes the contribution due to orographic wave drag and orographic blocking (Beljaars et al., 2004) or TI3 that composites divergence tendency which may capture the generation of inertia GWs via geostrophic adjustment processes or spontaneous imbalance (e.g., Ellrod and Knox, 2010; Knox et al., 2008; Lee et al., 2022), to better characterize the preconditioning of the atmosphere for instability. Further insights into the impact of the tropopause on the GWs by means of additional measurements is desirable not only because the modification of the wave energy is distributed in the atmosphere but also because commercial aircraft tend to fly in the tropopause region. Breaking and trapped GWs as well as mountain waves can cause turbulence (Sharman et al., 2006, 2012).

- While Chapter 5 provides a quasi-climatological view of resolved GW activity and associated shear using ERA5 reanalysis, a more detailed statistical characterization of GWs processes remains an open challenge. In particular, large-eddy simulations of individual events across different geographical regions could help to quantify variability, intermittency, and the underlying physical mechanisms governing GW–shear interactions. Moreover, establishing a more direct relationship between GW momentum flux and phase speed would provide valuable physical insight into processes commonly parameterized in models. This could also improve the realism of GW drag parameterizations in weather and climate models, enabling better representation of TSL and turbulence hotspots.
- Although GW propagation through the tropopause and LMS has been investigated, the impact of GW dissipation on the onset and evolution of shear instabilities under a multi-latitudinal framework remains insufficiently understood. Future work should focus on addressing this which will require both high-resolution modeling and targeted observations to resolve small-scale dissipation processes. Expanding case studies based on in situ observations and combining them with climatological analyses, as demonstrated here, can provide complementary perspectives on GW-induced shear and turbulence. Such an approach can help refine our understanding of GW contributions to the atmospheric energy budget, tropopause shear layer formation, and turbulent transport processes.

In addition to this, current high-resolution global models are capable of resolving GWs, at least partially. In this context, new challenges concerning high-resolution global models have emerged. It is essential to implement scale-aware parameterizations that reduce the influence of parameterized GW forces as resolution enhances, thereby preventing the double counting of the GW effect. Nonetheless, the resolvability of GWs and the influence of GW drag in models characterized by varying dynamical cores (such as spectral models in contrast to grid models) presents a complex and intriguing challenge, representing yet another domain of ongoing research.

Yet, many issues remain open, including the effect of GW on water vapor distribution in the UTLS. Some results from this thesis triggered questions that would require a very different refined approach to be tackled. Although, all this could not be evaluated during doctoral work, it shows the potential of the TSL and importance of GWs topic to open new and interesting lines for future research.

Other possible research topics for the future are listed below:

- For process understanding and as a benchmark for mesoscale parameterization development, it is essential to assess how accurately shear layers, GWs, and the associated mixing in the LS are represented in different reanalysis datasets (such as ERA-Interim (Dee et al., 2011), MERRA-2 (Gelaro et al., 2017), JRA-55 (Kobayashi et al., 2015) and JRA-3Q (Kosaka et al., 2024)) and model simulations. Of particular interest is how the relationship between GWs and shear layers changes with model resolution, e.g., from km-scale to the coarser scales typical of reanalysis and climate models. Further questions should include how these features differ across regions and time periods, whether hemispheric asymmetries or zonal variations exist, and whether their frequency or intensity has changed over time.
- The use of reanalyses for TSL research is encouraged by the results presented in Chapter 5 and Kaluza et al. (2021). The monthly variability of the observed TSL can be compared to the TSL produced by reanalyses mentioned above and if the correlations are good, the TSL can be reconstructed back in time. This way, the TSL variability linked to large-scale processes such as ExTL, Brewer–Dobson circulation and the El-Niño–Southern Oscillation can be estimated with multi-linear regression analysis. Also the multilinear regression analysis is able to separate the different modes of variability associated with the processes mentioned above thanks to their different time-scales.
- In continuation to GWs, the amplitude variations of planetary waves and synoptic scale extratropical waves including Rossby waves, mixed Rossby-GWs, different scale GWs, can be tested against the linear theory: through wave energy density conservation, a relation between wave amplitude and shear should follow, and deviations from this can be detected to show where and when non-linearities occur.

List of Figures

1.1	Schematic of the upper troposphere and lower stratosphere with processes and associated transport time scales, adapted from Hoor (2022).	1
1.2	Averaged profiles of temperature (left) and buoyancy frequency squared (right) representative for northern hemispheric mid-latitudes. Dotted lines indicate sea level based average, solid lines indicate tropopause-based average, and dashed lines indicate profiles of the U.S. standard atmosphere at 45° N. Horizontal lines denote corresponding tropopause altitude. Figure adapted from Birner (2006).	2
1.3	Schematic diagram of an oscillating air parcel in stably stratified atmosphere, where temperature changes with altitude shown by grey line. The temperature of the air parcel follows the dry adiabatic lapse rate T_d (Eq. 3.53 from Wallace and Hobbs, 2006) given as $\Gamma_d = \frac{g}{c_p} = -\left(\frac{dT}{dz}\right)_{dry}$. The buoyancy (B) acts as a restoring force and is calculated from the temperature (T) difference between atmosphere and air parcel temperature and acceleration due to gravity (g). Figure is adapted from Gisinger (2018).	5
1.4	Visible phenomena influenced by gravity waves: (a) undulatus clouds over Trondheim, Norway, (b) rotor clouds over Vienna, Austria (photo by P. Punde), (c) photo taken on board German High Altitude Long (HALO) research aircraft at 27.09.2017, 15:03 UTC during WISE RF07 showing Kelvin–Helmholtz cloud billows on top of a cirrus cloud deck (photo by P. Hoor), (d) lenticular clouds above Mosier, Oregon, USA, (e) wind shear along the upper surface of one cloud was producing Kelvin-Helmholtz billows (photo by K. Pogue), (f) small-scale structures in cirrus clouds over Bodenheim, taken directly south of Mainz (by author), and (g) New Zealand (photo by B. Kaifler), (h) wave structures in noctilucent clouds over Stockholm (photo by K. Cho). Source: Photo in d, e, g, and h are taken from Wikipedia.	6
1.5	Schematic of seven year temporal and zonal average (2002–2008) of (a) ozone and (b) carbon monoxide for winter in the Ex-UTLS in tropopause relative coordinates, adapted from Gettelman et al. (2011). The thermal tropopause is indicated with thick black line. The dashed black line indicates the 100 ppbv ozone contour, whereas dashed white lines represent isentropes from 310 K (bottom) to 480 K (top). The distributions reveal strong horizontal and vertical tracer gradients across the tropopause in both species.	8
1.6	Vertical profile of CO obtained during SPURT 6 mission as function of (left) potential temperature and, (right) potential temperature relative to the local tropopause $\Delta\Theta$, adapted from Hoor et al. (2004). The distributions reveal more compact $\Delta\Theta$ profile and rather sharp change of the gradients of CO.	9

- 1.7 Vertical cross section of annual and zonal mean static stability calculated using the GPS temperature profiles from the CHAMP (Challenging Minisatellite Payload) satellite. The thick solid black line shows the annual and zonal mean thermal tropopause height. The thin white contours shows the shading intervals for values $N^2 \geq 6 \times 10^{-4} \text{ s}^{-2}$. The annual mean is based on data averaged over April 2002–March 2008. Figure adapted from Grise et al. (2010). ©American Meteorological Society. 10
- 1.8 Vertical profiles of zonal mean N^2 (10^{-4} s^{-2} ; black), H_2O mixing ratio (ppmv; blue), O_3 (ppmv; solid grey) and CO (dashed grey; factor 20) relative to thermal tropopause for June-July-August (JJA) at 70° N , adapted from Hegglin et al. (2009). 11
- 1.9 Occurrence frequency distribution of $S^2 \geq S_r^2$ with tropopause-based vertical coordinate system based on 10 year Northern hemispheric ERA5 climatology. The solid thick line shows mean lapse rate tropopause altitude. The occurrence frequencies are shown with logarithmic frequency contours, vertically binned with $\Delta z = 500 \text{ m}$. Dashed thin black line indicates the effect of the cut-off of 1.5 km above orography. Solid (dotted) white line indicates where decreasing (increasing) horizontal winds with altitude constitute 75% of $S^2 \geq S_r^2$. Figure adapted from Kaluza et al. (2021). 12
- 2.1 Illustration of (a) an icosahedron mapped onto the sphere, (b) the corresponding global ICON grid at **R2B2** resolution, and (c) regular latitude–longitude grid for comparison. 24
- 2.2 Vertical cross-section of vertical velocity at the equator comparing (a) the non-hydrostatic EULAG simulation with (b) non-hydrostatic and (c) hydrostatic IFS simulations for a linearly-sheared flow past a quasi-two-dimensional obstacle at the equator on the reduced-size sphere. The atmosphere is vertically-stratified and there is a zonal flow of 10 m s^{-1} impinging on the mountain near the surface, increasing linearly to 35 m s^{-1} at 10.5 km (or approximately 687 hPa) and constant above. Contour interval is 0.05 m s^{-1} ; blue/red lines denote positive/negative contours. Figure adapted from Wedi and Malardel (2010). 32
- 2.3 Example of small-scale deviations from the large-scale flow in an MS_GWaM (Multi-Scale Gravity Wave Model) simulation at 11 km altitude. Panels (a, b) show the distribution of total horizontal wind components (u and v), while panel (c, d) presents the decomposed divergent (u_{div} and v_{div}) wind components gained after using Helmholtz decomposition technique. Panels (e, f) show the perturbation components (u' and v') byproduct after the spectral filtering applied to the u_{div} and v_{div} components. 36
- 2.4 Schematic of the hodograph method, adapted from Strelnikova et al. (2020). The altitude profile of horizontal velocity fluctuations (a), the colored are marks the altitude range of one wavelength where wave amplitude is most significant. The corresponding hodograph ellipse of GW horizontal velocity variations (u' and v') from the marked region in (a) is shown in panel (b). Dashed line shows major axis of ellipse depicting propagation direction of the wave, number around ellipse shows altitude. 38

2.5	Schematic of tracer-tracer correlation (a) N_2O – CO and (c) O_3 – CO , and (b) vertical profile of N_2O with Θ in vertical. The purple, black axis lines in (a) and (c) form the “L” shape characteristic of conditions without mixing. The two straight red dashed lines in (a) and (c) represent rapid, isentropic exchange and thus irreversible mixing between the troposphere and stratosphere, that are also seen in the vertical profile in (b). The curved blue line indicates incomplete or slow mixing, during which stratospheric CO has been chemically degraded.	39
3.1	Zonally symmetric balanced initial conditions at 30° E longitude: zonal wind ‘ u ’ (shaded contours, 5 m s^{-1} spacing), potential temperature ‘ Θ ’ (solid black lines, 15 K spacing, starting with 280 K in the lower right corner) and specific humidity q_v for values $0.002, 0.02, 0.05, 0.2, 0.5, 1.0 \text{ g kg}^{-1}$ (dotted lines, from bottom to top), the thick dashed line marks the location of dynamical tropopause, defined as the 3.5 pvu potential vorticity isosurface.	45
3.2	The evolution of the baroclinic life cycle for the (a) REF_{wind} and (b) $\text{REF}_{\text{stream}}$ simulation. Horizontal cross sections of potential vorticity at 340 K isentropic surface and surface pressure (dashed contours) over the Northern Hemisphere after $240, 264, 288$ and 312 h of model integration. The solid black line represents the 3.5 PVU , regarded as a dynamical tropopause.	47
3.3	The evolution of the GWs for the (a) REF_{wind} and (b) $\text{REF}_{\text{stream}}$ simulation. Horizontal cross sections of horizontal divergence at 11 km altitude over the Northern Hemisphere after $240 \text{ h}, 264 \text{ h}, 288 \text{ h}$ and 312 h of model integration time, respectively. The solid black line represents the dynamical tropopause.	48
3.4	Evolution of GWs for simulations with varying grid spacings. Panels (a-d) represent simulations with wind perturbations for experiments $\text{REF}, \text{HRES}, \text{MRES},$ and MRES40 , respectively, while panels (e-f) show simulations with stream perturbations for the same configurations. The figure displays the distribution of the horizontal divergence field at 11 km altitude over the Northern Hemisphere after 288 h of model integration.	50
3.5	Time evolution from 192 h to 264 h , of surface pressure (dashed contours), surface potential temperature (solid contours, every 5 K), and (for the moist simulation only) relative humidity at 850 hPa (colored, %). (a) REF_{wind} , (b) $\text{REF}_{\text{wind}} \text{ MOIST}$ and (c) $\text{REF}_{\text{wind}} \text{ TURB MOIST}$ simulations.	51
3.6	As in Figure 3.4 but after 264 h for the simulations with varying physical processes. Top panel (a, g) represents the corresponding reference simulations.	52
3.7	Horizontal evolution of 11 km perturbation vertical velocity w' in mm s^{-1} from 240 h to 312 h of model integration for REF_{wind} and $\text{REF}_{\text{stream}}$ experiment. The absolute GW momentum flux ($1.0, 1.5$ and 2.0 in $\log_{10}(\text{mpa})$; black) and vertical wind shear perturbations S^2 ($1.0, 2.5, 4.0$ in 10^{-4} s^{-2} ; red) from the spectral domain. The turquoise lines denote the 11 km dynamical tropopause where potential vorticity equals 3.5 PVU	54
3.8	Horizontal evolution of static stability N^2 at 11 km from 240 h to 312 h of model integration for REF_{wind} experiment. The dashed black lines denote the 11 km dynamical tropopause where PV equals 3.5 PVU	55

3.9	The temporal evolution of PDFs of static stability, N^2 in the LMS for dry reference experiments.	55
3.10	The temporal evolution of PDFs of vertical wind shear, S^2 in the LMS for dry reference experiments. The dashed histograms represents shear perturbations $S^{2'}$ from spectral domain for the respective REF simulations.	56
3.11	Temporal evolution of relative occurrence frequency distribution of N^2 (a, d), S^2 (b, e) and $S^{2'}$ (c, f) in the LMS over the Northern Hemisphere. Upper panel (a, b, c) represents grid spacing sensitivity experiments. Lower panel (d, e, f) represents physics sensitivity experiments performed using wind perturbation function. LMS is defined as the region between 3.5 PVU, a dynamical tropopause and 380 K isentropic surface.	57
3.12	Relative occurrence frequency distribution of N^2 - S^2 (upper panel) and N^2 - $S^{2'}$ (lower panel) pair plot after 288 h for simulations with varying grid sensitivity over Northern Hemisphere in the LMS. Logarithmic occurrence frequency color scale is applied. Dashed lines indicates the gradient Richardson numbers.	58
3.13	As in Figure 3.12 but after 288 h for the REF _{wind} simulations with varying physical processes.	59
3.14	Vertical cross section of (a, b) turbulent kinetic energy (TKE, in m^2s^{-2}) and (c, d) buoyant heat flux (BHF, in $\text{K m}^2\text{s}^{-1}$) for simulations REF _{wind} TURB CMP & REF _{wind} TURB MOIST. The green lines in c and d indicate maximum TKE with cloud ice content (q_c , in kg kg^{-1}) in blue.	60
3.15	Relative occurrence frequency or probability density distribution of absolute momentum flux due to GWs–vertical shear perturbations $S^{2'}$ pair in the LMS for $Ri \leq 5$ after 288 h (upper panel) and 312 h (lower panel) for simulations with grid spacing sensitivity. Normalized counts of PDFs distribution is shown where logarithmic occurrence frequency color scale is applied.	61
3.16	As in Figure 3.15 but for simulations with physical processes sensitivity. Normalized counts of PDFs distribution is shown where logarithmic occurrence frequency color scale is applied.	61
3.17	The temporal evolution of (a) vertical cross section of shear through the identified regions of GWs from time 240 h onward for REF _{wind} simulation with $S^{2'}$ (dashed green), potential temperature (grey), zonal wind (30 m s^{-1} , red) and dynamical tropopause (black) and (b) the respective Northern hemispheric occurrence frequency distribution of grid volumes that exhibit $S^2 \geq S_t^2$. Logarithmic frequency contour, vertically binned in $dz=500 \text{ m}$ is applied. The zonal mean value of 3.5 PVU in the PV field (dashed black line), and the zonal mean value of 380 K in the potential temperature field (grey dashed line) is overlaid.	62
3.18	Vertical cross section of shear (a-d) through the identified regions of GWs at 264 h REF _{wind} simulations with physical processes sensitivity and the respective Northern Hemispheric occurrence frequency distribution of grid volumes that exhibit $S^2 \geq S_t^2$ (e-h). Logarithmic frequency contour, vertically binned in $dz=500 \text{ m}$ is applied. The zonal mean dynamical tropopause altitude is indicated by the dashed black line and tropical tropopause (380 K isentrope) by grey dashed line.	63

3.19	Initial background state of (a) JABW and (b) DCMIP test case, shaded contours represent static stability at 30° E longitude with potential temperature Θ (solid black lines, 10 K spacing, starting with 280 K in the lower right corner).	64
4.1	Flight pattern of WISE research flight 05. Color code indicates flight altitude, red dashed line shows surface projection of the flight path.	68
4.2	Snapshot of the atmosphere at 11:00 UTC on 23 September 2017 using ERA5 potential vorticity (PVU) and horizontal wind velocity (m s^{-1}). The two nested domain boundaries are set for the reference. Through potential vorticity contours one can clearly see the prominent tropopause fold and pv streamers. The star denotes the flight location at this time.	70
4.3	Time series of measured (a) N_2O (blue), Θ (red), and (b) ERA5 vertical shear, potential vorticity (navy) and gradient Richardson Ri interpolated on flight track. The black line denotes the flight altitude. Light yellow boxes indicates the flight section for the detailed mixing analysis. The corresponding altitude track is shown in Figure 4.2.	71
4.4	Vertical profile of (a) CO and (b) N_2O and tracer-tracer correlation of the mixing ratios of (c) N_2O and CO that were measured during WISE RF05.	72
4.5	Vertical profile of CO (a–c) and N_2O (d–f), and tracer-tracer correlation of the mixing ratios of N_2O and CO that were measured during WISE RF05 for time periods between 10:45-11:30 UTC (left), 11:30-12:40 UTC (middle) and 12:40-13:05 UTC (right), color-coded with potential temperature.	72
4.6	Power spectral density of (a, b) w and Θ from BAHAMAS and (c, d) of N_2O and CO measured during WISE RF05 zoom in for the shaded yellow regions of Figure 4.3. Black solid lines are introduced for better comparability. The black and red reference lines have slopes of 5/3 and 3.	74
4.7	Time series of (a) zonal (u , m s^{-1} ; green) and meridional (v , m s^{-1} ; orange) wind component from HALO for WISE RF05, whereas panel (b) shows perturbation of u and v obtained from Butterworth filter for the whole flight period. The shaded yellow regions highlight period of interest same as Figure 4.3.	75
4.8	Time series (a, c) of zonal (u , m s^{-1} ; green) and meridional (v , m s^{-1} ; orange) wind component measured during WISE RF05 zoom in for the shaded yellow regions of Figure 4.3. Perturbation hodographs for the corresponding flight period on left are shown in panel (c) and (d).	76
4.9	Distribution of horizontal divergence at 12.5 km altitude for (a) ERA5 and (b) IFS datasets. The dashed lines in upper panel represent corresponding horizontal wind speed for values greater than 30 m s^{-1} . The RF05 flight path from 10:55 UTC to 11:45 UTC is indicated in blue, HALO location at 11:00 UTC shown by blue star. The corresponding vertical cross sections of divergence at 14.05° W is shown in lower panel (c-d). The solid black line represent the 3.5 PVU as a dynamical tropopause whereas dashed lines in lower panel represent the potential temperature starting from 280 K (bottom) to 380 K (top) with 10 K increments.	77

- 4.10 Distribution of vertical wind shear at 12.5 km altitude for (a) ERA5 and (b) IFS. The dashed black lines in upper panel presents the horizontal wind speed for values greater than 30 m s^{-1} , 3.5 PVU isoline in magenta and solid lines represent the $Ri < 1$ (black) and $Ri = 1.25$ (grey) at 12.5 km altitude. The star marker indicates the position of flight at 11:00 UTC. The corresponding vertical cross sections of vertical shear at 14.05° W is shown in lower panel (c-d). The solid line in lower panel represents the 3.5 PVU as a dynamical tropopause whereas dashed lines represents the potential temperature starting from 280 K (bottom) to 380 K (top) with 10 K increments. 78
- 4.11 Relative occurrence frequency distribution of AMF- S^2 shear perturbations pair in the LMS for $0 \leq Ri \leq 1$ for (a) ERA5 and (b) IFS. Normalized counts of PDFs distribution is shown. Logarithmic occurrence frequency color scale is applied. 79
- 4.12 Distribution of turbulent indices TI1 (upper panel) and TI2 (lower panel) at 12.5 km altitude for ERA5 (a, c) and IFS (b, d). The dashed black lines indicate horizontal wind speeds exceeding 30 m s^{-1} 80
- 4.13 Relative occurrence frequency distribution of (a) TI1 and (b) TI2 for ERA5 and IFS in the LMS. Corresponding to histogram, colored dashed lines indicate threshold retrieved as the 95th percentile over the LMS domain distribution that is considered as threshold for light moderate category. Grey and aqua lines represent the threshold for moderate ($7.5\text{--}12 \times 10^{-7} \text{ s}^{-1}$) and moderate to greater (MOG; $>12 \times 10^{-7} \text{ s}^{-1}$) intensity CAT, respectively. 81
- 4.14 Relative occurrence frequency distribution of (a-b) TI1 and (c-d) TI2 and AMF pair in the LMS for ERA5 and IFS datasets. Normalized occurrence frequencies of the joint PDFs are shown in a logarithmic color scale. 82
- 4.15 Distribution of horizontal divergence (upper panel) and vertical wind shear (lower panel) at 12.5 km altitude for ICON 13 km, 6.5 km and 3.3 km resolution nested simulations overlaid with flight location at 11:00 UTC shown by star. The dashed line represent corresponding horizontal wind speed for values greater than 30 m s^{-1} 83
- 4.16 Relative occurrence frequency distribution of absolute momentum flux due to GWs-vertical shear perturbations pair in the LMS for $0 \leq Ri \leq 1$ for ICON 13 km, 6.5 km and 3.3 km resolution nested simulations at 11:00 UTC. Normalized counts of PDFs distribution is shown. Logarithmic occurrence frequency color scale is applied. 84
- 4.17 Distribution of turbulence indices TI1 (upper panel) and TI2 (lower panel) at 12.5 km altitude for ICON 13 km, 6.5 km and 3.3 km resolution nested simulations. The dashed line represent corresponding horizontal wind speed for values greater than 30 m s^{-1} 85
- 4.18 Relative occurrence frequency distribution of (a) TI1 and (b) TI2 for three ICON nested domains in the LMS. Corresponding to histogram, colored dashed lines indicate threshold retrieved as the 95th percentile over the LMS domain distribution that is considered as threshold for light moderate category. Grey and aqua lines represent the threshold for moderate ($7.5\text{--}12 \times 10^{-7} \text{ s}^{-1}$) and moderate to greater ($>12 \times 10^{-7} \text{ s}^{-1}$) intensity CAT, respectively. 85

4.19	Frequency (%) distribution of absolute momentum flux–turbulent indices TI1 (a-c), TI2 (d-f) in pairs over the LMS for ICON 13 km, 6.5 km and 3.3 km resolution nested simulations at 11:00 UTC. Normalized counts of PDFs distribution is shown. Logarithmic occurrence frequency color scale is applied.	86
5.1	Potential vorticity at 340 K isentropic surface over the Northern Hemisphere on 11 September 2017, 00:00 UTC. The solid black lines represents the horizontal wind beginning at 30 m s^{-1} in steps of 15 m s^{-1} at 200 hPa pressure surface. Magenta shaded areas represent regions of $S^2 \geq S_t^2$ where $S_t^2 = 4 \times 10^{-4} \text{ s}^{-2}$, between 3.5 PVU dynamical tropopause and 1 km above. (Adapted from Kaluza et al. (2021) Figure 01).	93
5.2	Occurrence frequency distribution of (a) $S^2 \geq S_t^2$ from March 2017 to February 2018. The occurrence frequencies are shown with logarithmic frequency contours, displaying the data in bins of sizes $\Delta y = 0.4^\circ$ and $\Delta z = 500 \text{ m}$. The zonal-mean dynamical tropopause (3.5 PVU isosurface; black solid line) and the zonal-mean 380 K isentrope of potential temperature (black dashed line) are overlaid.	94
5.3	The 200-hPa monthly mean zonal wind (shaded; m s^{-1}) and horizontal wind vectors (arrows) over the North Atlantic from March 2017 to February 2018. Magenta shaded areas represent monthly mean occurrences of strong vertical wind shear $S^2 \geq S_t^2$ between 3.5 PVU dynamical tropopause and 1.5 km above.	95
5.4	Occurrence frequency distribution of $S^2 \geq S_t^2$ over the LMS in the NA from March 2017 to February 2018. The solid black lines represents the horizontal wind $>30 \text{ m s}^{-1}$ at 11 km altitude.	96
5.5	Zonal mean resolved GW absolute momentum flux (AMF, $\log_{10}(\text{mPa})$) conditioned on regions where $S^2 \geq S_t^2$ from March 2017 to February 2018. The data is shown in bins of sizes $\Delta y = 0.4^\circ$ and $\Delta z = 500 \text{ m}$. The zonal-mean dynamical tropopause (3.5 PVU isosurface; black solid line) and the zonal-mean 380 K isentrope of potential temperature (black dashed line) are overlaid.	97
5.6	Monthly occurrence frequency distribution of $0 \leq Ri \leq 1$ with tropopause-based vertical coordinate system from March 2017 to February 2018. The occurrence frequencies are shown with logarithmic frequency contours, displaying the data in bins of sizes $\Delta y = 0.4^\circ$ and $\Delta z = 500 \text{ m}$. The zonal mean dynamical tropopause (3.5 PVU isosurface; black solid line) and the zonal mean 380 K isentrope of potential temperature (black dashed line) are overlaid.	99
5.7	Monthly occurrence frequency distribution of $TI1 \geq 7 \times 10^{-7} \text{ s}^{-1}$ from March 2017 to February 2018. The occurrence frequencies are shown with logarithmic frequency contours, displaying the data in bins of sizes $\Delta y = 0.4^\circ$ and $\Delta z = 500 \text{ m}$, alongwith the zonal mean dynamical tropopause (3.5 PVU isosurface; black solid line), and the zonal mean 380 K isentrope of potential temperature (black dashed line).	99
5.8	As in Figure 5.7 but for TI2.	100
5.9	Monthly occurrence frequency distribution of VMFC (in $\text{m s}^{-1} \text{ day}^{-1}$) between dynamical tropopause and 1.5 km above in the North Atlantic from March 2017 to February 2018. The solid black lines represents the horizontal wind $>30 \text{ m s}^{-1}$ at 11 km altitude.	102
5.10	Same as Figure 5.9 but for the distribution of GW absolute momentum flux (in $\log_{10}(\text{mPa})$).	103

5.11	Relative occurrence frequency distribution of N^2-S^2 pairs from March 2017 to February 2018. The occurrence frequencies are shown with logarithmic frequency contours. The black dashed line represent the $Ri=1$	104
5.12	Relative occurrence frequency distribution of (a) Ri in the vicinity of $S^2 \geq S_r^2$ and (b) the logarithm of absolute momentum flux conditioned on $S^2 \geq S_r^2$ associated with $0 \leq Ri \leq 1$ displayed in panel (a) in the LMS from March 2017 (blue) to February 2018 (red). The black dashed line in (a) represent the $Ri=1$	104
5.13	Relative frequency distribution of (a) S^2 , (b) $S^{2'}$ and (c) absolute GW momentum flux over the LMS from March 2017 to February 2018.	105
5.14	Relative occurrence frequency distribution of AMF due to GWs and shear perturbations pair in the LMS for $0 \leq Ri \leq 1$ over the NA from March 2017 to February 2018. Normalized counts of PDFs distribution with the logarithmic occurrence frequency color scale is shown.	106
5.15	Same as Figure 5.14 but for VMFC vs. vertical shear S^2 . Dashed white line indicate $S^2=S_r^2$. Vertical dashed lines mark the ± 0.5 range for readability.	107
S3.1	The distribution of horizontal divergence at 11 km altitude after 288 h in the LRES experiment indicates that gravity wave signatures are virtually absent in the lower-resolution simulation.	144
S3.2	Temporal evolution of relative occurrence frequency distribution of N^2-S^2 pairs for simulations with varying grid sensitivity over Northern Hemisphere in the lowermost stratosphere. Logarithmic occurrence frequency color scale is applied. Dashed lines indicates the gradient Richardson numbers.	145
S3.3	Temporal evolution of relative occurrence frequency distribution of $N^2-S^{2'}$ pairs for simulations with varying grid sensitivity over Northern Hemisphere in the lowermost stratosphere. Logarithmic occurrence frequency color scale is applied. Dashed lines indicates the gradient Richardson numbers.	146
S3.4	As in Figure S3.2 but for the REF _{wind} simulations with varying physical processes. . . .	147
S3.5	As in Figure S3.3 but for the REF _{wind} simulations with varying physical processes. . . .	148

List of Tables

2.1	Commonly used ICON resolutions in R_nB_k notation.	24
2.2	Physics parameterization schemes used for ICON_NWP simulations used in Chapter 4.	34
3.1	Summary of idealized DCMIP experiments performed using ICON *MOIST: only saturation adjustment, CMP: saturation adjustment + bulk microphysics scheme	46
6.1	Use of AI tools throughout the work.	149

Acronyms

AMF Absolute Momentum Flux

BAHAMAS Basic HALO Measurement and Sensor System

BDC Brewer–Dobson circulation

BLC baroclinic life cycles

CAT Clear air turbulence

CPT Cold Point Tropopause

Cy43r3 IFS model cycle identifier

DJF December January February

ECMWF European Centre for Medium-Range Weather Forecast

ENSO El Niño Southern Oscillation

ERA5 Fifth generation of atmospheric reanalysis from the ECMWF

ExTL Extratropical transition layer

ExUTLS Extratropical Upper Troposphere Lower Stratosphere

GW Gravity Wave

GWMF Gravity wave absolute momentum flux

HALO High Atitude LOng range aircraft

ICON ICOSahedral Non-hydrostatic model

IFS Integrated Forecasting System

JGU Johannes Gutenberg-University

JJA June July August

KHI Kelvin-Helmholtz instability

LC1 Life cycle 1

LC2 Life cycle 2

LMS Lowermost Stratosphere

LRT Lapse Rate Tropopause

LS Lower Stratosphere

MAM March April May

MF Momentum Flux

PFJ Polar Front jet

PV Potential Vorticity

RF Research flight

RRTM Rapid Radiative Transfer Model

SON September October November

STE Stratosphere-troposphere exchange

STJ Subtropical jet

STT Stratosphere-Troposphere-Transport

TEJ Tropical easterly jet

TIL Tropopause inversion layer

TSL Tropopause Shear Layer

TST Troposphere to stratosphere transport

TTL Tropical tropopause layer

TURBDIFF TURBulent DIFFusion

UMAQS University of Mainz Airborne Quantum Cascade Laser Spectrometer

UT Upper Troposphere

UTC Universal Time Coordinated

UTLS Upper Troposphere Lower Stratosphere

WCB Warm Conveyor Belt

WISE Wave-driven ISentropic Exchange

WMO World Meteorological Organization

WRF Weather Research and Forecasting

Bibliography

- Achatz, U., Alexander, M. J., Becker, E., Chun, H.-Y., Dörnbrack, A., Holt, L., Plougonven, R., Polichtchouk, I., Sato, K., Sheshadri, A., Stephan, C. C., van Niekerk, A., and Wright, C. J.: Atmospheric Gravity Waves: Processes and Parameterization, *Journal of the Atmospheric Sciences*, 81, 237–262, <https://doi.org/10.1175/jas-d-23-0210.1>, 2024.
- Alexander, M. J. and Dunkerton, T. J.: A Spectral Parameterization of Mean-Flow Forcing due to Breaking Gravity Waves, *Journal of the Atmospheric Sciences*, 56, 4167–4182, [https://doi.org/10.1175/1520-0469\(1999\)056<4167:aspomf>2.0.co;2](https://doi.org/10.1175/1520-0469(1999)056<4167:aspomf>2.0.co;2), 1999.
- Alexander, M. J., Geller, M., McLandress, C., Polavarapu, S., Preusse, P., Sassi, F., Sato, K., Eckermann, S., Ern, M., Hertzog, A., Kawatani, Y., Pulido, M., Shaw, T. A., Sigmond, M., Vincent, R., and Watanabe, S.: Recent developments in gravity-wave effects in climate models and the global distribution of gravity-wave momentum flux from observations and models, *Quarterly Journal of the Royal Meteorological Society*, 136, 1103–1124, <https://doi.org/10.1002/qj.637>, 2010.
- Andrews, D. G., Taylor, F. W., and McIntyre, M. E.: The Influence of Atmospheric Waves on the General Circulation of the Middle Atmosphere [and Discussion], *Philosophical Transactions of the Royal Society of London. Series A, Mathematical and Physical Sciences*, 323, 693–705, <http://www.jstor.org/stable/38143>, 1987.
- Appenzeller, C., Holton, J. R., and Rosenlof, K. H.: Seasonal variation of mass transport across the tropopause, *Journal of Geophysical Research: Atmospheres*, 101, 15 071–15 078, <https://doi.org/10.1029/96jd00821>, 1996.
- Assmann, R.: Über die Existenz eines wärmeren Luftstromes in der Höhe von 10 bis 15 km (On the existence of a warmer airflow at heights from 10 to 15 km), *Sitzungsberichte der Königlich Preussischen Akademie der Wissenschaften zu Berlin*, 24, 495–504, 1902.
- Assonov, S., Brenninkmeijer, C., Schuck, T., and Umezawa, T.: N₂O as a tracer of mixing stratospheric and tropospheric air based on CARIBIC data with applications for CO₂, *Atmospheric Environment*, 79, 769–779, <https://doi.org/10.1016/j.atmosenv.2013.07.035>, 2013.
- Banerjee, T., Borchert, S., Kim, Y.-H., Kosareva, A., Kunkel, D., Masur, G. T., Procházková, Z., Schmidli, J., Voelker, G. S., and Achatz, U.: The Impact of Non-Orographic Gravity Waves on Transport and Mixing: Effects of Oblique Propagation and Coupling to Turbulence, <https://arxiv.org/abs/2508.20562>, 2025.
- Bechtold, P., Köhler, M., Jung, T., Doblas-Reyes, F., Leutbecher, M., Rodwell, M. J., Vitart, F., and Balsamo, G.: Advances in simulating atmospheric variability with the ECMWF model: From synoptic to decadal time-scales, *Quarterly Journal of the Royal Meteorological Society*, 134, 1337–1351, <https://doi.org/10.1002/qj.289>, 2008.
- Bechtold, P., Semane, N., Lopez, P., Chaboureaud, J.-P., Beljaars, A., and Bormann, N.: Representing Equilibrium and Nonequilibrium Convection in Large-Scale Models, *Journal of the Atmospheric Sciences*, 71, 734–753, <https://doi.org/10.1175/jas-d-13-0163.1>, 2014.
- Beljaars, A. C. M., Brown, A. R., and Wood, N.: A new parametrization of turbulent orographic form drag, *Quarterly Journal of the Royal Meteorological Society*, 130, 1327–1347, <https://doi.org/>

- 10.1256/qj.03.73, 2004.
- Bense, V.: Modifikation von Schwerewellen bei Propagation durch die Tropopause - Idealisierte Modellstudien, Ph.D. thesis, Johannes Gutenberg-Universität Mainz, <https://doi.org/10.25358/OPENSOURCE-2356>, 2019.
- Berthet, G., Esler, J. G., and Haynes, P. H.: A Lagrangian perspective of the tropopause and the ventilation of the lowermost stratosphere, *Journal of Geophysical Research: Atmospheres*, 112, <https://doi.org/10.1029/2006jd008295>, 2007.
- Birner, T.: Fine-scale structure of the extratropical tropopause region, *Journal of Geophysical Research: Atmospheres*, 111, <https://doi.org/10.1029/2005jd006301>, 2006.
- Birner, T.: Residual Circulation and Tropopause Structure, *Journal of the Atmospheric Sciences*, 67, 2582–2600, <https://doi.org/10.1175/2010jas3287.1>, 2010.
- Birner, T., Dörnbrack, A., and Schumann, U.: How sharp is the tropopause at midlatitudes?, *Geophysical Research Letters*, 29, <https://doi.org/10.1029/2002gl015142>, 2002.
- Bolton, D.: The Computation of Equivalent Potential Temperature, *Monthly Weather Review*, 108, 1046–1053, [https://doi.org/10.1175/1520-0493\(1980\)108<1046:tcoept>2.0.co;2](https://doi.org/10.1175/1520-0493(1980)108<1046:tcoept>2.0.co;2), 1980.
- Broutman, D. and Grimshaw, R.: The energetics of the interaction between short small-amplitude internal waves and inertial waves, *Journal of Fluid Mechanics*, 196, 93–106, 1988.
- Butterworth, S. et al.: On the theory of filter amplifiers, *Wireless Engineer*, 7, 536–541, 1930.
- Colson, D. and Panofsky, H. A.: An index of clear air turbulence, *Quarterly Journal of the Royal Meteorological Society*, 91, 507–513, <https://doi.org/10.1002/qj.49709139010>, 1965.
- Danielsen, E. F.: The laminar structure of the atmosphere and its relation to the concept of a tropopause, *Archiv für Meteorologie, Geophysik und Bioklimatologie Serie A*, 11, 293–332, <https://doi.org/10.1007/bf02247210>, 1959.
- Danielsen, E. F.: Stratospheric-Tropospheric Exchange Based on Radioactivity, Ozone and Potential Vorticity, *Journal of the Atmospheric Sciences*, 25, 502–518, [https://doi.org/10.1175/1520-0469\(1968\)025<0502:stebor>2.0.co;2](https://doi.org/10.1175/1520-0469(1968)025<0502:stebor>2.0.co;2), 1968.
- de Medeiros, J. and Williams, P. D.: Future Trends in Upper-Atmospheric Shear Instability from Climate Change, *Journal of the Atmospheric Sciences*, 82, 2375–2392, <https://doi.org/10.1175/jas-d-24-0283.1>, 2025.
- Dee, D. P., Uppala, S. M., Simmons, A. J., Berrisford, P., Poli, P., Kobayashi, S., Andrae, U., Balmaseda, M. A., Balsamo, G., Bauer, P., Bechtold, P., Beljaars, A. C. M., van de Berg, L., Bidlot, J., Bormann, N., Delsol, C., Dragani, R., Fuentes, M., Geer, A. J., Haimberger, L., Healy, S. B., Hersbach, H., Hólm, E. V., Isaksen, I., Kållberg, P., Köhler, M., Matricardi, M., McNally, A. P., Monge-Sanz, B. M., Morcrette, J., Park, B., Peubey, C., de Rosnay, P., Tavolato, C., Thépaut, J., and Vitart, F.: The ERA-Interim reanalysis: configuration and performance of the data assimilation system, *Quarterly Journal of the Royal Meteorological Society*, 137, 553–597, <https://doi.org/10.1002/qj.828>, 2011.
- Doms, G., Förstner, J., Heise, E., Herzog, H.-J., Mironov, D., Raschendorfer, M., Reinhardt, T., Ritter, B., Schrodin, R., Schulz, J.-P., and Vogel, G.: Consortium for Small-Scale Modelling A Description of the Nonhydrostatic Regional COSMO Model Part II : Physical Parameterization, *Www.Cosmo-Model.Org*, p. 152, 2011.
- Dörnbrack, A.: Turbulent mixing by breaking gravity waves, *Journal of Fluid Mechanics*, 375, 113–141,

- <https://doi.org/10.1017/S0022112098002833>, 1998.
- Dörnbrack, A., Bechtold, P., and Schumann, U.: High-Resolution Aircraft Observations of Turbulence and Waves in the Free Atmosphere and Comparison With Global Model Predictions, *Journal of Geophysical Research: Atmospheres*, 127, <https://doi.org/10.1029/2022jd036654>, 2022.
- Dörnbrack, A., Lachnitt, H., Hoor, P., and Imazio, P. R.: Multiscale Dynamical Processes Shaping a Mixing Line, *Journal of Geophysical Research: Atmospheres*, 130, <https://doi.org/10.1029/2025jd043527>, 2025.
- Dunkerton, T. J.: The role of gravity waves in the quasi-biennial oscillation, *Journal of Geophysical Research: Atmospheres*, 102, 26 053–26 076, <https://doi.org/https://doi.org/10.1029/96JD02999>, 1997.
- Durrán, D. R.: Pseudomomentum Diagnostics for Two-Dimensional Stratified Compressible Flow, *Journal of Atmospheric Sciences*, 52, 3997 – 4009, [https://doi.org/10.1175/1520-0469\(1995\)052<3997:PDFTDS>2.0.CO;2](https://doi.org/10.1175/1520-0469(1995)052<3997:PDFTDS>2.0.CO;2), 1995.
- ECMWF: IFS Documentation CY41R2 - Part IV: Physical Processes, ECMWF, <https://doi.org/10.21957/TR5RV27XU>, 2016b.
- ECMWF: Convection, pp. 75–95, European Centre for Medium-Range Weather Forecasts (ECMWF), Reading, UK, 2017.
- Ellrod, G., Knox, J., Lester, P., and Ehernberger (Retired), L.: AVIATION METEOROLOGY | Clear Air Turbulence, p. 177–186, Elsevier, ISBN 9780123822253, <https://doi.org/10.1016/b978-0-12-382225-3.00104-3>, 2015.
- Ellrod, G. P. and Knapp, D. I.: An Objective Clear-Air Turbulence Forecasting Technique: Verification and Operational Use, *Weather and Forecasting*, 7, 150–165, [https://doi.org/10.1175/1520-0434\(1992\)007<0150:aocatf>2.0.co;2](https://doi.org/10.1175/1520-0434(1992)007<0150:aocatf>2.0.co;2), 1992.
- Ellrod, G. P. and Knox, J. A.: Improvements to an Operational Clear-Air Turbulence Diagnostic Index by Addition of a Divergence Trend Term, *Weather and Forecasting*, 25, 789–798, <https://doi.org/10.1175/2009waf2222290.1>, 2010.
- Endlich, R. M. and McLean, G. S.: Jet-Stream Structure over the Central United States Determined from Aircraft Observations, *Journal of Applied Meteorology*, 4, 83–90, [https://doi.org/10.1175/1520-0450\(1965\)004<0083:jssotc>2.0.co;2](https://doi.org/10.1175/1520-0450(1965)004<0083:jssotc>2.0.co;2), 1965.
- Erler, A. R. and Wirth, V.: The static stability of the tropopause region in adiabatic baroclinic life cycle experiments, *Journal of the Atmospheric Sciences*, 68, 1178–1193, <https://doi.org/10.1175/2010JAS3694.1>, 2011.
- Ertel, H.: Ein neuer hydrodynamischer Erhaltungssatz, *Die Naturwissenschaften*, 30, 543–544, <https://doi.org/10.1007/bf01475602>, 1942.
- Fischer, H., Wienhold, F. G., Hoor, P., Bujok, O., Schiller, C., Siegmund, P., Ambaum, M., Scheeren, H. A., and Lelieveld, J.: Tracer correlations in the northern high latitude lowermost stratosphere: Influence of cross-tropopause mass exchange, *Geophysical Research Letters*, 27, 97–100, <https://doi.org/10.1029/1999gl010879>, 2000.
- Forbes, R. and Tompkins, A.: An improved representation of cloud and precipitation, ECMWF, <https://doi.org/10.21957/NFGULZHE>, 2011.
- Forbes, R. M. and Ahlgrim, M.: On the Representation of High-Latitude Boundary Layer Mixed-Phase Cloud in the ECMWF Global Model, *Monthly Weather Review*, 142, 3425–3445, <https://doi.org/>

- 10.1175/mwr-d-13-00325.1, 2014.
- Fritts, D. C. and Alexander, M. J.: Gravity wave dynamics and effects in the middle atmosphere, *Reviews of Geophysics*, 41, 1–64, <https://doi.org/10.1029/2001RG000106>, 2003.
- Gelaro, R., McCarty, W., Suárez, M. J., Todling, R., Molod, A., Takacs, L., Randles, C. A., Darmenov, A., Bosilovich, M. G., Reichle, R., Wargan, K., Coy, L., Cullather, R., Draper, C., Akella, S., Buchard, V., Conaty, A., da Silva, A. M., Gu, W., Kim, G.-K., Koster, R., Lucchesi, R., Merkova, D., Nielsen, J. E., Partyka, G., Pawson, S., Putman, W., Rienecker, M., Schubert, S. D., Sienkiewicz, M., and Zhao, B.: The Modern-Era Retrospective Analysis for Research and Applications, Version 2 (MERRA-2), *Journal of Climate*, 30, 5419–5454, <https://doi.org/10.1175/jcli-d-16-0758.1>, 2017.
- Geller, M. A., Alexander, M. J., Love, P. T., Bacmeister, J., Ern, M., Hertzog, A., Manzini, E., Preusse, P., Sato, K., Scaife, A. A., and Zhou, T.: A Comparison between Gravity Wave Momentum Fluxes in Observations and Climate Models, *Journal of Climate*, 26, 6383–6405, <https://doi.org/10.1175/jcli-d-12-00545.1>, 2013.
- Gottelman, A. and Wang, T.: Structural diagnostics of the tropopause inversion layer and its evolution, *Journal of Geophysical Research: Atmospheres*, 120, 46–62, <https://doi.org/10.1002/2014jd021846>, 2015.
- Gottelman, a., Pan, L. L., Randel, W. J., Hoor, P., Birner, T., and Hegglin, M. I.: the Extratropical Upper Troposphere and Lower Stratosphere, *Reviews of Geophysics*, 49, 1–31, <https://doi.org/10.1029/2011RG000355>.INTRODUCTION, 2011.
- Gisinger, S.: Gravity waves in the lower atmosphere in mountainous regions and the role of the tropopause, Ph.D. thesis, Ludwig-Maximilians-Universität München, Munich, Germany, https://elib.dlr.de/120802/1/Sonja_Gisinger.pdf, dissertation; retrieved from DLR eLibrary, 2018.
- Gisinger, S., Wagner, J., and Witschas, B.: Airborne measurements and large-eddy simulations of small-scale gravity waves at the tropopause inversion layer over Scandinavia, *Atmospheric Chemistry and Physics*, 20, 10 091–10 109, <https://doi.org/10.5194/acp-20-10091-2020>, 2020.
- Gomes, M. B., Shapiro, A., Parsons, D. B., and Gebauer, J. G.: Using a Numerical Model to Evaluate a Proposed Mechanism for Nocturnal Low-Level Jets and Ascent over a Warm Tongue, *Monthly Weather Review*, 153, 1265–1281, <https://doi.org/10.1175/mwr-d-24-0111.1>, 2025.
- Grise, K. M., Thompson, D. W. J., and Birner, T.: A Global Survey of Static Stability in the Stratosphere and Upper Troposphere, *Journal of Climate*, 23, 2275–2292, <https://doi.org/10.1175/2009jcli3369.1>, 2010.
- Guest, F. M., Reeder, M. J., Marks, C. J., and Karoly, D. J.: Inertia–Gravity Waves Observed in the Lower Stratosphere over Macquarie Island, *Journal of the Atmospheric Sciences*, 57, 737–752, [https://doi.org/10.1175/1520-0469\(2000\)057<0737:igwoit>2.0.co;2](https://doi.org/10.1175/1520-0469(2000)057<0737:igwoit>2.0.co;2), 2000.
- Gultepe, I., Sharman, R., Williams, P. D., Zhou, B., Ellrod, G., Minnis, P., Trier, S., Griffin, S., Yum, S. S., Gharabaghi, B., Feltz, W., Temimi, M., Pu, Z., Storer, L. N., Kneringer, P., Weston, M. J., Chuang, H.-y., Thobois, L., Dimri, A. P., Dietz, S. J., França, G. B., Almeida, M. V., and Neto, F. L. A.: A Review of High Impact Weather for Aviation Meteorology, *Pure and Applied Geophysics*, 176, 1869–1921, <https://doi.org/10.1007/s00024-019-02168-6>, 2019.
- Günther, G., Müller, R., von Hobe, M., Stroh, F., Konopka, P., and Volk, C. M.: Quantification of transport across the boundary of the lower stratospheric vortex during Arctic winter 2002/2003, *Atmospheric Chemistry and Physics*, 8, 3655–3670, <https://doi.org/10.5194/acp-8-3655-2008>, 2008.

- Gupta, A., Birner, T., Dörnbrack, A., and Polichtchouk, I.: Importance of Gravity Wave Forcing for Springtime Southern Polar Vortex Breakdown as Revealed by ERA5, *Geophysical Research Letters*, 48, <https://doi.org/10.1029/2021GL092762>, 2021.
- Gupta, A., Sheshadri, A., Alexander, M. J., and Birner, T.: Insights on Lateral Gravity Wave Propagation in the Extratropical Stratosphere From 44 Years of ERA5 Data, *Geophysical Research Letters*, 51, <https://doi.org/10.1029/2024gl108541>, 2024.
- Hartmann, D. L., Chan, K. R., Gary, B. L., Schoeberl, M. R., Newman, P. A., Martin, R. L., Loewenstein, M., Podolske, J. R., and Strahan, S. E.: Potential vorticity and mixing in the south polar vortex during spring, *Journal of Geophysical Research: Atmospheres*, 94, 11 625–11 640, <https://doi.org/10.1029/jd094id09p11625>, 1989.
- Hastings, D. A., Dunbar, P. K., Elphinstone, G. M., Bootz, M., Murakami, H., and et al.: The Global Land One-kilometer Base Elevation (GLOBE) Digital Elevation Model, Version 1.325, (cit. on p. 30), 1999.
- Hegglin, M. I., Boone, C. D., Manney, G. L., and Walker, K. A.: A global view of the extratropical tropopause transition layer from Atmospheric Chemistry Experiment Fourier Transform Spectrometer O₃, H₂O, and CO, *Journal of Geophysical Research Atmospheres*, 114, 1–18, <https://doi.org/10.1029/2008JD009984>, 2009.
- Heller, R., Voigt, C., Beaton, S., Dörnbrack, A., Giez, A., Kaufmann, S., Mallaun, C., Schlager, H., Wagner, J., Young, K., and Rapp, M.: Mountain waves modulate the water vapor distribution in the UTLS, *Atmospheric Chemistry and Physics*, 17, 14 853–14 869, <https://doi.org/10.5194/acp-17-14853-2017>, 2017.
- Hersbach, H., Bell, B., Berrisford, P., Hirahara, S., Horányi, A., Muñoz-Sabater, J., Nicolas, J., Peubey, C., Radu, R., Schepers, D., Simmons, A., Soci, C., Abdalla, S., Abellan, X., Balsamo, G., Bechtold, P., Biavati, G., Bidlot, J., Bonavita, M., De Chiara, G., Dahlgren, P., Dee, D., Diamantakis, M., Dragani, R., Flemming, J., Forbes, R., Fuentes, M., Geer, A., Haimberger, L., Healy, S., Hogan, R. J., Hólm, E., Janisková, M., Keeley, S., Laloyaux, P., Lopez, P., Lupu, C., Radnoti, G., de Rosnay, P., Rozum, I., Vamborg, F., Villaume, S., and Thépaut, J.: The ERA5 global reanalysis, *Quarterly Journal of the Royal Meteorological Society*, 146, 1999–2049, <https://doi.org/10.1002/qj.3803>, 2020.
- Hirota, I. and Niki, T.: Inertia-Gravity Waves in the Troposphere and Stratosphere Observed by the MU Radar, *Journal of the Meteorological Society of Japan. Ser. II*, 64, 995–999, https://doi.org/10.2151/jmsj1965.64.6_995, 1986.
- Hodges Jr., R. R.: Generation of turbulence in the upper atmosphere by internal gravity waves, *Journal of Geophysical Research (1896-1977)*, 72, 3455–3458, <https://doi.org/https://doi.org/10.1029/JZ072i013p03455>, 1967.
- Hoerling, M. P., Schaack, T. K., and Lenzen, A. J.: Global Objective Tropopause Analysis, *Monthly Weather Review*, 119, 1816–1831, [https://doi.org/10.1175/1520-0493\(1991\)119<1816:gota>2.0.co;2](https://doi.org/10.1175/1520-0493(1991)119<1816:gota>2.0.co;2), 1991.
- Hoffmann, L., Günther, G., Li, D., Stein, O., Wu, X., Griessbach, S., Heng, Y., Konopka, P., Müller, R., Vogel, B., and Wright, J. S.: From ERA-Interim to ERA5: the considerable impact of ECMWF's next-generation reanalysis on Lagrangian transport simulations, *Atmospheric Chemistry and Physics*, 19, 3097–3124, <https://doi.org/10.5194/acp-19-3097-2019>, 2019.
- Hogan, R. J. and Bozzo, A.: A flexible and efficient radiation scheme for the ECMWF model, *Journal of*

- Advances in Modeling Earth Systems, 10, 1990–2008, <https://doi.org/10.1029/2018MS001364>, 2018.
- Hoinka, K. P.: Die Tropopause: Entdeckung, Definition, Bestimmung, *Meteorologische Zeitschrift*, 6, 281–303, <https://doi.org/10.1127/metz/6/1997/281>, 1997.
- Holton, J. R., Haynes, P. H., McIntyre, M. E., Douglass, A. R., Rood, R. B., and Pfister, L.: Stratosphere-troposphere exchange, *Reviews of Geophysics*, 33, 403–439, <https://doi.org/10.1029/95RG02097>, 1995.
- Hoor, P.: The tropopause region in a changing atmosphere (TPchange), Tech. rep., Institute for Atmospheric Physics, Johannes Gutenberg University Mainz, <https://utls.ipa.uni-mainz.de/tpchange/>, accessed: 2026-02-06, 2022.
- Hoor, P., Fischer, H., Lange, L., Lelieveld, J., and Brunner, D.: Seasonal variations of a mixing layer in the lowermost stratosphere as identified by the CO-O₃ correlation from in situ measurements, *Journal of Geophysical Research: Atmospheres*, 107, <https://doi.org/10.1029/2000jd000289>, 2002.
- Hoor, P., Gurk, C., Brunner, D., Hegglin, M. I., Wernli, H., and Fischer, H.: Seasonality and extent of extratropical TST derived from in-situ CO measurements during SPURT, *Atmospheric Chemistry and Physics*, 4, 1427–1442, <https://doi.org/10.5194/acp-4-1427-2004>, 2004.
- Hoor, P., Wernli, H., Hegglin, M. I., and Bönisch, H.: Transport timescales and tracer properties in the extratropical UTLS, *Atmospheric Chemistry and Physics*, 10, 7929–7944, <https://doi.org/10.5194/acp-10-7929-2010>, 2010.
- Hoskins, B. J., McIntyre, M. E., and Robertson, A. W.: On the use and significance of isentropic potential vorticity maps, *Quarterly Journal of the Royal Meteorological Society*, 111, 877–946, <https://doi.org/10.1002/qj.49711147002>, 1985.
- Jablonowski, C. and Williamson, D. L.: A baroclinic instability test case for atmospheric model dynamical cores, *Quarterly Journal of the Royal Meteorological Society*, 132, 2943–2975, <https://doi.org/10.1256/qj.06.12>, 2006.
- Jewtoukoff, V., Hertzog, A., Plougonven, R., Cámara, A. d. I., and Lott, F.: Comparison of Gravity Waves in the Southern Hemisphere Derived from Balloon Observations and the ECMWF Analyses, *Journal of the Atmospheric Sciences*, 72, 3449–3468, <https://doi.org/10.1175/jas-d-14-0324.1>, 2015.
- Kaluza, T., Kunkel, D., and Hoor, P.: Composite analysis of the tropopause inversion layer in extratropical baroclinic waves, *Atmospheric Chemistry and Physics*, 19, 6621–6636, <https://doi.org/10.5194/acp-19-6621-2019>, 2019.
- Kaluza, T., Kunkel, D., and Hoor, P.: On the occurrence of strong vertical wind shear in the tropopause region: a 10-year ERA5 northern hemispheric study, *Weather and Climate Dynamics*, 2, 631–651, <https://doi.org/10.5194/wcd-2-631-2021>, 2021.
- Kaluza, T., Kunkel, D., and Hoor, P.: Analysis of Turbulence Reports and ERA5 Turbulence Diagnostics in a Tropopause-Based Vertical Framework, *Geophysical Research Letters*, 49, <https://doi.org/10.1029/2022gl100036>, 2022.
- Kim, J.-H. and Chun, H.-Y.: Statistics and Possible Sources of Aviation Turbulence over South Korea, *Journal of Applied Meteorology and Climatology*, 50, 311–324, <https://doi.org/10.1175/2010jamc2492.1>, 2011.
- Kim, J.-H., Sharman, R., Strahan, M., Scheck, J. W., Bartholomew, C., Cheung, J. C. H., Buchanan, P., and Gait, N.: Improvements in Nonconvective Aviation Turbulence Prediction for the World Area

- Forecast System, *Bulletin of the American Meteorological Society*, 99, 2295–2311, <https://doi.org/10.1175/bams-d-17-0117.1>, 2018.
- Kim, Y., Eckermann, S. D., and Chun, H.: An overview of the past, present and future of gravity-wave drag parametrization for numerical climate and weather prediction models, *Atmosphere-Ocean*, 41, 65–98, <https://doi.org/10.3137/ao.410105>, 2003.
- Knox, J. A.: Possible Mechanisms of Clear-Air Turbulence in Strongly Anticyclonic Flows, *Monthly Weather Review*, 125, 1251–1259, [https://doi.org/10.1175/1520-0493\(1997\)125<1251:pmocat>2.0.co;2](https://doi.org/10.1175/1520-0493(1997)125<1251:pmocat>2.0.co;2), 1997.
- Knox, J. A., McCann, D. W., and Williams, P. D.: Application of the Lighthill–Ford Theory of Spontaneous Imbalance to Clear-Air Turbulence Forecasting, *Journal of the Atmospheric Sciences*, 65, 3292–3304, <https://doi.org/10.1175/2008jas2477.1>, 2008.
- Kobayashi, S., OTA, Y., HARADA, Y., EBITA, A., MORIYA, M., ONODA, H., ONOGI, K., KAMAHORI, H., KOBAYASHI, C., ENDO, H., MIYAOKA, K., and TAKAHASHI, K.: The JRA-55 Reanalysis: General Specifications and Basic Characteristics, *Journal of the Meteorological Society of Japan. Ser. II*, 93, 5–48, <https://doi.org/10.2151/jmsj.2015-001>, 2015.
- Koch, P., Wernli, H., and Davies, H. C.: An event-based jet-stream climatology and typology, *International Journal of Climatology*, 26, 283–301, <https://doi.org/10.1002/joc.1255>, 2006.
- Koch, S. E. and Caracena, F.: Predicting clear-air turbulence from diagnosis of unbalanced flow, *Preprints, 10th Conf. on Aviation, Range, and Aerospace Meteorology*, Portland, OR, Amer. Meteor. Soc., 10.4, <http://ams.confex.com/ams/pdfpapers/39012.pdf>, last access: 25 June 2025, 2002.
- Koch, S. E., Jamison, B. D., Lu, C., Smith, T. L., Tollerud, E. I., Girz, C., Wang, N., Lane, T. P., Shapiro, M. A., Parrish, D. D., and Cooper, O. R.: Turbulence and Gravity Waves within an Upper-Level Front, *Journal of the Atmospheric Sciences*, 62, 3885–3908, <https://doi.org/10.1175/jas3574.1>, 2005.
- Köhler, M., Ahlgrimm, M., and Beljaars, A.: Unified treatment of dry convective and stratocumulus-topped boundary layers in the ECMWF model, *Quarterly Journal of the Royal Meteorological Society*, 137, 43–57, <https://doi.org/10.1002/qj.713>, 2011.
- Köhler, R.: Towards seasonal prediction, Ph.D. thesis, <https://doi.org/10.25932/PUBLISHUP-48723>, 2021.
- Kosaka, Y., KOBAYASHI, S., HARADA, Y., KOBAYASHI, C., NAOE, H., YOSHIMOTO, K., HARADA, M., GOTO, N., CHIBA, J., MIYAOKA, K., SEKIGUCHI, R., DEUSHI, M., KAMAHORI, H., NAKAEGAWA, T., TANAKA, T. Y., TOKUHIRO, T., SATO, Y., MATSUSHITA, Y., and ONOGI, K.: The JRA-3Q Reanalysis, *Journal of the Meteorological Society of Japan. Ser. II*, 102, 49–109, <https://doi.org/10.2151/jmsj.2024-004>, 2024.
- Krautstrunk, M. and Giez, A.: The Transition From FALCON to HALO Era Airborne Atmospheric Research, p. 609–624, Springer Berlin Heidelberg, ISBN 9783642301834, https://doi.org/10.1007/978-3-642-30183-4_37, 2012.
- Kruse, C. G. and Smith, R. B.: Gravity Wave Diagnostics and Characteristics in Mesoscale Fields, *Journal of the Atmospheric Sciences*, 72, 4372–4392, <https://doi.org/10.1175/jas-d-15-0079.1>, 2015.
- Kunkel, D., Hoor, P., and Wirth, V.: Can inertia-gravity waves persistently alter the tropopause inversion layer?, *Geophysical Research Letters*, 41, 7822–7829, <https://doi.org/10.1002/2014GL061970>, 2014.

- Kunkel, D., Hoor, P., and Wirth, V.: The tropopause inversion layer in baroclinic life-cycle experiments: The role of diabatic processes, *Atmospheric Chemistry and Physics*, 16, 541–560, <https://doi.org/10.5194/acp-16-541-2016>, 2016.
- Kunkel, D., Hoor, P., Kaluza, T., Ungermann, J., Kluschat, B., Giez, A., Lachnitt, H. C., Kaufmann, M., and Riese, M.: Evidence of small-scale quasi-isentropic mixing in ridges of extratropical baroclinic waves, *Atmospheric Chemistry and Physics*, 19, 12 607–12 630, <https://doi.org/10.5194/acp-19-12607-2019>, 2019.
- Kunz, A., Konopka, P., Müller, R., Pan, L. L., Schiller, C., and Rohrer, F.: High static stability in the mixing layer above the extratropical tropopause, *Journal of Geophysical Research: Atmospheres*, 114, <https://doi.org/10.1029/2009jd011840>, 2009.
- Kunz, A., Konopka, P., Müller, R., and Pan, L. L.: Dynamical tropopause based on isentropic potential vorticity gradients, *Journal of Geophysical Research*, 116, <https://doi.org/10.1029/2010jd014343>, 2011.
- Lachnitt, H. C., Hoor, P., Kunkel, D., Bramberger, M., Dörnbrack, A., Müller, S., Reutter, P., Giez, A., Kaluza, T., and Rapp, M.: Gravity-wave-induced cross-isentropic mixing: A DEEPWAVE case study, *Atmospheric Chemistry and Physics*, 23, 355–373, <https://doi.org/10.5194/acp-23-355-2023>, 2023.
- Lane, T. P.: Does Lower-Stratospheric Shear Influence the Mesoscale Organization of Convection?, *Geophysical Research Letters*, 48, 1–10, <https://doi.org/10.1029/2020GL091025>, 2021.
- Lane, T. P. and Sharman, R. D.: Gravity wave breaking, secondary wave generation, and mixing above deep convection in a three-dimensional cloud model, *Geophysical Research Letters*, 33, <https://doi.org/10.1029/2006gl027988>, 2006.
- Lane, T. P., Reeder, M. J., and Clark, T. L.: Numerical Modeling of Gravity Wave Generation by Deep Tropical Convection, *Journal of the Atmospheric Sciences*, 58, 1249–1274, [https://doi.org/10.1175/1520-0469\(2001\)058<1249:nmogwg>2.0.co;2](https://doi.org/10.1175/1520-0469(2001)058<1249:nmogwg>2.0.co;2), 2001.
- Lane, T. P., Sharman, R. D., Clark, T. L., and Hsu, H.-M.: An Investigation of Turbulence Generation Mechanisms above Deep Convection, *Journal of the Atmospheric Sciences*, 60, 1297–1321, [https://doi.org/10.1175/1520-0469\(2003\)60<1297:aiotgm>2.0.co;2](https://doi.org/10.1175/1520-0469(2003)60<1297:aiotgm>2.0.co;2), 2003.
- Lane, T. P., Doyle, J. D., Plougonven, R., Shapiro, M. A., and Sharman, R. D.: Observations and Numerical Simulations of Inertia–Gravity Waves and Shearing Instabilities in the Vicinity of a Jet Stream, *Journal of the Atmospheric Sciences*, 61, 2692–2706, <https://doi.org/10.1175/jas3305.1>, 2004.
- Lee, D.-B., Chun, H.-Y., and Kim, J.-H.: Evaluation of Multimodel-Based Ensemble Forecasts for Clear-Air Turbulence, *Weather and Forecasting*, 35, 507–521, <https://doi.org/10.1175/waf-d-19-0155.1>, 2019.
- Lee, J. H., Kim, J., Sharman, R. D., Kim, J., and Son, S.: Climatology of Clear-Air Turbulence in Upper Troposphere and Lower Stratosphere in the Northern Hemisphere Using ERA5 Reanalysis Data, *Journal of Geophysical Research: Atmospheres*, 128, <https://doi.org/10.1029/2022jd037679>, 2022.
- Lee, M. H. F. and Sprenger, M.: Clear-air turbulence derived from in situ aircraft observation – a weather feature-based typology using ERA5 reanalysis, *Weather and Climate Dynamics*, 6, 1583–1604, <https://doi.org/10.5194/wcd-6-1583-2025>, 2025.
- Lehmann, C. I., Kim, Y.-H., Preusse, P., Chun, H.-Y., Ern, M., and Kim, S.-Y.: Consistency between Fourier transform and small-volume few-wave decomposition for spectral and spatial variability of

- gravity waves above a typhoon, *Atmospheric Measurement Techniques*, 5, 1637–1651, <https://doi.org/10.5194/amt-5-1637-2012>, 2012.
- Leuenberger, D., Koller, M., Fuhrer, O., and Schär, C.: A Generalization of the SLEVE Vertical Coordinate, *Monthly Weather Review*, 138, 3683–3689, <https://doi.org/10.1175/2010mwr3307.1>, 2010.
- Lin, Y.-L.: *Mesoscale Dynamics*, Cambridge University Press, Cambridge, UK, ISBN 9780511372629, 2007.
- Lindzen, R. S.: Turbulence and stress owing to gravity wave and tidal breakdown, *Journal of Geophysical Research: Oceans*, 86, 9707–9714, 1981.
- Liu, H.: Large Wind Shears and Their Implications for Diffusion in Regions With Enhanced Static Stability: The Mesopause and the Tropopause, *Journal of Geophysical Research: Atmospheres*, 122, 9579–9590, <https://doi.org/10.1002/2017jd026748>, 2017.
- Lott, F. and Miller, M. J.: A new subgrid-scale orographic drag parametrization: Its formulation and testing, *Quarterly Journal of the Royal Meteorological Society*, 123, 101–127, <https://doi.org/10.1002/qj.49712353704>, 1997.
- Louis, J.-F., Tiedtke, M., and Geleyn, J.-F.: A Short History of the Operational PBL Parameterization at ECMWF, *Ecmwf workshop on boundary layer parametrization, European Centre for Medium-Range Weather Forecasts (ECMWF)*, Reading, UK, 1982.
- Luderer, G., Trentmann, J., Hungershofer, K., Herzog, M., Fromm, M., and Andreae, M. O.: Small-scale mixing processes enhancing troposphere-to-stratosphere transport by pyro-cumulonimbus storms, <https://doi.org/10.5194/acpd-7-10371-2007>, 2007.
- Müller, S., Hoor, P., Berkes, F., Bozem, H., Klingebiel, M., Reutter, P., Smit, H. G. J., Wendisch, M., Spichtinger, P., and Borrmann, S.: In situ detection of stratosphere-troposphere exchange of cirrus particles in the midlatitudes, *Geophysical Research Letters*, 42, 949–955, <https://doi.org/10.1002/2014gl062556>, 2015.
- Müller, S., Hoor, P., Bozem, H., Gute, E., Vogel, B., Zahn, A., Bönisch, H., Keber, T., Krämer, M., Rolf, C., Riese, M., Schlager, H., and Engel, A.: Impact of the Asian monsoon on the extratropical lower stratosphere: trace gas observations during TACTS over Europe 2012, *Atmospheric Chemistry and Physics*, 16, 10 573–10 589, <https://doi.org/10.5194/acp-16-10573-2016>, 2016.
- Müller, S. K., Manzini, E., Giorgetta, M., Sato, K., and Nasuno, T.: Convectively Generated Gravity Waves in High Resolution Models of Tropical Dynamics, *Journal of Advances in Modeling Earth Systems*, 10, 2564–2588, <https://doi.org/10.1029/2018MS001390>, 2018.
- Newton, C. W. and Persson, A. V.: Structural characteristics of the subtropical jet stream and certain lower-stratospheric wind systems, *Tellus A: Dynamic Meteorology and Oceanography*, 14, 221–241, <https://doi.org/10.3402/tellusa.v14i2.9542>, 1962.
- Okui, H., Koshin, D., Watanabe, S., and Sato, K.: Roles of Gravity Waves in Preconditioning of a Stratospheric Sudden Warming, *Journal of Geophysical Research: Atmospheres*, 129, <https://doi.org/10.1029/2023JD039881>, 2024.
- Olsen, M. A., Douglass, A. R., and Kaplan, T. B.: Variability of extratropical ozone stratosphere–troposphere exchange using microwave limb sounder observations, *Journal of Geophysical Research: Atmospheres*, 118, 1090–1099, <https://doi.org/10.1029/2012jd018465>, 2013.
- Orr, A., Bechtold, P., Scinocca, J., Ern, M., and Janiskova, M.: Improved middle atmosphere climate

- and forecasts in the ECMWF model through a non-orographic gravity wave drag parametrization, ECMWF, <https://doi.org/10.21957/DM64CMPJ>, 2010.
- O'sullivan, D. and Dunkerton, T. J.: Generation of Inertia–Gravity Waves in a Simulated Life Cycle of Baroclinic Instability, *Journal of Atmospheric Sciences*, 52, 3695 – 3716, [https://doi.org/10.1175/1520-0469\(1995\)052<3695:GOIWIA>2.0.CO;2](https://doi.org/10.1175/1520-0469(1995)052<3695:GOIWIA>2.0.CO;2), 1995.
- Pan, L. L., Randel, W. J., Gary, B. L., Mahoney, M. J., and Hints, E. J.: Definitions and sharpness of the extratropical tropopause: A trace gas perspective, *Journal of Geophysical Research: Atmospheres*, 109, <https://doi.org/10.1029/2004jd004982>, 2004.
- Pan, L. L., Konopka, P., and Browell, E. V.: Observations and model simulations of mixing near the extratropical tropopause, *Journal of Geophysical Research Atmospheres*, 111, 1–15, <https://doi.org/10.1029/2005JD006480>, 2006.
- Plougonven, R. and Snyder, C.: Gravity waves excited by jets: Propagation versus generation, *Geophysical Research Letters*, 32, 1–4, <https://doi.org/10.1029/2005GL023730>, 2005.
- Plougonven, R. and Snyder, C.: Inertia-gravity waves spontaneously generated by jets and fronts. Part I: Different baroclinic life cycles, *Journal of the Atmospheric Sciences*, 64, 2502–2520, <https://doi.org/10.1175/JAS3953.1>, 2007.
- Plougonven, R. and Zhang, F.: Internal gravity waves from atmospheric jets and fronts, *Reviews of Geophysics*, 52, 33–76, <https://doi.org/10.1002/2012RG000419>, 2014.
- Plougonven, R., Teitelbaum, H., and Zeitlin, V.: Inertia gravity wave generation by the tropospheric midlatitude jet as given by the Fronts and Atlantic Storm-Track Experiment radio soundings, *Journal of Geophysical Research: Atmospheres*, 108, <https://doi.org/10.1029/2003jd003535>, 2003.
- Plougonven, R., Hertzog, A., and Teitelbaum, H.: Observations and simulations of a large-amplitude mountain wave breaking over the Antarctic Peninsula, *Journal of Geophysical Research Atmospheres*, 113, 1–17, <https://doi.org/10.1029/2007JD009739>, 2008.
- Plougonven, R., Jewtoukoff, V., Cámara, A. d. I., Lott, F., and Hertzog, A.: On the Relation between Gravity Waves and Wind Speed in the Lower Stratosphere over the Southern Ocean, *Journal of the Atmospheric Sciences*, 74, 1075–1093, <https://doi.org/10.1175/jas-d-16-0096.1>, 2017.
- Plumb, R. A.: Stratospheric Transport, *Journal of the Meteorological Society of Japan. Ser. II*, 80, 793–809, <https://doi.org/10.2151/jmsj.80.793>, 2002.
- Podglajen, A., Bui, T. P., Dean-Day, J. M., Pfister, L., Jensen, E. J., Alexander, M. J., Hertzog, A., Kärcher, B., Plougonven, R., and Randel, W. J.: Small-scale wind fluctuations in the tropical tropopause layer from aircraft measurements: Occurrence, nature, and impact on vertical mixing, *Journal of the Atmospheric Sciences*, 74, 3847–3869, <https://doi.org/10.1175/JAS-D-17-0010.1>, 2017.
- Podglajen, A., Hertzog, A., Plougonven, R., and Legras, B.: Lagrangian gravity wave spectra in the lower stratosphere of current (re)analyses, *Atmospheric Chemistry and Physics*, 20, 9331–9350, <https://doi.org/10.5194/acp-20-9331-2020>, 2020.
- Polichtchouk, I., Shepherd, T. G., Hogan, R. J., and Bechtold, P.: Sensitivity of the Brewer–Dobson Circulation and Polar Vortex Variability to Parameterized Nonorographic Gravity Wave Drag in a High-Resolution Atmospheric Model, *Journal of the Atmospheric Sciences*, 75, 1525–1543, <https://doi.org/10.1175/jas-d-17-0304.1>, 2018b.

- Polichtchouk, I., van Niekerk, A., and Wedi, N.: Resolved Gravity Waves in the Extratropical Stratosphere: Effect of Horizontal Resolution Increase from O(10) to O(1) km, *Journal of the Atmospheric Sciences*, 80, 473–486, <https://doi.org/10.1175/jas-d-22-0138.1>, 2023.
- Preusse, P., Ern, M., Bechtold, P., Eckermann, S. D., Kalisch, S., Trinh, Q. T., and Riese, M.: Characteristics of gravity waves resolved by ECMWF, *Atmospheric Chemistry and Physics*, 14, 10 483–10 508, <https://doi.org/10.5194/acp-14-10483-2014>, 2014.
- Prill, F., Reinert, D., Rieger, D., and Zängl, G.: ICON tutorial 2020, <https://doi.org/10.5676/DWD>, 2020.
- Prusa, J. M., Smolarkiewicz, P. K., and Wyszogrodzki, A. A.: EULAG, a computational model for multiscale flows, *Computers and Fluids*, 37, 1193–1207, <https://doi.org/10.1016/j.compfluid.2007.12.001>, 2008.
- Raschendorfer, M.: The new turbulence parameterization of LM, COSMO Newsletter No. 1, pp. 89–97, 2001.
- Reed, R. J.: A STUDY OF A CHARACTERISTIC TYPE OF UPPER-LEVEL FRONTOGENESIS, *Journal of Meteorology*, 12, 226–237, [https://doi.org/10.1175/1520-0469\(1955\)012<0226:asoact>2.0.co;2](https://doi.org/10.1175/1520-0469(1955)012<0226:asoact>2.0.co;2), 1955.
- Remmler, S.: Gravity-Wave Breaking and Turbulence in the Atmosphere, Phd thesis, Ludwig-Maximilians-Universität München, Munich, Germany, 2016.
- Rieger, D., Köhler, M., Hogan, R. J., Schäfer, S. A., Seifert, A., de Lozar, A., and Zängl, G.: Reports on ICON 004: ecRad in ICON - Implementation Overview, Deutscher Wetterdienst, https://doi.org/10.5676/DWD_PUB/NWV/ICON_004, 2019.
- Schäfler, A., Harvey, B., Methven, J., Doyle, J. D., Rahm, S., Reitebuch, O., Weiler, F., and Witschas, B.: Observation of Jet Stream Winds during NAWDEX and Characterization of Systematic Meteorological Analysis Errors, *Monthly Weather Review*, 148, 2889–2907, <https://doi.org/10.1175/mwr-d-19-0229.1>, 2020.
- Schäfler, A., Sprenger, M., Wernli, H., Fix, A., and Wirth, M.: Case study on the influence of synoptic-scale processes on the paired H₂O–O₃ distribution in the UTLS across a North Atlantic jet stream, *Atmospheric Chemistry and Physics*, 23, 999–1018, <https://doi.org/10.5194/acp-23-999-2023>, 2023.
- Schilling, T., Lübken, F., Wienhold, F. G., Hoor, P., and Fischer, H.: TDLAS Trace Gas Measurements within Mountain Waves Over Northern Scandinavia during the POLSTAR Campaign in Early 1997, *Geophysical Research Letters*, 26, 303–306, <https://doi.org/10.1029/1998gl900314>, 1999.
- Schwenk, C. and Miltenberger, A.: The role of ascent timescales for warm conveyor belt (WCB) moisture transport into the upper troposphere and lower stratosphere (UTLS), *Atmospheric Chemistry and Physics*, 24, 14 073–14 099, <https://doi.org/10.5194/acp-24-14073-2024>, 2024.
- Scinocca, J. F.: An Accurate Spectral Nonorographic Gravity Wave Drag Parameterization for General Circulation Models, *Journal of the Atmospheric Sciences*, 60, 667–682, [https://doi.org/10.1175/1520-0469\(2003\)060<0667:aaangw>2.0.co;2](https://doi.org/10.1175/1520-0469(2003)060<0667:aaangw>2.0.co;2), 2003.
- Seifert, A.: On the parameterization of evaporation of raindrops as simulated by a one-dimensional rainshaft model, *Journal of the Atmospheric Sciences*, 65, 3608–3619, <https://doi.org/10.1175/2008JAS2586.1>, 2008.
- Seifert, A. and Beheng, K. D.: A two-moment cloud microphysics parameterization for mixed-phase clouds. Part 1: Model description, *Meteorology and Atmospheric Physics*, 92, 45–66, <https://doi.org/>

- 10.1007/s00703-005-0112-4, 2005.
- Selz, T.: Calculation of Potential Vorticity on the ICON Grid, Tech. rep., Deutscher Wetterdienst (DWD), Offenbach am Main, Germany, https://www.dwd.de/EN/ourservices/reports_on_icon/pdf_einzelbaende/2019_02.pdf;jsessionid=C9FCFE3B59C0EDD25AABFC030AE6F47E.live31091?__blob=publicationFile&v=2, 2019.
- Shao, J., Zhang, J., Wang, W., Zhang, S., Yu, T., and Dong, W.: Occurrence frequency of subcritical Richardson numbers assessed by global high-resolution radiosonde and ERA5 reanalysis, *Atmospheric Chemistry and Physics*, 23, 12 589–12 607, <https://doi.org/10.5194/acp-23-12589-2023>, 2023.
- Shapiro, M. A.: The Role of Turbulent Heat Flux in the Generation of Potential Vorticity in the Vicinity of Upper-Level Jet Stream Systems, *Monthly Weather Review*, 104, 892–906, [https://doi.org/10.1175/1520-0493\(1976\)104<0892:trothf>2.0.co;2](https://doi.org/10.1175/1520-0493(1976)104<0892:trothf>2.0.co;2), 1976.
- Shapiro, M. A.: Further Evidence of the Mesoscale and Turbulent Structure of Upper Level Jet Stream–Frontal Zone Systems, *Monthly Weather Review*, 106, 1100–1111, [https://doi.org/10.1175/1520-0493\(1978\)106<1100:feotma>2.0.co;2](https://doi.org/10.1175/1520-0493(1978)106<1100:feotma>2.0.co;2), 1978.
- Shapiro, M. A.: Turbulent Mixing within Tropopause Folds as a Mechanism for the Exchange of Chemical Constituents between the Stratosphere and Troposphere, *Journal of the Atmospheric Sciences*, 37, 994–1004, [https://doi.org/10.1175/1520-0469\(1980\)037<0994:tmwtf>2.0.co;2](https://doi.org/10.1175/1520-0469(1980)037<0994:tmwtf>2.0.co;2), 1980.
- Sharman, R. and Lane: Aviation Turbulence, Springer International Publishing, ISBN 9783319236308, <https://doi.org/10.1007/978-3-319-23630-8>, 2016.
- Sharman, R., Tebaldi, C., Wiener, G., and Wolff, J.: An Integrated Approach to Mid- and Upper-Level Turbulence Forecasting, *Weather and Forecasting*, 21, 268–287, <https://doi.org/10.1175/waf924.1>, 2006.
- Sharman, R. D. and Pearson, J. M.: Prediction of Energy Dissipation Rates for Aviation Turbulence. Part I: Forecasting Nonconvective Turbulence, *Journal of Applied Meteorology and Climatology*, 56, 317–337, <https://doi.org/10.1175/jamc-d-16-0205.1>, 2017.
- Sharman, R. D., Trier, S. B., Lane, T. P., and Doyle, J. D.: Sources and dynamics of turbulence in the upper troposphere and lower stratosphere: A review, *Geophysical Research Letters*, 39, 1–9, <https://doi.org/10.1029/2012GL051996>, 2012.
- Sharman, R. D., Cornman, L. B., Meymaris, G., Pearson, J., and Farrar, T.: Description and Derived Climatologies of Automated In Situ Eddy-Dissipation-Rate Reports of Atmospheric Turbulence, *Journal of Applied Meteorology and Climatology*, 53, 1416–1432, <https://doi.org/10.1175/jamc-d-13-0329.1>, 2014.
- Shaw, T. A., Baldwin, M., Barnes, E. A., Caballero, R., Garfinkel, C. I., Hwang, Y.-T., Li, C., O’Gorman, P. A., Rivière, G., Simpson, I. R., and Voigt, A.: Storm track processes and the opposing influences of climate change, *Nature Geoscience*, 9, 656–664, <https://doi.org/10.1038/ngeo2783>, 2016.
- Shepherd, T. G.: Transport in the Middle Atmosphere, *Journal of the Meteorological Society of Japan*. Ser. II, 85B, 165–191, <https://doi.org/10.2151/jmsj.85B.165>, 2007.
- Smith, R. B., Woods, B. K., Jensen, J., Cooper, W. A., Doyle, J. D., Jiang, Q., and Grubišić, V.: Mountain Waves Entering the Stratosphere, *Journal of the Atmospheric Sciences*, 65, 2543–2562, <https://doi.org/10.1175/2007jas2598.1>, 2008.

- Song, I. S., Lee, C., Chun, H. Y., Kim, J. H., Jee, G., Song, B. G., and Bacmeister, J. T.: Propagation of gravity waves and its effects on pseudomomentum flux in a sudden stratospheric warming event, *Atmospheric Chemistry and Physics*, 20, 7617–7644, <https://doi.org/10.5194/acp-20-7617-2020>, 2020.
- Spreitzer, E., Attinger, R., Boettcher, M., Forbes, R., Wernli, H., and Joos, H.: Modification of potential vorticity near the tropopause by nonconservative processes in the ECMWF model, *Journal of the Atmospheric Sciences*, 76, 1709–1726, <https://doi.org/10.1175/JAS-D-18-0295.1>, 2019.
- Stephan, C. C. and Mariaccia, A.: The signature of the tropospheric gravity wave background in observed mesoscale motion, *Weather and Climate Dynamics*, 2, 359–372, <https://doi.org/10.5194/wcd-2-359-2021>, 2021.
- Stephan, C. C., Strube, C., Klocke, D., Ern, M., Hoffmann, L., Preusse, P., and Schmidt, H.: Inter-comparison of Gravity Waves in Global Convection-Permitting Models, *Journal of the Atmospheric Sciences*, 76, 2739–2759, <https://doi.org/10.1175/jas-d-19-0040.1>, 2019.
- Stephan, C. C., Schmidt, H., Zülicke, C., and Matthias, V.: Oblique Gravity Wave Propagation During Sudden Stratospheric Warmings, *Journal of Geophysical Research: Atmospheres*, 125, <https://doi.org/10.1029/2019JD031528>, 2020.
- Stephan, C. C., Duras, J., Harris, L., Klocke, D., Putman, W. M., Taylor, M., Wedi, N. P., Žagar, N., and Ziemann, F.: Atmospheric Energy Spectra in Global Kilometre-Scale Models, *Tellus A: Dynamic Meteorology and Oceanography*, 74, 280–299, <https://doi.org/10.16993/tellusa.26>, 2022.
- Stohl, A., Bonasoni, P., Cristofanelli, P., Collins, W., Feichter, J., Frank, A., Forster, C., Gerasopoulos, E., Gäggeler, H., James, P., Kentarchos, T., Kromp-Kolb, H., Krüger, B., Land, C., Meloan, J., Papayannis, A., Priller, A., Seibert, P., Sprenger, M., Roelofs, G. J., Scheel, H. E., Schnabel, C., Siegmund, P., Tobler, L., Trickl, T., Wernli, H., Wirth, V., Zanis, P., and Zerefos, C.: Stratosphere-troposphere exchange: A review, and what we have learned from STACCATO, *J. Geophys. Res.*, 108, 2003.
- Strelnikova, I., Baumgarten, G., and Lübken, F.-J.: Advanced hodograph-based analysis technique to derive gravity-wave parameters from lidar observations, *Atmospheric Measurement Techniques*, 13, 479–499, <https://doi.org/10.5194/amt-13-479-2020>, 2020.
- Strube, C., Ern, M., Preusse, P., and Riese, M.: Removing spurious inertial instability signals from gravity wave temperature perturbations using spectral filtering methods, *Atmospheric Measurement Techniques*, 13, 4927–4945, <https://doi.org/10.5194/amt-13-4927-2020>, 2020.
- Sunilkumar, S., Muhsin, M., Parameswaran, K., Venkat Ratnam, M., Ramkumar, G., Rajeev, K., Krishna Murthy, B., Sambhu Namboodiri, K., Subrahmanyam, K., Kishore Kumar, K., and Shankar Das, S.: Characteristics of turbulence in the troposphere and lower stratosphere over the Indian Peninsula, *Journal of Atmospheric and Solar-Terrestrial Physics*, 133, 36–53, <https://doi.org/10.1016/j.jastp.2015.07.015>, 2015.
- Sutherland, B.: Internal wave reflection in uniform shear, *Quarterly Journal of the Royal Meteorological Society*, 126, 3255–3286, 2000.
- Sutherland, B. R.: Finite-amplitude internal wavepacket dispersion and breaking, *Journal of Fluid Mechanics*, 429, 343–380, 2001.
- Teisserenc de Bort, L.: Variations de la température de l'air libre dans la zone comprise entre 8 km et 13 km d'altitude, *Compt. Rend. Seances Acad. Sci. Paris*, 134, 987–989, 1902.
- Thompson, C. F. and Schultz, D. M.: The Release of Inertial Instability Near an Idealized Zonal Jet,

- Geophysical Research Letters, 48, <https://doi.org/10.1029/2021gl092649>, 2021.
- Thorncroft, C. D., Hoskins, B. J., and McIntyre, M. E.: Two paradigms of baroclinic-wave life-cycle behaviour, *Quarterly Journal of the Royal Meteorological Society*, 119, 17–55, <https://doi.org/10.1002/qj.49711950903>, 1993.
- Tiedtke, M.: A Comprehensive Mass Flux Scheme for Cumulus Parameterization in Large-Scale Models, *Monthly Weather Review*, 117, 1779–1800, [https://doi.org/10.1175/1520-0493\(1989\)117<1779:acmfsf>2.0.co;2](https://doi.org/10.1175/1520-0493(1989)117<1779:acmfsf>2.0.co;2), 1989.
- Trier, S. B., Sharman, R. D., Muñoz-Esparza, D., and Lane, T. P.: Environment and Mechanisms of Severe Turbulence in a Midlatitude Cyclone, *Journal of the Atmospheric Sciences*, 77, 3869–3889, <https://doi.org/10.1175/jas-d-20-0095.1>, 2020.
- Turhal, K., Plöger, F., Clemens, J., Birner, T., Weyland, F., Konopka, P., and Hoor, P.: Variability and trends in the potential vorticity (PV)-gradient dynamical tropopause, *Atmospheric Chemistry and Physics*, 24, 13 653–13 679, <https://doi.org/10.5194/acp-24-13653-2024>, 2024.
- Ullrich, P. A., Melvin, T., Jablonowski, C., and Staniforth, A.: A proposed baroclinic wave test case for deep- and shallow-atmosphere dynamical cores, *Quarterly Journal of the Royal Meteorological Society*, 140, 1590–1602, <https://doi.org/10.1002/qj.2241>, 2014.
- Ullrich, P. A., Jablonowski, C., Kent, J., Lauritzen, P. H., Nair, R., Reed, K. A., Zarzycki, C. M., Hall, D. M., Dazlich, D., Heikes, R., Konor, C., Randall, D., Dubos, T., Meurdesoif, Y., Chen, X., Harris, L., Kühnlein, C., Lee, V., Qaddouri, A., Girard, C., Giorgetta, M., Reinert, D., Klemp, J., Park, S. H., Skamarock, W., Miura, H., Ohno, T., Yoshida, R., Walko, R., Reinecke, A., and Viner, K.: DCMIP2016: A review of non-hydrostatic dynamical core design and intercomparison of participating models, *Geoscientific Model Development*, 10, 4477–4509, <https://doi.org/10.5194/gmd-10-4477-2017>, 2017.
- Umbarkar, M. and Kunkel, D.: Contribution of gravity waves to shear in the extratropical lowermost stratosphere: insights from idealized baroclinic life cycle experiments, *Atmospheric Chemistry and Physics*, 25, 10 159–10 182, <https://doi.org/10.5194/acp-25-10159-2025>, 2025.
- Umbarkar, M., Kunkel, D., Miltenberger, A., Lachnitt, H.-C., Kaluza, T., Schwenk, C., and Hoor, P.: Evidence of gravity wave contribution to vertical shear and mixing in the lower stratosphere: a WISE case study, *Atmospheric Chemistry and Physics*, <https://doi.org/10.5194/egusphere-2025-5142>, preprint, 2025.
- Wagner, J., Dörnbrack, A., Rapp, M., Gisinger, S., Ehard, B., Bramberger, M., Witschas, B., Chouza, F., Rahm, S., Mallaun, C., Baumgarten, G., and Hoor, P.: Observed versus simulated mountain waves over Scandinavia – improvement of vertical winds, energy and momentum fluxes by enhanced model resolution?, *Atmospheric Chemistry and Physics*, 17, 4031–4052, <https://doi.org/10.5194/acp-17-4031-2017>, 2017.
- Wallace, J. M. and Hobbs, P. V.: *Atmospheric Science: An Introductory Survey*, vol. 92 of *International Geophysics Series*, Academic Press, 2 edn., ISBN 978-0-12-732951-2, 2006.
- Wang, M. and Fu, Q.: Stratosphere-Troposphere Exchange of Air Masses and Ozone Concentrations Based on Reanalyses and Observations, *Journal of Geophysical Research: Atmospheres*, 126, <https://doi.org/10.1029/2021jd035159>, 2021.
- Wang, P. K.: Moisture plumes above thunderstorm anvils and their contributions to cross-tropopause transport of water vapor in midlatitudes, *Journal of Geophysical Research: Atmospheres*, 108, <https://doi.org/10.1029/2002jd002581>, 2003.

- Warner, C. D. and McIntyre, M. E.: On the Propagation and Dissipation of Gravity Wave Spectra through a Realistic Middle Atmosphere, *Journal of the Atmospheric Sciences*, 53, 3213–3235, [https://doi.org/10.1175/1520-0469\(1996\)053<3213:otpad0>2.0.co;2](https://doi.org/10.1175/1520-0469(1996)053<3213:otpad0>2.0.co;2), 1996.
- Watanabe, S., Sato, K., and Takahashi, M.: A general circulation model study of the orographic gravity waves over Antarctica excited by katabatic winds, *Journal of Geophysical Research: Atmospheres*, 111, <https://doi.org/10.1029/2005jd006851>, 2006.
- Wedi, N. and Malardel, S.: Non-hydrostatic modelling at ECMWF, European Centre for Medium-Range Weather Forecasts (ECMWF), <https://doi.org/10.21957/RZOJR98E>, 2010.
- Wei, J. and Zhang, F.: Mesoscale gravity waves in moist baroclinic jet-front systems, *Journal of the Atmospheric Sciences*, 71, 929–952, <https://doi.org/10.1175/JAS-D-13-0171.1>, 2014.
- Wei, J. and Zhang, F.: Tracking gravity waves in moist baroclinic jet-front systems, *Journal of Advances in Modeling Earth Systems*, 7, 67–91, <https://doi.org/10.1002/2014ms000395>, 2015.
- Wei, J., Zhang, F., and Richter, J. H.: An Analysis of Gravity Wave Spectral Characteristics in Moist Baroclinic Jet–Front Systems, *Journal of the Atmospheric Sciences*, 73, 3133–3155, <https://doi.org/10.1175/jas-d-15-0316.1>, 2016.
- Wei, J., Zhang, F., Richter, J. H., Alexander, M. J., and Sun, Y. Q.: Global Distributions of Tropospheric and Stratospheric Gravity Wave Momentum Fluxes Resolved by the 9-km ECMWF Experiments, *Journal of the Atmospheric Sciences*, 79, 2621–2644, <https://doi.org/10.1175/jas-d-21-0173.1>, 2022.
- Weyland, F., Hoor, P., Kunkel, D., Birner, T., Plöger, F., and Turhal, K.: Long-term changes in the thermodynamic structure of the lowermost stratosphere inferred from reanalysis data, *Atmospheric Chemistry and Physics*, 25, 1227–1252, <https://doi.org/10.5194/acp-25-1227-2025>, 2025.
- Whiteway, J. A., Pavelin, E. G., Busen, R., Hacker, J., and Vosper, S.: Airborne measurements of gravity wave breaking at the tropopause, *Geophysical Research Letters*, 30, 2–6, <https://doi.org/10.1029/2003GL018207>, 2003.
- Whiteway, J. A., Klaassen, G. P., Bradshaw, N. G., and Hacker, J.: Transition to turbulence in shear above the tropopause, *Geophysical Research Letters*, 31, 2–5, <https://doi.org/10.1029/2003GL018509>, 2004.
- Wilcox, L. J., Hoskins, B. J., and Shine, K. P.: A global blended tropopause based on ERA data. Part II: Trends and tropical broadening, *Quarterly Journal of the Royal Meteorological Society*, 138, 576–584, <https://doi.org/10.1002/qj.910>, 2011.
- Wirth, V. and Szabo, T.: Sharpness of the extratropical tropopause in baroclinic life cycle experiments, *Geophysical Research Letters*, 34, 10–13, <https://doi.org/10.1029/2006GL028369>, 2007.
- WMO: Definition of the Tropopause, *WMO Bulletin*, 6, 136, 1957.
- Woiwode, W., Dörnbrack, A., Bramberger, M., Friedl-Vallon, F., Haenel, F., Höpfner, M., Johansson, S., Kretschmer, E., Krisch, I., Latzko, T., Oelhaf, H., Orphal, J., Preusse, P., Sinnhuber, B. M., and Ungermann, J.: Mesoscale fine structure of a tropopause fold over mountains, *Atmospheric Chemistry and Physics*, 18, 15 643–15 667, <https://doi.org/10.5194/acp-18-15643-2018>, 2018.
- Yoshida, L., Tomikawa, Y., Ejiri, M. K., Tsutsumi, M., Kohma, M., and Sato, K.: Large-Amplitude Inertia Gravity Waves Over Syowa Station: Comparison of PANSY Radar and ERA5 Reanalysis Data, *Journal of Geophysical Research: Atmospheres*, 129, <https://doi.org/10.1029/2023jd040490>, 2024.

- Zahn, A., Brenninkmeijer, C. A. M., Maiss, M., Scharffe, D. H., Crutzen, P. J., Hermann, M., Heintzenberg, J., Wiedensohler, A., Güsten, H., Heinrich, G., Fischer, H., Cuijpers, J. W. M., and van Velthoven, P. F. J.: Identification of extratropical two-way troposphere-stratosphere mixing based on CARIBIC measurements of O₃, CO, and ultrafine particles, *Journal of Geophysical Research: Atmospheres*, 105, 1527–1535, <https://doi.org/10.1029/1999jd900759>, 2000.
- Zängl, G., Reinert, D., Rípodas, P., and Baldauf, M.: The <sc>ICON</sc> (ICOsahedral Non-hydrostatic) modelling framework of <sc>DWD</sc> and <sc>MPI-M</sc>: Description of the non-hydrostatic dynamical core, *Quarterly Journal of the Royal Meteorological Society*, 141, 563–579, <https://doi.org/10.1002/qj.2378>, 2014.
- Zängl, G., Reinert, D., Rípodas, P., and Baldauf, M.: The ICON (ICOsahedral Non-hydrostatic) modelling framework of DWD and MPI-M: Description of the non-hydrostatic dynamical core, *Quarterly Journal of the Royal Meteorological Society*, 141, 563–579, <https://doi.org/10.1002/qj.2378>, 2015.
- Zhang, F.: Generation of mesoscale gravity waves in upper-trophospheric jet-front systems, *Journal of the Atmospheric Sciences*, 61, 440–457, [https://doi.org/10.1175/1520-0469\(2004\)061<0440:GOMGWI>2.0.CO;2](https://doi.org/10.1175/1520-0469(2004)061<0440:GOMGWI>2.0.CO;2), 2004.
- Zhang, F., Wei, J., Zhang, M., Bowman, K. P., Pan, L. L., Atlas, E., and Wofsy, S. C.: Aircraft measurements of gravity waves in the upper troposphere and lower stratosphere during the START08 Field Experiment, <https://doi.org/10.5194/acpd-15-4725-2015>, 2015a.
- Zhang, W., Peng, J., Zhang, W., Wang, S., Li, Z., and Hanyan, W.: Sensitivity of Gravity Wave Momentum Flux Estimates on Separation Methods, *Monthly Weather Review*, 153, 1721–1742, <https://doi.org/10.1175/mwr-d-24-0272.1>, 2025.
- Zhang, Y., Zhang, S., Huang, C., Huang, K., Gong, Y., and Gan, Q.: The interaction between the tropopause inversion layer and the inertial gravity wave activities revealed by radiosonde observations at a midlatitude station, *Journal of Geophysical Research*, 120, 8099–8111, <https://doi.org/10.1002/2015JD023115>, 2015b.
- Zhang, Y., Zhang, S., Huang, C., Huang, K., and Gong, Y.: The Tropopause Inversion Layer Interaction With the Inertial Gravity Wave Activities and Its Latitudinal Variability, *Journal of Geophysical Research: Atmospheres*, 124, 7512–7522, <https://doi.org/10.1029/2019JD030309>, 2019.
- Zülicke, C. and Peters, D.: Simulation of Inertia–Gravity Waves in a Poleward-Breaking Rossby Wave, *Journal of the Atmospheric Sciences*, 63, 3253–3276, <https://doi.org/10.1175/jas3805.1>, 2006.

Appendix

A. Supplementary information to Chapter 3

Gravity wave occurrence: impact of horizontal and vertical grid spacing

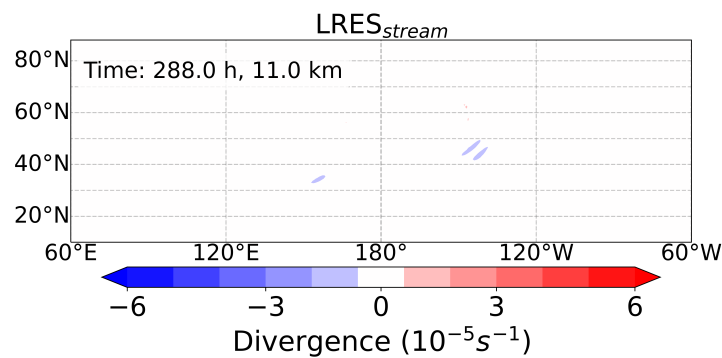


Figure S3.1: The distribution of horizontal divergence at 11 km altitude after 288 h in the LRES experiment indicates that gravity wave signatures are virtually absent in the lower-resolution simulation.

Occurrence of dynamic instability and turbulence

In this section, further analysis of the temporal evolution of N^2 , S^2 and $S^{2'}$ with respect to the occurrence of gradient Richardson number Ri and their implications turbulence and dynamic instability in the LMS across various simulations is provided. The results are derived from two-dimensional probability density functions (PDFs), which quantify the distribution of N^2 - S^2 , and N^2 - $S^{2'}$ pairs in the LMS for 240, 264, 288 and 312 h of model integration.

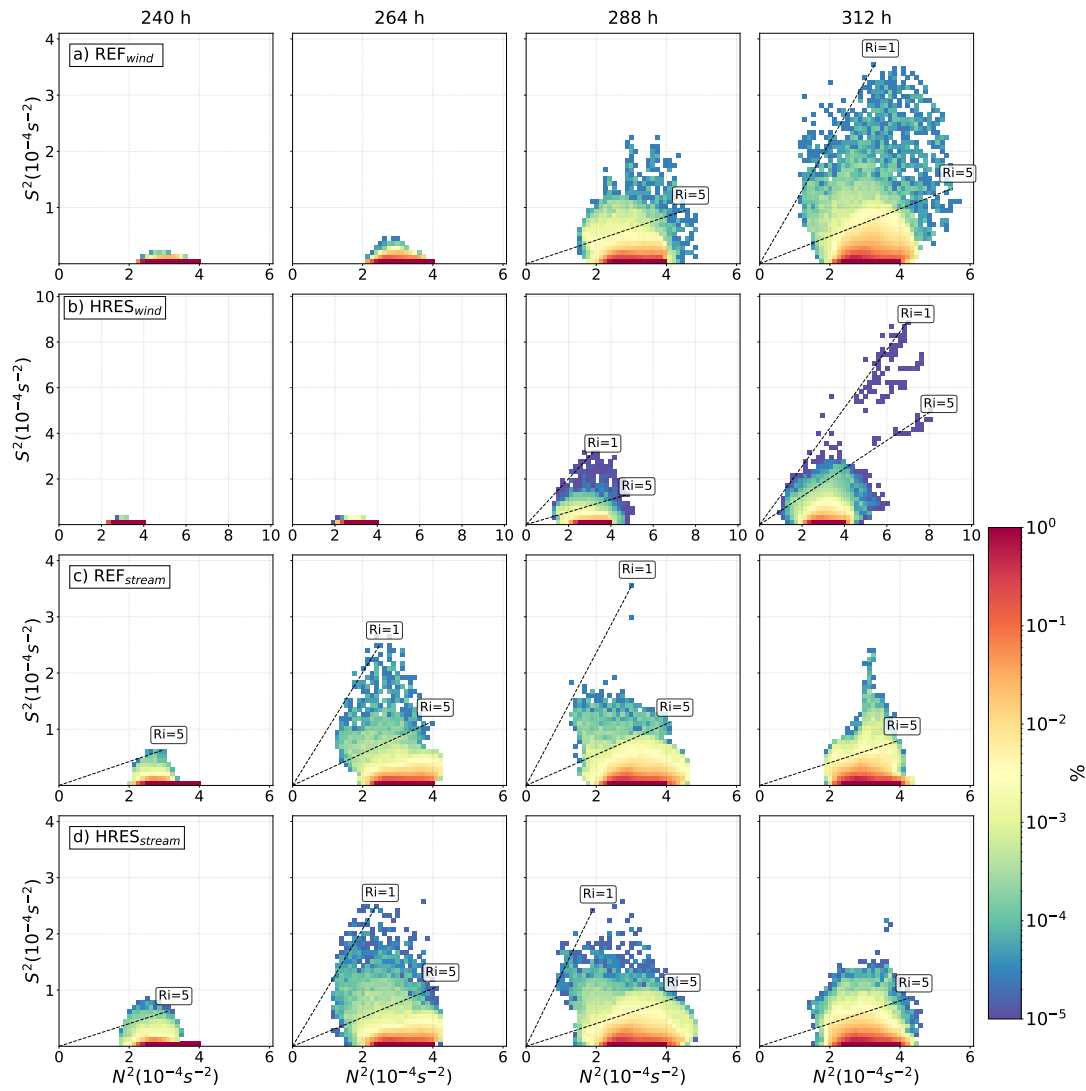


Figure S3.2: Temporal evolution of relative occurrence frequency distribution of N^2 - S^2 pairs for simulations with varying grid sensitivity over Northern Hemisphere in the lowermost stratosphere. Logarithmic occurrence frequency color scale is applied. Dashed lines indicates the gradient Richardson numbers.

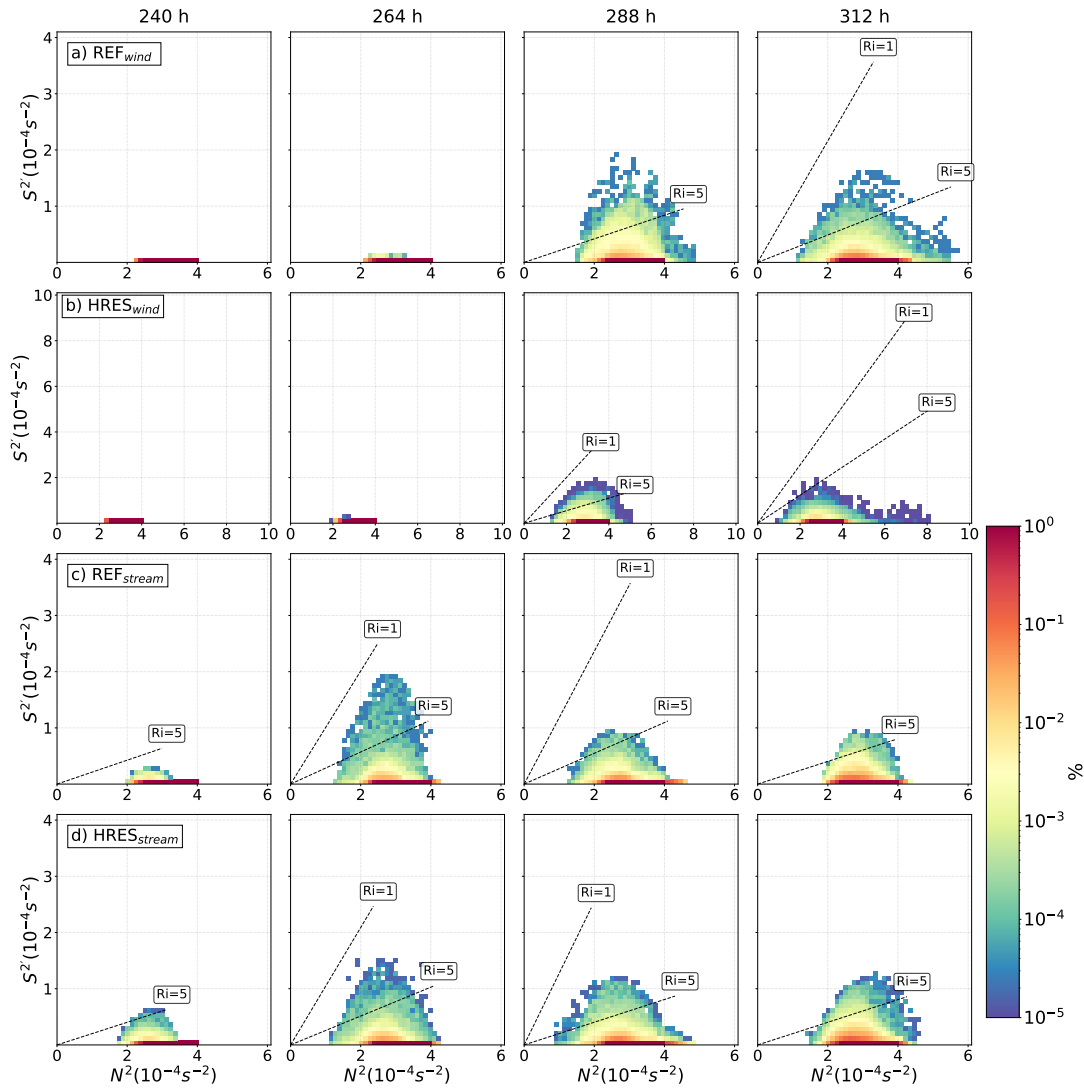


Figure S3.3: Temporal evolution of relative occurrence frequency distribution of N^2 - S^2' pairs for simulations with varying grid sensitivity over Northern Hemisphere in the lowermost stratosphere. Logarithmic occurrence frequency color scale is applied. Dashed lines indicates the gradient Richardson numbers.

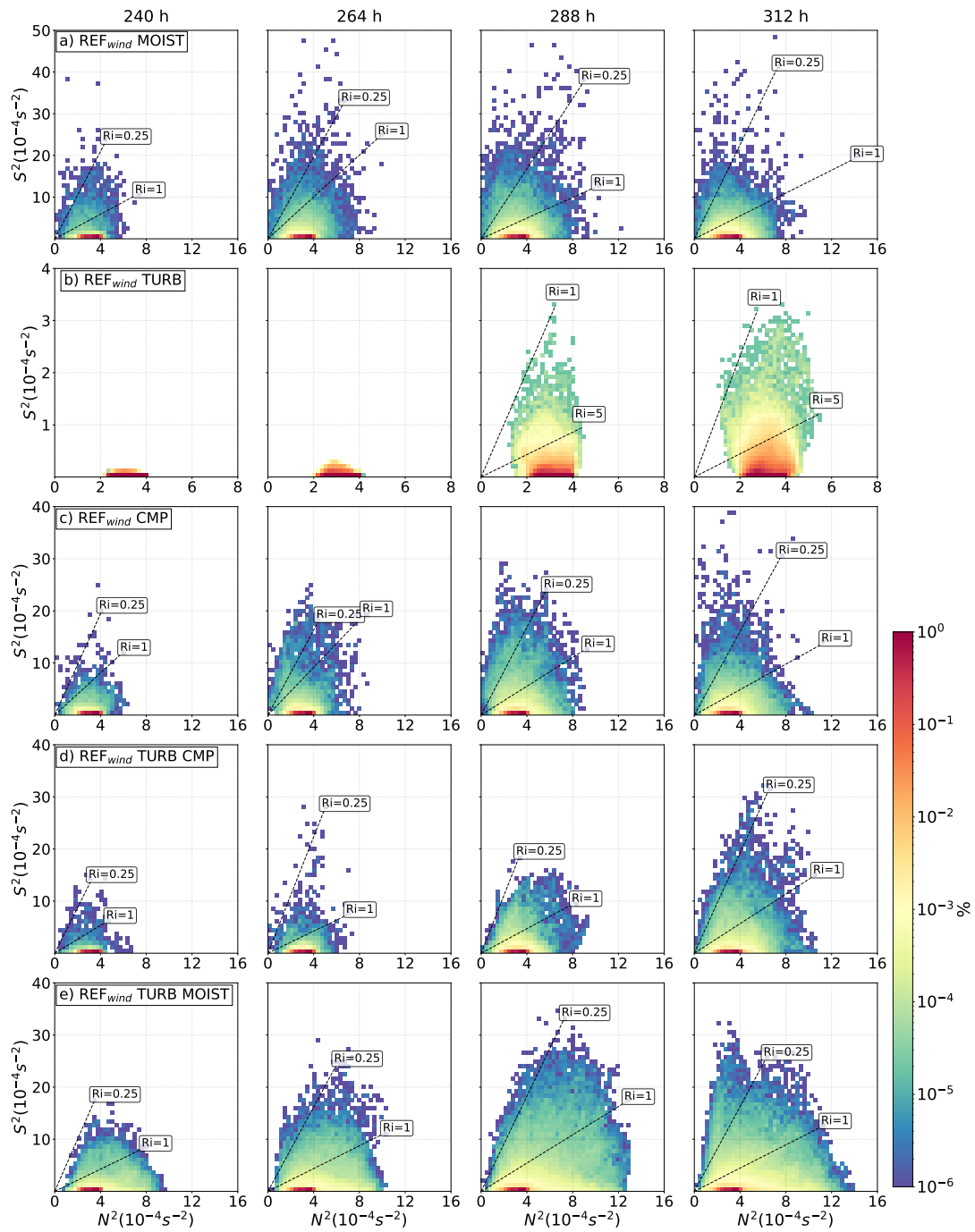


Figure S3.4: As in Figure S3.2 but for the REF_{wind} simulations with varying physical processes.

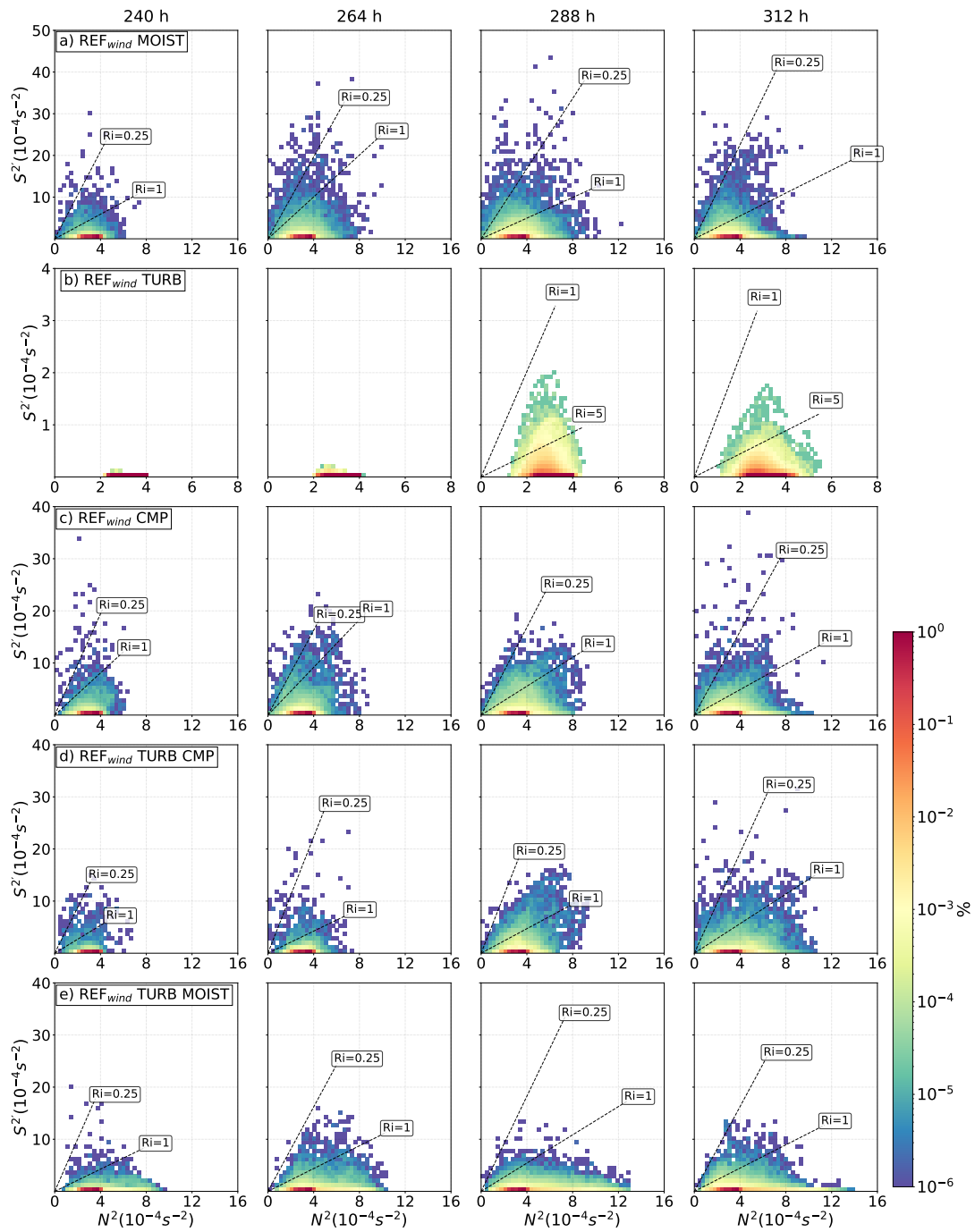


Figure S3.5: As in Figure S3.3 but for the REF_{wind} simulations with varying physical processes.

B. Use of AI Tools

Table 6.1: Use of AI tools throughout the work.

AI tool	Used for	Reason	When
DeepL Translate	Translation and rephrasing	To improve clarity and understanding of technical text written in non-native English	Literature review and manuscript preparation
QuillBot	Grammar and improvement of written language	Better readability	Initial drafting of literature review and writing
ChatGPT-4o/5o	Improvement of written language	Better readability	Initial drafting of the manuscript
Grammarly	Grammar	Better readability	Throughout the manuscript

Acknowledgement

For data protection reasons, the acknowledgements are not included in the digital version. I would like to thank everyone who supported me during my doctoral studies, especially those whose encouragement and assistance have been instrumental in helping me achieve this milestone in my career.

-

Curriculum Vitae

-